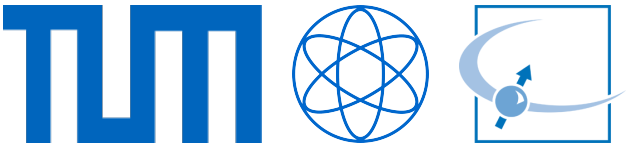

TECHNISCHE UNIVERSITÄT MÜNCHEN
Physik Department
Lehrstuhl für Neutronenstreuung

Neutron Scattering Studies of Magnetic Anisotropies in Chiral Magnets

Alfonso Arturo Chacón Roldán, M.Sc

Vollständiger Abdruck der von der
Fakultät für Physik der Technischen Universität München
zur Erlangung des akademischen Grades eines

Doktors der Naturwissenschaften (Dr. rer. nat.)

genehmigten Dissertation.

Vorsitzender:		Prof. Dr. Johannes Knolle
Prüfer der Dissertation:	1.	Prof. Dr. Peter Böni
	2.	Priv.-Doz. Dr. habil. Rudolf Hackl

Die Dissertation wurde am 17.10.2019 an der Technischen Universität München eingereicht und durch die Fakultät für Physik am 31.01.2020 angenommen.

ABSTRACT

This dissertation studies the role that magnetic anisotropies play in the magnetic phase diagram of cubic chiral magnets. During the last decade, this type of materials has been at the center of much scientific interest driven mainly by the discovery of a skyrmion lattice phase. Skyrmions are topological non-trivial magnetic textures, which means that they cannot be smoothly and continuously transform into trivial kinds of magnetic order, such as ferromagnetism. This topological characteristic yields novel physical properties which make magnetic skyrmions very interesting for future spintronic and memory storage devices. Skyrmions have now been observed in heterostructures, ultrathin magnetic films, and bulk samples with very different properties.

Magnetocrystalline anisotropies determine the preferred propagation direction of the helimagnetic order, which represents the ground state of the systems studied. Applying a magnetic field results in the conical phase after a reorientation of the magnetic helices so that they propagate along the field direction, lifting the degeneracy between equivalent crystallographic directions observed at zero-field. Professor Dr. Markus Garst carried out a detailed theoretical analysis of the role of magnetocrystalline anisotropies in this reorientation for the case of MnSi, for which the magnetic helices propagate along the $\langle 111 \rangle$ axes at zero magnetic field. He identified three distinct cases depending on the crystallographic direction the magnetic field is applied along. His results were corroborated by a thorough magnetization, ac-susceptibility and small-angle neutron scattering study. Overall the experimental observations match the theoretical predictions quite well, and the discrepancies observed could be explained by the formation of topological non-trivial defects at the boundaries between domains as these are fused together. The properties of these topological defects are mainly unknown, and might hold interesting novel physics.

The first theoretical study of the possibility of skyrmions in MnSi expected an additional uniaxial anisotropy to be necessary for their stabilization, as a mean field analysis consistently yielded a higher free energy than the one calculated for the conical phase. It turns out that thermal fluctuations are enough to reduce the energy of the skyrmion lattice below that of the conical state for temperatures just below the transition to the paramagnetic regime. The effects of an external uniaxial anisotropy were studied by means of ac-susceptibility and small-angle neutron scattering using a bespoke uniaxial pressure cell. Applying a magnetic field perpendicular to a finite uniaxial stress, results in an expansion of the stable region of the skyrmion lattice to lower temperatures, while a magnetic field parallel to the pressure axis will prefer a conical magnetic order. Small pressures in the order of a few kbar are enough to completely suppress the skyrmion lattice phase.

The thesis concludes with the discussion of a second skyrmion phase observed in Cu_2OSeO_3 at low temperatures just below the transition to the field polarized phase, when the magnetic field is applied along a $\langle 100 \rangle$ axis, which is the preferred axis of propagation of the helices in this compound. This new phase is stabilized by cubic magneto crystalline anisotropies, which gain in strength with decreasing temperature. This is the first example of two separate skyrmion phases in any material studied so far.

Diese Dissertation untersucht die Rolle, die magnetische Anisotropien in dem Phasendiagramm von kubischen chiralen Magneten spielen. In den letzten Jahren sind diese Art von Materialien auf Grund der Entdeckung von magnetischen Skyrmionen in den wissenschaftlichen Fokus gerückt. Skyrmionen sind topologisch nicht-triviale magnetische Texturen, was bedeutet, dass sie nicht kontinuierlich in eine topologisch triviale Anordnung, wie z. B. Ferromagnetismus, überführt werden können. Diese topologische Eigenschaft bewirkt neue physikalische Phänomene, wodurch magnetische Skyrmionen für zukünftige spintronische Technologien und Speichermedien besonders geeignet sind. Magnetische Skyrmionen wurden bislang in Heterostrukturen, ultradünnen Schichten und in verschiedenen Sorten von chiralen Magneten nachgewiesen.

Magnetokristalline Anisotropien bestimmen in diesen Systemen die bevorzugte Propagationsrichtung der helimagnetischen Ordnung, welche den Grundzustand darstellt. Legt man ein Magnetfeld an, findet ein Phasenübergang in die sogenannte konische Phase statt. Dabei drehen sich die Helices kontinuierlich bis sie in Richtung des angelegten Magnetfeldes propagieren, wodurch die von Symmetrien des Systems bedingte Entartung aufgehoben wird. Professor Dr. Markus Garst führte eine theoretische Analyse der Rolle von magnetokristallinen Anisotropien bezüglich eines solchen Übergangs in MnSi durch. In MnSi propagieren die Helices im Nullfeld entlang den $\langle 111 \rangle$ kristallographischen Achsen des Systems. Professor Garst identifizierte drei unterschiedliche Fälle, die von der Richtung des Magnetfelds bezüglich der Kristallstruktur bestimmt werden. Diese theoretischen Vorhersagen wurden durch ausführliche Messungen der Magnetisierung und der ac-Suszeptibilität, sowie mit Hilfe von Kleinwinkelneutronenstreuung überprüft. Experimentelle Ergebnisse und theoretische Vorhersagen stimmen sehr gut überein. Die Unstimmigkeiten, die beobachtet wurden, konnten durch die Entstehung von topologisch nicht-trivialen Defekten an den Grenzen zwischen Domänen erklärt werden. Ihre Eigenschaften sind bislang unbekannt und könnten interessante neue Physik offenbaren.

Die ersten theoretischen Studien zu Skyrmionen in MnSi erwarteten, dass eine zusätzliche uniaxiale Anisotropie notwendig sein würde, um diese magnetischen Texturen zu stabilisieren. Mit der Entdeckung des Skyrmionengitters in MnSi wurde klar, dass thermische Fluktuationen ausreichend sind, um die Skyrmionen in einem kleinen Temperaturbereich an der Grenze zum Übergang zum paramagnetischen Bereich zu stabilisieren. Die Effekte von zusätzlichen uniaxialen Anisotropien wurden anhand von ac-Suszeptibilität Messungen und Kleinwinkelneutronenstreuung mit Hilfe einer maßgefertigten, uniaxialen Druckzelle untersucht. Legt man ein Magnetfeld senkrecht zur uniaxialen Druckachse an, wird der stabile Bereich des Skyrmiongitters bezüglich tieferer Temperaturen erweitert. Legt man das Magnetfeld stattdessen parallel zur uniaxialen Druckachse an, wird die Skyrmion Phase unterdrückt und die konische Propagation bevorzugt. Uniaxialer Stress in der Ordnung von ein paar kilobar reicht aus um die Skyrmiongitter vollkommen zu unterdrücken.

Die Arbeit schließt mit der Diskussion einer zweite Skyrmion Phase in Cu_2OSeO_3 bei tiefen Temperaturen unterhalb des Übergangs zum feldpolarisierten Bereich für Magnetfelder entlang einer $\langle 100 \rangle$ Achse ab. Diese Phase wird von kubischen, magnetokristallinen Anisotropien stabilisiert, die mit sinkenden Temperaturen stärker werden. Diese ist das erste Bespiel, in dem zwei unabhängige Skyrmionen Phasen in einem Material beobachtet werden.

CONTENTS

MOTIVATION

In a late-night in 1980, at the high magnetic field laboratory in Grenoble, Klaus von Klitzing observed for the first time that the Hall conductance of a two-dimensional electron gas at very low temperatures and high magnetic fields takes specific values as a function of magnetic field strength, resulting in a sequence of wide plateaus [1]. The same values were measured for different sample shapes, and even different chemical compositions. Von Klitzing received the Nobel physics prize just five years later for the discovery of the so-called integer quantum hall effect (IQHE). David Thouless and colleagues recognized just two years after von Klitzing measurements that topology was at the heart of the problem [2]. However, in the following years, the IQHE was considered a somewhat special case, due in fact to the extreme experimental conditions necessary to observe these phenomena. Two decades later experimental studies of graphene reignited the subject of topologically driven states in two dimensional systems, which led Charles Kane and Eugene Mele to theorize that graphene could show topological characteristic without the presence of magnetic field, due to spin-orbit coupling, where the role of the magnetic field is played by the spin of the electron, as had been proposed by Haldane in work published during the 80s [3–5]. Graphene's spin-orbit coupling is not strong enough to result in topological states, but soon thereafter Shou-Cheng Zhang and collaborators at the Stanford University proposed new topological systems, these were studied in the group of Laurens Molenkamp and the first so-called topological insulators were confirmed [6, 7]. To date, topological materials fuel the study of new physical phenomena and the imagination of researchers as to what kind of interesting new physics could be observed in these systems. The study of Weyl semimetals and the use of topological states in quantum computing is only a small part.

A different aspect of topology in physics is captured by topologically non-trivial magnetic textures. These have drawn substantial scientific interest, as they are very promising in the context of consumer low-power spintronic devices, due to their real space topological properties [8–10]. The type of non-trivial magnetic order most studied so far are so-called magnetic skyrmions. First observed as lattices stabilized by thermal fluctuations in cubic chiral magnets such as MnSi and FeGe, among others, skyrmions have now been identified in ultrathin films and multilayers [11–13]. Their size ranges between a few nm and 100 nm, which makes them very attractive for information storage devices, especially due to their increased stability, since they cannot be continuously deformed into a trivial spin arrangement. Their non-trivial topology also results in emergent electrodynamics resulting in an additional contribution to the Hall effect, the so-called topological Hall effect, by which the electrons are deviated of their trajectories due to the emergent magnetic flux of the skyrmion [14]. In turn, the skyrmion also feels a force exerted by the electrons flowing through the sample, when the current exceeds a critical value to unpin the lattice, this is referred to as the skyrmion Hall effect [15–17].

The electrical current densities necessary to set the skyrmion in motion are four orders of magnitude smaller, than those required to move conventional domain walls in ferromagnets [15]. This property makes skyrmions particularly interesting for race track memories, in which the skyrmions would represent "1" bit and their absence would represent a "0" bit. To read the information on the racetrack, bits are moved using electrical currents instead of moving the reader, as is done in conventional hard drives. Hence, a skyrmion racetrack memory would consume much less power, than one moving ferromagnetic domains [18, 19]. The particle-

like nature of skyrmions could be exploited in new types of transistors and logic gates, as has been demonstrated in micromagnetic simulations [20, 21]. Furthermore, skyrmion devices have been proposed in the field neuromorphic computing, which attempts to implement the brain's ability to work on a large multitude of tasks in parallel and with low power consumption [22]. The study of the interactions of skyrmions with light and other types of magnetic structures, as well as with other topological excitations such as superconducting vortices and Majorana fermions, promises new phenomena and exotic states of matter.

The stabilization of skyrmions is particularly important for the development of the devices mentioned above. While the amount of materials able to host skyrmions keeps increasing, these are mostly confined to temperatures well below room temperature and require finite magnetic fields. This thesis studies the role of magnetic anisotropies in the phase diagrams of cubic chiral magnets, a family that can host magnetic skyrmions and includes different types of materials, such as metals and insulators. The experimental technique chosen is primarily small-angle neutron scattering, which exploits the incommensurability and large lattice constant of the skyrmion crystals, when compared with atomic lattices. The identification of several coexisting phases is also possible by exploiting different experimental geometries, without the need to change the experimental parameters such as temperature and field direction.

Chapter 1 gives a short introduction into magnetic interactions, topological magnetic order and a compact overview of the research carried out in the last decade in the field of magnetic skyrmions. Small angle neutron scattering and the specific large facility instruments used are discussed in chapter 2. The effects of magnetocrystalline anisotropies on the transition from the helical to the conical phase in MnSi are presented in chapter 3. Chapter 4 reports the effects on the magnetic order in MnSi of introducing an additional uniaxial anisotropy by means of a helium loaded uniaxial pressure cell. The recent discovery of a second skyrmion lattice phase stabilized at low temperatures and magnetic fields just below the transition to the field polarized phase is discussed in chapter 5. The thesis is concluded with a short summary and outlook.

1

MAGNETIC SKYRMIONS AND TOPOLOGY IN MAGNETISM

Technological applications of magnetism, and more specifically magnetic order, are ubiquitous in modern everyday life. Most of these take advantage of ferromagnetic order, where all spins of the system align in a preferred direction. Fridge magnets, computer hard drives, small motors found in children toys, among many others, are examples of this. At the core of magnetic order is the interaction between unpaired electrons, which results in correlated behavior among large ensembles of particles. There are different types of interactions that affect the resulting phenomena arising from these correlations. This thesis explores the observation of large topological non-trivial magnetic structures consisting of magnetic spin whirls known as skyrmions, which originate from electron correlations. This chapter first reviews different magnetic interactions, followed by an introduction to magnetic skyrmions discussing their discovery as well as the research state of the art. The concept of topology, at the core of the study of magnetic skyrmions, is then introduced. The chapter finishes by examining the resulting emergent electrodynamics at the center of the technological potential of magnetic skyrmions.

1.1 MAGNETIC ORDER AND MAGNETIC ANISOTROPY

Consider the Coulomb interaction between two electrons and a fixed positive charge Ze, the Hamiltonian reads:

$$\mathcal{H} = \mathcal{H}_0(\boldsymbol{r}_1) + \mathcal{H}_0(\boldsymbol{r}_2) + \frac{e^2}{4\pi\epsilon_0|\boldsymbol{r}_1 - \boldsymbol{r}_2|} \tag{1.1}$$

where $\mathcal{H}_0$ is the one electron Hamiltonian, given by:

$$\mathcal{H}_0 = -\frac{\hbar^2}{2m}\nabla^2 + V \tag{1.2}$$

where V is the potential of the positive point charge. Note that this Hamiltonian is ignoring the spin-orbit interaction. Electrons are fermions, thus their wave function must be antisymmetric. This condition can be fulfilled by either an antisymmetric spin part and a symmetric spatial component, resulting in a singlet state Ψ_S ($S = 0$), or by a symmetric spin part and an antisymmetric spatial component, resulting in a triplet state Ψ_T ($S = 1$):

$$\Psi_S = \frac{1}{\sqrt{2}}\left[\psi_a(\boldsymbol{r}_1)\psi_b(\boldsymbol{r}_2) + \psi_a(\boldsymbol{r}_2)\psi_b(\boldsymbol{r}_1)\right]\chi_S \tag{1.3}$$

$$\Psi_T = \frac{1}{\sqrt{2}}\left[\psi_a(\boldsymbol{r}_1)\psi_b(\boldsymbol{r}_2) - \psi_a(\boldsymbol{r}_2)\psi_b(\boldsymbol{r}_1)\right]\chi_T \tag{1.4}$$

with $\psi_a(\boldsymbol{r}_1)$ and $\psi_b(\boldsymbol{r}_2)$ the state of the first and and second electron, respectively. One can write an effective Hamiltonian to produce the same eigenvalues taking advantage that the energy difference can be parameterized as a function of spin:

$$\hat{\mathcal{H}} = \frac{1}{4}(E_S + 3E_T) - (E_S - E_T)\boldsymbol{S}_1 \cdot \boldsymbol{S}_2 \tag{1.5}$$

with E_S and E_T the energies of the singlet and triplet state respectively, and S_1, S_2 the spin states. The effective Hamiltonian consists of a constant term and spin dependent term, which, together with the exchange constant J:

$$J = \frac{E_S - E_T}{2} = \int \psi_a^*(\boldsymbol{r}_1)\psi_b^*(\boldsymbol{r}_2)\hat{\mathcal{H}}\psi_a(\boldsymbol{r}_2)\psi_b(\boldsymbol{r}_1)\mathrm{d}\boldsymbol{r}_1\mathrm{d}\boldsymbol{r}_2 \tag{1.6}$$

reads:

$$\hat{\mathcal{H}}_{\text{spin}} = -2J\boldsymbol{S}_1 \cdot \boldsymbol{S}_2. \tag{1.7}$$

Hence, since energy has to be minimized, the Coulomb interaction results in a preferred alignment of the spins of both electrons, either parallel or antiparallel, depending on the sign of the exchange constant. This is called the exchange interaction.

The spin Hamiltonian above can be readily derived for a system of two electrons, see, for example, [23, 24]. The generalization to a system of N particles, however, is quite complex. Instead, different models can be used to approximate the interactions in an extensive system, such as the Heisenberg model with the Hamiltonian

$$\hat{\mathcal{H}} = -\sum_{ij} J_{ij}\boldsymbol{S}_i\boldsymbol{S}_j. \tag{1.8}$$

Note that the spins here are usually some relevant sum over the interacting atoms and the factor of 2 is recovered due to double counting.

There are other types of exchange interactions which include an intermediary between the spins. A typical example is superexchange, where the interacting magnetic ions couple through a non-magnetic atom that sits in-between. Allowing the electron to hop between the magnetic ions reduces the energy of the system and typically favors antiferromagnetism, i. e., antiparallel magnetic ordering. In metals, the conduction band electrons mediate the indirect exchange, also known as the RKKY interaction.

A different type of exchange plays a vital role in the materials studied in this thesis, the so-called Dzialoshinskii-Moriya interaction, with the Hamiltonian

$$\hat{\mathcal{H}}_{\text{DM}} = \boldsymbol{D} \cdot \boldsymbol{S}_1 \times \boldsymbol{S}_2. \tag{1.9}$$

Proposed first by Dzialoshinskii on a phenomenological basis [25], it was derived by Moriya by expanding the theory of superexchange interaction to include spin-orbit coupling [26]. It is also known as the antisymmetric exchange since $\boldsymbol{D}$ vanishes when the crystal has inversion symmetry. This interaction drives spins to align perpendicular to each other in a plane perpendicular to $\boldsymbol{D}$, often this results in small deviation of the spins from the order dictated by stronger terms in the Hamiltonian, e. g., in some antiferromagnets it leads to a small canting of spins perpendicular to the propagation vector resulting in so-called weak ferromagnetism, for example in insulating and superconducting cuprates [27].

Magnetocrystalline Anisotropy

The Heisenberg Hamiltonian presented above is isotropic, i. e., there is no preferred space direction in which the spins should point. Only their relative direction to each other is important. Anisotropic effects break this symmetry. Their contribution to the Hamiltonian is usually small but essential for technological applications. In their absence, a magnetized state defined by its direction, would not be very stable since it would be very sensitive to small changes in the

magnetic field direction. One can define anisotropic contributions as the energetic differences when magnetizing a given compound along different crystallographic directions. In the case of ferromagnets, they manifest, among others, in the saturation fields. These tend to be very small when applied along the preferred axis of magnetization, also called the easy-axis of the system and can become quite large when the magnetic field points along its hard-axis.

Typically we observe anisotropy concerning the crystalline structure of the object or its shape. The former is known as magnetocrystalline anisotropy and its mainly a consequence of spin-orbit interaction, the latter is known as shape anisotropy, and its microscopic origin lies in dipole-dipole interaction. Spin-orbit coupling is a relativistic phenomenon, and it is explained briefly below.

Consider an electron orbiting around a positive charged nucleus. In the frame of reference of the electron the nucleus appear to be orbiting around it, resulting in a magnetic field:

$$\boldsymbol{B} = \frac{\boldsymbol{\mathcal{E}} \times \boldsymbol{v}}{c^2} \tag{1.10}$$

with

$$\boldsymbol{\mathcal{E}} = -\nabla V(r) = -\frac{\boldsymbol{r}}{r}\frac{dV(r)}{dr} \tag{1.11}$$

the electric field of the nucleus at the electron and $V(r)$ the related potential energy. For a hydrogen like atom of charge Ze the electric field $\boldsymbol{\mathcal{E}}$ reads:

$$\boldsymbol{\mathcal{E}} = -\frac{Ze\boldsymbol{r}}{4\pi\epsilon_0 r^3}. \tag{1.12}$$

The interaction of the electron spin with this magnetic field is captured by the Hamiltonian:

$$\mathcal{H}_{\text{so}} = -\frac{1}{2}\boldsymbol{\mu}_s \cdot \boldsymbol{B} = \frac{g\mu_B^2 Z}{4\pi\epsilon_0 r^3}\boldsymbol{S}\cdot\boldsymbol{L} \tag{1.13}$$

with the angular momentum of the electron $\hbar\boldsymbol{L} = m_e\boldsymbol{r}\times\boldsymbol{v}$, the magnetic moment $\boldsymbol{\mu}_s = g\mu_B\boldsymbol{S}$ and the Bohr magneton μ_B. The factor of one half is a relativistic correction called the Thomas precession [28] arising from the fact that the reference frame is rotating in the opposite direction, for an elegant derivation from the Dirac equation please review [23]. Spin-orbit coupling can be interpreted as a coupling between the electron and its orbital motion, which is in turn coupled to the crystal lattice, hence the anisotropic contribution to the Hamiltonian.

Instead of considering all microscopic contributions to the anisotropy, one can use a phenomenological approach base on the spatial symmetry of the system. In the case of cubic crystals there are three equivalent directions which can be defined as the x,y, and z axes.

Consider a system with magnetization $\boldsymbol{M}$. The magnitude of $\boldsymbol{M}$ is not relevant for the calculation, only its direction, hence the anisotropic free energy contribution is expanded as a function of the components of a unit vector $\boldsymbol{m} = \frac{\boldsymbol{M}}{|\boldsymbol{M}|}$, m_x, m_y and m_z. The anisotropic energy as a function of the lowest order combination of $\boldsymbol{m}$ components that satisfy the cubic symmetry reads

$$F_a = K_0 + K_1\left(m_x^2m_y^2 + m_y^2m_z^2 + m_z^2m_x^2\right) + K_2m_x^2m_y^2m_z^2 + ... \tag{1.14}$$

Note that a term of the form $m_x^4 + m_y^4 + m_z^4$ is also compatible with the symmetry operations, however it is not independent of the combinations presented above, since

$$m_x^4 + m_y^4 + m_z^4 = 1 - 2\left(m_x^2m_y^2 + m_y^2m_z^2 + m_z^2m_x^2\right). \tag{1.15}$$

One can ignore K_0 since it represents an isotropic contribution. If $K_2 = 0$, the situation is fairly simple. For $K_1 > 0$ the preferred axis of magnetization are the main crystallographic directions $\langle 100 \rangle$, i. e., there exist six equivalent energy minima, the space diagonals are hard axes, and the $\langle 110 \rangle$ axes are saddle points and considered medium-hard axes, which is the case of body-centered-cubic iron. If $K_1 < 0$ then the situation is turned around, the space diagonals $\langle 111 \rangle$ become easy axis resulting in eight equivalent energy minima, while the main axes become energetically unfavorable. Taking into account contributions from the sixth order term, i. e., $K_2 \neq 0$, six different scenarios are possible depending on the relative strength and sign of K_1 and K_2, and even the face diagonals $\langle 110 \rangle$ can become the easy axis of the system.

The results of the study on the role of magnetocrystalline anisotropy in the phase transitions and magnetic phase diagram of cubic chiral magnets are addressed in chapters 3 and 5 respectively.

Stress anisotropy

The magnetoelastic coupling between spins and orbital configuration may result in a distortion of the position of the ions if it results in a net reduction of the free energy, also known as magnetostriction. Similarly, a deformation of the lattice by the application of stress σ_{ij} might affect the magnetic order. Consider the case of uniaxial stress σ applied along $\boldsymbol{\gamma}$, the contribution to the free energy from the magnetoelastic coupling writes

$$F_\sigma = -\frac{3}{2}\lambda_{100}\sigma \sum_i m_i^2 \gamma_i^2 - 3\lambda_{111}\sigma \sum_{i \neq j} m_i m_j \gamma_i \gamma_j \tag{1.16}$$

with the magnetostriction constants λ_{100} and λ_{111} defined by

$$\lambda_{100} = \frac{-2}{3}\frac{B_1}{c_{11} - c_{12}} \qquad \lambda_{111} = -\frac{1}{3}\frac{B_2}{c_{44}} \tag{1.17}$$

where B_1 and B_2 are the magnetoelastic coupling constants, while c_{11}, c_{12} and c_{44} are the crystal elastic stiffness constants. The stress anisotropic energy depends on the direction of the magnetization. In case stress is applied along the $\langle 100 \rangle$ or $\langle 111 \rangle$, the contribution to the free energy simplifies to

$$F_\sigma = \text{const.} + \frac{3}{2}\lambda_{100}\sigma \sin^2\theta \tag{1.18}$$

and

$$F_\sigma = \text{const.} + \frac{3}{2}\lambda_{111}\sigma \sin^2\theta, \tag{1.19}$$

respectively, with θ the angle between the axis of magnetization and the stress axis, i. e., $\boldsymbol{m} \cdot \boldsymbol{\gamma} = \cos\theta$. Both of these cases describe a uniaxial anisotropy, which, depending on the sign of $\lambda\sigma$, can be either easy-axis or easy-plane.

A study of the effects of uniaxial pressure on the magnetic phase diagram of MnSi is presented in chapter 4.

1.2 MAGNETIC SKYRMIONS

The different contributions mentioned above result in a arrangement of different types of magnetic order, some of these are collinear, such as ferromagnetism, antiferromagnetism,

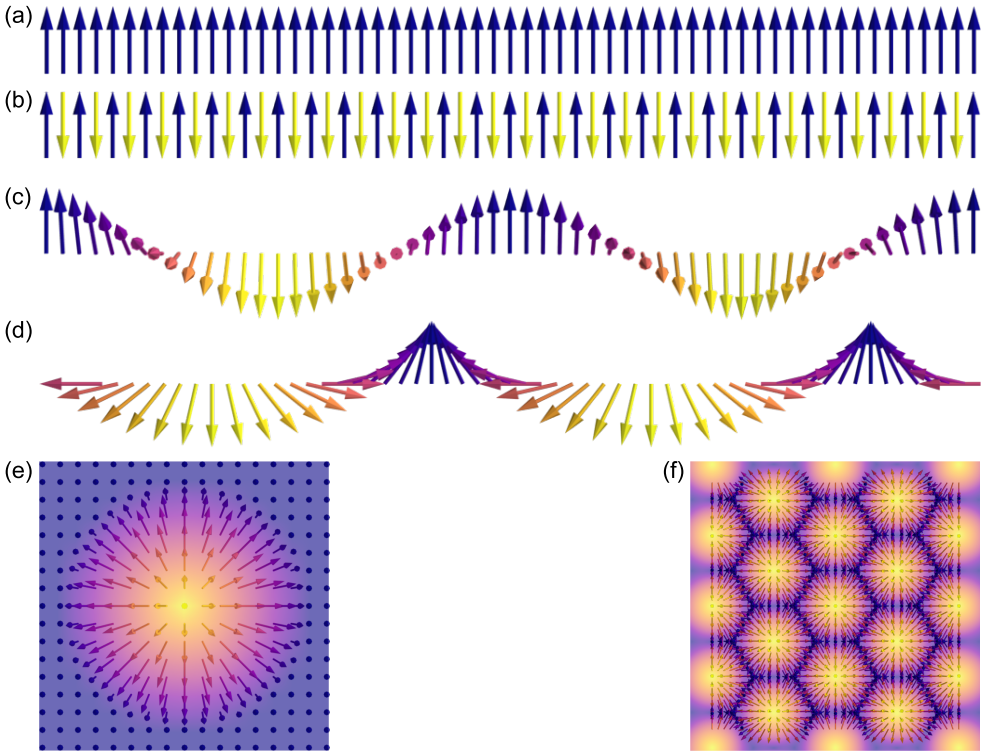

Figure 1.1: (a) - (d) Schematic representations of different types of magnetic order: ferromagnetic, antiferromagnetic, helical and cycloidal order. (e) Single Néel Skyrmion. (f) Néel Skyrmion lattice.

and ferrimagnetism, others are non-collinear, for example, spirals, helices, helicoids, and the skyrmion crystal, among others. This thesis focuses on the study of non-collinear forms of magnetic order, such as magnetic helices and skyrmion crystals, represented schematically in figure 1.1.

The name skyrmion is derived from the work of Tony Skyrme in the 1960s. Skyrme recognized that non-trivial topological solitons of pion fields can describe nucleons. Thus explaining the significant lifetime of particles as a consequence of their topological characteristics [29–31]. Over time, the name skyrmion has been used to refer to localized and non-trivial solutions in different areas of physics, from particle physics to condensed matter physics [32–37].

Magnetic skyrmions were first proposed in 1989 by Bogdanov and Yablonskii as possible ground state solutions in a zero temperature model for magnetic materials of the crystallographic classes $C_n, C_{n,v}, D_n, S_4$, or D_{2d} with $n = 3, 4, 6$ [38]. In collaboration with Hubert, Bogdanov then calculated the strength of the effective anisotropic coupling constants in order for a skyrmion lattice to become stable, and identified the cubic systems MnSi, FeGe, as well as the families $Fe_{1-x}Co_xSi$ and $Mn_{1-x}Co_xSi$, as promising candidates when an easy axis is superimposed externally [39]. In subsequent works, through a collaboration with Rößler, Bogdanov studied the possibility of skyrmion lattices in thin films and multilayers, driven by the lack of inversion symmetry at the interfaces and surface of these systems [40]. Bogdanov, Rößler and Pfleiderer use the name skyrmion for the first time in a 2006 article, where the skyrmion model was extended to consider a magnetization with variable amplitude, motivated by the magnetization of metals, such as the cubic magnet MnSi [41].

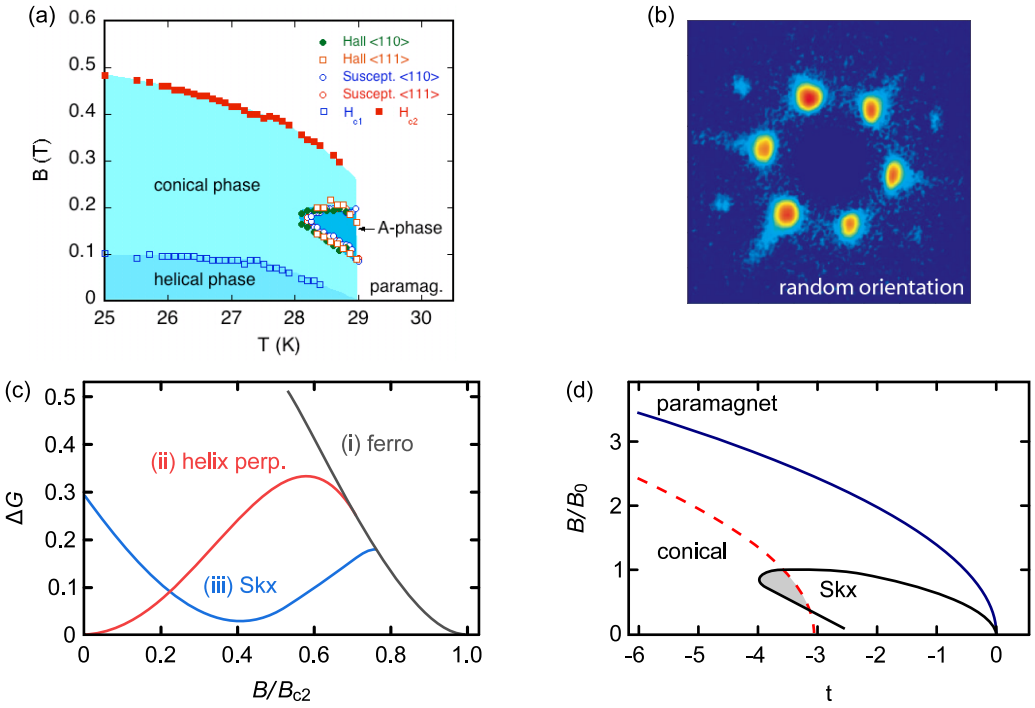

Figure 1.2: (a) Magnetic phase diagram of MnSi consisting of a helical phase at low fields and a conical phase in the largest portion of the phase diagram. The skyrmion lattice is observed within the A-phase. (b) Neutron scattering pattern obtained for a magnetic field applied parallel to the incoming neutron beam along a random crystallographic direction. (c) Difference in energy with respect to the conical phase, without corrections from thermal fluctuations. (d) Resulting theoretical phase diagram when thermal fluctuations are considered, only results below the dashed line are reliable. Figures adapted from [11].

It was thus surprising when in 2009 the first skyrmion lattice was identified with the help of small-angle neutron scattering (SANS) in the so-called A-phase of MnSi, a small pocket in the magnetic phase diagram at medium magnetic fields, relative to the transition to the field polarized phase, closed to the helimagnetic transition temperature [11], cf. figure 1.2 (a). In the past, the experimental observations within the A-phase were interpreted as a spontaneous discrete reorientation of the helical propagation direction [42, 43]. Previous SANS experiments were carried out with a magnetic field applied perpendicular to the neutron beam, since the conical propagation lies parallel to the former and would not be observable in a different configuration. Hence, the scattering pattern showed only two of the propagation vectors corresponding to the skyrmion lattice. Mühlbauer *et al.* carried out their experiment with a magnetic field parallel to the neutron beam, resulting in a six-fold pattern of propagation vectors, originating from a hexagonal skyrmion lattice depicted in figure 1.2 (b).

As mentioned above, MnSi is a cubic crystal. Thus, from the models studied, an additional uniaxial anisotropy was expected in order to stabilize the skyrmionic state. This discrepancy is resolved by considering the free energy

$$\exp -\mathcal{G} = \int D\boldsymbol{M} \exp(-F[\boldsymbol{M}]) \tag{1.20}$$

with $F[\boldsymbol{M}]$ the Ginzburg Landau energy functional

$$F[\boldsymbol{M}] = \int d^3r \left[r_0 \boldsymbol{M}^2 + J\left(\nabla \boldsymbol{M}\right)^2 + 2D\boldsymbol{M} \cdot (\nabla \times \boldsymbol{M}) + U\boldsymbol{M}^4 - \boldsymbol{B} \cdot \boldsymbol{M} \right]. \tag{1.21}$$

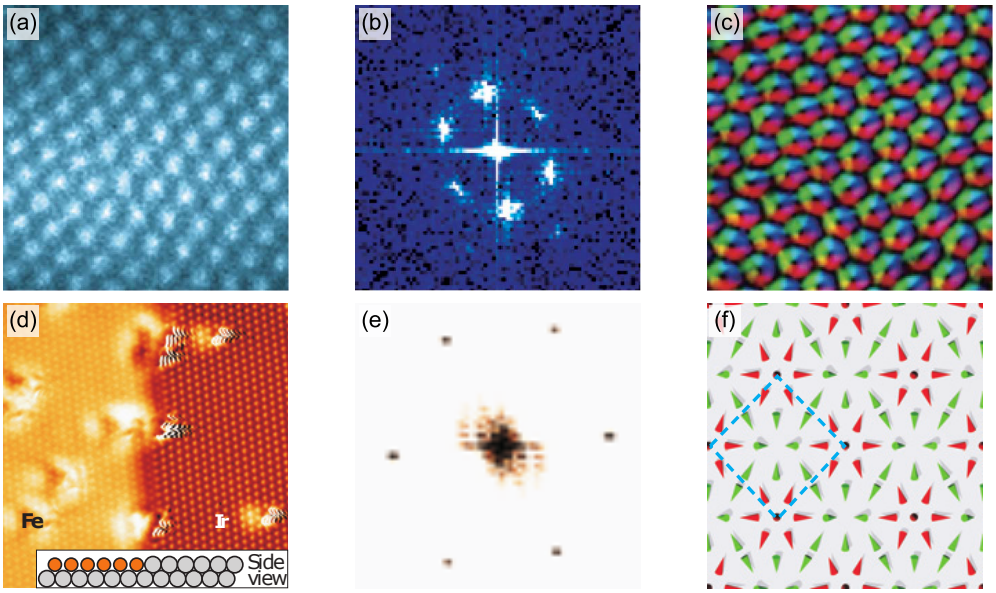

Figure 1.3: (a) Real space image of the skyrmion lattice in $Fe_{0.5}Co_{0.5}Si$ obtained via Lorentz TEM. (b) Fast fourier transformation pattern from the real image in (a). (c) Image of the in-plane component of the magnetization in the skyrmion lattice, the colors represent the different direction of the in-plane component. (d) Image of the Fe monolayer on $Ir(111)$. (e) Fourier transformation of the image in (a), the Fe atoms order hexagonally. (f) Schematic representations of the nanoskyrmions observed in the monolayers, the cones represent the Fe atoms and are pointing in the magnetization direction, note that the skyrmions are arranged on a square lattice. (a) - (c) adapted from [44], (d) - (f) adapted from [12].

This mean-field free energy of the skyrmion lattice is consistently higher than that of a conical magnetic order, as shown in figure 1.2 (c). By including the leading correction arising from Gaussian fluctuations to mean-field theory

$$\mathcal{G} \approx F\left[\boldsymbol{M}_0\right] + \frac{1}{2}\log\det\left(\frac{\partial^2 F}{\partial \boldsymbol{M}\partial \boldsymbol{M}}\right)\Bigg|_{\boldsymbol{M}_0} \tag{1.22}$$

Mühlbauer *et al.* were able to show that thermal fluctuations stabilized the skyrmion lattice with respect to the conical state [11], without the need of an additional uniaxial anisotropy. Figure 1.2 (d) depicts the resulting phase diagram. The discovery of the skyrmionic state in MnSi was followed by the real space imaging of the novel magnetic structure by Yu *et al.*, using Lorentz force transmission electron microscopy on a thinned sample of $Fe_{0.5}Co_{0.5}Si$[44], cf. figure 1.3 (a) - (c) and the observation of magnetic skyrmions in Fe monolayers grown on Ir(111) by spin-polarized scanning tunneling microscopy [12]. The latter represents an entirely different avenue of stabilization of skyrmions. As mentioned above the DM interaction originates from a lack of inversion symmetry, which in MnSi and $Fe_{0.5}Co_{0.5}Si$ is embedded in the crystal structure. In the ferromagnetic thin films, the DM interaction arises from the break of inversion symmetry at the interface and the strong spin-orbit coupling between the heavy metals [12]. The result is a ground state below $T = 30\,\mathrm{K}$ consisting of a skyrmion lattice phase, cf. figure 1.3 (d) - (f).

The first potential technological applications for magnetic skyrmions were proposed just a few years after their discovery. Albert Fert and collaborators proposed using skyrmions in a racetrack memory [18], introduced by Stuart Parkin years before [45]. Logic gates, variations of the racetrack ideas and new spintronic devices have followed since [19–21]. These

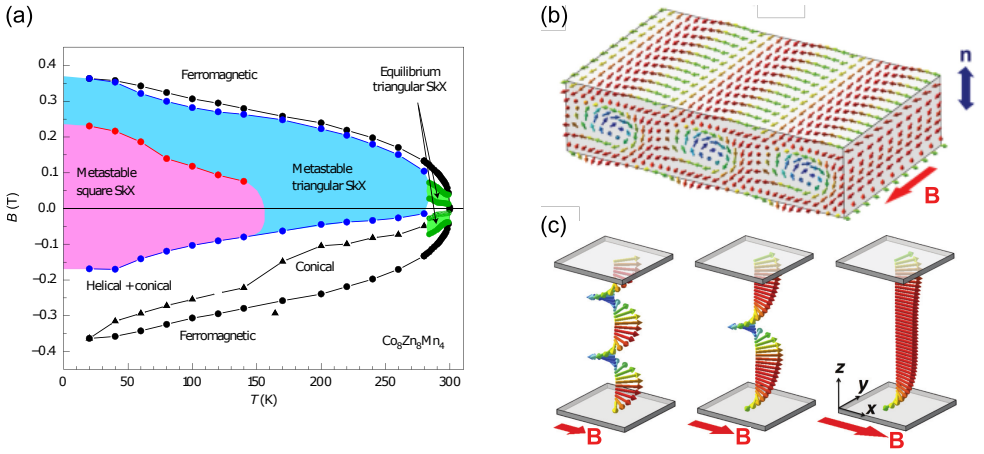

Figure 1.4: (a) Magnetic phase diagram of $Co_8Zn_8Mn_4$. The thermodynamical stable skyrmion phase sits around room temperature and at moderate magnetic field values [46]. (b) In plane skyrmions proposed as the magnetic order in MBE grown MnSi thin films for fields applied in plane [47]. (c) Concurring interpretation of experimental data in MnSi thin films. Instead of in plane skyrmions, discrete changes in the helical propagation length are observed [48].

technologies demand the stabilization of individual small skyrmions at room temperature and zero magnetic field, efficient manufacturing, and a process which allows tailoring materials for specific characteristic in the resulting magnetic structures.

These requirements have led a large portion of the scientific community to focus on multilayered systems, stacking magnetic and non-magnetic heavy metals thin films, for example, a combination of Ir, Co, and Pt [13]. By adjusting the number of layers and their thicknesses, the size of the skyrmions and the observation of lattices or individual quasiparticles can be affected. Up to the writing of this thesis, however, the right combination of parameters to obtain the desired type of skyrmions has not been found. In the case of memory storage devices, the skyrmion should be smaller than $10\,\mathrm{nm}$ [8]. At the moment, the smallest skyrmions observed in multilayer samples have a diameter of $\sim 30\,\mathrm{nm}$ and most other materials host skyrmions of a few hundred nanometers. A different section of the research community, led mainly by the work directed by Yoshinori Tokura and collaborators, is searching for bulk systems that might be able to host skyrmions at room temperature. Their search bear fruit with the study β-Mn-type $Co_xZn_yMn_z$ ($x+y+z=20$) alloys, which show a skyrmion lattice as a thermodynamic stable phase at ($Co_8Zn_8Mn_4$ [46]) and above room temperature (several compounds [49, 50]), cf. figure 1.4 (a). The wavelength of the skyrmion lattice is of the order of $\sim 125\,\mathrm{nm}$, which is deemed too large for the development of novel technology. In contrast to the other cubic materials studied before, which have a $P2_13$ space group, this material family crystallizes in either $P4_132$ or $P4_332$ space groups, thus expanding the search avenues for systems with the right conditions for the development of skyrmionic devices.

Skyrmion hosting cubic chiral magnets share the same universal phase diagram, consisting mainly of a helical magnetic order at low fields, a conical phase at medium fields and, as mentioned above, a small pocket where the skyrmion crystal is stable. Already the first experiments by Yu realized that the region of stability of the skyrmion lattice expanded dramatically as a function of sample thickness [44]. This development, albeit observed at low temperatures, was auspicious for the prospect of skyrmion based spintronics, as one would like to reduce the amount of material necessary to construct any such devices. Hence, different groups soon pursued the study of epitaxially grown samples of cubic chiral magnets.

Figure 1.5: Topologically a donut and a coffee cup are equivalent, introducing a space to hold your donut in the cofee mug, does not change its homotopy. However a coffee in the shape of a donut (important is the whole in the middle) does not belong to the same homotopy group as the other three.

Early in this effort, the observation of skyrmions in thin samples if MnSi was reported [51], this claim was disputed by Monchesky and collaborators, at the same time as they published a series of works proposing discrete helicoid transitions and in-plane skyrmions for magnetic fields applied parallel to the thin film, and a pure conical phase for fields perpendicular to the thin film [47, 52–54], these are in part depicted in figure 1.4 (b) and (c). Yokouchi and collaborators interpreted signals measured in a planar-hall effect configuration as arising from the skyrmion lattice phase [55], while Wiedemann *et al.* see no evidence of skyrmions, instead, confirming the observations of the Monchesky group, regarding helicoids and a pure conical phase for out-of-plane magnetic fields [56].

In FeGe, the situation seems to be more explicit. Thin epitaxially grown samples host skyrmions. With increasing thickness the skyrmion phase disappears [57, 58], compatible with experimental results from small-angle neutron scattering on a stack of thin films [59]. Additionally, so-called chiral bobbers [60], localized particle-like objects, that can be visualized as skyrmions truncated by a Bloch-point close to the surface, were observed in thick FeGe epitaxially grown films [61].

Only ten years after their first experimental observation, a large amount of magnetic skyrmions hosting materials have been identified, including metals, semiconductors, and insulators, with critical temperatures ranging from a few kelvin up to above room temperature. Their radius span a couple of lattice sites up to a few micrometers and the geometries of the samples range from thin films a few nanometers in thickness to samples several cubic millimeters in volume. Skyrmions have been proposed for unconventional computing and as well as spintronic devices, and their interactions with other topological phenomena, as well as different types of magnetic order, promise new rich and exciting states of matter.

1.3 TOPOLOGICAL MAGNETIC ORDER

The main reason behind the broad interest in these spin swirls is mainly their non-trivial topology and the associated emergent electronic properties. Its non-trivial topology implies that skyrmions cannot be continuously deformed into a field polarized configuration. Such considerations are at the center of topology, the study of the properties of topological spaces that are invariant under continuous transformation [62]. In the present case, the topological

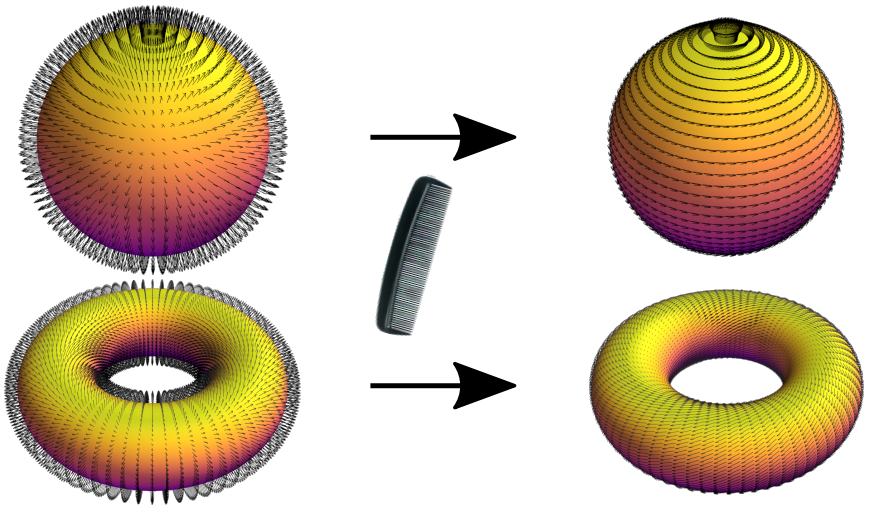

Figure 1.6: Combing a hairy sphere results in a cowlick at its poles. In contrast combing a hairy torus, yields a smooth stylish surface.

space is the spin texture. In order to provide the reader with a better grasp of essential concepts related to topology, such as homotopy groups and winding numbers, the following paragraphs briefly introduce them. This section ends with a short discussion of emergent electrodynamics, which arise as a consequence of the skyrmions' topological properties.

From a topological point of view, objects one would think are very different may be equivalent. A prominent example is the transformation of a doughnut into a coffee cup, cf. figure 1.5. Another example is an attempt to comb the hairs on a hairy ball so that they all lay flat on the surface, which is impossible since there will always be a "cowlick", as was proven by Brouwer in 1911 [63]. Note that a torus, for example, can be combed without a "cowlick", this is illustrated in figure 1.6. The existence of the "cowlick" after combing the hairs is a property which remains invariant under continuous transformation.

The invariant properties studied in topology are called topological equivalences. Such an equivalence is homotopy. Consider mappings f from a 1-sphere into the order parameter space X, $S^1 \to X$, described by loops ending and starting at the same point x_0. A homotopy is the continuous deformation of a mapping f into a mapping g. If there exists such a deformation then f and g are topologically equivalent and have the same homotopy class, $[f] = [g]$. The homotopy class of the identity $[e]$ defines as topological trivial all homotopy classes for which it holds $[f] = [e]$, i. e., one can reduce the mapping f to a point such that $f \sim 0$. In the context of magnetic textures, this class of the identity is the uniformly magnetized state. These mappings are also referred to as a null-homotopic [64].

In order to obtain a group structure for a set of homotopy classes one takes advantage of the concatenation operation of loops with the same base point x_0, $[f] \circ [g] \equiv [f \circ g]$, which results in a new mapping by following first the loop f and then g. For $S^1 \to X$ this group is called "the first homotopy group" of X at x_0 and is denoted $\pi_1(X, x_0)$. If this group is Abelian, which is the case for the relevant cases of magnetic order, there is an isomorphism between first homotopy groups with different base points, i. e., $\pi_1(X, x_0) \cong \pi_1(X, y_0)$. Thus, there exists an abstract first homotopy group $\pi_1(X)$, whose elements correspond to classes of unbased homotopic loops. Similarly, for the classification of point defects in three dimensions, one maps a 2-sphere into order parameter space X. As before, if this sphere cannot be reduced to a point, then the defect is topologically non-trivial. The homotopy classes of 2-spheres into X correspond to the second homotopy group $\pi_2(X)$.

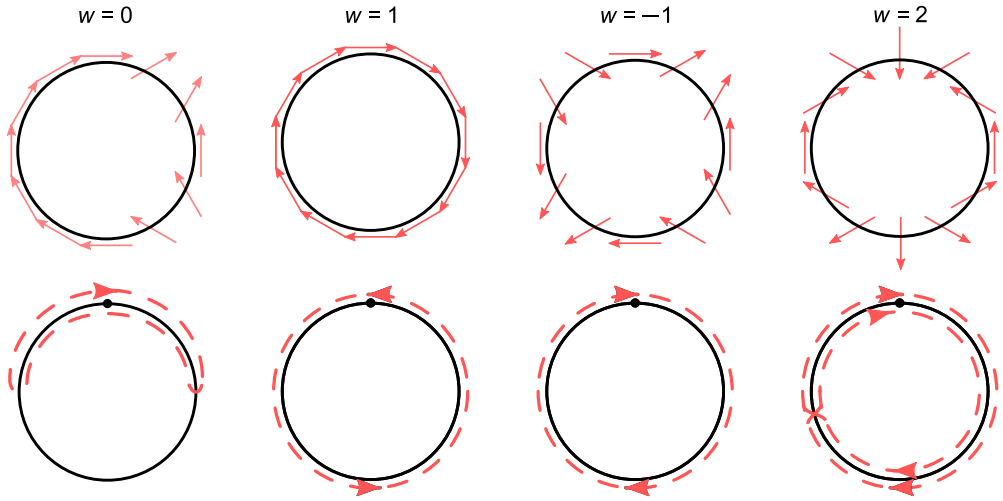

Figure 1.7: Winding number for different spin orders in 2D. The direction of the spin around the circle is shown in the first row, while the second row is the mapping into order parameter space. Adapted from [65] page 12.

In general f maps a base manifold M to a target manifold N. In the case of smooth magnetic textures, M is given by real space $\mathcal{R}^m$. The mapping must include infinity since the edge of the sample breaks the smoothness condition. Using a stereographic projection $\mathcal{R}^m$ is mapped onto S^2 and infinity is mapped to a single point, resulting in the boundary condition $m_\infty = const$. In the case of single topological defects, the base manifold is a m-sphere, enclosing the former. The order parameter space, i. e., the target manifold N, may correspond to Ising spins S^0 which is an easy-axis geometry, S^1 for easy-plane spins and S^2 for Heisenberg, or isotropic spins. Hence, the homotopy group is given by $\pi_m(S^n)$. If both manifolds have the same dimensions and $n \geq 1$, then the homotopy group becomes:

$$\pi_n(S^n) \cong \mathcal{Z} \tag{1.23}$$

and is thus Abelian. Each homotopy class is associated with an integer. The latter is given by the winding number w and essentially represents how many times one can wrap the base manifold around the target manifold, see figure 1.7 for examples of winding numbers for different spins configurations in two dimensions. Consider now, for example, $\pi_2(S^2)$, i. e., the mapping of a 2-sphere to a 2-sphere. Imagine wrapping a plastic bag around a ball. By twisting the plastic bag after each wrap, one increases the number of times it can go over the ball. The winding number is counting those twists which may have one of two orientations and twists of different orientations cancel each other through deformation. A finite winding number characterizes non-trivial topological base-manifolds and can be found for homotopy groups $\pi_n(S^n)$. Magnetic textures, or point defects, of different winding numbers cannot be continuously deformed into each other attaining so-called topological stability associated with an infinite energy barrier. The barrier becomes finite due to the discreteness of the underlying field. Furthermore, the anisotropies in a real system are finite. Thus, while it might be suitable to describe a configuration in a reduced order parameter space, in reality, the spins are not constrained to it. Consider, for example, a spin vortex. Its target manifold is initially described by S^1 in which it is a non-trivial spin configuration. However, due to the finiteness of the easy-plane anisotropy, its actual spin configuration space is S^2. Hence, it is possible to "unwind" the vortex through the "escape via the third dimension", i. e., applying a magnetic

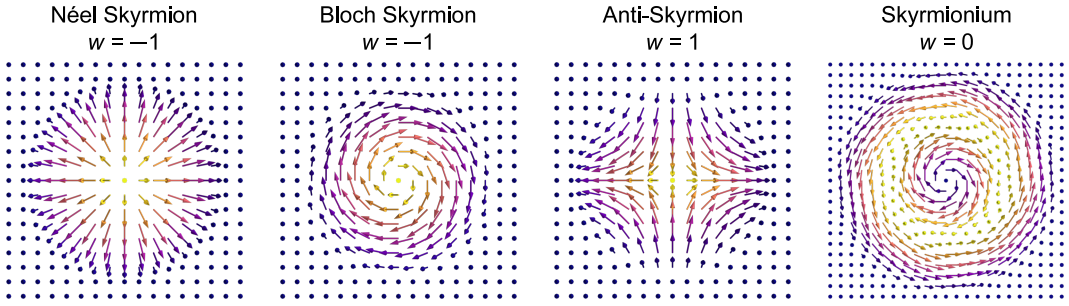

Figure 1.8: Schematic representation of different magnetic skyrmions and the associated winding number.

field perpendicular to it will lead to a reorientation of the spins out of the plane when reaching a critical magnetic field.

The winding number of magnetic textures with target space S^2 is given by:

$$w_S^2 = \frac{1}{4\pi}\int_M \boldsymbol{m}\cdot(\partial_1\boldsymbol{m}\times\partial_2\boldsymbol{m})\,dx_1dx_2 \tag{1.24}$$

where m is the normalized magnetic texture and M is the base manifold, which is two-dimensional and can be parameterized by two variables x_1 and x_2 (for a thorough derivation see [66]). If x_1 and x_2 are cartesian, the winding number is often called the "skyrmion number". As mentioned before, a skyrmion number of 0, denotes a magnetic configuration which can be deformed into the uniformly polarized state. Each finite winding number has different representations which describe essentially the same object. Note that the sign of the winding number, while not strictly defined, is of relevance when comparing magnetic textures, since objects of different sign and same absolute value $|w|$, would mutually annihilate.

The skyrmions discussed above have a winding number $w = -1$, and the community differentiates between Néel-type and Bloch-type, the former is the stereographic projection of a spin anti-hedgehog, while the latter the one of a combed anti-hedgehog. The sense of rotation of the skyrmion, also known as helicity, does not affect the winding number of the skyrmion, changing the polarization direction of the background leads to a change in sign. Antiskyrmions were recently experimentally observed in Heusler compounds [67], and different types of topologically trivial and non-trivial magnetic bubbles have been studied as an alternative to avoid some undesirable consequences of non-trivial topology [68]. Note that in the community, the exact definition of a skyrmion is not strict. The most common approach is to regard as bubble skyrmions magnetic textures which appear simultaneously with both left-hand and right-hand chirality. Different types of magnetic structures are depicted schematically in figure 1.8.

1.4 EMERGENT ELECTRODYNAMICS

Magnetic skyrmions have a significant potential for novel spintronic and electronic devices originating, especially, in spin-transfer torques, that is, the transfer of momentum from the itinerant electrons to the magnetic structure as the former passes through it. The forces exerted by the electron consist of a gyrocoupling, which depends on the non-trivial topology of the skyrmion, and a dissipative force. They compete against pinning due to defects, which break the translational symmetry. If the current velocity is large enough, one can neglect the pinning forces and, in the limit of small damping, the velocity of the skyrmions is about the same as

that of the electrons [69]. Hence, there is a critical current which leads to the motion of the skyrmion.

Jonietz *et al.* first observed these spin-transfer torque effects in a small-angle neutron scattering experiment [15]. An additional thermal gradient results in a spin density gradient, thus the forces on the lattice vary across the sample resulting in a rotation of the skyrmion crystal which depends on the directions of the gradient and the electric current. The critical currents necessary to put the skyrmions in motion are $10^6\,\mathrm{A\,m^{-2}}$, about four orders of magnitude smaller than those measured before in the motion of magnetic domain walls in ferromagnets ($10^{10}\,\mathrm{A\,m^{-2}}$).

The spin-transfer torque on the skyrmion lattice corresponds to a force from the skyrmion lattice on the electron. The effects of this force can be analyzed using the Schrödinger equation of an electron traversing a magnetic texture $\boldsymbol{m}$. Due to the exchange interaction, the electron spin would prefer a parallel alignment with the local magnetization field. In an adiabatic approximation, using a local base to diagonalize the coupling to the magnetic texture, emergent gauge fields arise. The skyrmion lattice shows no variation as a function of the z component. Thus, the corresponding emergent magnetic and electric fields read:

$$\boldsymbol{B}_e^z = -\frac{2\pi\hbar}{e}\rho^{\mathrm{top}} \tag{1.25}$$

$$\boldsymbol{E}_e^\alpha = \frac{2\pi\hbar}{e}\epsilon_{0\alpha\beta} j_\beta^{\mathrm{top}} \tag{1.26}$$

with the topological charge and current densities, j_β^{top} and ρ^{top}, which are defined by:

$$\rho^{\mathrm{top}} = \frac{1}{4\pi}\boldsymbol{m}\left(\partial_x\boldsymbol{m}\times\partial_y\boldsymbol{m}\right) \tag{1.27}$$

$$j_\alpha^{\mathrm{top}} = \frac{1}{4\pi}\epsilon_{0\alpha\beta}\boldsymbol{m}\left(\partial_\beta\boldsymbol{m}\times\partial_t\boldsymbol{m}\right) \tag{1.28}$$

where $\epsilon_{0\alpha\beta}$ is the totally antisymmetric tensor with $\epsilon_{0xy}=1$.

Integrating the topological charge density over a primitive magnetic unit cell yields unity, hence each magnetic unit cell holds effectively one skyrmion. If the magnetization holds no singularities the topological charge and current density are related through a continuity equation:

$$\partial_t\rho^{\mathrm{top}} + \partial_\alpha j_\alpha^{\mathrm{top}} = 0 \tag{1.29}$$

with $\alpha = x, y$. This conservation law can be expressed using the emergent fields:

$$\partial_t\boldsymbol{B}_e = -\nabla\times\boldsymbol{E}_e. \tag{1.30}$$

The emergent magnetic field $\vec{B}_e$ deflects the electron of its path, in a manner described by a fictitious Lorentz force

$$\boldsymbol{F} = -e\boldsymbol{v}_s\times\boldsymbol{B}_e. \tag{1.31}$$

Therefore, there is an additional contribution to the Hall effect, called the topological Hall effect. It was first measured in MnSi, where an increase in the Hall resistivity was observed when the applied field and sample temperature where within the regime of the skyrmion crystal phase (see figure 1.9 (a)), which is also related to the formation of a Non-Fermi liquid under hydrostatic pressure [14, 70–72]. The value of the topological hall effect is given by:

$$\rho_{xy}^{\mathrm{top}} = PR_0B_e^z \tag{1.32}$$

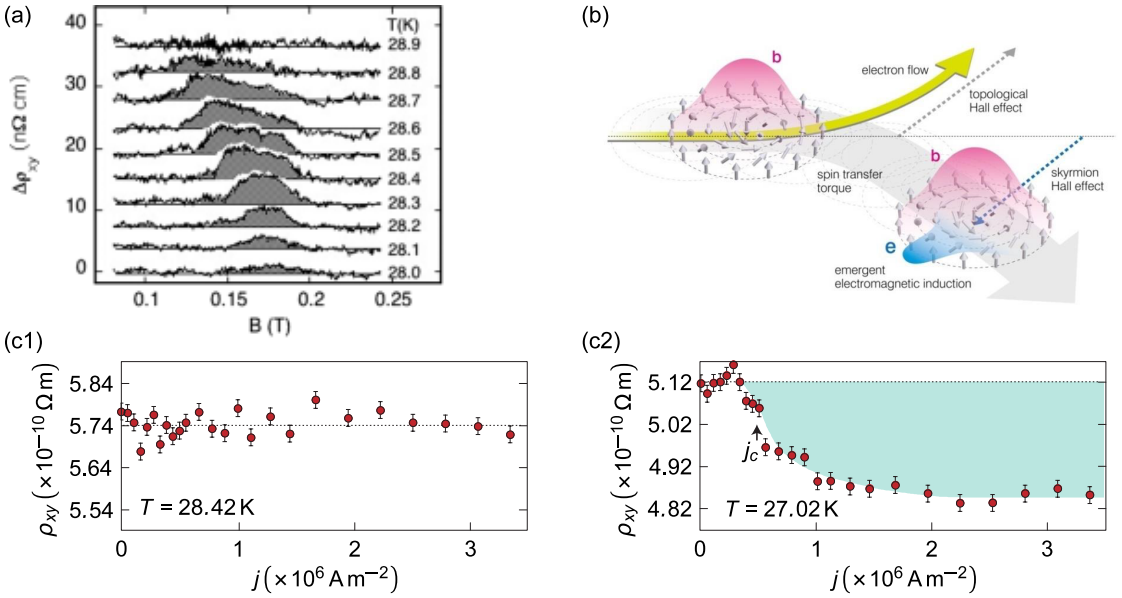

Figure 1.9: (a) Additional contribution to the hall effect in MnSi within the A-phase arising from the deviation of the electron path when traversing a skyrmion due to its topology [14]. (b) Schematic representation of the emergent fields associated with the skyrmion motion [9]. (c1) -(c2) Hall resistivity as a function of dc current measured in MnSi. Outside of the A-phase no change is observed as there are no skyrmions that could flow. Within the A-phase there is a reduction in the Hall resistivity associated with the motion of the skyrmions and the resulting emergent electrical field [17].

with the Hall constant R_0 and the effective spin polarization ratio P. The topological charge density determines the value of the emergent magnetic flux. Hence, for a static skyrmion crystal, it amounts to a single flux quantum $\frac{2\pi\hbar}{e}$ per magnetic unit cell. In a semiclassical picture, the emergent magnetic field can be understood as a Berry phase which the electron picks up in his trajectory through the skyrmion while its spins realign adiabatically with the local magnetization direction. This Berry phase is in real space. It is possible to collect a Berry phase in momentum space as well, which is the origin of the anomalous Hall effect [73]. The motion of the electron results in a skyrmion crystal flow if the current velocity is high enough, giving rise to the emergent electric field discussed above. This motion of the skyrmion crystal results in a suppression of the topological hall effect [17], referred to as the skyrmion-flow Hall effect, akin to the flux-flow Hall effect in type-II superconductors [74], cf. figure 1.9 (c1) and (c2).

The quantized emergent magnetic flux demands that emergent magnetic monopoles, also known as Bloch points, mediate the creation and annihilation of skyrmions. Consider for clarification the merging of two skyrmions mediated by a monopole. At the beginning of the merging process, we have two units of quantized flux, by the end of it, only one flux quantum remains. Hence the monopole mediating the melting process has to carry a negative quantum flux. There are other processes to annihilate a skyrmion. The spontaneous formation of an antimonopole - monopole pair in the middle of the skyrmion can lead to its deletion as both monopoles traverse it and leave the sample at the surface. Milde *et al.* obtained the first experimental evidence of these processes by using magnetic force microscopy to study a sample of $Fe_{0.5}Co_{0.5}Si$[75]. Further studies of the lifetime of skyrmions have been carried out recently, revealing that entropy limits the so-called topological protection and how controlled doping can enhance the lifetime of metastable skyrmions [76, 77].

As it was mentioned above, the following chapters address the role of anisotropies in the phase diagram of cubic chiral magnets and mainly the stabilization of skyrmion lattices. The primary experimental method utilized in these studies is small-angle neutron scattering, introduced in chapter 2. Chapter 3 discusses the transition from the helical to the conical phase in MnSi and the different phase transitions originating from the magnetocrystalline anisotropy. Chapter 4 presents the manipulation of the skyrmion lattice phase by introducing additional anisotropy with uniaxial pressure. Finally, the chapter 5 presents the first observation of two separate skyrmion phases in any system studied so far.

2

INTRODUCTION TO SMALL-ANGLE NEUTRON SCATTERING

The magnetic textures introduced in the previous chapter are typically between a few nm and at most a couple of µm in size. Most of the experimental techniques used to study skyrmions are well suited for one part of this range but not for all of it. Real-space microscopy is more suited for structures towards the larger size end of the spectrum, while small-angle neutron scattering (SANS) can deal with skyrmions towards the smaller sizes. Additionally, SANS can also be combined with other types of physical probes, thanks to the physical characteristics of neutrons, such as their low probability of interaction. Hence, most of the data presented in this thesis are the result of SANS experiments. This chapter gives a brief and incomplete introduction to neutron scattering with particular focus on magnetic scattering, finishing with a description of small-angle neutron scattering instruments and typical resolution capabilities.

2.1 SCATTERING IN THE STUDY OF CONDENSED MATTER

In 1912 Max von Laue and collaborators delivered direct proof of the microscopic arrangement of atoms in crystals when they observed and interpreted x-rays interference patterns after being scattered from a copper single crystal [78]. Much of our understanding of the microscopic structure of condensed matter results from x-ray diffraction. X-rays, however, interact strongly with the electron cloud of the atoms. Hence, the probability of a scattering process increases with the atomic number, reducing penetration. Thus, the observation of light elements, such as hydrogen, in samples which include substantially heavier atoms is challenging. The discovery of the neutron by James Chadwick in 1932 expanded the possibilities of scattering in the study of condensed matter [79]. In contrast to x-rays, neutrons interact with the atoms mainly by the strong force interaction and the probability to be scattered by a specific nucleus depends on its internal structure. This results in substantial varying interaction probabilities for atoms and isotopes of similar atomic number allowing to separate the scattering of hydrogen from deuterium, for example. Furthermore, the neutron carries a magnetic moment and interacts with the spin or orbital moment of unpaired electrons via the dipole-dipole interaction, resulting in a contribution of comparable magnitude as the nuclear scattering.

The main issue with neutrons is their availability. Research reactors based on nuclear fission were the first source of free neutrons needed for the study of condensed matter. From the start, there was a synergy between neutron production and the study of the properties of matter. The former is exceptionally efficient when the neutrons from the fission are moderated into thermal neutrons, which means their kinetic energy is about the same as the thermal energy at room temperature, i. e., $\sim 25\,\mathrm{meV}$. Thermal neutrons have a wavelength of about the same size as typical distances between atoms in solids, and their energy is in the same range as that of dynamical processes in crystals. Thus, they are very well suited for their study.

The interaction of a neutron with the scattering system is very weak and represents only a small perturbation of the latter, leading to a transition from one quantum state to another, but leaving the nature of the state unchanged. Hence the differential scattering cross-section $(d\sigma/d\Omega)_{\lambda_i \to \lambda_f}$, which represents the sum of all processes that result in a transition of the scattering system from state λ_i to λ_f, while the state of the neutron changes from $\boldsymbol{k_i}$ to

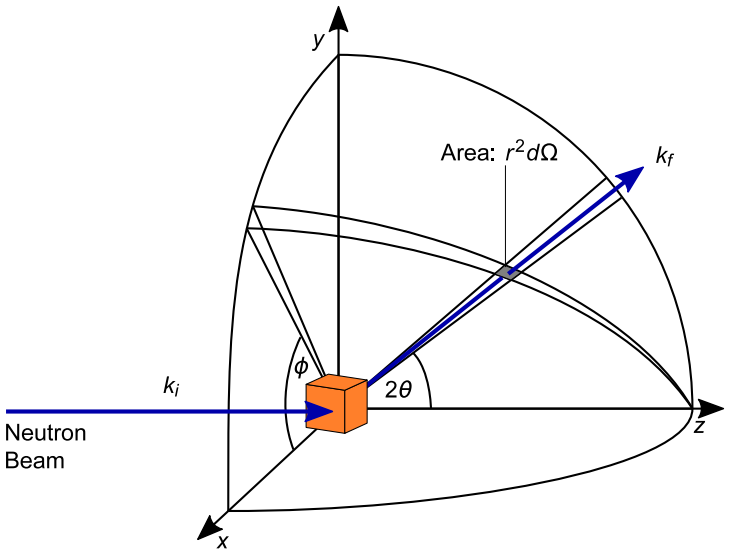

Figure 2.1: Schematic representation of the scattering process. The incoming neutron beam with wavevector $\boldsymbol{k_i}$ is scattered into the solid angle $d\Theta$ with wavevector $\boldsymbol{k_f}$.

$\boldsymbol{k_f}$, can be evaluated using Fermi's golden rule, cf. figure 2.1. The derivation below follows primarily the one given by G. L. Squires in [80].

The differential cross-section is defined as

$$\frac{d\sigma}{d\Omega} = \frac{\text{number of neutrons scattered per second into } d\Omega}{\Phi d\Omega}, \tag{2.1}$$

with Φ the incident neutron flux, the product of neutron density and velocity . Thus:

$$\left.\frac{d\sigma}{d\Omega}\right|_{\lambda_i \to \lambda_f} = \frac{1}{\Phi}\frac{1}{d\Omega}\sum_{\boldsymbol{k_f}} W_{\boldsymbol{k_i},\lambda_i \to \boldsymbol{k_f},\lambda_f} \tag{2.2}$$

with $W_{\boldsymbol{k_i},\lambda_i \to \boldsymbol{k_f},\lambda_f}$, the number of transitions per second between the initial and the final state. This can be rewritten using Fermi's golden rule to

$$\sum_{\boldsymbol{k_f}} W_{\boldsymbol{k_i},\lambda_i \to \boldsymbol{k_f},\lambda_f} = \frac{2\pi}{\hbar}\rho_{\boldsymbol{k_f}} |\langle \boldsymbol{k_f}\lambda_f | V | \boldsymbol{k_i}\lambda_i \rangle|^2, \tag{2.3}$$

with $\rho_{\boldsymbol{k_f}}$ the total number of states in $d\Omega$ per unit energy range for neutrons in state $\boldsymbol{k}$. Using the box normalisation one can evaluate the expression 2.2 and obtain an expression for $\rho_{\boldsymbol{k_f}}$ ([80]):

$$\rho_{\boldsymbol{k_f}} = \frac{Y}{(2\pi)^3} k_f \frac{m_\mathrm{n}}{\hbar^2} d\Omega \tag{2.4}$$

with the volume of the box Y and the mass of the neutron m_n. Considering plane waves and a neutron density of one neutron per box volume yields

$$\Phi = \frac{1}{Y}\frac{\hbar}{m_n} k_i \tag{2.5}$$

for the incident neutrons' flux. Hence the differential cross-section reads

$$\left.\frac{d\sigma}{d\Omega}\right|_{\lambda_i \to \lambda_f} = \frac{k_f}{k_i}\left(\frac{m_\mathrm{n}}{2\pi\hbar^2}\right)^2 \left|\langle \boldsymbol{k_f}\lambda_f | V | \boldsymbol{k_i}\lambda_i \rangle\right|^2 \tag{2.6}$$

where the matrix element is rewritten as

$$\langle \boldsymbol{k_f}\lambda_f|V|\boldsymbol{k_i}\lambda_i\rangle = \frac{1}{Y}\int \exp\left(-i\boldsymbol{k_f}\cdot\boldsymbol{r}\right)\chi^*_{\lambda_f} V \exp\left(i\boldsymbol{k_i}\right)\chi_{\lambda_i} d\boldsymbol{R}d\boldsymbol{r} = \frac{1}{Y}\langle \boldsymbol{k_f}\lambda_f|V|\boldsymbol{k_i}\lambda_i\rangle. \tag{2.7}$$

If the energy transfer of the neutron is considered, the results obtained relate to the partial differential cross-section $\frac{d^2\sigma}{d\Omega dE_f}$, which is related to the differential cross-section through:

$$\frac{d\sigma}{d\Omega} = \int_0^\infty \left(\frac{d^2\sigma}{d\Omega dE}\right) dE_f. \tag{2.8}$$

Due to energy conservation the energy distribution of scattered neutrons is a δ-function and the partial differential cross-section is given by

$$\left.\frac{d\sigma}{d\Omega dE_f}\right|_{\lambda_i\to\lambda_f} = \frac{k_f}{k_i}\left(\frac{m_\mathrm{n}}{2\pi\hbar^2}\right)^2 \left|\langle \boldsymbol{k_f}\lambda_f|V|\boldsymbol{k_i}\lambda_i\rangle\right|^2 \delta(\hbar\omega + E_i - E_f). \tag{2.9}$$

Due to the weak interaction with the scattering centers, the Born approximation can be used to evaluate equation 2.9 in more detail. Consider both incoming and scattered neutrons as plane waves; then the matrix element can be rewritten as

$$\left|\langle \boldsymbol{k_f}\lambda_f|V|\boldsymbol{k_i}\lambda_i\rangle\right|^2 = V(\boldsymbol{q})\langle\lambda_f|\sum_j e^{i\boldsymbol{q}\cdot\boldsymbol{r}_j}|\lambda_i\rangle \tag{2.10}$$

with $\boldsymbol{r}_j$ the position of the jth scattering center, all of which are assumed equal, the scattering vector $\boldsymbol{q} = \boldsymbol{k_i} - \boldsymbol{k_f}$ and the nuclear potential

$$V(\boldsymbol{q}) = \int d\boldsymbol{r} V(\boldsymbol{r}) e^{i\boldsymbol{q}\cdot\boldsymbol{r}} \tag{2.11}$$

which is essentially a δ function in $\boldsymbol{r}$, due to the short-range interaction, and simplifies to

$$V(\boldsymbol{q}) = \frac{2\pi\hbar^2}{m_\mathrm{n}} b \tag{2.12}$$

with b the nuclear scattering length. Altogether the new expression for the differential cross-section reads:

$$\left.\frac{d^2\sigma}{d\Omega_f dE_f}\right|_{\lambda_i\to\lambda_f} = \frac{k_f}{k_i}\sum P(\lambda_i)\left|\langle\lambda_f|b\sum_j e^{i\boldsymbol{q}\cdot\boldsymbol{r}_j}|\lambda_i\rangle\right|^2 \delta(\hbar\omega + E_i - E_f) \tag{2.13}$$

where $P(\lambda_i)$ is the statistical weight factor for the initial state λ_i.

By considering only coherent elastic scattering from a crystalline sample, the partial differential cross-section can be simplified to

$$\left.\frac{d\sigma}{d\Omega_f}\right|_\mathrm{el} = N_n \frac{(2\pi)^3}{\nu_o}\sum_{\boldsymbol{G}} \delta(\boldsymbol{q}-\boldsymbol{G})|F_N(\boldsymbol{G})|^2, \tag{2.14}$$

with N_n the number of nuclei, ν_0 the unit-cell volume and $\boldsymbol{G}$ the reciprocal-lattice vectors corresponding to the Bravais lattice of the sample. The sum is carried out over all $\boldsymbol{G}$, only $\boldsymbol{q}$ vectors equal to such a reciprocal vector result in scattering. Depending on the details of the crystal structure and the basis of the sample some of the Bragg reflexes may be extinguished. This information is contained in the nuclear structure factor $F_N(\boldsymbol{G})$, given by:

$$F_N(\boldsymbol{G}) = \sum_j \overline{b}_j e^{i\boldsymbol{G}\cdot\boldsymbol{d}_j} e^{-W_j}, \tag{2.15}$$

where $\boldsymbol{d}_j$ is the position within the unit cell of j-th atom and mean displacements are captured within the Debye-Waller factor W_j.

2.2 MAGNETIC NEUTRON SCATTERING

Neutrons carry a finite magnetic moment which leads to scattering events due to dipole-dipole interaction with the atom. The experimental work presented here consists mainly of analyzing such magnetic scattering for different types of magnetic order.

The neutron's magnetic moment is given by

$$\boldsymbol{m}_{\mathrm{n}} = -\gamma \mu_{\mathrm{n}} \boldsymbol{\sigma}, \tag{2.16}$$

where γ is the gyromagnetic ratio, μ_{n} is the nuclear magneton and σ is the spin operator. The distribution of magnetic moments associated with the unpaired electrons is captured by the magnetic form factor $f(\boldsymbol{q})$, given by the Fourier transformation of the normalized spin-density $\rho_m(r)$ of an atom:

$$f(\boldsymbol{q}) = \int \rho_m(\boldsymbol{r}) e^{i\boldsymbol{q}\cdot\boldsymbol{r}} d\boldsymbol{r} \tag{2.17}$$

with

$$f(0) \equiv 1. \tag{2.18}$$

In 1939, Halpern and Johnson [81] derived the cross-section for magnetic scattering, neglecting contributions from the angular momentum of the electrons. The resulting cross-section depends on the initial and final wave vectors of the scattered neutrons, as well as their respective spin states $s_i = \sigma_i/2$ and $s_f = \sigma_f/2$. Generalizing equation 2.13 to account for the magnetic interaction the differential cross-section results in:

$$\left.\frac{d^2\sigma}{d\Omega_f dE_f}\right|_{s_i \to s_f} = \frac{k_f}{k_i} \sum P(\lambda_i) \left| \langle \lambda_f | \sum_j e^{i\boldsymbol{q}\cdot\boldsymbol{r}_j} U_j^{s_i s_f} | \lambda_i \rangle \right|^2 \delta(\hbar\omega + E_i - E_f). \tag{2.19}$$

The spin component is contained in the atomic scattering amplitude $U_j^{s_i s_f}$ from spin state s_i to s_f at the j-th atomic position,

$$U_j^{s_i s_f} = \langle s_f | b_j - p_j \boldsymbol{S}_{\perp j} \cdot \boldsymbol{\sigma} + \boldsymbol{H}_j \boldsymbol{I}_j \cdot \boldsymbol{\sigma} | s_i \rangle \tag{2.20}$$

with the nuclear coherent scattering amplitude b, the spin-dependent nuclear amplitude $\boldsymbol{B}$ and the nuclear spin operator $\boldsymbol{I}$. The second term is composed of the magnetic interaction vector $\boldsymbol{S}_\perp$ and a factor p including the magnetic form factor $f(\boldsymbol{q})$ and the Landé splitting factor g,

$$p = \left(\frac{\gamma r_0}{2}\right) g f(\boldsymbol{q}), \tag{2.21}$$

with

$$\frac{\gamma r_0}{2} = 0.2695 \times 10^{-12}\,\mathrm{cm}, \tag{2.22}$$

where $r_0 = e^2/m_e c^2$ is the classical electron radius, with e and m_e the charge and mass of an electron, and c is the velocity of light.

The magnetic interaction vector was first introduced by de Gennes in 1963 [82],

$$\begin{aligned} \boldsymbol{S}_\perp &= \hat{\boldsymbol{q}} \times (\boldsymbol{S} \times \hat{\boldsymbol{q}}), \\ &= \boldsymbol{S} - \hat{\boldsymbol{q}}(\hat{\boldsymbol{q}} \cdot \boldsymbol{S}), \end{aligned} \tag{2.23}$$

here $\hat{\boldsymbol{q}}$ is a unit vector pointing along the direction of the scattering vector $\boldsymbol{q}$. Note that only components of the spin amplitude $\boldsymbol{S}$ which are perpendicular to $\boldsymbol{q}$ contribute to the scattering amplitude.

Up until now only contributions from spin angular momentum and the corresponding magnetization density

$$\boldsymbol{M}(\boldsymbol{q}) = \mu_B g \boldsymbol{S} f(\boldsymbol{q}), \tag{2.24}$$

with g = 2, have been taken into account. Consider now the radial wave function of the unpaired spin $\Phi(r)$, then the magnetic form factor reads:

$$f(\boldsymbol{q}) = \int_0^\infty dr\, r^2 j_0(qr) |\Phi(r)|^2 \equiv \langle j_0 \rangle, \tag{2.25}$$

where $j_n(qr)$ is a spherical Bessel function of order n and aspherical effects have been neglected. For small q the orbital moment can be included simply and the magnetization density is given by:

$$\boldsymbol{M}(\boldsymbol{q}) = \mu_B (2\langle j_0 \rangle \boldsymbol{S} + (\langle j_0 \rangle + \langle j_2 \rangle)\boldsymbol{L}), \tag{2.26}$$

with the angular momentum vector $\boldsymbol{L}$.

As it was the case for nuclear scattering, considering only coherent elastic scattering reduces the partial differential cross-section for magnetic scattering from a magnetic crystal to

$$\left.\frac{d\sigma}{d\Omega_f}\right|_{\text{el}} = N_{\text{M}} \frac{(2\pi)^3}{v_{\text{M}}} \sum_{\boldsymbol{G}_{\text{M}}} \delta(\boldsymbol{q} - \boldsymbol{G}_{\text{M}}) |\boldsymbol{F}_{\text{M}}(\boldsymbol{G}_{\text{M}})|^2, \tag{2.27}$$

where the subindex M refers to the magnetic unit cell. The magnetic structure factor reads

$$\boldsymbol{F}_{\text{M}}(\boldsymbol{G}_{\text{M}}) = \sum_j p_j \boldsymbol{S}_{\perp j} e^{i\boldsymbol{G}_{\text{M}} \cdot \boldsymbol{d}_j} e^{-W_j}, \tag{2.28}$$

remember that the magnetic form factor is contained in p.

2.3 NEUTRON SCATTERING FROM CUBIC HELIMAGNETS

The magnetic structures resulting in coherent elastic scattering discussed above tend to have larger magnetic unit cells than the underlying crystal lattice. The periodicity of the magnetic arrangements corresponds to a larger wavelength λ defined by the amplitude of the propagation vector $Q = 2\pi/\lambda$. A common case is that of antiferromagnets with a propagation vector $\boldsymbol{Q} = (\frac{1}{2}, \frac{1}{2}, \frac{1}{2})$, while ferromagnets represent a special case with $Q = 0$. The ground state of cubic helimagnets consists of an incommensurable magnetic helix whose spin density can be described by [83]:

$$\boldsymbol{S}(\boldsymbol{r}) = \boldsymbol{\alpha}_Q \sin(\boldsymbol{Q}\boldsymbol{r}) + \boldsymbol{\beta}_Q \cos(\boldsymbol{Q}\boldsymbol{r}) \tag{2.29}$$

where $\boldsymbol{\alpha}_Q$ and $\boldsymbol{\beta}_Q$ are vectors defining the plane of rotation. For a perfect helix these vectors have the same length, are orthogonal to each other and to the propagation vector $\boldsymbol{Q}$.

The Fourier transformation of the spin density is then given by:

$$\boldsymbol{S}(\boldsymbol{q}) = \int \boldsymbol{S}(\boldsymbol{r}) e^{i\boldsymbol{q}\boldsymbol{r}} d\boldsymbol{r} \tag{2.30}$$

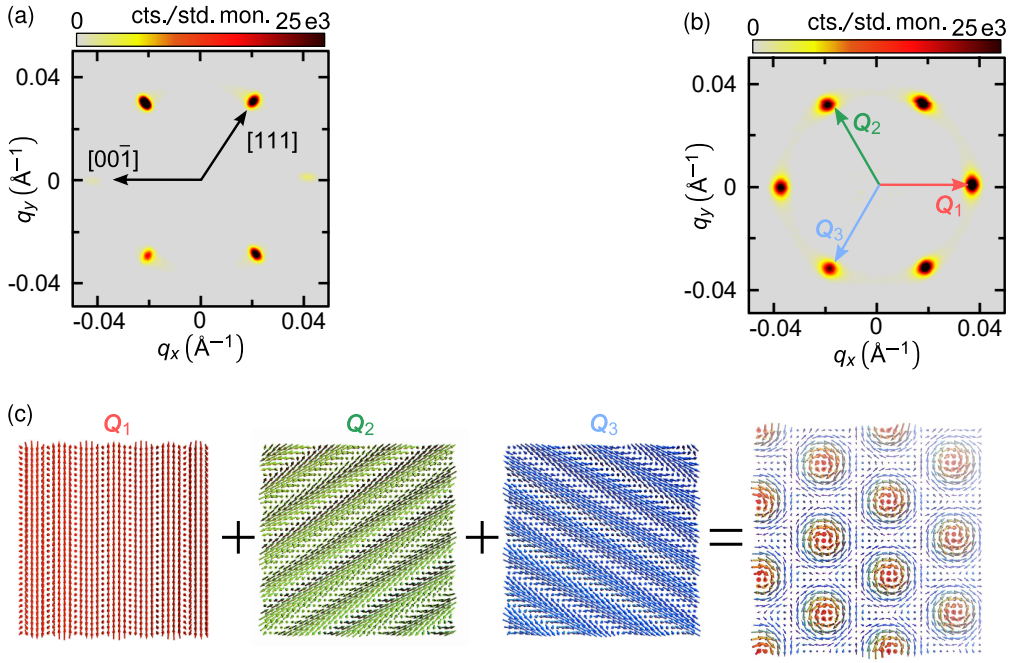

Figure 2.2: Typical scattering patterns from MnSi (a) Typical scattering pattern of two helical domains with a scattering length of $Q \approx 0.036\,\text{Å}^{-1}$. (b) Typical scattering pattern for the skyrmion lattice. (c) The scattering pattern of the skyrmion lattice can be understood as the coherent superposition of three helical propagations, which result in the hexagonal configuration of the skyrmion lattice.

and leads in turn to a differential cross-section proportional to:

$$\frac{d\sigma}{d\Omega} \propto S_Q \frac{(2\pi)^3}{v_0} \sum_G \delta(\boldsymbol{q} - \boldsymbol{G} - \boldsymbol{Q}) + S_Q^* \frac{(2\pi)^3}{v_0} \sum_G \delta(\boldsymbol{q} - \boldsymbol{G} + \boldsymbol{Q}), \tag{2.31}$$

with $S_Q = \alpha_Q + i\beta_Q$. The sum is carried out over all reciprocal vectors $\boldsymbol{G}$ and results in satellite Bragg peaks at $\boldsymbol{q} = \boldsymbol{G} \pm \boldsymbol{Q}$, i. e., around each reciprocal vector of the sample a pair of Bragg peaks can be measured along the propagation direction of the helix.

Cubic helimagnets exhibit helices with wavelengths from ~ 30 Å to ~ 1000 Å, which in turn result is very small propagation vectors. The corresponding scattering angle is also very small. Hence the Bragg condition is fulfilled when the propagation vector of these helices is almost perpendicular to the incoming neutron beam. Thus small-angle neutron scattering is very well suited for the study of these magnetic structures. In such an experimental configuration the satellites measured lie around the origin of the reciprocal space $\boldsymbol{G} = (000)$ which is identical with the direct beam.

Typically, the symmetry of the system allows for multiple domains to coexist, each of them resulting in an additional pair of satellite Bragg peaks. In the case of MnSi, there are four preferred directions of propagation, i. e., the $\langle 111 \rangle$ crystallographic axes. Due to the resolution of the instrument and, substantially, the magnetic mosaicity of the crystal, it is possible to measure two domains simultaneously, when the neutron beam is parallel to a high symmetry axis, cf. Fig. 2.2 (a).

In addition to the helimagnetic order, cubic helimagnets also exhibit the so-called skyrmion lattice, consisting of magnetic whirls arranged in a hexagonal lattice perpendicular to the applied magnetic field $\boldsymbol{B}$, in a small region of the phase diagram. The skyrmions can be described by the coherent superposition of three helical propagations perpendicular to $\boldsymbol{B}$.

Thus the corresponding scattering pattern consists of three pairs of satellite Bragg peaks around each reciprocal vector $\boldsymbol{G}$. The lattice constant of the hexagonal order is almost the same as the helical propagation length. Hence the Bragg angle remains in the order of $\sim 2°$, cf. Fig 2.2 (b) and (c).

2.4 RESOLUTION OF A SMALL-ANGLE NEUTRON SCATTERING INSTRUMENT

As mentioned above, large structures in real space lead to very small scattering angles and, thus, scattering patterns closed to the direct beam. Optimizing an instrument for such measurements overwhelmingly addresses the size and divergence of the neutron beam. An schematic instrument setup is shown in figure 2.3 (a). A poly-chromatic neutron beam is filtered using either a monochromator or a so-called velocity selector to choose a neutron wavelength λ_n for the experiment, depending on the component used the resulting monochromatic neutron beam has a distribution of wavelengths around the desired one, which typically has a width of a few percents. Behind it the neutron beam is collimated over a large distance L_1 (between 1.5 m to 20 m), to reduce the divergence of the incident beam. After interacting (or not) with the sample, the neutrons continue their path in an evacuated scattering tube to avoid scattering with the air. The detector can be positioned at a distance L_2 of the sample, the flexibility, and range of the detector position determine the range of resolvable scattering lengths q.

The resolution of such an instrument is determined mainly by three contributions:

- the geometrical optical resolution of the slit system
- the wavelength spread $\frac{\Delta\lambda_n}{\lambda_n}$
- the resolution of the detector

Based on the geometry of the scattering processes, two resolution widths can be defined, cf figure 2.3 (b). The first one, $\Delta\beta_1$, corresponding to the plane formed by the neutron wave vectors, i. e., $\boldsymbol{k_i}$ and $\boldsymbol{k_f}$, is defined as [84]:

$$\Delta\beta_1 = \frac{2R_1}{L_1} - \frac{1}{2}\frac{R_2^2}{R_1}\frac{\cos^4(2\theta)}{L_2^2 L_1}\left(L_1 + \frac{L_2}{\cos^2(2\theta)}\right)^2 \qquad \text{for} \quad \alpha_1 \geq \alpha_2$$

$$\Delta\beta_1 = 2R_2\left(\frac{1}{L_1} + \frac{\cos^2(2\theta)}{L_2}\right) - \frac{1}{2}\frac{R_1^2}{R_2}\frac{L_2}{L_1}\frac{1}{\cos^2(2\theta)(L_1 + L_2/\cos^2(2\theta))} \qquad \text{for} \quad \alpha_1 < \alpha_2$$

The second, $\Delta\beta_2$, is related to the resolution perpendicular to the former plane, cf. Fig. 2.3 (b) and its given by:

$$\Delta\beta_2 = \frac{2R_1}{L_1} - \frac{1}{2}\frac{R_2^2}{R_1}\frac{\cos^2(2\theta)}{L_2^2 L_1}\left(L_1 + \frac{L_2}{\cos(2\theta)}\right)^2 \qquad \text{for} \quad \alpha_1 \geq \alpha_2$$

$$\Delta\beta_2 = 2R_2\left(\frac{1}{L_1} + \frac{\cos(2\theta)}{L_2}\right) - \frac{1}{2}\frac{R_1^2}{R_2}\frac{L_2}{L_1}\frac{1}{\cos(2\theta)(L_1 + L_2/\cos(2\theta))} \qquad \text{for} \quad \alpha_1 < \alpha_2$$

Both equations include the scattering angle θ, the distances of the slit system L_1 and L_2, as well as the radius of the slits R_1 and R_2, cf. figure 2.3.

The wavelength spread $\frac{\Delta\lambda_n}{\lambda_n}$ depends of the specific selector or monochromator used and results in an angle error

$$\Delta\beta_{\lambda_n} = \frac{\Delta\lambda_n}{\lambda} \cdot 2 \cdot \theta$$

An additional uncertainty arises from the detector which is determined by its resolution ΔD and its distance to the sample

$$\Delta\beta_{\text{det}} = \arctan \Delta D / L_2$$

Adding these sources of uncertainty, while considering their propagation as well, yields the azimuthal $\Delta\beta_{\text{az}}$ and radial resolution $\Delta\beta_Q$ of the setup. The experiments discussed in this thesis were carried out at different instruments at the Heinz Meier-Leibnitz Center (MLZ) using different parameters. Thus specific resolution values are discussed in the relevant chapters.

Most data presented here were measured at the MIRA diffractometer [85]. It is not a typical small-angle scattering instrument since it was designed with flexibility in mind. Specifically, one can carry out both elastic and inelastic measurements, as it can change its configuration from a SANS machine to a triple-axis-spectrometer, cf. Fig. 2.4. Furthermore, by combining two different neutron beam ports (designated MIRA-1 and MIRA-2) it is able to provide neutrons in a wide wavelength range (3.5 Å $< \lambda_n <$ 20 Å) with a very small spread $\frac{\Delta\lambda_n}{\lambda_n} \approx 3\,\%$. Additionally, several additional devices have been developed to increase its capabilities, such as elliptical focusing guides which allow bundling the neutron intensity in a minimal space,

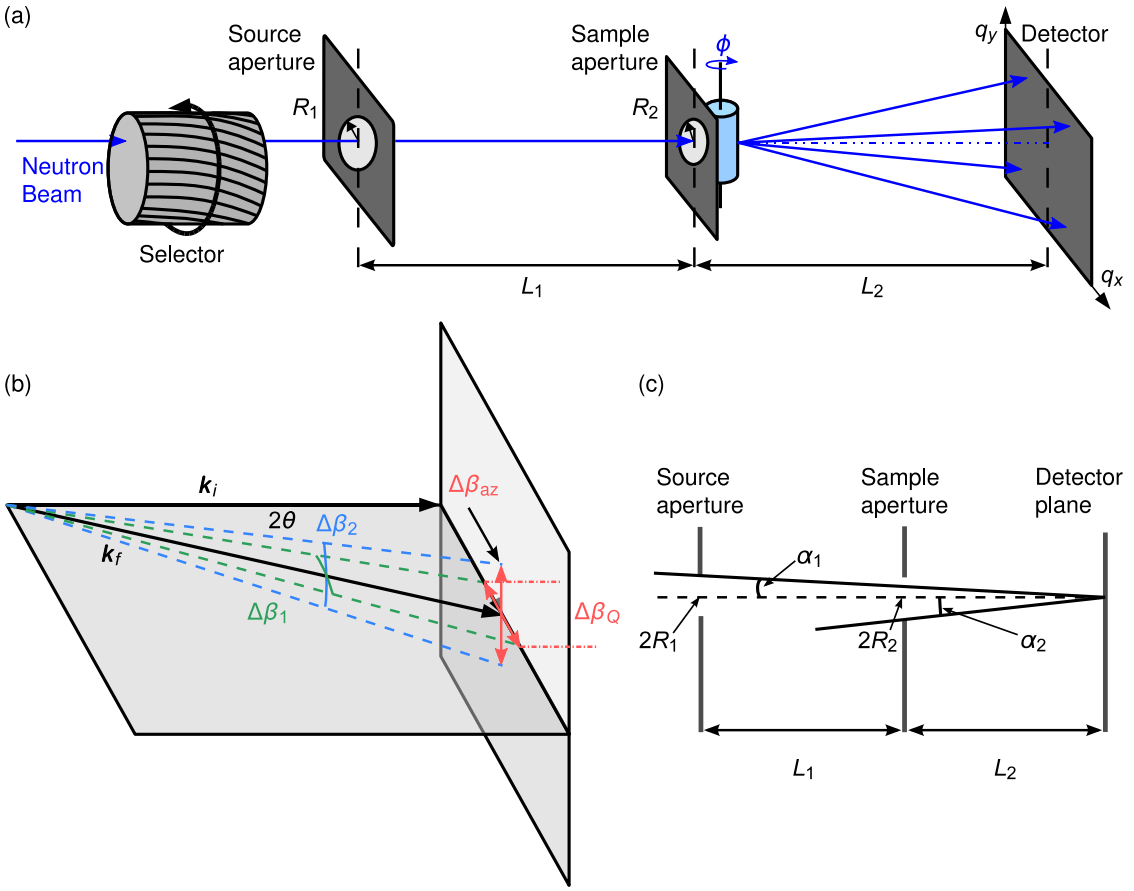

Figure 2.3: (a) Schematic representation of a small-angle scattering experiment. The neutron beam is filtered by the selector and collimated over a length L_1. The scattered neutrons are registered with a detector positioned at a distance L_2 from the sample. (b) Resolution widths defined by the scattering plane spanned by the neutron wavevectors $\boldsymbol{k}_i$ and $\boldsymbol{k}_f$. $\Delta\beta_1$ (green) is the resolution within the plane, while $\Delta\beta_2$ is related to the resolution perpendicular to the scattering plane. (c) The angles α_1 defined by the source aperture and α_2 defined by the sample aperture determined the exact form of the resolution functions, see text.

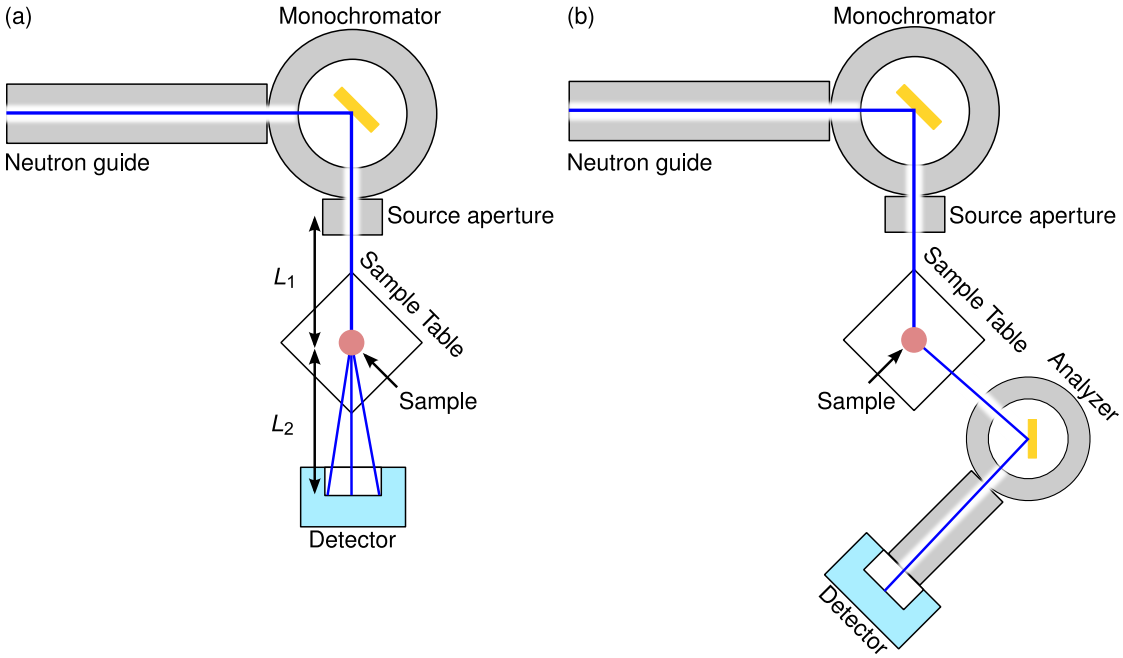

(c)

Figure 2.4: (a) MIRA in a SANS configuration. A monochromator yields a neutron beam with a very small wavelength spread. After source aperture the neutrons travel in air, resulting in a reduction of flux at the sample due to scattering. The total length available to distribute between L_1 and L_2 is $\sim$ 5 m. (b) MIRA in triple-axis-spectrometer mode. (c) Instrument MIRA in a two-axis configuration. The detector can be seen on the left, the sample table is in the middle and mounted on it are bespoke elliptical focusing guides, which increase the neutron flux at the sample.

increasing the efficiency dramatically when measuring microscopic samples [86]. In a typical SANS configuration, the detector can be placed about 3 m behind the sample and is the largest constraint when measuring large magnetic structures. Currently, neutrons are recorded using a CASCADE detector [87] and through the standard sample environment of the MLZ magnetic fields up to 7 T can be applied, and samples can be cooled down to 50 mK.

SANS-1, in contrast, is a typical small-angle scattering instrument, the neutron beam can be collimated over a distance of 20 m [88]. Scattered neutrons are detected with an array of 128 3He position-sensitive tubes. The total area of the detector is about 1 m^2 with a resolution of 8 mm. Alternatively, one can choose to use a secondary high-resolution detector, with a spatial pixel width of 3 mm and a total active area of 0.25 m^2. A high-resolution velocity selector which yields a wavelength spread of $\frac{\Delta\lambda_n}{\lambda_n} = 6\,\%$, otherwise it is 10 %.

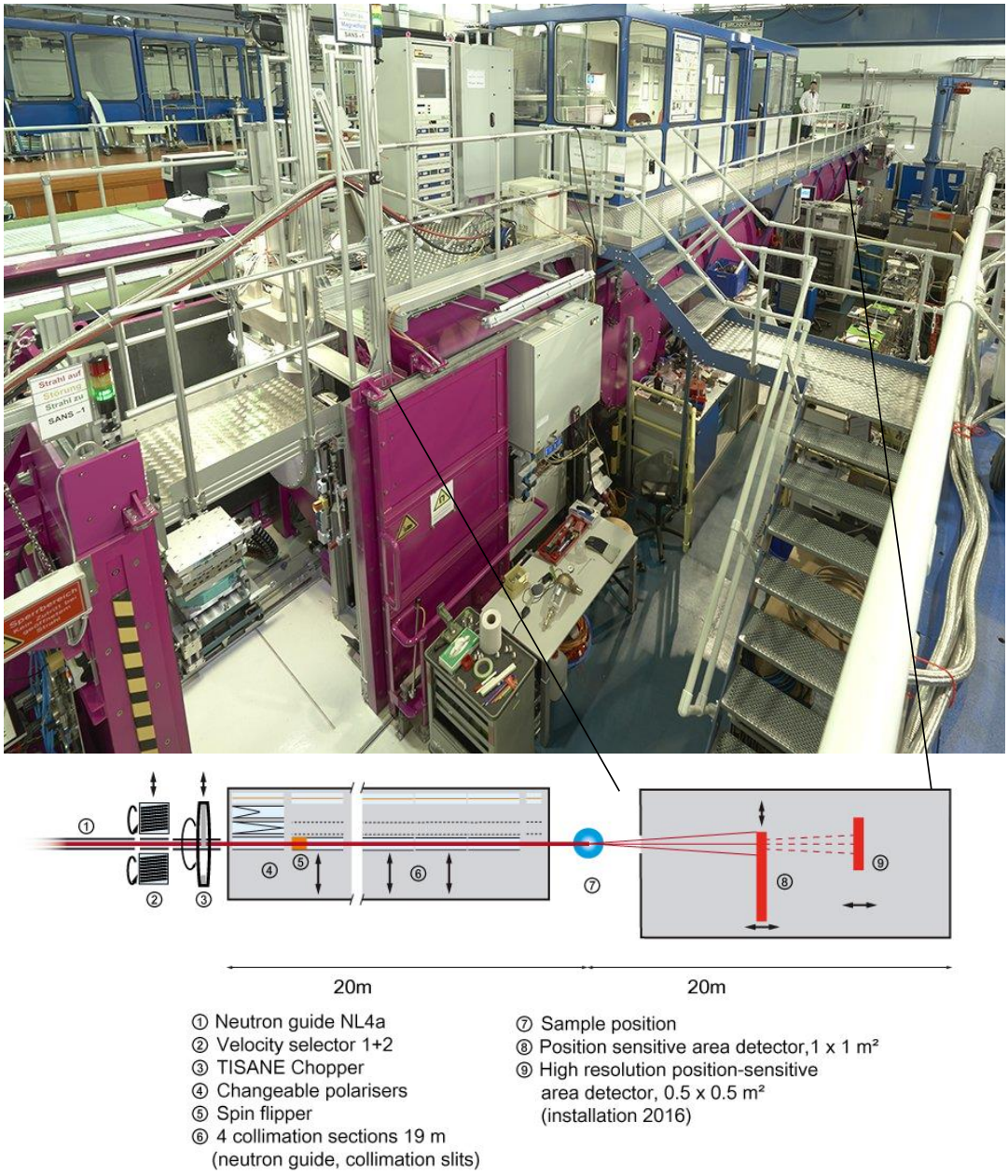

Figure 2.5: Top: Photograph of SANS-1 instrument at MLZ. The sample chamber, the measurement cabin and part of the evacuated detector chamber are visible. Bottom: Schematic representation of the instrument including available experimental options.

3

FIELD-INDUCED HELIX REORIENTATION IN MNSI

As mentioned in the introduction, the discovery of skyrmion lattices in cubic chiral magnets fueled a substantial increase in the scientific interest drawn by these compounds [9, 11, 14, 44, 89, 90]. It is not the first time that these materials are at the center of fundamental developments in condensed matter physics. In the late 1970s studies by Ishikawa [91] and Motoya [92] identified helimagnetism as the ground state of the B20 compound MnSi. Shortly thereafter it was recognized to be one of the first examples of an incommensurate long-wavelength magnetic modulation driven by the Dzyaloshinskii-Moriya interaction [26, 83, 93, 94], and subsequent work addressing the spin fluctuation spectra, electronic structure, and magnetic equation of state of MnSi were not only substantial for the study of itinerant magnetism but also laid the groundwork for the field of quantum phase transitions [95, 96].

Efforts to describe the origins of the magnetic order in MnSi excluded magnetic anisotropies due to their relatively small magnitude in comparison to other contributions. However, a full understanding of all of the aforementioned properties requires a detailed consideration of the role of magnetic anisotropies in the system, as it pertains to (i) the incommensurability of the helical state at zero-field, (ii) itinerant-electron magnetism and the non-Fermi liquid behavior reported under hydrostatic pressure [72, 97, 98] and, specially, (iii) the formation of the skyrmion lattice phase, since magnetic anisotropies were an essential part of the theoretical framework predicting its existence [38, 41, 99] (see also Chapter 4).

This chapter discusses a combined experimental and theoretical study of the reorientation process of the helix in MnSi driven by a competition of the Zeeman energy and magnetocrystalline anisotropies. A detailed characterization of this transition was obtained via neutron scattering, magnetization, and ac-susceptibility measurements, for magnetic fields applied along a range of different crystallographic directions. A careful comparison of these results with theoretical predictions, derived from an effective potential for the helix vector $\boldsymbol{Q}$, reveal the reorientation process to be a crossover phenomenon for general magnetic field directions, accompanied by a discontinuous first-order transition to depopulate energetically unfavorable domains present in the case of zero-field cooling. For a subset of high-symmetry directions, a residual $\mathbb{Z}_2$ is broken through a second-order transition. A particular case arises for fields along $\langle 100 \rangle$ axes where a $\mathbb{Z}_2 \times \mathbb{Z}_2$ symmetry is broken via two subsequent transitions. Overall, theoretical predictions match the experimental observations very well, allowing to determine the parameters of the magnetocrystalline potential quantitatively.

The chapter is organized as follows: section 3.1 discusses the general phase diagram of chiral magnets, including a detailed account of previous work concerning the magnetic anisotropies in chiral magnets. Section 3.2 introduces an effective theory for the helix vector $\boldsymbol{Q}$ in the limit of weak magnetocrystalline anisotropies. The experimental results obtained from small-angle neutron scattering (SANS) used to obtain the specific parameters for the case of MnSi are presented in section 3.3 followed by a discussion of the magnetic susceptibility and the different time scales of the magnetic response in section 3.4. The role of finite temperature effects for the accurate description of the experimental results after zero-field cooling (ZFC) are discussed in 3.5. Section,3.6 the chapter concludes with a discussion of the main results obtained and the emergence of topological defects as part of the process of domain coalescence at the second-order phase transition

3.1 THE MAGNETIC PHASE DIAGRAM OF CHIRAL MAGNETS

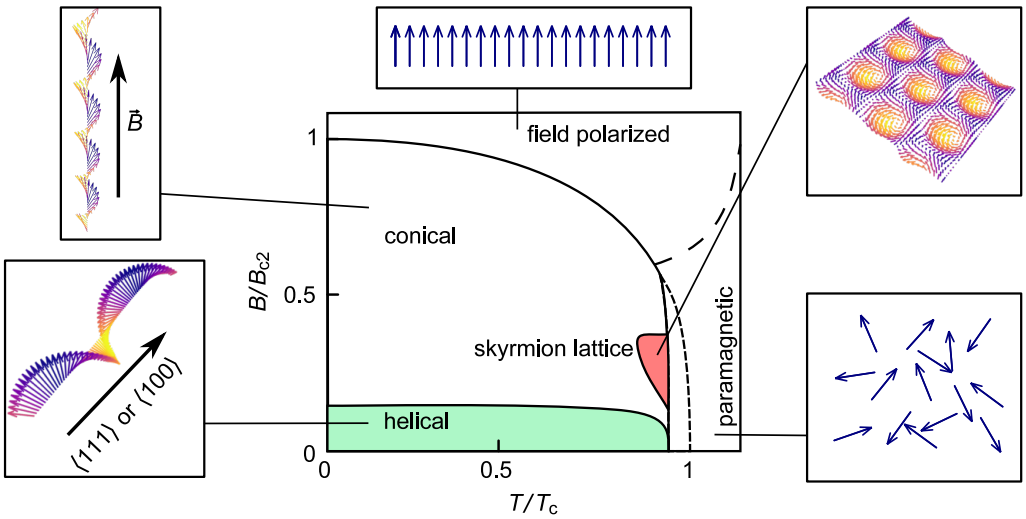

Figure 3.1: Schematic phase diagram of cubic chiral magnets. At low temperatures and small magnetic fields, the magnetic order consists of helical propagations along the easy-axis of the system, either the $\langle 100 \rangle$ or $\langle 111 \rangle$ axes. Increasing the magnetic field leads to a reorientation of the helix so that it propagates along the magnetic field direction, while the spins tilt towards the propagation axis. At the critical field B_{c2}, the system reaches the field polarized region. Just below the critical temperature T_c and at moderate magnetic fields, there is a small phase pocket where the skyrmion lattice is observed. At higher temperatures, the system shows a paramagnetic state.

The class of cubic chiral magnets encompasses compounds with a chiral crystal structure, which allows for the Dzyaloshinskii-Moriya (DM) interaction due to the lack of inversion symmetry. Until recently, all known skyrmions hosting materials included in these class crystallize with the $P2_13$ space group. The discovery of skyrmion lattices in Co-Zn-Mn alloys with β-Mn-type structure adds the $P4_132$ and $P4_332$ space groups to the mixture. In general, β-Mn-type materials and B20 compounds display similar physical characteristics. This correspondence leads to the conclusion that the origin of the magnetic order observed in these β-Mn compounds is most likely the same as for the more conventional chiral magnets. The helimagnetic order in the latter is the consequence of a well-understood hierarchy of energies, where the ferromagnetic exchange interaction is the dominant contribution. By its own, it would lead to a colinear magnetic order, but the inclusion of the DM interaction produces a small continuous twist between neighboring spins, resulting in a helical propagation. The relative strength of the ferromagnetic and the DM interactions determines the length scale of the magnetic modulation. The latter is proportional to spin-orbit coupling, which is small in MnSi and even weaker in other cubic chiral magnets. Hence, the helical periodicities are large when compared with crystal lattice constant. Last but not least, the magnetocrystalline anisotropies determine the preferred propagation direction which is constrained to either $\langle 100 \rangle$ or $\langle 111 \rangle$ axes.

The interplay of these three contributions produces a rich magnetic phase diagram, schematically depicted in figure 3.1. At zero-field, the magnetic order consists of a multi-domain state with equally populated domains of helices propagating along the equivalent easy axes of the system, known as the *helical phase*. Applying a magnetic field along a general direction leads to a rotation of the propagation vector $\boldsymbol{Q}$ towards the magnetic field $\boldsymbol{B}$, while its magnitude $|\boldsymbol{Q}|$ remains unchanged. At the characteristic magnetic field B_{c1} the system transitions into

the *conical phase*, where $\boldsymbol{Q} \parallel \boldsymbol{B}$. Thus, the system undergoes a macroscopic reconfiguration of the magnetization, and the spins gain Zeeman energy by canting towards the propagation axis. This angle is reduced continuously with increasing magnetic fields until it vanishes at the critical field B_{c2} in a second-order transition into the *field polarized* state. A small region just below T_{c} and medium magnetic fields completes the phase diagram. Here the *skyrmion lattice phase* is stabilized by coupling to thermal fluctuations, representing a great example of order-by-disorder [11, 100, 101]. As mentioned above the latter has attracted much scientific interest since its discovery. However, this chapter focuses on the transition at B_{c1} and the specific role of magnetocrystalline anisotropies play in it.

Ishikawa *et al.* gave the first experimental account of the helix reorientation in MnSi based on SANS measurements [91, 102]. Their work also discussed the depopulation of magnetic domains. Similar observations were made by Lebech *et al.* for FeGe [103], Grigoriev *et al.* for $Fe_{1-x}Co_xSi$ [104], and Adams *et al.* for Cu_2OSeO_3 [90]. Note that before the identification of the skyrmion lattice in the so-called A-phase in B20 compounds, the observed scattering pattern in this region of the magnetic phase diagram was misinterpreted as a spontaneous reorientation of the helix. The smooth change in the direction of the helix propagation vector $\boldsymbol{Q}$ results in a nonlinear dependence of the magnetization on the applied magnetic field, which was observed first by Bloch *et al.* [105] and associated with the reorientation process by Hansen [106]. A recent study comparing different B20 compounds can be found here [107]. The aforementioned scientific work indeed includes the main features of the transition; however, the focus laid on a few high symmetry axes and the necessary detail for a full analysis of the transition was not part of their scope.

Plumer and Walker [108], as well as, Nakanishi and Kataoka [109] study the reorientation process of the helical magnetic order in the framework of the Ginzburg-Landau theory. The first pair focus on MnSi, while the latter carried out their analysis for several point groups without inversion symmetry. Both these studies identified the reorientation process as a competition between the Zeeman energy and the magnetocrystalline anisotropy. Plumer and Walker identified the second-order phase transitions at a critical field B_{c1} expected for magnetic fields applied parallel to the $\langle 100 \rangle$ and $\langle 110 \rangle$ axes, and the ratio of the critical fields $B_{\mathrm{c1}}^{\langle 100 \rangle} / B_{\mathrm{c1}}^{\langle 110 \rangle}$ to be $\sqrt{2}$. Both of these publications explain the nonlinear magnetization observed at low fields in MnSi by the rotation process of the propagation vector. Walker expanded on these analyses and studied the transition for a magnetic field applied along a $\langle 100 \rangle$ crystallographic axes further, recognizing that the transition separates in two under decreasing magnetic fields [110]. This prediction had not been previously verified. These studies did not address the transitions quantitatively due to the lack of a value for the magnetic susceptibility perpendicular to the helical propagation vector $\chi_{\perp}$. Grigoriev and collaborators calculated the latter in the limit of zero magnetic field. However, they did not carry out a full analysis of the helix reorientation process [43, 104].

3.2 THEORETICAL ANALYSIS OF THE HELIX REORIENTATION IN MNSI

In MnSi the characteristic magnetic field for the transition from the helical phase to the conical phase B_{c1} is small in comparison to the critical field B_{c2}, where the system reaches the field polarized state. The relative size of the transition magnetic field values is an indication of small spin-orbit coupling λ_{SOC}, since $B_{\mathrm{c1}} / B_{\mathrm{c2}} \sim \lambda_{\mathrm{SOC}}^2$. For such a case, the reorientation process can be derived from a Landau potential $\mathcal{V}$ that only depends on the helix propagation vector $\boldsymbol{Q}$. The properties of the magnetization enter through the magnetic susceptibility tensor

χ_{ij}. Magnetocrystalline anisotropies generate only slight deformations to the helix magnetization, observed experimentally in terms of higher harmonics $e^{\pm 2Qr}$, with very small amplitudes [103, 111, 112]. Therefore, the magnetization of the pristine helix determines the magnetic susceptibility. The latter is derived below based on the supplementary information provided by Janoschek *et al.* in [113], neglecting corrections due to cubic anisotropies.

Ginzburg-Landau theory of chiral magnets

Cubic chiral magnets can be described by a Ginzburg-Landau functional $\mathcal{F} = \int d^3x\, f$, with the energy density $f = f_0 + f_{\text{cub}}$, where [83, 94]:

$$f_0 = \frac{1}{2}\boldsymbol{\psi}\left(r - J\nabla^2\right)\boldsymbol{\psi} + D\boldsymbol{\psi}\left(\nabla \times \boldsymbol{\psi}\right) + \frac{u}{4!}\left(\boldsymbol{\psi}^2\right)^2 - \mu\boldsymbol{\psi}\boldsymbol{B}. \tag{3.1}$$

The three-component order parameter field $\boldsymbol{\psi}$ has dimensionless units, leading to a magnetization density $\boldsymbol{M} = \mu\boldsymbol{\psi}$, with $\mu = \mu_B$/f.u.. In the case of MnSi, it results in a single Bohr magneton per formula unit f.u.$= 24.018\,\text{Å}^3$. The parameter r indicates the distance to the phase transition, while the parameters J and u represent the exchange stiffness and the interaction of the ferromagnetic exchange, respectively. D corresponds to the DM interaction and is proportional to the strength of spin-orbit coupling λ_{SOC}. The last term in 3.1 accounts for the Zeeman coupling to a magnetic field $\boldsymbol{B}$. Note that terms of higher-order in spin-orbit coupling contained in f_{cub} break the rotation symmetry of f_0 at $\boldsymbol{B} = 0$ due to cubic anisotropies. The ansatz for a single conical helix is

$$\boldsymbol{\psi}_{\text{hel}}(\boldsymbol{r}) = \hat{\psi}_0\psi_0 + \Psi_{\text{hel}}\hat{e}^- e^{i\boldsymbol{Q}\boldsymbol{r}} + \Psi^*_{\text{hel}}\hat{e}^+ e^{-i\boldsymbol{Q}\boldsymbol{r}} \tag{3.2}$$

with the homogeneous magnetization ψ_0 and the complex modulation Ψ_{hel} of the helical order characterized by the propagation vector $\boldsymbol{Q}$. The normalized dreibein $\hat{e}_1 \times \hat{e}_2 = \hat{e}_3 \equiv \boldsymbol{Q}/|\boldsymbol{Q}|$ yields the vectors $\hat{e}^{\pm} = (\hat{e}_1 \pm \hat{e}_2/)\sqrt{2}$. Evaluating the energy density using this ansatz yields the mean-field potential $\mathcal{V}_{\text{MF}} = \mathcal{V}_0 + \mathcal{V}_{\text{cub}}$. The first term determines the strength of the amplitudes, and it reads:

$$\begin{aligned}\mathcal{V}_0 = {} & \frac{r}{2}\psi_0^2 + (r + J|\boldsymbol{Q}|^2 - 2D|\boldsymbol{Q}|)|\Psi_{\text{hel}}|^2 + \frac{u}{4!}(\psi_0^2 + 2|\Psi_{\text{hel}}|^2)^2 \\ & - \mu\psi_0|\boldsymbol{B}|,\end{aligned} \tag{3.3}$$

while the second term, which the following derivation neglects, includes all contributions leading to the orientation of the propagation vector $\boldsymbol{Q}$ and the homogeneous magnetization. One can reduce the potential at $\boldsymbol{B} = 0$ to:

$$\mathcal{V}_{\text{MF}} \approx \delta|\Psi_{\text{hel}}|^2 + \frac{u}{3!}|\Psi_{\text{hel}}|^4, \tag{3.4}$$

with the propagation length $|\boldsymbol{Q}| \approx D/J$, obtained from minimization with respect to $|\boldsymbol{Q}|$, and by introducing the helimagnetic tuning parameter

$$\delta = r - J|\boldsymbol{Q}|^2. \tag{3.5}$$

Helical magnetic order emerges if δ becomes negative, i. e., if r is smaller than the DM energy density $r \leq J|\boldsymbol{Q}|^2$. Minimizing the potential with respect to the helix amplitude yields $|\Psi_{\text{hel}}|^2 = -3\delta/u$.

Magnetic susceptibility of helimagnetic order

The susceptibility tensor contains the fluctuations around the mean-field solution, and it writes

$$\chi^{-1}_{0,i,j}\left(\boldsymbol{r},\boldsymbol{r'}\right) = \frac{\delta^2 \int d^3x f/\left(k_B T\right)}{\left[\delta\boldsymbol{\psi}_i\left(\boldsymbol{r}\right)\delta\boldsymbol{\psi}_j\left(\boldsymbol{r'}\right)\right]} \tag{3.6}$$

$$\begin{aligned} &= \frac{1}{k_B T}\Big\{(r - J\nabla^2_{\boldsymbol{r}})\delta_{ij} - 2D\varepsilon_{ijn}\nabla_{\boldsymbol{r}_n} \\ &\quad + \frac{u}{3!}\left[\boldsymbol{\psi}(\boldsymbol{r})\boldsymbol{\psi}(\boldsymbol{r})\delta_{ij} + 2\boldsymbol{\psi}_i(\boldsymbol{r})\boldsymbol{\psi}_j(\boldsymbol{r})\right]\Big\} \\ &\quad \times \delta(\boldsymbol{r}-\boldsymbol{r'}) + \chi^{-1}_{\mathrm{cub}\,ij}(\boldsymbol{r},\boldsymbol{r'}) \end{aligned} \tag{3.7}$$

with the mean-field order parameter $\boldsymbol{\psi}(\boldsymbol{r})$ and χ^{-1}_{cub}, the contributions arising from cubic anisotropies f_{cub}.

The magnetic susceptibility is obtained from the generalized matrix $\chi^{-1}_{0,ij}(\boldsymbol{k},\boldsymbol{k'})$ taken at zero momenta. In the helical phase $|\boldsymbol{\Psi}_{\mathrm{hel}}| > 0$, thus the mean field order parameter $\boldsymbol{\psi}(\boldsymbol{r})$ carries a finite momentum $\boldsymbol{Q}$ and the susceptibility is non-diagonal in momentum space

$$\begin{aligned} k_B T\chi^{-1}_{0,ij}(\boldsymbol{k},\boldsymbol{k'}) &= k_B T\chi^{-1}_{0,ij}(\boldsymbol{k})\delta_{0,\boldsymbol{k}+\boldsymbol{k'}} \\ &\quad + \frac{u}{3}\Psi^2_{\mathrm{hel}}\hat{e}^-_i\hat{e}^-_j\delta_{2\boldsymbol{Q},\boldsymbol{k}+\boldsymbol{k'}} + \frac{u}{3}\Psi^{*2}_{\mathrm{hel}}\hat{e}^+_i\hat{e}^+_j\delta_{-2\boldsymbol{Q},\boldsymbol{k}+\boldsymbol{k'}} \\ &\quad + \frac{u}{3}\Psi_{\mathrm{hel}}\psi_0(\hat{e}^-_i\hat{\psi}_{0j} + \hat{e}^-_j\hat{\psi}_{0i})\delta_{\boldsymbol{Q},\boldsymbol{k}+\boldsymbol{k'}} \\ &\quad + \frac{u}{3}\Psi^*_{\mathrm{hel}}\psi_0(\hat{e}^+_i\hat{\psi}_{0j} + \hat{e}^+_j\hat{\psi}_{0i})\delta_{-\boldsymbol{Q},\boldsymbol{k}+\boldsymbol{k'}} \end{aligned} \tag{3.8}$$

where $\chi^{-1}_{0,ij}(\boldsymbol{k})$ is the part diagonal in momenta and it reads:

$$\begin{aligned} \chi^{-1}_{0,ij}(\boldsymbol{k}) = \frac{1}{k_B T}\Big[&(r + Jk^2)\delta_{ij} - 2D\varepsilon_{ijn}i\boldsymbol{k}_n \\ &+ \frac{u}{3!}\psi_0^2(\delta_{ij} + 2\hat{\psi}_{0i}\hat{\psi}_{0j}) + \frac{u}{3}|\Psi_{hel}|^2(2\delta_{ij} - \hat{Q}_i\hat{Q}_j)\Big]. \end{aligned} \tag{3.9}$$

The thermodynamic dimensionless magnetic susceptibility of a single helimagnetic domain is then given by $\chi_{\mathrm{ij}} = \frac{\mu_0\mu^2}{k_B T}\chi_{0,ij}(0,0)$. Note that due to the momentum carried by the order parameter $\chi_{0,ij}(0,0) \neq \left[\chi^{-1}_{0,ij}(0,0)\right]^{-1}$. At zero magnetic field $|\boldsymbol{B}| = 0$ there is no homogeneous magnetization and the dimensionless magnetic susceptibility is reduced to:

$$\begin{aligned} \chi_{\mathrm{ij}} &= \chi_{\parallel}\hat{Q}_i\hat{Q}_j + \chi_{\perp}(\delta_{ij} - \hat{Q}_i\hat{Q}_j) \\ &= \frac{\mu_0\mu^2}{JQ^2}\left[\hat{Q}_i\hat{Q}_j + \frac{1 - \delta/(J|\boldsymbol{Q}|^2)}{1 - 2\delta/(J|\boldsymbol{Q}|^2)}(\delta_{ij} - \hat{Q}_i\hat{Q}_j)\right], \end{aligned} \tag{3.10}$$

using $|\boldsymbol{\Psi}_{\mathrm{hel}}| = 3\delta/u$ from the equation of state (3.4) and the helimagnetic tuning parameter δ (cf. equation 3.5). The terms in the first line are the susceptibilities longitudinal $\chi_{\parallel}$ and transverse $\chi_{\perp}$ to the propagation vector $\boldsymbol{Q}$. In the limit $\delta \to -\infty$, i. e., deep in the helical phase, $\chi_{\parallel} = 2\chi_{\perp}$. In the case of MnSi, a numerical value $\chi_{\parallel}$ for the helix can be obtained from ac susceptibility χ_{ac} measurements along a $\langle 111\rangle$ axis after cooling the sample in an applied magnetic field $|\boldsymbol{B}| \gg B_{\mathrm{c2}}$, thus preparing a single domain state. The measured quantity $\tilde{\chi}_{\parallel}$ includes demagnetization effects and relates to $\chi_{\parallel}$ via

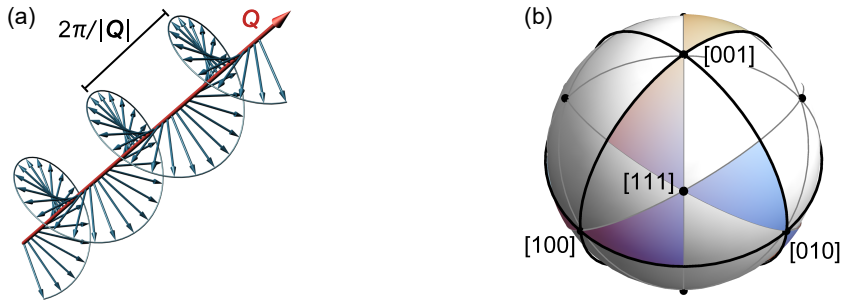

Figure 3.2: Helimagnetism in the cubic B20 compound MnSi. (a) Representation of a helical modulation with pitch vector $\boldsymbol{Q}$ (red arrow). In the case of MnSi the helices propagate along the $\langle 111\rangle$ crystal axes. (b) Representation of the tetrahedral point group T of MnSi. It contains threefold rotation axes along $\langle 111\rangle$ and twofold rotation axes along $\langle 100\rangle$. Note the big black circles, connecting two $\langle 100\rangle$ axis through a $\langle 110\rangle$ axis, separating the spheres into octants around each $\langle 111\rangle$.

$$\tilde{\chi}_\nu = \frac{\chi_\nu}{(1+\chi_\nu N)}, \tag{3.11}$$

with the demagnatization factor N. Taking this into consideration one obtains $\chi_\parallel = 0.34$.

Effective Landau potential for the helical propagation in MnSi

The magnetization of a helix with amplitude M_s is given by (cf. 3.2):

$$\boldsymbol{M}(\boldsymbol{r}) = M_s \left[\hat{e}_1 \cos(\boldsymbol{Q}\boldsymbol{r}) + \hat{e}_2 \sin(\boldsymbol{Q}\boldsymbol{r})\right], \tag{3.12}$$

and characterized by the propagation vector $\boldsymbol{Q}$, see figure 3.2,(a). As mentioned above the size of $\boldsymbol{Q}$ is determined by the Dzyaloshinskii-Moriya (DM) interaction that is proportional to spin-orbit coupling λ_{SOC} and weak in MnSi. Thus the Landau potential $\mathcal{V}$ can be expanded in a Taylor series in $\boldsymbol{Q} \propto \lambda_{\mathrm{SOC}}$ including the lowest order terms only. In MnSi the length of the propagation vector $|\boldsymbol{Q}|$ is essentially constant. Furthermore the helix is invariant under the transformation $\boldsymbol{Q} \to -\boldsymbol{Q}$ and $\hat{e}_2 \to -\hat{e}_2$, thus the orientation $\hat{Q} = \boldsymbol{Q}/|\boldsymbol{Q}|$ can be considered a director. Hence the potential $\mathcal{V}(\hat{Q}) = \mathcal{V}_B + \mathcal{V}_T$ is an even function of $\hat{Q}$, consisting of the Zeeman energy $\mathcal{V}_B$ and a term arising from the magnetocrystalline anisotropies $\mathcal{V}_T$. In small fields, the former reads explicitly

$$\mathcal{V}_B(\hat{Q}) = \frac{-1}{2}\chi_{ij}\boldsymbol{B}_i\boldsymbol{B}_j = \frac{-1}{2}\left[\chi_\perp \boldsymbol{B}^2 + (\chi_\parallel - \chi_\perp)(\boldsymbol{B}\hat{Q})^2 + \cdots\right]. \tag{3.13}$$

In leading order in λ_{SOC}, $\mathcal{V}_B$ is determined by the susceptibility tensor of the helix magnetization with a *fixed* pitch vector $\boldsymbol{Q}$ (cf. equation 3.10). In order to compare the theory with the experimental results, one has to take the sample shape into account, i. e., the demagnetization factor N. Most of the data presented here were measured on a spherical sample. The remaining results were measured on cubic samples with a magnetic field along the edges. In all cases $N = 1/3$, and the Zeeman energy must be rewritten with $\tilde{\chi}_\nu$ from equation 3.11 for $\nu = \parallel, \perp$. Using the value for the longitudinal susceptibility derived above, one obtains:

$$\tilde{\chi}_\parallel \approx 0.31, \qquad \tilde{\chi}_\perp \approx 0.16 \tag{3.14}$$

It is important to remark that shape anisotropies generally would break the symmetry of the Zeeman potential in Eq. 3.13. Since the study presented here was carried out on a spherical sample, such corrections are not considered further.

The potential attributed to the magnetocrystalline anisotropies $\mathcal{V}_T$ dictates the behavior of the helix at zero magnetic field. The symmetry operations of the crystal structure restrict the terms allowed. MnSi crystallizes in the cubic space group $P2_13$ and its symmetry operations are defined by the tetrahedral point group T, cf. figure 3.2 (b), and include a twofold rotation symmetry C_2 around the $\langle 100\rangle$ cubic axes and a threefold rotation symmetry C_3 around the $\langle 111\rangle$. The lack of inversion symmetry breaks the $\langle 111\rangle$ axes in two classes, i. e., the $[111]$ axis is not equivalent to the $[\bar{1}\bar{1}\bar{1}]$. However, we consider the orientation of the helix $\hat{Q}$ to be a director. Thus $\langle 111\rangle$ refers to both classes. Taking the symmetry operations into consideration, the corresponding potential for $\hat{Q}$ reads

$$\mathcal{V}_T(\hat{Q}) = \varepsilon_T^{(1)}(\hat{Q}_x^4 + \hat{Q}_y^4 + \hat{Q}_z^4) + \varepsilon_T^{(2)}(\hat{Q}_x^2\hat{Q}_y^4 + \hat{Q}_y^2\hat{Q}_z^4 + \hat{Q}_z^2\hat{Q}_x^4) + \cdots. \tag{3.15}$$

The leading first term with energy density $\varepsilon_T^{(1)} \sim \lambda_{\mathrm{SOC}}^4$ is fourth-order in spin-orbit coupling. Although there exists another term of fourth-order in λ_{SOC} of the form $(\hat{Q}_x^2\hat{Q}_y^2 + \text{cycl.})$, it is equivalent to the first term in Eq. 3.15 up to a constant and thus superfluous. The energy contribution from $\varepsilon_T^{(2)}$ is sixth order in λ_{SOC}, nevertheless necessary to break the fourfold rotation symmetry C_4 still contained in the $\varepsilon_T^{(1)}$ term. Other terms of order $\mathcal{O}(\lambda_{\mathrm{SOC}}^6)$ retain the C_4 symmetry and are less important. These, as well as terms of higher-order, are represented by the dots in Eq. 3.15 and will be neglected going forward. Moreover, crystalline anisotropies reduce the rotation symmetry and modify the susceptibility of the Zeeman potential $\mathcal{V}_B$ by way of a term $(B_x^2\hat{Q}_y^2 + \text{cycl.})$. A previous analysis of the Ginzburg-Landau theory for the reorientation transition at B_{c1} demonstrates that this term is of order $O(\lambda_{\mathrm{SOC}}^6)$, thus comparably important as $\varepsilon_T^{(2)}$ for the helix reorientation description. Nonetheless, the accuracy of our results does not allow to distinguish between the various terms of sixth order in spin-orbit coupling. Therefore such corrections to Eq. 3.13 are not included.

An analysis of the transition measured in small-angle neutron scattering experiments yields the specific values for the parameters $\varepsilon_T^{(1)}$ and $\varepsilon_T^{(2)}$, see also section 3.3. An excellent agreement between theoretical and experimental results was reached for

$$\varepsilon_T^{(1)} \approx 0.0034\,\mu\mathrm{eV}/\mathrm{\AA}^3, \qquad \varepsilon_T^{(2)} \approx 0.35\,\varepsilon_T^{(1)} \tag{3.16}$$

Trajectories for the helix reorientation

Minimizing the Landau potential $\mathcal{V} = \mathcal{V}_B + \mathcal{V}_T$ with respect to $\hat{Q}$ provides the orientation of the helix for a given magnetic field $\boldsymbol{B}$. In zero magnetic field, the direction of the helical domains is determined solely by the potential arising from the magnetocrystalline anisotropies $\mathcal{V}_T$. Since $\varepsilon_T^{(1)} > 0$, the potential is minimized for $\hat{Q} \parallel \langle 111\rangle$. If the state is prepared by cooling the system in zero magnetic field, then four equivalent domains pointing along the volume diagonals of the crystal structure, i. e.,$[111]$, $[1\bar{1}\bar{1}]$,$[\bar{1}1\bar{1}]$ and $[\bar{1}\bar{1}1]$, are equally populated. At magnetic fields $\boldsymbol{B} > B_{\mathrm{c1}}$, helices propagating along $\boldsymbol{B}$ minimize the Zeeman contribution. One can distinguish between this two starting points, i. e., multi-domain state at zero magnetic field with $\hat{Q} \parallel \langle 111\rangle$ and a single domain state with $\hat{Q} \parallel \boldsymbol{B}$ at large fields. An analysis of the potential $\mathcal{V}$ for different field directions yields three distinct scenarios:

- $\boldsymbol{B}$ points within one of the octants of the unit sphere separated by the black great circle in figure 3.2,(b) centered around a $\langle 111\rangle$

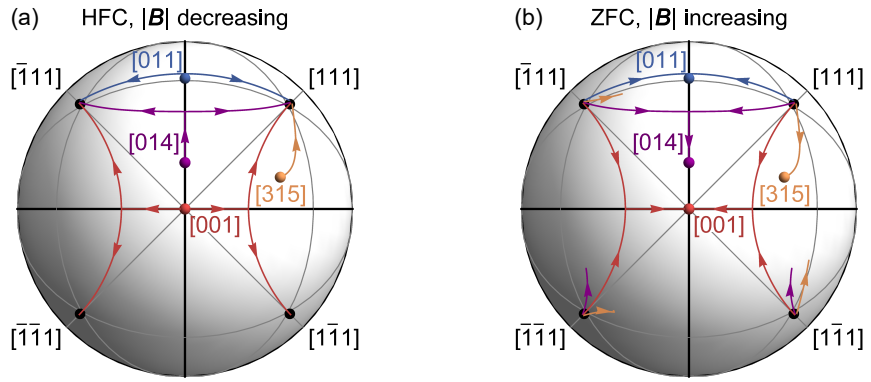

Figure 3.3: Trajectories of the helix pitch vector $\hat{Q}$ for decreasing and increasing magnetic field values and different field directions $\boldsymbol{B}$. (a) High-field cooling (HFC) yields a single domain conical propagation as the starting point. Typically, decreasing the magnetic field leads to a single domain state propagating along the $\langle 111 \rangle$ axis closest to $\boldsymbol{B}$. The bifurcation observed for magnetic field directions on the big circles (cf. Fig. 3.2) indicates elastic Ising transitions. (b) Zero-field cooling prepares the system in a multi-domain state, with helical propagations along all $\langle 111 \rangle$ axes. In comparison to the HFC scenario, trajectories for domains with a large angle with respect to $\boldsymbol{B}$ are discontinuous, characteristic of first-order transitions.

- $\boldsymbol{B}$ points along a direction on one of the great circle
- $\boldsymbol{B} \parallel \langle 100 \rangle$

In the first situation, and starting from large magnetic fields, decreasing the field leads to a smooth change of direction of the propagation vector until it points along the corresponding $\langle 111 \rangle$ axis. Such a case is illustrated in figure 3.3 (a) for a magnetic field along a $[315]$. When increasing the field in a multi-domain state at zero magnetic field, only the domain closest to the magnetic field direction will reorient smoothly, the other three domains show a discontinuous transition. Figure 3.3 (b) depicts this transition. The energetically unfavorable domains show a trajectory up to their spinodal point, at which they reconfigure to show that same propagation direction as the stable domain. For a magnetic field applied along one of the great circles connecting the $\langle 100 \rangle$ axes, shown in black in figure 3.3, the four domains are separated into two energetically degenerate pairs. For example, for a $\boldsymbol{B} \parallel [011]$ the first group consists of domains with a propagation vectors $\boldsymbol{Q}$ along the $[111]$ and $[\bar{1}11]$ axes. These have the same angle between propagation vector and magnetic field direction, specifically $\theta^{(1)}_{[011]} \approx 35°$. Domains propagating along the $[1\bar{1}1]$ and $[11\bar{1}]$ axes, which are perpendicular to the magnetic field direction, comprise the second group. The latter group has a discontinuous transition as explained above, while a second-order phase transition is expected as a function of field-strength at B_{c1} for the first group of domains. A stability analysis of the orientation vector $\hat{Q}$ around the field direction $\hat{B}$ provides a detailed characterization of this transition. For that purpose the field direction in parametrized by a polar angle α, i. e., $\hat{B} = (0, \sin\alpha, \cos\alpha)$, and the direction of the pitch vector can be written as $\hat{Q} = \hat{B}\sqrt{1 - x_1^2 - x_2^2} + x_1\hat{v}_1 + x_2\hat{v}_2$, with the orthonormal vectors $\hat{v}_1 = (1, 0, 0)$ and $\hat{v}_2 = (0, \cos\alpha, -\sin\alpha)$. Therefore the coordinate x_1 corresponds to deviations away from the big circle, while x_2 represents deviations on it.

At the critical field B_{c1} the orientation vector $\hat{Q}$ must choose between two directions away from the great circle, i. e., $x_1 > 0$ or $x_1 < 0$, stabilizing a helimagnetic domain along $[111]$ or $[\bar{1}11]$. Thus the coordinate x_1 is an Ising order parameter of the helimagnetic reorientation transition. This situation is illustrated in figure 3.3 for a magnetic field along $[011]$ and $[014]$. In

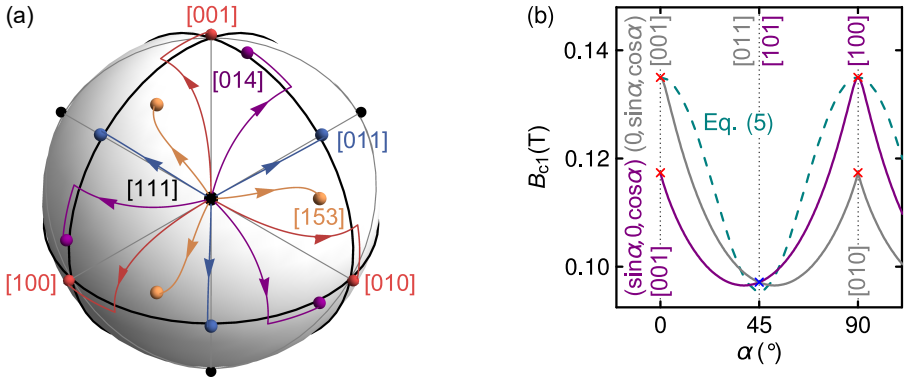

Figure 3.4: Trajectories of the helix pitch vector $\hat{Q}$ for decreasing and increasing magnetic field values and different field directions $\boldsymbol{B}$. (a) High-field cooling (HFC) yields a single domain conical propagation as the starting point. Typically, decreasing the magnetic field leads to a single domain state propagating along the $\langle 111 \rangle$ axis closest to $\boldsymbol{B}$. The bifurcation observed for magnetic field directions on the big circles (cf. Fig. 3.2) indicates elastic Ising transitions. (b) Zero-field cooling prepares the system in a multi-domain state, with helical propagations along all $\langle 111 \rangle$ axes. In comparison to the HFC scenario, trajectories for domains with a large angle with respect to $\boldsymbol{B}$ are discontinuous characteristic of first-order transitions.

both cases, decreasing the field leads to a bifurcation of the $\hat{Q}$ trajectory at B_{c1}, at which point the phase can separate into two domains. For increasing magnetic fields the propagation vectors of each domain $\hat{Q}$ move first smoothly towards the great circle and coalesce on it at B_{c1}. For $\boldsymbol{B} \parallel [014]$ the orientation vector still has a finite angle with respect to $\boldsymbol{B}$ at the point of coalescence, thus the reorientation process is concluded through a smooth rotation towards the magnetic field.

Finally, applying the magnetic field along a $\langle 100 \rangle$ crystallographic axis leads to a distinctive case, as it is a crossing point of the two great circles (cf. Fig. 3.1 (b)). The finite contribution from $\varepsilon_T^{(2)}$ lowers the symmetry of the effective theory for the vector (x_1, x_2) from $\mathbb{Z}_4$, i. e., $\varepsilon_T^{(2)} = 0$, down to $\mathbb{Z}_2 \times \mathbb{Z}_2$. Furthermore, it favors between x_1 and x_2 depending on the sign of $\varepsilon_T^{(2)}$. Consequently, a single $\mathbb{Z}_4$ transition is split into two subsequent $\mathbb{Z}_2$ Ising transitions, as predicted by Walker [110]. In MnSi $\varepsilon_T^{(2)} > 0$, thus the orientation vector $\hat{Q}$ tilts along one of the x_1 directions at $B_{c1,>}^{\langle 100 \rangle}$ when the field is reduced. A further reduction results in a smooth rotation of $\hat{Q}$ along the great circle and away from the field direction until a second instability is reached at $B_{c1,<}^{\langle 100 \rangle}$, where the propagation vector tilts anew, this time away from the great circle along one of the x_2 directions. This is depicted by the red trajectories in figure 3.3 for $\boldsymbol{B} \parallel [001]$.

The low symmetry of the system is also reflected in the trajectories of the helical domains for fields along $[hkl]$, $[lhk]$, and $[klh]$ $(k, l, h > 0)$ depicted in figure 3.4 (a). These are equivalent, and related by a $2\pi/3$ rotation symmetry around the $[111]$ axis, included in the tetrahedral point group T. This symmetry operation leads to the same transition field value for $[hk0]$, $[k0h]$, and $[0hk]$, which differs from the one of the second equivalent group, i. e., $[kh0]$, $[h0k]$, and $[0kh]$. In figure 3.4 (b) the evolution of B_{c1} as a function of angle α is compared for fields $\boldsymbol{B}$ pointing along $(0, \sin\alpha, \cos\alpha)$ and $(\sin\alpha, 0, \cos\alpha)$. With the exception of $\boldsymbol{B} \parallel \langle 110 \rangle$ the values of B_{c1} are different. Morover the upper and lower transition fields of the $\mathbb{Z}_2 \times \mathbb{Z}_2$ transition, $B_{c1,>}^{[001]}$ and $B_{c1,<}^{[001]}$, respectively, are obtained from the limiting values of $B_{c1}(\alpha)$ for $\alpha \to 0$. For the sake of comparison the critical field for $\varepsilon_T^{(2)}$, given by

$$B_{c1}(\alpha)\big|_{\varepsilon_T^{(2)}=0} = \sqrt{\frac{\varepsilon_T^{(1)}\,[3+\cos(4\alpha)]}{\mu_0(\chi_\parallel - \chi_\perp)}}, \tag{3.17}$$

plotted in figure 3.4 (b). Note that in this approximation the critical fields along $\langle 100\rangle$ and $\langle 110\rangle$ satisfy the ratio $B_{c1}^{\langle 100\rangle} \approx \sqrt{2} B_{c1}^{\langle 110\rangle}$, as was discussed by Plumer and Walker in [108].

A more detailed characterization of the effects of a finite value of $\varepsilon_T^{(2)}$ on the magnetization is obtained from the computation of the magnetic susceptibility χ_B. For a macroscopic single domain, i. e., high-field cooled conditions, χ_B follows from the effective Landau potential

$$\begin{aligned}\chi_B \equiv \frac{dM}{dB} &= -\frac{1}{\mu_0}\frac{\partial^2 \mathcal{V}(\hat{Q}_{\min})}{\partial B^2} \\ &= \chi_\perp + (\chi_\parallel - \chi_\perp)(\hat{B}\hat{Q}_{\min})^2 - \frac{1}{\mu_0}\frac{\partial^2 \mathcal{V}(\hat{Q}_{\min})}{\partial \hat{Q}^i_{\min}\partial \hat{Q}^j_{\min}}\frac{\partial \hat{Q}^i_{\min}}{\partial B}\frac{\partial \hat{Q}^j_{\min}}{\partial B},\end{aligned} \tag{3.18}$$

where $\hat{Q}_{\min}(\boldsymbol{B})$ minimizes $\mathcal{V}$ for a given field $\boldsymbol{B}$ and $B = |\boldsymbol{B}|$. Figure 3.5 (a) illustrates the distinct behavior of the transition at B_{c1} observed for fields parallel to $[0x1]$ in comparison to those pointing along $[x01]$, with $1 > x > 0$, by means of the magnetic susceptibility χ_B. For $x = 0$ two sharp critical signatures (red arrows) are observed related with the subsequent $\mathbb{Z}_2$ Ising transitions observed for fields along $\langle 100\rangle$ axes. Tilting the field away from this high symmetry axis, i. e., $x > 0$, breaks one of the Ising symmetries explicitly. Thus the corresponding signature in χ_B is no longer sharp but rounded, resulting in different susceptibility curves and transition fields B_{c1} for $[0x1]$ and $[x01]$. For increasing values of x the signature of the broken symmetry disappears completely and the field value of the transition for both cases discussed come closer, attaining the same value for $\boldsymbol{B} \parallel [101]$ and $\boldsymbol{B} \parallel [011]$, cf. Fig. 3.5 (a) and (b). Similar effects can be observed for generic field directions, albeit more subtle.

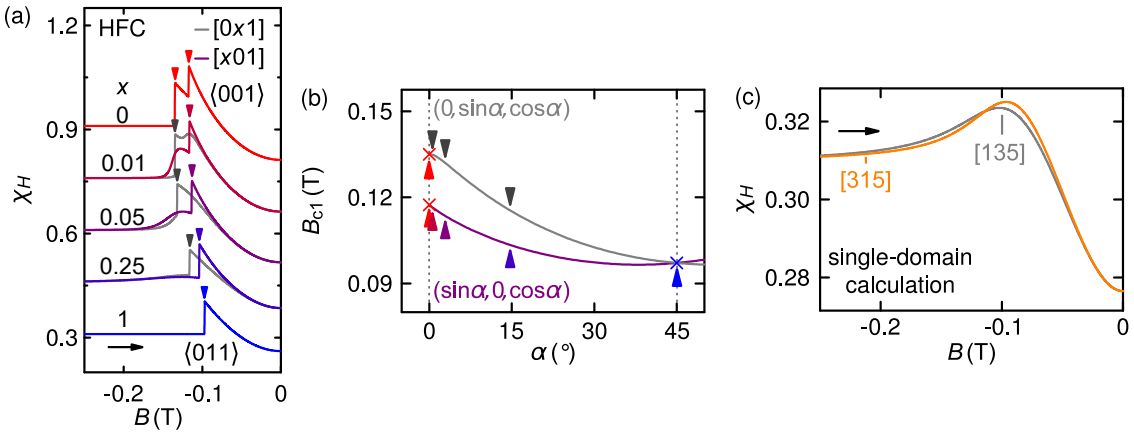

Figure 3.5: Magnetic susceptibility χ_B obtained for single-domain calculations, i. e., high-field cooled (HFC), showing the dependence of the helix reorientation transition on the field direction. (a) Susceptibility for fields along $[0x1]$ and $[x01]$, for different values of x (data have been shifted for clarity). The $\mathbb{Z}_2$ Ising transitions, identified by sharp signatures (arrows), have different values depending on the field direction. (b) Critical field B_{c1} as a function of angle alpha, i. e., the field direction. Arrows depict the values for the transitions shown in (a). (c) Subtle differences can be observed for generic field directions due to magnetocrystalline anisotropies.

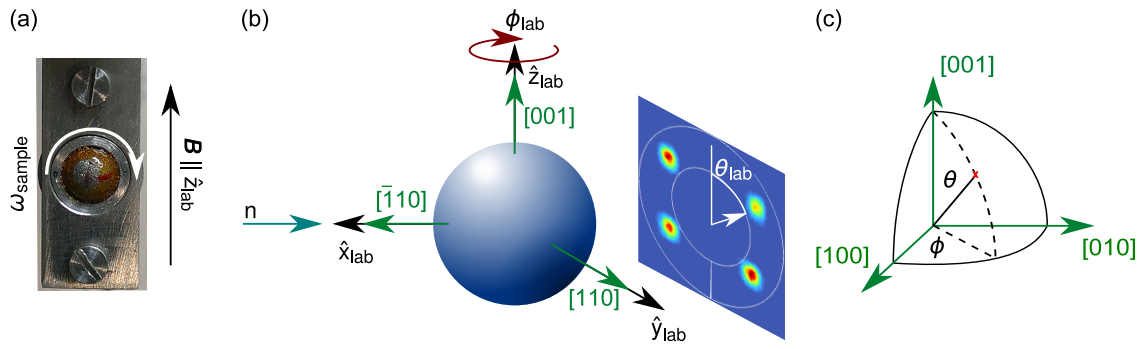

Figure 3.6: Experimental setup for small-angle neutron scattering experiments. (a) Spherical sample specially prepared for these measurements. The sample can be rotated around a $[110]$ axis (out of the page) by an angle ω, thus allowing to apply $\boldsymbol{B}$ along any crystallographic axis of the system. (b) Experimental setup for SANS experiments. In order to follow the trajectories of the magnetic propagations, the sample can be rotated around the z_{lab} axis by an angle ϕ_{lab}. On the scattering pattern the position of the Bragg peaks is defined by an angle θ_{lab} (c) Definition of the θ and ϕ angles in the sample coordinate system.

As an example the magnetic susceptibility for fields along $[315]$ and $[135]$, respectively, is in figure 3.5 (c). The curve progression is qualitatively similar, but the exact position and shape of the peak related to the transition differ slightly.

3.3 NEUTRON SCATTERING STUDY OF THE HELIX REORIENTATION IN MNSI

The long wave characteristic of the helical magnetic order in MnSi make it an ideal subject for small-angle neutron scattering experiments (SANS) since long periodical structures lead to small scattering vectors, in this case specifically $|\boldsymbol{Q}| \approx 0.035\,\text{Å}^{-1}$. A spherical sample (diameter: 5.75 mm was measured at the diffractometer MIRA2 at the Heinz Maier-Leibnitz Zentrum (MLZ) [85] to map the evolution of the Bragg Peaks related to the magnetic order in MnSi. The incident neutron beam of wavelength $\lambda = 4.5\,\text{Å}$ was collimated with two $3 \times 3\,\text{mm}^2$ apertures, placed 1.4 m and 0.5 m in front of the sample, respectively. A CASCADE detector [87] positioned 2.6 m behind the sample was used to record scattered neutrons. This experimental configuration results in an azimuthal resolution $\Delta\theta = 14.5°$. The azimuthal spread originating from the magnetic mosaicity is extracted by deconvoluting the instrument's resolution. Low temperatures were reached using a closed-cycle cryostat and magnetic fields generated by a bespoke set of water-cooled Cu solenoids in a Helmholtz configuration.

The sample was attached with GE varnish to a bespoke sample holder. The latter was constructed such that the sample could be rotated by an angle ω_{sample} around the axis C_{sample} perpendicular to the holder, cf. Fig. 3.6 (a). The external field $\boldsymbol{B}$ was applied along the vertical axis of the laboratory system $\hat{z}_{\text{lab}}$, thus the angle ω_{sample} defined the crystallographic axis parallel to $\boldsymbol{B}$. Moreover, the sample holder was attached to a rotatable sample stick, its rotation axis C_{stick} was parallel to the applied magnetic field. Different scattering planes for a given $\boldsymbol{B}$ could be accessed by rotating the sample by angle ϕ_{lab} around C_{stick}. Within such a scattering plane, the position of Bragg peak is defined by the azimuthal angle θ_{lab}, as illustrated in figure 3.6 (b). Thus, the parametrization $\hat{Q} = (\sin\theta_{\text{lab}}\cos\phi_{\text{lab}}, \sin\theta_{\text{lab}}\sin\phi_{\text{lab}}, \cos\theta_{\text{lab}})$ describes the position of an intensity maxima in the laboratory coordinate system $(\phi_{\text{lab}}, \theta_{\text{lab}},$ which is transformed to a fixed sample coordinate system (ϕ, θ) to compare the resulting trajectories to the theoretical results presented above, Sec. 3.2. Here, ϕ and θ are the azimuthal

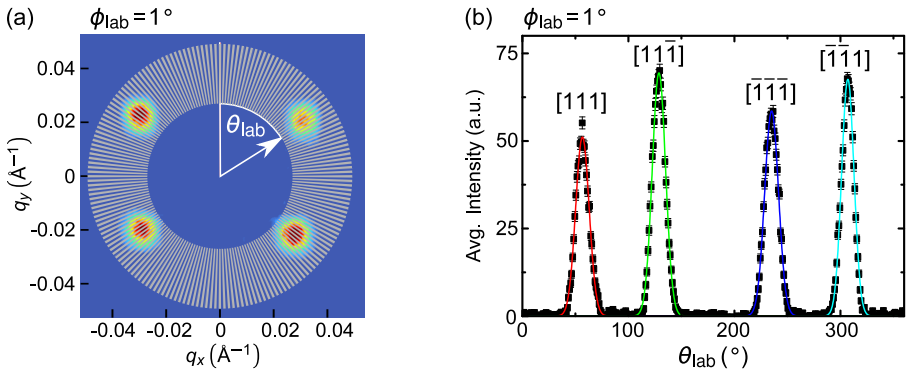

Figure 3.7: Analysis of the scattering patterns obtained from SANS. (a) Typical scattering pattern of the helical phase. The scattered intensity is averaged over 1° wide sectors between $|\boldsymbol{q}| = 0.022^{-1}$ and $|\boldsymbol{q}| = 0.038^{-1}$. (b) The calculated averaged intensity as a function of θ_{lab} is then fitted with Gaussian functions to obtain the positioned of the Bragg peaks for a given angle ϕ_{lab}. The intensity spheres shown on figures 3.8 and 3.9 consist of the averaged intensity as a function of θ_{lab} for all ϕ_{lab} measured.

and polar angle of a unit sphere, with an equatorial plane spanned by the crystal axes $[100]$ and $[010]$, cf. Fig. 3.6 (c).

In order to measure the reorientation process of the helix for all three different cases presented in the previous section, the rotation axis C_{sample} should be parallel to a $\langle 110 \rangle$ crystallographic axis. Thus, general field directions within an octant around a $\langle 111 \rangle$ axes are accessible, as are $\langle 1\bar{1}0 \rangle$ and $\langle 001 \rangle$, representatives of the high symmetry special cases. In this ideal experimental setup, the coordinate systems $(\phi_{lab}, \theta_{lab})$ are identical for $\boldsymbol{B} \parallel [001]$. However, due to the design of the sample holder, small misalignments in the sample orientation with respect to the ideal experiment cannot be avoided. Furthermore, the rotation axis C_{stick} does not go through the center of the sample, resulting in a small precession of the latter as a function of ϕ_{lab}. The analysis presented here accounts for both of these errors and corrects them, when necessary, through spherical transformations. Appendix A discusses the details of these corrections.

Intensity maps at different magnetic fields

This SANS study focuses on the transitions for magnetic fields along the $[001]$ and $[110]$ crystallographic axes, both of which show elastic Ising transitions. Scattering patterns were recorded at different fields and low temperatures, well below the onset of the helimagnetic order at T_c, starting from a multi-domain helical state after zero-field cooling (ZFC) or a single domain conical state, i. e., $\hat{Q} \parallel \boldsymbol{B}$, after high-field cooled (HFC) at large negative fields $|\boldsymbol{B}| > B_{c1}$.

At each magnetic field value two-dimensional scattering patterns were measured in a range $\phi_{lab} = 0 - 180°$ in 1° steps. A typical pattern is shown in figure 3.7 (a). The scattered intensity is then averaged over areas with 1° width in θ_{lab} and $0.022\,\text{Å}^{-1}$ width in $|\boldsymbol{Q}|$ around $|\boldsymbol{Q}_c| = 0.038\,\text{Å}^{-1}$, cf. Fig 3.7 (a). By fitting a gaussian function to the maxima observed in the averaged intensity as a function of angle θ_{lab}, we obtain the azimuthal position of a Bragg peak, e. g., $\theta_{lab}^{[111]}$. The recorded scattered neutrons around this position are then integrated as a function of the polar angle and fitting the resulting maxima yield $\phi_{lab}^{[111]}$, as well as $\phi_{lab}^{[1\bar{1}1]}$.

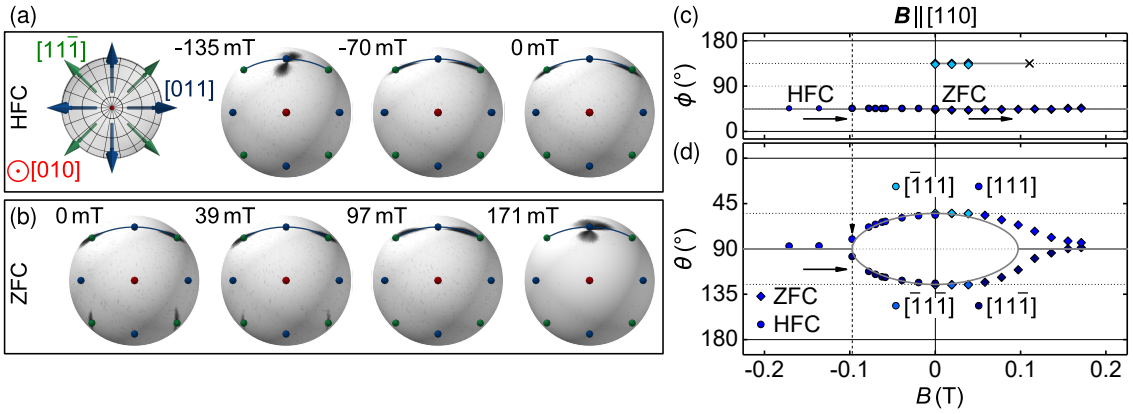

Figure 3.8: Small-angle neutron scattering data for $\boldsymbol{B} \parallel [110]$ at low temperatures. (a) Schematic representation of the orientation of the spherical sample. Spheres display typical scattered intensities for a measurement starting from a single domain state after high-field cooling (HFC) in large negative fields. Colored points mark high symmetry directions $\langle 111 \rangle$ (green), $\langle 110 \rangle$ (blue), and $\langle 100 \rangle$ (red). (b) Sphere of scattered intensity for a transition starting from a multi-domain state after zero-field cooled (ZFC). The domains at the bottom of the sphere lie perpendicular to the magnetic field and are depopulated discontinuously at $\sim 50\,\mathrm{mT}$. The domains at the top of the spheres rotate smoothly with increasing field and coalesce at high fields. (c) and (d) show the positions of the intensity maxima of (a) and (b) on a unit sphere $\hat{Q} = (\sin\theta\cos\phi, \sin\theta\sin\phi, \cos\theta)$ parametrized by the angles ϕ and θ for increasing fields (black arrows) for both HFC and ZFC. After HFC there is a sharp signature on θ at $|B_{c1}^{[110]}| \approx 95\,\mathrm{mT}$ where multiple domains form due to phase separation. The experimental observations match the theoretical prediction (solid gray line) very well. The same signatures become smeared when multiple domains merge, leading to a deviation from the expected behavior from theory.

After applying the necessary corrections mentioned above, the positions of the Bragg peaks related to each domain are transformed to the fixed sample coordinate system (ϕ, θ). In the process points with $\theta_{\mathrm{lab}} = 180 - 360°$ are mapped to $\theta'_{\mathrm{lab}} \equiv 360° - \theta_{\mathrm{lab}}$ and $\phi'_{\mathrm{lab}} \equiv \phi_{\mathrm{lab}} + 180°$. Finally, the averaged intensity values evaluated above are plotted on a spherical mesh expanded by the values of ϕ and θ. In a nutshell, the spheres are the raw scattered neutron data in the momentum region of interest. Note that small angles of θ lead to a broadening of the Bragg peak along ϕ by a factor $1/\sin\theta$.

Figure 3.8 depicts the results obtained for a magnetic field applied along $[110]$. On the left are the raw scattered intensity spheres in the fixed sample coordinate system as seen from a $[010]$ direction. The sample was cooled from $T > T_c$ in an applied magnetic field $\boldsymbol{B}$ with $|\boldsymbol{B}| > B_{c1}$ yielding a conical state as the starting point of the measurement. Thus at $|\boldsymbol{B}| = -135\,\mathrm{mT}$ a single domain the propagation vector $\boldsymbol{Q}$ pointing along the magnetic field is observed, hence $\phi = 45°$ and $\theta = 90°$. At this point, reducing the field does not affect the scattering pattern until the Ising transition is reached at $\mu_0 B_{c1} \approx 95\,\mathrm{mT}$, indicated by a spontaneous bifurcation in θ. The latter follows from the separation of the magnetic structure into two domains. Further reduction of the applied field leads to a smooth reorientation of each of these domains towards a $[11\bar{1}]$ and a $[111]$ respectively, cf. Fig. 3.8 (a).

The gray solid line in figure 3.8 (b) is a fit taking into consideration the effective potential $\mathcal{V}$ presented in section 3.2. The agreement with the experimental data is excellent. Below the critical field B_{c1} the theoretical curve for ϕ differs slightly from 45°, less than 0.5° just beneath B_{c1}. The experimental resolution did not allow to resolve this deviation in the experimental data.

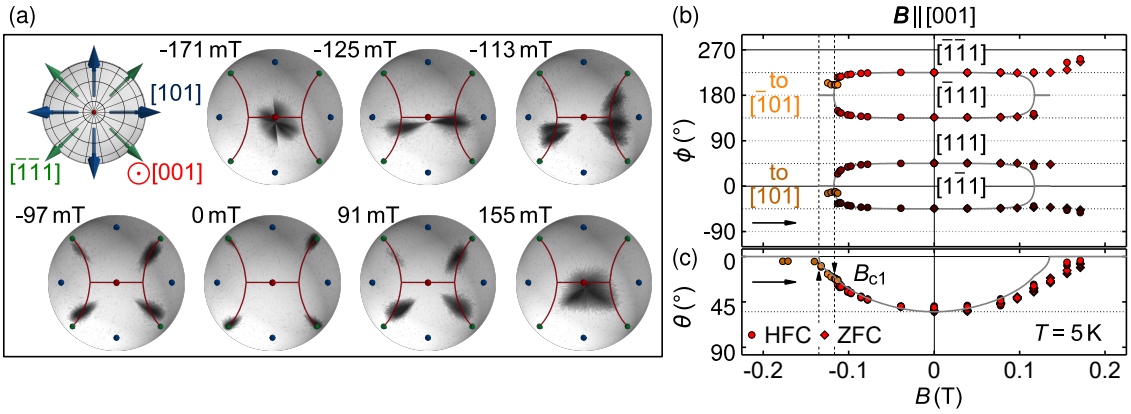

Figure 3.9: Small-angle neutron scattering data for $\boldsymbol{B} \parallel [001]$ at low temperatures analogous to figure 3.8. (a) Spheres of scattered intensity starting from a high-field cooled (HFC) state at large negative fields. Upon increasing the magnetic field, the maxima split twice related to the Ising transitions discussed in the main text. However, when starting from a multi-domain state, increasing the magnetic field leads to a smoother transition. The latter is apparent in (b) and (c) showing the positions of the Bragg peaks parametrized by the angles ϕ and θ. When transitioning from a single state to a multi-domain state two bifurcations can be observed at the critical fields $B_{c1}^{[001]} \approx 135\,\mathrm{mT}$ and $B_{c1}^{[001]} \approx 118\,\mathrm{mT}$ (vertical dashed lines). In contrast, the transition at positive fields from a multi-domain state lacks sharp signatures when the domains coalesce.

Starting from a zero-field cooled (ZFC) multi-domain state, the discrepancies between theory and the experimental result is more prominent. As predicted, one observes discrete transitions of energetically unfavorable domains. These are related to the two maxima on the lower part of the sphere on figure 3.8 (b). The scattered intensity from these domains vanishes around $\sim 50\,\mathrm{mT}$, which is about half the value of the spinodal point expected form theory. Furthermore, the sharp Ising transition at B_{c1} smears out, cf. Fig. 3.8 (c).

The similar procedure is followed after rotating the sample so that $\boldsymbol{B} \parallel [001]$. Starting from the conical phase, well above the first of the two predicted transitions, the intensity observed belongs to a single domain with $\boldsymbol{Q} \parallel \boldsymbol{B}$. In this region the polar angle ϕ is not defined and $\theta = 90°$. At the first transition $B_{c1,>}^{[001]}$, the scattered intensity splits into two maxima, indicating the first Ising transition. Note that the bifurcation is along $[110]$. By definition ϕ should take the value of $0°$ and $180°$, respectively. The discrepancy between the expected and the calculated values of ϕ originates mainly on the fact that $\boldsymbol{B}$ is about $3°$ off a $[001]$ axis. Both domains move smoothly until at $B_{c1,<}^{[001]}$ the intensity splits again, resulting in 4 maxima each associated with a domain, which smoothly reorients to point along a $\langle 111 \rangle$ axes. The transition is sharp in ϕ and quickly reaches the four values associated with each domain, i. e., $[111](\phi = 45°)$, $[\bar{1}11](\phi = 135°)$, $[11\bar{1}](\phi = 225°)$ and $[1\bar{1}1](\phi = 315° \mathrel{\hat{=}} -45°)$. Furthermore, a kink in θ, which is predicted from theory and observable in our experimental data, marks the transition. On further reduction of the magnetic field value, the helices smoothly rotate until they reach their respective $\langle 111 \rangle$ axes. This motion is observed in the angle θ, which increases continuously until the final value of $54.7°$ is reached.

One observes a completely different behavior than expected from theory for increasing magnetic fields starting from a multi-domain state or after zero-field cooled (ZFC). Instead of two Ising transitions with sharp signatures in the angle ϕ, the latter remains constant, and all domains coalesce smoothly as shown by the continuous decrease of the azimuthal angle θ. The onset of the conical state takes place at a field value much larger than $B_{c1}\,[001]_{c1,>}$

observed for decreasing field magnitudes as discussed above. As it was the case for $\boldsymbol{B} \parallel [110]$ our experimental results are in very good agreement with theory for decreasing fields magnitudes starting from high negative fields, as evident from the grays solid line in both figures 3.8 (c), (d) and 3.9 (b), (c). The good agreement is somewhat surprising since, as mentioned before, the magnetic field direction was off by a couple of degrees from the $[001]$ axis. In the theory presented here, such a misalignment is enough to smear the transitions signatures substantially, since one or two of the domains are preferred, cf. Fig. 3.5 (a). The fits to theory shown in figures 3.8 and 3.9 yield the values in equation 3.16.

Sharp signatures related to the transitions are expected in the magnetic susceptibility. Thus, before discussing the possible origin of the discrepancy between HFC and ZFC measurements, typical susceptibility experiments will be discussed in the following section.

3.4 MAGNETIC SUSCEPTIBILITY OF THE HELIMAGNETIC ORDER

Magnetic susceptibility was obtained by means of the real part of the ac susceptibility Re χ_{ac} and the derivative of the magnetization dM/dB. Both were measured using a Quantum Design physical property measurement system with an excitation frequency of 911 Hz and an amplitude of 1 mT. Samples were prepared from single crystals of MnSi growns by means of optical float zoning under ultrahigh vacuum compatible conditions [114, 115], with a residual resistivity ratio of ~ 80, which is a typical value for samples reported in the literature. From the single-crystal ingots two cubes were prepared with edge length 2 mm and surfaces perpendicular to $[110]$, $[1\bar{1}0]$, $[001]$, and $[110]$, $[1\bar{1}1]$, and $[\bar{1}12]$, respectively. These samples can be readily compared to the sphere sample used in the neutron scattering experiments, since cubes exhibit a demagnetization factor of $N = 1/3$ for fields along its edges, as is the case for spheres. The samples prepared permit the measurement of the magnetic susceptibility for the three representative cases discussed above, i. e., $\boldsymbol{B} \parallel \langle 100\rangle$, $\langle 110\rangle$, $\langle 111\rangle$.

Figure 3.10 shows the data obtained, starting with the results for a $\boldsymbol{B} \parallel \langle 001\rangle$. After zero-field cooling all domains are populated and contribute equally to the magnetic susceptibility leading to a reduced value $\chi_\perp + \frac{1}{3}(\chi_\parallel - \chi_\perp) \approx 0.21$ [113], measured in both the Re χ_{ac} (solid symbols) and the derivative of the magnetization dM/dB (open symbols). Increasing the magnetic field leads to a smooth increase of Re χ_{ac} towards the constant value deep in the conical state given by $\chi_\parallel \approx 0.31$ also observed in dM/dB. Furthermore, the transition is related to a peak in dM/dB, deviating from the behavior observed in χ_{ac}. This discrepancy is an indicator of the important role of slow dynamics, to which χ_{ac} is not sensitive, in the reorientation of the helical domains, cf. references [116–118]. Starting from large negative fields in the single domain conical state reducing the field strength results in a sharp signature in dM/dB where two distinct peaks can be distinguished, related to the two subsequent Ising transitions, cf Fig. 3.10 (b). While the ac susceptibility does not follow the behavior shown by dM/dB two clear kinks can be observed at $B_{c1,>}^{[001]}$ and $B_{c1,<}^{[001]}$. After all domains are populated again, increasing the field on the positive side yields a smeared signature in dM/dB at the transition from the multi-domain helical state to the conical state, resembling the hysteresis observed in the neutron scattering experiment.

In the case of fields applied parallel to a $\langle 110\rangle$ axis, two distinct signatures can be observed when increasing the magnetic field after zero-field cooling, as shown in figure 3.10 (c). The first signature relates to the depopulation of the domains propagating perpendicular to the applied magnetic field observed around ~ 50 mT (cf. Fig. 3.8 (c)), while the second indicates the Ising transition expected. Again the Reχ_{ac} does not show any peaks but rather distinct

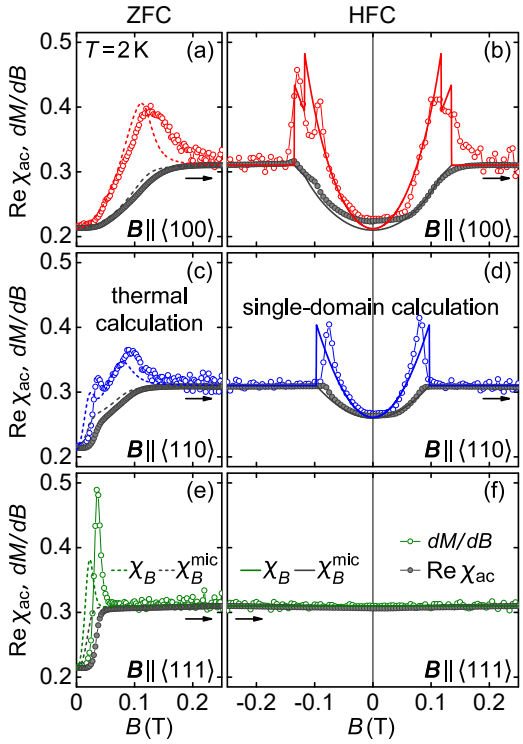

Figure 3.10: Magnetic susceptibility around the transition between helical and conical state. (a) and (b) Results for $\boldsymbol{B} \parallel \langle 100 \rangle$ obtained after zero-field cooling (ZFC) and high-field cooling (HFC), respectively. Solid symbols depict values of the real part of the ac susceptibility Re χ_{ac} measured at 911 Hz, while open symbols illustrate values of the derivative of the magnetization dM/dB. Discrepancies between the two indicate the importance of slow dynamics in the helical reorientation transition. Dashed and solid lines result from theoretical calculations, for details see text. (c)-(f) Analogous results for $\boldsymbol{B} \parallel \langle 110 \rangle$ and $\boldsymbol{B} \parallel \langle 111 \rangle$.

kinks related to the peaks observed in dM/dB. When starting from the conical single domain state the Ising transition leads to a sharp peak in dM/dB at $|B_{c1}^{[110]}|$ for both negative and positive values. Note that the domains perpendicular to the field are not populated, which leads to a higher value of the magnetic susceptibility at zero magnetic field. There are small discrepancies between the phase transitions at negative and positive values, but remarkably more subtle than those observed for $\boldsymbol{B} \parallel \langle 100 \rangle$.

Finally, for a field applied along a $\langle 111 \rangle$ axis, a sharp signature is observed only after zero-field cooled. At this field value, all other three domains make a discrete transition to propagate along the direction parallel to the field. When starting from large negative fields in the single domain conical state, there are no transitions. Both Zeeman energy and magnetocrystalline anisotropies are minimized simultaneously by a helical propagation the remains parallel to the field and parallel to the $\langle 111 \rangle$ axis, populating the other possible domains, would increase the Zeeman contribution. Thus the susceptibility remains constant with the value of $\chi_{\parallel}$.

At the end of section 3.2, the evolution of the transition signatures in the magnetic susceptibility as obtained from equation 3.18 was presented. A closer look reveals that the derived expression for the magnetic susceptibility can be separated into two contributions:

$$\begin{aligned} \chi_B &= \chi_B^{\text{mic}} + \chi_B^{\text{mac}} \\ \chi^{\text{mic}} &= \chi_\perp + (\chi_\parallel - \chi_\perp)(\hat{B}\hat{Q}_{\text{min}})^2 \end{aligned} \tag{3.19}$$

$$\chi^{\text{mac}} = -\frac{1}{\mu_0}\frac{\partial^2 \mathcal{V}(\hat{Q}_{\text{min}})}{\partial \hat{Q}^i_{\text{min}} \partial \hat{Q}^j_{\text{min}}}\frac{\partial \hat{Q}^i_{\text{min}}}{\partial B}\frac{\partial \hat{Q}^j_{\text{min}}}{\partial B}, \tag{3.20}$$

where $B = |\boldsymbol{B}|$ and $\hat{Q}_{\text{min}}(\boldsymbol{B})$ is the propagation vector that minimizes the Landau potential for a given $\boldsymbol{B}$, cf. Sec. 3.2. The first term accounts for the response of the microscopic magnetization for a given direction vector $\hat{Q}_{\text{min}}$, while the second term is associated with the reorientation of helical domains on a macroscopic scale as a function of the magnetic field.

The macroscopic reorientation process, captured by χ_H^{mac}, exhibits a large time scale $\tau_{\hat{Q}}$. In case of fluctuations at frequencies $f_{\text{ac}} \gg 1/\tau_{\hat{Q}}$ the pitch vector is not able to follow the oscillating field and the contribution from χ_B^{mac} is suppresed. Thus, Re χ_{ac} probes only χ_B^{mic} which responds to changes much faster than typical time scales for this type of measurements. In contrast the derivative of the magnetization represents the static limit ($f_{\text{ac}} = 0$) and is sensitive to both scales of the magnetic response, i. e., $dM/dB = \chi_B$. Bauer *et al.* showed that Re χ_{ac} and dM/dB differ from each other even at low frequencies and high temperatures close to the magnetic transition, i. e., $(T_{\text{c}} - T)/T_{\text{c}} \approx 5\,\%$ [116]. Thus providing an estimate for the low boundary of $\tau_{\hat{Q}} \geq 1$ ms.

Both χ_B and χ_B^{mic}, as calculated using the values given in equations 3.14 and 3.16 obtained from the neutron scattering data, are plotted in figure 3.10. Here $f_{\text{ac}} = 911$ Hz $\gg 1/\tau_{\hat{Q}}$ and χ_B^{mic} reproduces the values of Re χ_{ac} for transitions starting from a conical state (right column) very well. Furthermore the critical signatures observed in dM/dB at different Ising transitions are in excellent agreement with the computed χ_B. Note that the derivative $\partial_B \hat{Q}^i_{\text{min}}$ is linear in B for $B \to 0$, because the Zeeman potential $\mathcal{V}_B$ is quadratic in $\boldsymbol{B}$, resulting in $\chi_B|_{B=0} = \chi_B^{\text{mic}}$. In general only small inconsistencies are observed for $\boldsymbol{B} \parallel \langle 100 \rangle$, which most likely originate from deviations of the field direction from the actual $\langle 100 \rangle$ axis in the experiment.

3.5 ACCOUNTING FOR MULTIPLE DOMAINS

As mentioned above all four domains are populated equally after cooling the sample in zero magnetic field. Typically, some of these domains become metastable with increasing field and jump into the favored direction at first-order transitions. Such transitions were shown for $\boldsymbol{B} \parallel [110]$ around ~ 50 mT in neutron scattering, cf. Fig. 3.8 (b), and for fields along $\langle 110 \rangle$ and $\langle 111 \rangle$, as deduced from the magnetic susceptibility and the derivative of the magnetization. Especially for the latter case, the signature is relatively strong. The theoretical susceptibilities plotted on the right column of figure 3.10 are calculated based on a single domain model. This approach does not capture the transitions observed after zero-field cooling, shown on the left column of figure 3.10. Instead, consider thermally populated domains with energy density

$$f = \frac{k_{\text{B}} T}{\xi^3_{\text{dom}}} \log Z \tag{3.21}$$

$$Z = \int d\hat{Q}\, e^{-\xi^3_{\text{dom}} \mathcal{V}(\hat{Q})/(k_{\text{B}} T)}, \tag{3.22}$$

with the finite linear size ξ_{dom}. The resulting susceptibilities $\langle \chi_B \rangle \equiv -\partial_B^2 f/\mu_0$ are plotted as dashed lines in the left column of figure 3.10 and referred to as 'thermal calculation'. Here a thermal energy density $k_{\mathrm{B}}T/\xi_{\mathrm{dom}}^3 = t\varepsilon_T^{(1)}$ was considered, with the dimensionless temperature $t = 0.02$ corresponding to a linear length $\xi_{\mathrm{dom}} = 136$ Å at $T = 2$ K. This is rather unrealistic since ξ_{dom} is of the order of the pitch length in MnSi. However such calculations do reproduce the signatures observed qualitatively, cf. Fig. 3.10 (c), (e), albeit the expected transitions fields are consistently smaller than those measured in experiment.

A different approach is to consider domains which are macroscopically large so that they are essentially trapped in their local minimum of $\mathcal{V}(\hat{Q})$. In this case, these domains remain metastable until they reach their spinodal point, at which there is a spontaneous switch of the propagation direction to point along the field in a first-order manner. As a consequence, the calculated susceptibility shows critical first-order spikes at these transitions. Figure 3.11 shows the expected susceptibility for these macroscopic domains and, for the sake of comparison, the computed susceptibility for small domains, as discussed above, for both $t = 0.02$ and $t = 0.05$. The latter is smooth and resemble the experimental results very well. In contrast, the experimental susceptibility data does not reproduce the very sharp peaks arising from the macroscopic metastable domains. Furthermore, the neutron scattering experiment established that unfavorable domains are depopulated at fields much lower than their spinodal point. Thus, large macroscopic domains are not suitable for describing the zero-field cooling behavior.

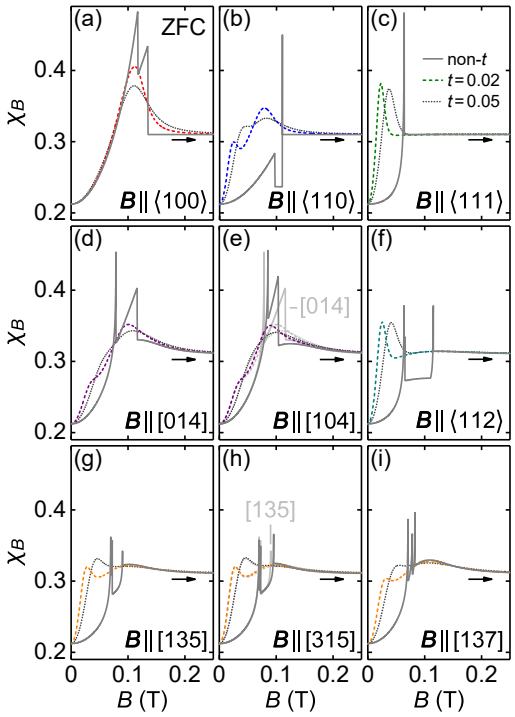

Figure 3.11: Theoretically computed magnetic susceptibility for different field orientations for zero-field cooled (ZFC) samples. The coalescence of different domains is addressed utilizing macroscopic domains that switch at their spinodal point, solid lines. For comparison, the dashed and dotted lines represent ensembles of domains thermally populated for two different dimensionless temperatures t. Note that concerning the thermal calculation, macroscopic domains have larger critical fields associated with sharp signatures in the magnetic susceptibility, in direct contrast with the experimental observations.

Additionally, the results for $t = 0.05$ seem to be in better quantitatively agreement with the magnetic susceptibility measured for all field directions, as evident in figure 3.11 (b) where the critical signatures fo the domains reorientations, both discrete and continuous are much smoother than measured, cf. Fig. 3.10 (c). Furthermore, such a value of t demands for even smaller domains than those discussed above for $t = 0.02$. A more realistic approach would take into account, among others, an array of domain sizes and the contributions from the domain walls.

The excellent agreement between theory and experiment demonstrated above is put more generally to the test by calculating the derivative of the magnetization for several different field directions. For this purpose, the latter was measured on the spherical sample presented in the neutron scattering experiments, cf. Fig. 3.6 (a), using an Oxford Instruments vibrating sample magnetometer. The external magnetic field was applied in directions $\hat{B} = (\frac{\sin\beta}{\sqrt{2}}, \frac{\sin\beta}{\sqrt{2}}, \cos\beta)$, cf. figure 3.12 (a), on one the great gray circles on the unit sphere in figure 3.12 (b). The angle β was determined using an optical microscope, which results in an uncertainty of $\pm 1°$. The field was increased in 1 mT steps. At each step, the magnetization was determined by integrating oscillations at 62.35 Hz over 3 s while the field was kept constant. The derivative was calculated numerically and smoothed using a fourth-order Savitzky-Golay filter over 40 data points.

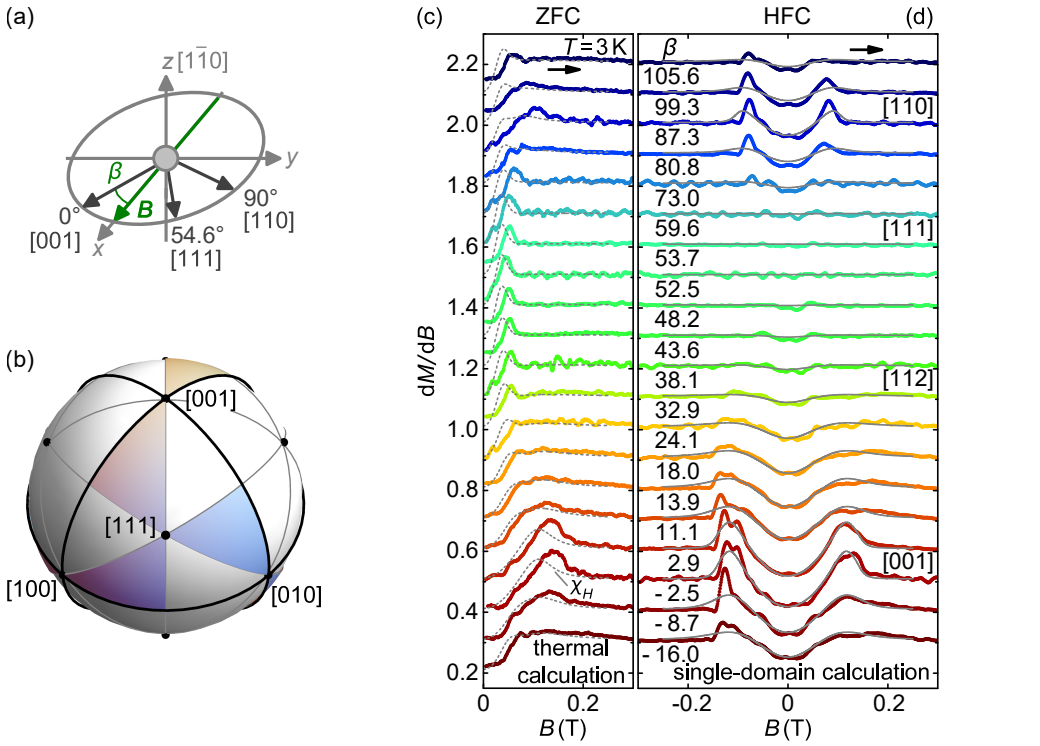

Figure 3.12: Derivative of the magnetization for different orientations of $\boldsymbol{B} = (\frac{\sin\beta}{\sqrt{2}}, \frac{\sin\beta}{\sqrt{2}}, \cos\beta)$ as shown in (a), tracing a gray big circle on the unit sphere (b). (c) Data measured after zero-field cooling (ZFC), for comparison the magnetic susceptibility computed from a thermal ensemble calculation with $k_B T/\xi^3_{\text{dom}} = 0.05\varepsilon^{(1)}_T$ are shown as dashed gray lines. Data has been shifted by 0.1. (d) Data obtained starting from a single domain state achieved after high-field cooling (HFC), correspondingly the solid lines are calculation of χ_B for a single macroscopic domain. Overall the agreement between theory and experimental data is very good.

When comparing the results for different directions, one can neglect the demagnetizing effects thanks to the spherical shape of the sample. Recorded data is plotted on figure 3.12 (c) and (d). As was the case so far, two different scenarios are considered: starting from a multi-domain state after zero-field cooling depicted on the left column and starting from the single-domain conical state after high-field cooling on the right column. The expected values of the magnetic susceptibility, as obtained from a thermal calculation for ZFC measurements and from a single domain for HFC measurements, are shown by the grey dashed and solid lines, respectively. The dependency on the angle β is captured very well by the theoretical model, albeit some consistent deviations point to contributions well beyond the mean-field approximation presented here.

In the case of zero-field cooling, the transition is regularly at higher fields than expected from theory, as was already shown in figure 3.10. A systematic error from the smoothing algorithm results in an additional discrepancy in the absolute value of the magnetic susceptibility at zero-field. When starting from the conical state, the agreement between theory and experiment is remarkable. Both differ only for field directions closed to the critical fields for $\boldsymbol{B} \parallel [110]$ and $\boldsymbol{B} \parallel [001]$. At the transition, dM/dB is larger, and critical signatures are sharper than expected from theory. Notably, two subsequent maxima related to the Ising transitions are observed in the experimental data for field directions around a $[001]$, but deviating substantially from it. In the theoretically derived susceptibility, these deviations lead to the smearing of the maxima. Furthermore, hysteresis can be observed between decreasing and increasing field strength. Multiple domains coalesce for the latter corresponding with weaker signatures in the susceptibility, consistent with the neutron scattering results, cf. Fig. 3.9 (c).

3.6 BEYOND THE MEAN-FIELD APPROXIMATION

In this chapter, the reorientation process of the helimagnetic in MnSi was discussed in the framework of an effective mean-field theory in the limit of weak anisotropies and corroborated with thorough neutron scattering, magnetization, and magnetic susceptibility measurements. A few phenomenological parameters are sufficient to account for the tetrahedral point group T of the cubic chiral magnets and successfully described the trajectory of the helical propagation vector $\boldsymbol{Q}$ and the magnetic response to an external magnetic field $\boldsymbol{B}$.

The transition from the helical to the conical phase in MnSi involves two elastic Ising transitions for $\boldsymbol{B} \parallel \langle 100 \rangle$ which break a $\mathcal{Z}_2 \times \mathcal{Z}_2$ symmetry subsequently. For general field orientations along $\langle hk0 \rangle$ with $h, k \neq 0$, a single elastic Ising transition occurs at the critical field B_{c1}, while the reorientation represents a crossover phenomenon for all other directions.

The overall agreement, both quantitatively and qualitatively, between experiment and theory is remarkable and lays the ground to identify specific aspects of this transition where interesting new physical phenomena in these systems could be studied. Specifically, there are two distinct discrepancies between the experimental results and the theory:

- Hysteresis is observed at nominal continuous elastic Ising transitions
- Sharper and more robust signatures when the transition is approached from the single domain conical state

It should be evident that the approach presented here is by no means complete. Corrections arising from thermal fluctuations may lead to the enhanced signatures mentioned above, while the emergence of non-trivial topological defects in the helimagnetic order could be

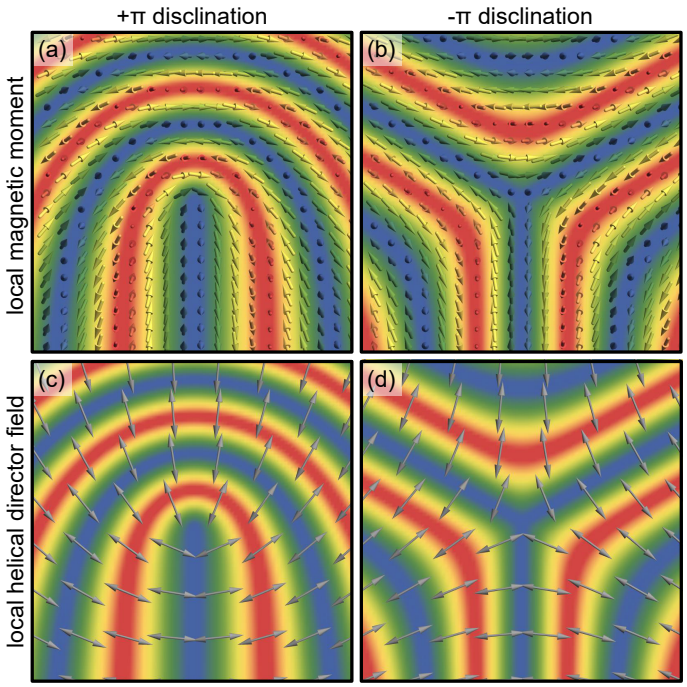

Figure 3.13: (a) and (b) Two different type of disclinations of helimagnetic order. The arrows represent magnetic moments around $+\pi$ and $-\pi$ disclinations. The color map represents the value of the out-of-plane moment. (c) and (d) Director fields of the helimagnetic order. The disclinations represent vortices where the propagation directions rotate by $+\pi$ and $-\pi$ respectively. The color map is the same as in (a) and (b) for comparison.

the cause behind the hysteresis observed in the experimental data, as they inhibit the coalescence of domains [119]. The magnetic susceptibility measurements establish that slow dynamics are a crucial aspect of the transition yielding a relatively long relaxation time $\tau_{\hat{Q}}$. The relaxation time scale probably becomes even larger than the typical probing times of our experimental methods, giving rise to the hysteretic behavior.

In order to relieve stress in a helical domain wall plastic deformations of the magnetic arrangements, i. e., disclinations, may form, cf. Fig. 3.13 (a) and (b). The helix propagation vector rotates by $+\pi$ and $-\pi$ around such defects respectively, cf. Fig. 3.13 (c) and (d), thus creating vortices in the pitch-director field and are therefore topologically non-trivial. Consequently, domains adjacent to such defects do not join smoothly. Instead, the topological disclinations need to be removed first, resulting in slow relaxation processes. Disorder in the sample leads to pinning of these defects, which in turn increases the relaxation time scale. Interestingly the role of topological defects in the relaxation processes in helimagnetic order was recently studied for the case of FeGe using magnetic force microscopy [120].

The non-trivial characteristic of skyrmions is at the center of the properties that have generated so much interest recently, cf. [9]. In contrast studies of topologically non-trivial disclinations defects in chiral magnets are sparse, and their properties remain largely unknown. The technological possibilities from single macroscopic topological objects in a different region of the phase diagram in chiral magnets merit further research.

4

MAGNETIC ORDER IN MNSI UNDER UNIAXIAL PRESSURE

As mentioned in the introduction, Alexei Bogdanov proposed the existence of a thermodynamical skyrmion lattice phase similar to the vortex lattices observed in superconductors in a seminal theoretical work in the late 80s [38]. His study focused on the mean-field theory of easy-axis ferromagnets with chiral spin-orbit interactions. While a hexagonal skyrmion lattice represents the ground state for specific parameters, it demands the presence of easy-axis anisotropy [39, 121]. Thus, cubic crystals were excluded from the predicted skyrmion hosting material due to their symmetry. It was thus surprising as the first observation of this novel type of magnetic order was in the cubic chiral magnet MnSi by Mühlbauer and collaborators [11]. The latter publication established that the coupling of the magnetic structure to thermally driven fluctuation leads to a reduction in energy sufficient for the skyrmion lattice to become the ground state of the system at temperatures close to the helimagnetic to paramagnetic transition and medium magnetic fields. Recently systems have been identified, where strong anisotropies play a vital role in the stabilization of skyrmions, albeit changing an intrinsic characteristic, i. e., switching from bloch to néel skyrmions [122]. The role of uniaxial anisotropy in systems with high symmetry, such as B20 compounds, remained an open question and is the subject of the present chapter.

Butenko and collaborators carried out a theoretical study considering the effects of uniaxial magnetic anisotropy induced by pressure [99]. They concluded that skyrmions can be stabilized by uniaxial stress in the order of a few kbar. The results presented below confirmed this prediction. The main effect of uniaxial stress is indeed to control the stability of the skyrmion lattice. However, the relation between stress and the magnetic field is crucial. If they lie parallel to each other, the skyrmion lattice is suppressed, as the uniaxial stress and the magnetic field favor a conical propagation pointing in their direction. The skyrmion lattice is preferred when the magnetic field points perpendicular to the stress axis. Seki obtained similar results when studying the effects of tensile strain on thin single-crystal samples of Cu_2OSeO_3 [123]. In situ application of stress is even able to switch from the skyrmion lattice to the conical phase, as demonstrated by Nii and collaborators through magnetic susceptibility measurements [124]. Strain might represent an important component to understand the magnetic order in epitaxially grown samples of B20 compounds. However, recent extended x-ray absorption fine structure (EXAFS) measurements on MnSi thin films established that the strain originating in the 3% lattice mismatch between substrate and film is released after a few atomic layers [125]. Thus, the film is essentially unstrained.

This chapter presents a thorough recently published study of the effects of uniaxial pressure on the magnetic order of MnSi [126]. The first section introduces the experimental methods used, consisting of a bespoke uniaxial pressure cell and susceptometer. It is followed by a discussion of uniaxial pressure effects on the helical magnetic order in section 4.2, starting with measurements in zero magnetic field, continuing with the discussion of the competition between the Zeeman energy and the magnetic anisotropy. The section finishes by examining the suppression of the magnetic order. The effects of uniaxial stress on the skyrmion lattice are discussed in section 4.3. A discussion of the phase diagrams obtained from magnetic susceptibility measurements wraps up the chapter.

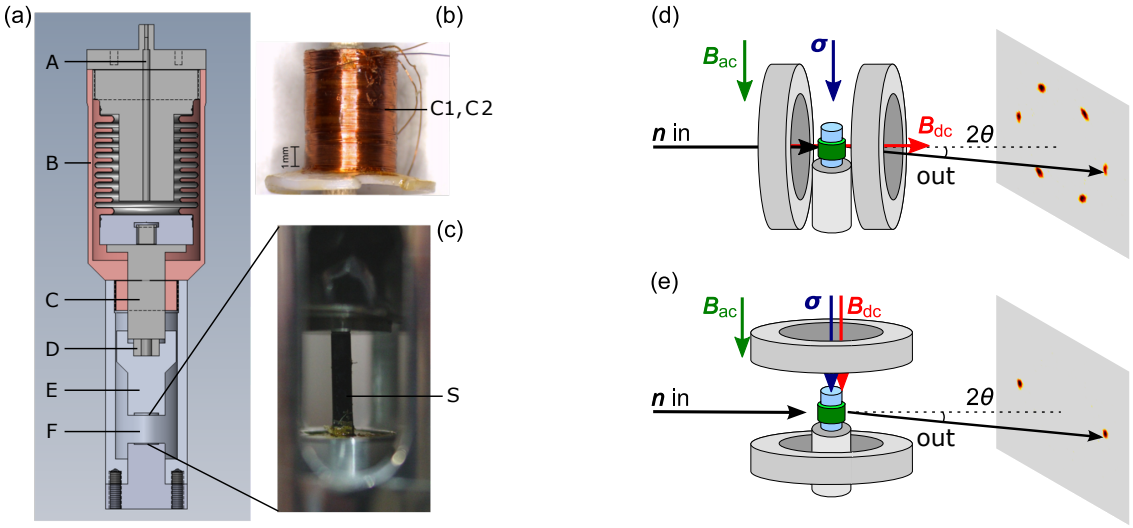

Figure 4.1: Schematic depiction of the uniaxial pressure cell and the SANS set up. (a) Cut-away view of the uniaxial pressure cell, which is based on He-activated bellows. **A** Helium gas capillary, **B** Cu:Be cage, **C** Force transmission, **D** Piezo Sensor, **E** Uniaxial pressure piston, and **F** Sample space. (b) Photograph of the pair of secondary detection coils of the ac susceptometer. (c) Photograph of the sample as mounted in the pressure cell for SANS measurements. (d) SANS configuration 1: The applied magnetic field $\boldsymbol{B}_{\mathrm{dc}}$ is perpendicular to both σ and the ac excitation field $\boldsymbol{B}_{\mathrm{ac}}$. (e) SANS configuration 2: The applied magnetic field $\boldsymbol{B}_{\mathrm{dc}}$ is parallel to the pressure axis and the ac excitation field $\boldsymbol{B}_{\mathrm{ac}}$.

4.1 EXPERIMENTAL ENVIRONMENT FOR UNIAXIAL PRESSURE EXPERIMENTS

Two main aspects were taking into consideration, when addressing the question of how to study the effects of uniaxial pressure on the skyrmion lattice in MnSi:

1. What is the best probing mechanism for changes to the magnetic order?
2. What type of uniaxial pressure cell is compatible with the chosen experimental method?

Small-angle neutron scattering is well suited for uniaxial pressure experiments. The type of materials able to withstand the forces and stresses that develop in these experiments, normally lead to a reduction of the beam flux due to absorption and scattering. The aluminum used for the pressure cell has high neutron transparency allowing must of the flux to go through. Tensile strains can be addressed by thickening the cell without a substantial loss of neutron transmission and using stronger materials for parts of the cell which the neutron beam does not illuminate. Magnetic neutron scattering is sensitive to specific domains and provides access to physical characteristics like propagation direction and population, that get lost in bulk measurements such as electrical transport and magnetization. However, some of the effects of uniaxial pressure can be tracked using this type of bulk measurements. The combination of both microscopic and macroscopic measurements allowed the thorough study presented in this chapter.

Uniaxial pressure cell

Uniaxial pressure was generated with a bespoke pressure cell based on a He-activated bellow system depicted [127, 128] in figure 4.1 (a). The materials of the cell were carefully

sample	size	σ	$\boldsymbol{B}_{\mathrm{dc}}$	$\boldsymbol{B}_{\mathrm{dc}}$ vs σ	Exp	MLZ	λ	detector
S1	10x2x2	$[110]$	$[\bar{1}10]$	$\perp$	SANS	MIRA-1	10.4	He^3 PSD
S1	10x2x2	$[110]$	$[001]$	$\perp$	ACS			
S1	10x2x2	$[110]$	$[110]$	$\parallel$	ACS			
S2	5x1x1	$[110]$	$[\bar{1}10]$	$\parallel$	SANS	MIRA-2	5	CASCADE
S3	5x1x1	$[001]$	$[\bar{1}10]$	$\perp$	SANS	MIRA-2	4.5	CASCADE
S3	5x1x1	$[001]$	$[001]$	$\parallel$	SANS	MIRA-2	4.5	CASCADE
S4	5x1x1	$[111]$	$[\bar{1}10]$	$\perp$	SANS	MIRA-2	4.5	CASCADE

Table 4.1: Summary of all sample dimensions, sample orientations, field orientations, SANS configurations (instrument, wavelength and type of detector) as well as measurements performed in the context of this study. SANS: small-angle neutron scattering, ACS: ac susceptibility

selected to balance mechanical stability and neutron transparency. Both were achieved by combining Cu:Be and Aluminum AW 7075. Pressurized He-Gas is filled into the metal-bellow through a capillary. The effective area of the metal bellow $\mathrm{A_{MB}}$ results in an effective axial force originating in the gas pressure. Thus the uniaxial stress on the sample is given by

$$\sigma = \frac{\mathrm{A_{MB}}}{\mathrm{A_{sample}}} P_{\mathrm{gas}} \tag{4.1}$$

The experimental setup included a piezo sensor (Kistler 9001A) to measure the applied force. The pressure of the He-Gas was determined using a Siemens Diptron 3 Digital Manometer. The gas handling system included a 10 L gas dump to reduce pressure variations driven by temperature changes within the cryostat. Pressure fluctuations throughout the experiments were less than 3 %. A detailed description of the uniaxial pressure cell can be found in the author's master thesis [129].

AC magnetic susceptibility

AC magnetic susceptibility was measured using a bespoke free-standing susceptometer [130] depicted in figure 4.1 (b). Specifically, figure 4.1 (b) shows the two secondary coils C1 and C2, wound concentrically with C2 on top of C1. These had an inner diameter of 3.1 mm with a height of 5.5 mm. The primary coil was large and placed outside of the pressure cell, to ensure a homogenous ac-magnetic field $\boldsymbol{B}_{\mathrm{ac}}$ across the sample. AC susceptibility χ_{ac} was recorded at typical excitation fields $\sim$ 1 mT and excitations frequencies of 900 Hz oriented parallel to the uniaxial stress σ. The data were calibrated against data recorded with a Quantum Design Physical Properties Measurement System.

External magnetic fields

Static external magnetic fields $\boldsymbol{B}_{\mathrm{dc}}$ were generated using two magnets. For measurements up to a few Tesla, a cryogen-free superconducting magnet was used whose magnetic field always pointed along the uniaxial stress direction. The second magnet consisted of a bespoke set of water-cooled Cu solenoids in a Helmholtz configuration with a maximum field strength

of $\sim$ 350 mT when Fe-cores were inserted in the solenoids. The magnetic field could be applied parallel or perpendicular to σ.

Experimental configurations

Two different experimental setups characterized by the relation between the external dc magnetic field $\boldsymbol{B}_{\mathrm{dc}}$ and the uniaxial pressure σ were used, namely:

- $\boldsymbol{B}_{\mathrm{dc}} \perp \sigma$
- $\boldsymbol{B}_{\mathrm{dc}} \parallel \sigma$.

Both are illustrated in figure 4.1 (d) and (e) respectively. In the first configuration, one is able to observe the full scattering pattern of the skyrmion lattice, since the external magnetic field is applied parallel to the incoming neutron beam. In the second experimental setup, one can observe the conical phase and a skyrmion lattice related signal, indicated by two Bragg reflections perpendicular to the applied field. Note that regardless of the external field direction, the ac-magnetic field is always parallel to σ.

Small-Angle neutron scattering

Neutron scattering was carried out at the MIRA-1 and MIRA-2 [85] diffractometers at the Heinz Maier-Leibnitz Center. For the measurements at MIRA-1 the neutron beam was collimated with two $5 \times 5\,\mathrm{mm}^2$ slits situtated $\sim$ 1.5 m and $\sim$ 0.5 m in front of the sample. Scattered neutrons were then recorded with a $20 \times 20\,\mathrm{cm}^2$ delayline ^{3}He area detector, with a spatial resolution of $2 \times 2\,\mathrm{mm}^2$ placed 0.85 m behind the sample. At MIRA-2 the apertures had a size of $2 \times 3\,\mathrm{mm}^2$ and $1 \times 1.4\,\mathrm{mm}^2$, respectively. Their positions were the same as at MIRA-1 with respect to the sample. The experimental setup was completed by a CASCADE detector [87] 2.3 m behind the sample. Magnetic fields were applied using the Helmholtz set mentioned above, however in this experiments the maximum field was limited to 250 mT.

Sample preparation

In order to study the interplay of the uniaxial stress with the magnetocrystalline anisotropies, four MnSi samples were prepared from optically float-zoned high-quality single crystals [114]. The dimensions of three of the samples were $5 \times 1 \times 1\,\mathrm{mm}^3$, with the long edge parallel to a $\langle 100 \rangle$, $\langle 110 \rangle$ and $\langle 111 \rangle$ respectively. The remaining sample had a size of $10 \times 2 \times 2\,\mathrm{mm}^3$ with its long axis parallel to a $\langle 110 \rangle$ crystallographic axis. The sample quality was comparable to those measured in previous studies [116]. A summary of all samples including the pressure and field directions, as well as the measurements performed, is shown on table 4.1.

4.2 MAGNETIC HELICES UNDER PRESSURE

At zero magnetic field and below the critical temperature $T_{\mathrm{c}} \sim 29\,\mathrm{K}$ the magnetic moments in MnSi order in helices propagating along the $\langle 111 \rangle$ axes of the system with a propagation length of $\lambda_{\mathrm{hel}} \sim 180\,\text{Å}$. The associated scattering pattern consists of satellite Bragg peaks at $|Q_{\mathrm{hel}}| = \frac{2\pi}{\lambda_{\mathrm{hel}}} \approx 0.35\,\text{Å}^{-1}$ along the $\langle 111 \rangle$ directions. With small-angle neutron scattering it

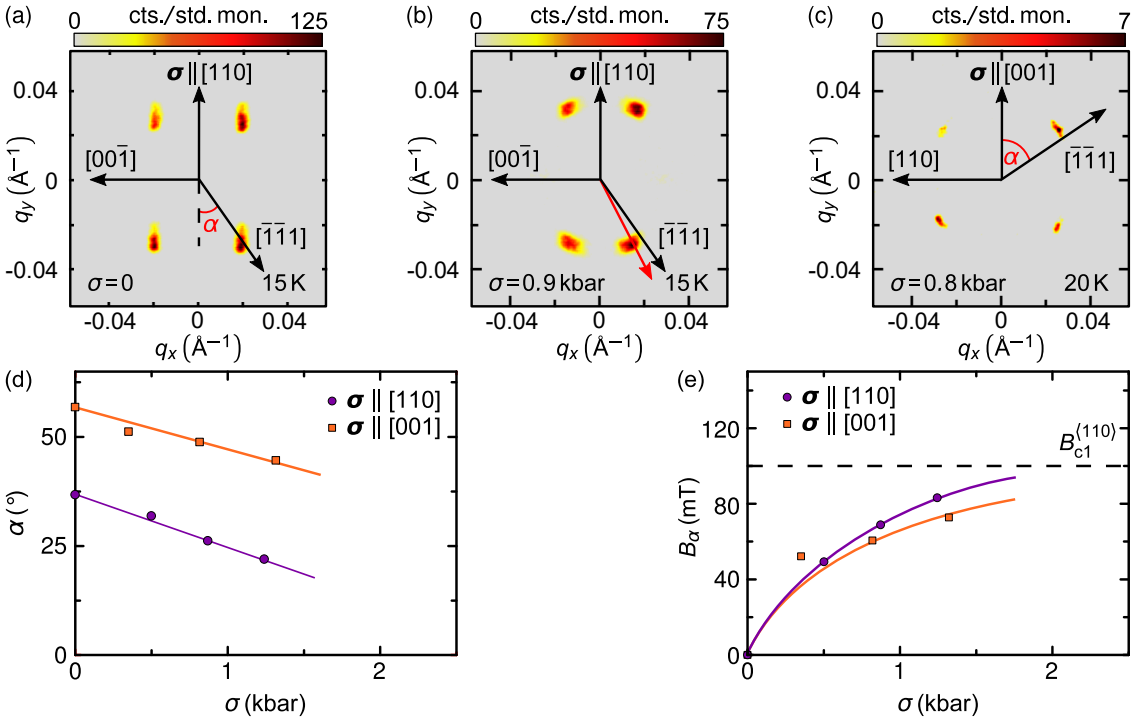

Figure 4.2: Reorientation of the helical phase for $\sigma \parallel \langle 110\rangle$ and $\sigma \parallel \langle 100\rangle$: (a) Scattering pattern of the helical phase at ambient pressures. Four Bragg peaks corresponding to the propagations $\pm\boldsymbol{Q}_{\text{hel}} \parallel [111]$ and $\pm\boldsymbol{Q}_{\text{hel}} \parallel [11\bar{1}]$ can be observed. (b) Upon applying a uniaxial pressure the propagation direction rotates towards the stress axis. (c) Similar reorientation of helical domains is captured for $\sigma \parallel \langle 100\rangle$. (d) Angle α between propagation direction and uniaxial pressure axis σ as a function of stress. (e) Corresponding field value B_α which yields the same rotation angle α of the helimagnetic propagation vector as a function of stress. The dashed line is the value of the critical field at which the helical phase points along the magnetic field for $\boldsymbol{B} \parallel \langle 110\rangle$.

is possible to image four such Bragg peaks at the same time for an incoming neutron beam parallel to a $\langle 110\rangle$ crystallographic axis. A typical example is shown on figure 4.2 (a).

Applying a uniaxial pressure breaks the symmetry of the system in a similar fashion as a magnetic field, creating a preferred propagation direction along σ. Thus, for $\sigma \parallel [110]$ we expect a continuous reorientation of the domains propagating along the $[111]$ and $[11\bar{1}]$ with increasing pressure, while discrete transitions take place for domains lying perpendicular to the uniaxial pressure axis,i. e., $[1\bar{1}1]$ and $[\bar{1}11]$. Similarly, $\sigma \parallel \langle 100\rangle$ leads to a smooth reorientation of all domains until they build a single domain state along σ. The rotation of the helices is captured by the angle α encompassed by the propagation vector and the uniaxial pressure axis. The reorientation, evident in the changes in α, is presented in figures 4.2 (b) and (c). Note that the sample was heated to $T \gg T_c$ before every increment in pressure. There is small smearing of the helical Bragg peaks, which is attributed to pressure inhomogeneities in the sample that do not affect the conclusions reported here.

In the range of pressures measured in this study, α decreases linearly with increasing σ. The strength of the uniaxial pressure coupling can be expressed in terms of the corresponding magnetic field B_α at which the same value of α is measured. The latter is plotted in figure 4.2. For $\sigma \parallel [110]$ B_α increases rapidly, reaching values close to the critical transition field B_{c1} for pressures just above 1 kbar. A comparable behavior is observed for $\sigma \parallel \langle 100\rangle$, albeit the effects of uniaxial stress seem to be somewhat weaker. In addition to the rotation within

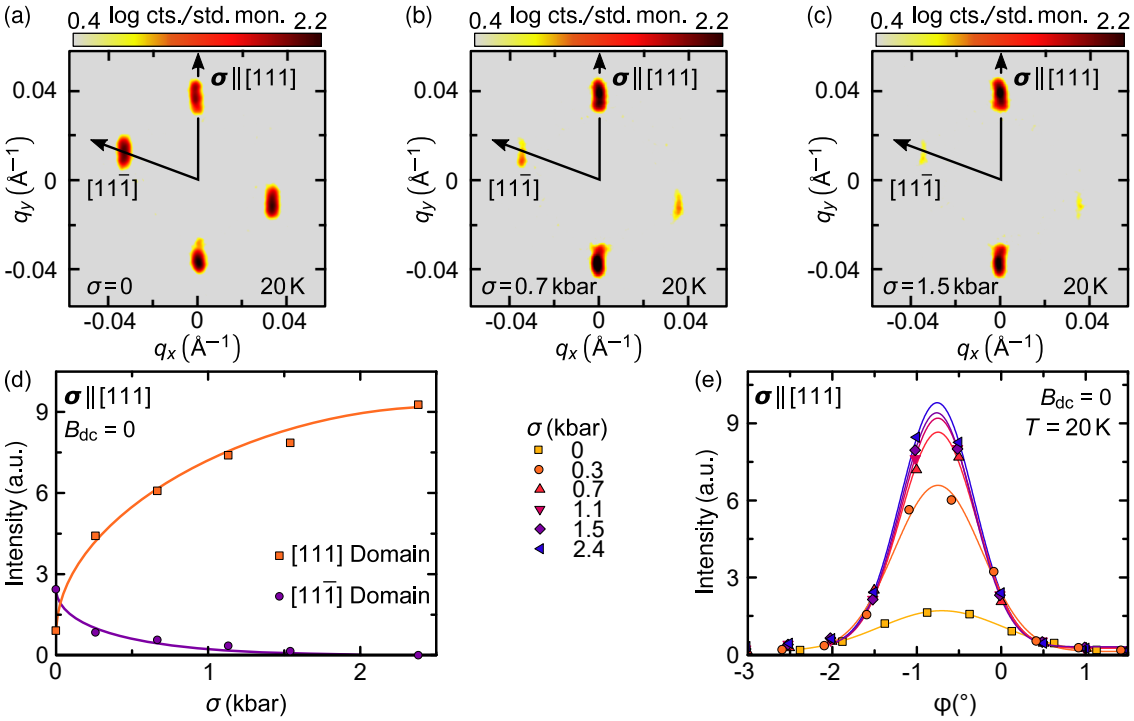

Figure 4.3: Uniaxial stress effects for $\sigma \parallel \langle 111 \rangle$. (a) Typical scattering pattern of the helical phase at ambient pressures. (b), (c) Uniaxial pressure along a $\langle 111 \rangle$ crystallographic axis leads a depopulation of the unfavorable domain, evident by the decrease in the intensity of the associated Bragg peaks. (d) Scattered intensity of the $[111]$ domain and the $[11\bar{1}]$ domain as a function of uniaxial pressure for $\sigma \parallel [111]$. Sample is heated up to $T \gg T_c$ before every pressure increment. Smallest pressure is sufficient to achieve substantial transfer of population from unfavorable domains to $[111]$. (e) Rocking curves for angle ϕ for different values of σ. With increasing uniaxial pressure the peaks become sharper indicating a reduction in magnetic mosaicity.

the scattering plane, theoretically one expects additional tilts 'away' from the scattering analogous to the magnetic field-driven transition to a conical state discussed in chapter 3, cf. Fig. 3.3. The mapping of these rotations was not part of the scope of the work in this thesis.

Uniaxial stress along a $\langle 111 \rangle$ axis breaks the symmetry between the different domains. For the following discussion, the pressure axis is defined as parallel to the $[111]$ axis. The SANS measurements presented here captured neutrons scattered from the $[111]$ domain and the domains propagating along $[11\bar{1}]$. A detailed measurement of all helical domains was out of the scope of this study. Due to the symmetry of the system observations made for $[11\bar{1}]$ are equivalent to the behavior from the other domains. Typical scattering patterns are shown in figure 4.3. Increasing uniaxial pressure leads to the depopulation of unfavorable domains resulting in a reduction of the associated scattering intensity, cf. Fig. 4.3 (b) and (c).

Figure 4.3 (d) shows the intensity of the $[111]$ and $[11\bar{1}]$ domains as a function of uniaxial stress. Already the smallest pressure applied results in a substantial transfer of intensity from the unfavorable domains to the one propagating parallel to the pressure axis. As for the other measurements, the sample was heated up to $T \gg T_c$ before every pressure increment. Going above the onset of the magnetic order enhances the effects of uniaxial pressure. Upon cooling the sample spins would align along the pressures axis due to the broken symmetry of the system, which breaks up the degeneracy between the space diagonals. If the pressure were to be increased well below the transition temperature, a macroscopic rearrangement of

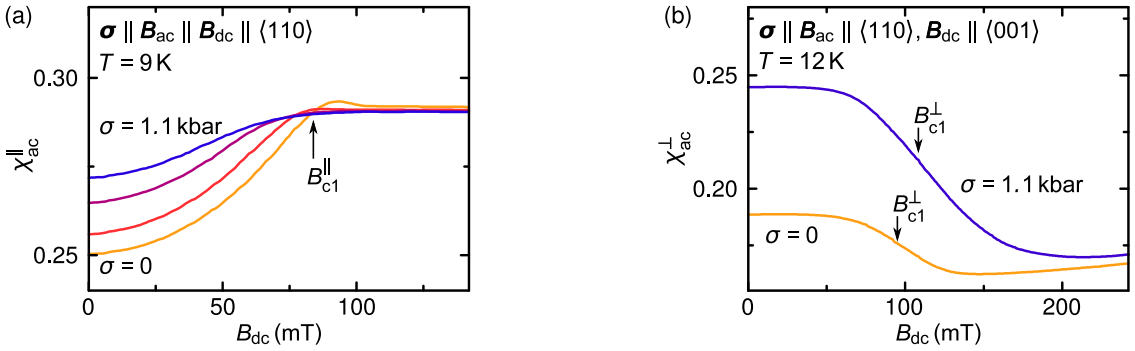

Figure 4.4: (a) Longitudinal magnetic susceptibility χ_{ac} as a function of external field B_{dc} at different values of σ. Both stress and magnetic field are applied along a $[110]$ axis. A rotation of the helix propagation vector towards $[110]$, either driven by pressure or magnetic field, results in a higher susceptibility. Consequently the critical field $B_{c1}^{\parallel}$ for the transition from helical to conical decreases with increasing pressure. (b) Magnetic susceptibility for an excitation field $\boldsymbol{B}_{dc} \parallel [110]$ as a function of external magnetic field $\boldsymbol{B}_{dc} \parallel [001]$ for different values of pressure $\sigma \parallel [110]$. The transition from the helical to the conical state at $B_{c1}^{\perp}$ is associated with a reduction in the magnetic susceptibility. Introduction of an uniaxial anisotropy perpendicular to the field results in a larger critical field $B_{c1}^{\perp}$.

helical domains would be needed as is the case for the magnetic field-driven transition. Thus larger pressures than the ones applied here would be necessary to achieve the transition to a single domain state because the unfavorable domains would remain metastable until they reach their spinodal point. The continuous increase in scattered intensity for the domain parallel σ observed in figure 4.3 (d) is associated with pressure inhomogeneities as well as a reduction of magnetic mosaicity. So-called rocking scans measure the width of the Bragg peak perpendicular to the observable plane, which is related to the magnetic mosaicity, by rotating the sample around a vertical axis perpendicular to the neutron beam and, if possible, perpendicular to the propagation axis. The resulting intensity dependence of rocking angle ϕ is shown in figure 4.3 (e) for different values of σ. With increasing uniaxial pressure, the maximum intensity increases, but the width of the peak does not broaden. Thus the full-width at half maximum decreases, which means that the more helical domains are oriented along the uniaxial stress axis, reducing the magnetic mosaicity.

Competition and cooperation between Zeeman energy and uniaxial anisotropy

As shown above, uniaxial pressure leads to a preferred axis of propagation parallel to the stress axis. As discussed in chapter 3, applying an external magnetic field $\boldsymbol{B}_{dc}$ also results in a reorientation of the helix to point towards the field direction. The interplay between uniaxial anisotropy and Zeeman energy at finite fields was studied through ac magnetic susceptibility measurements.

Two different scenarios depending on the geometrical relation of external magnetic field $\boldsymbol{B}_{dc}$ and uniaxial pressure axis σ can be distinguished:

- Cooperation: $\boldsymbol{B}_{dc} \parallel \sigma$,
- Competition: $\boldsymbol{B}_{dc} \perp \sigma$

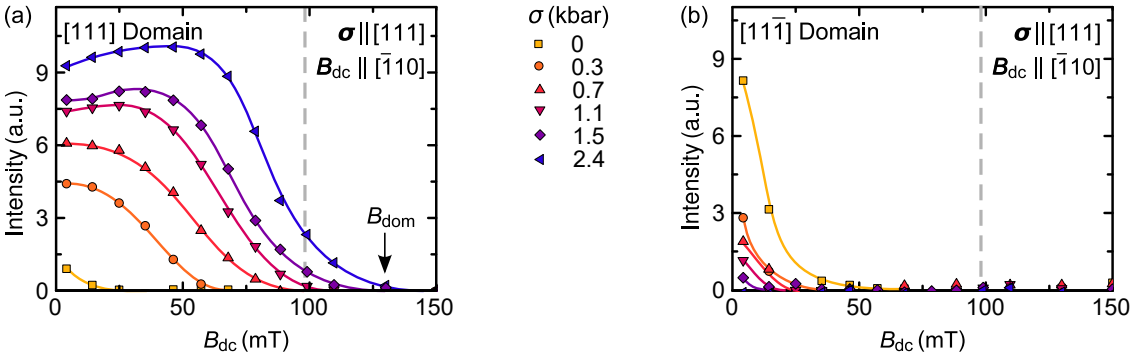

Figure 4.5: Scattered intensity from helical domains as a function of external magnetic field $\boldsymbol{B}_{\mathrm{dc}} \parallel [\bar{1}10]$ for different values of σ with $\sigma \parallel [111]$. (a) Intensity from helical domains with propagation vector $\boldsymbol{Q} \parallel [111]$. This domain is stabilized by the uniaxial stress, and survives up to higher values of the magnetic field with increasing uniaxial pressure, surpassing the typical critical field for pressures above 1 kbar. (b) Intensity from helical domain with propagation vector $\boldsymbol{Q} \parallel [11\bar{1}]$. The combination of stress and magnetic field makes this domain the most unfavorable one. Thus its population is depleted at very low magnetic field values.

while the excitation field $\boldsymbol{B}_{\mathrm{ac}}$ pointed always parallel to σ. These measurements were made on sample S1, cf. table 4.1, which had a $[110]$ axis along its long edge, while the shorter sides where parallel to $[001]$ and $[\bar{1}10]$.

Cooperation $\boldsymbol{B}_{\mathrm{dc}} \parallel \sigma$

The situation is cooperative when the uniaxial pressure σ is parallel to the external magnetic field $\boldsymbol{B}_{\mathrm{dc}}$. In the present case, both of these as well as the excitation field pointed along the $[110]$ axis. The measured magnetic susceptibility is the same as the one discussed in the previous chapter and is denoted longitudinal susceptibility since $\boldsymbol{B}_{\mathrm{dc}} \parallel \boldsymbol{B}_{\mathrm{ac}}$. Typical curves obtained at different values of σ are shown in figure 4.4 (a). These were measured after cooling the sample in a high negative magnetic field. Consequently, at zero magnetic field only the domains along $[111]$ and $[11\bar{1}]$ are populated as these are closest to the magnetic field direction, while the other two domains lie perpendicular to it, cf. chapter 3. Increasing the magnetic fields results in turn in a higher χ_{ac} as the domains rotate towards the field. The point of inflection of the susceptibility curve as a function of the magnetic field defines the critical field value B_{c1}, and in this case is $B_{\mathrm{c1}} \approx 100\,\mathrm{mT}$. At ambient pressure, there is a small peak associated with the transition. Consistent with the rotation of helical domains observed in the neutron scattering patterns, cf. Fig. 4.2 (b), the magnetic susceptibility χ_{ac} at zero magnetic field increases with increasing pressure approaching the value observed for the conical phase. Accordingly, the transition to the conical phase takes places at lower magnetic field values. The small peak observed at the transition vanishes as the pressure rises. That can be the consequence of large and fewer domains, as well as pressure inhomogeneities present in the sample that smear the critical behavior at the transition.

Competition $\boldsymbol{B}_{\mathrm{dc}} \perp \sigma$

Uniaxial stress pointing along a hkl[110] axis and an external magnetic field parallel to a $[001]$ permits the study of the competition between Zeemann energy and the induced uniaxial anisotropy. The crystallographic magnetic field direction was chosen to avoid the discrete

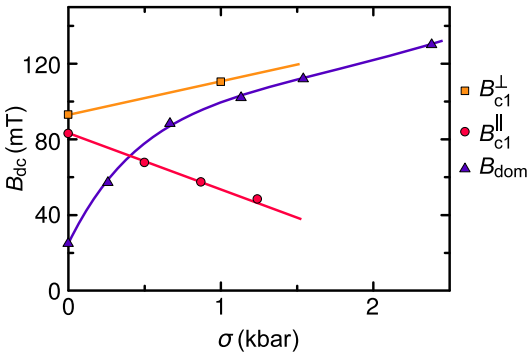

Figure 4.6: Pressure dependence of critical field B_{c1} for uniaxial pressures perpendicular and parallel to the external magnetic field, denoted by $B_{c1}^{\perp}$ and $B_{c1}^{\parallel}$, respectively. Uniaxial pressure was applied along a $[110]$, and fields were applied along $[001]$ and $[110]$ crystallographic axes, for perpendicular and parallel configurations, respectively. In a perpendicular geometry, the critical field increases with increasing pressure, while it decreases for a field parallel to pressure. Additionally, the characteristic field B_{dom} indicate the field at which domains parallel to $\sigma \parallel [111]$ are completely depopulated. The latter approaches $B_{c1}^{\perp}$ for pressures $\sim 1\,\text{kbar}$. Thus uniaxial anisotropy dominates anisotropic behavior for pressures above a few kbars.

transition of the domains closest to the uniaxial pressure axis under ambient pressure for a field parallel to $[\bar{1}10]$. As a reminder, in MnSi domains perpendicular to a magnetic field applied along a $\langle 110 \rangle$, are depopulated in a discrete transition at fields lower than B_{c1}. Due to the experimental setup constraints, the excitation field B_{ac} is perpendicular to the external static field B_{dc}. Thus probing a different diagonal component of the magnetic susceptibility tensor. The measured susceptibility is denoted ${\chi_{ac}}^{\perp}$ to avoid confusion with the more typical longitudinal susceptibility. Figure 4.4 (b) shows typical dependencies of ${\chi_{ac}}^{\perp}$ around the transition to the conical state. At zero magnetic field, the susceptibility measured is the same, as the field increases and the helical domains rotate towards it, the value of ${\chi_{ac}}^{\perp}$ decreases. Further increments of the magnetic field strength result in an increase of the susceptibility, associated with the rotation of the spins towards the propagation direction $\boldsymbol{Q}_{hel} \parallel \boldsymbol{B}_{dc}$.

It is instructive to consider the particular case of uniaxial stress applied parallel to $[111]$, in which the pressure enhances the energy gain from propagating along the easy axis of the system. Figures 4.5 (a) and (b) show the measured scattered intensity from the helical domains propagating along $[111]$ and $[11\bar{1}]$, respectively, as a function of an external magnetic field applied along $[\bar{1}10]$, for different values of uniaxial stress applied along $[111]$. As mentioned above, all other domains become depopulated as the pressure increases, and the $[111]$ domain is favored. At ambient pressure, the intensity for these domains vanishes just below $\sim 50\,\text{mT}$. The application of uniaxial stress increases the field region in which the helix along $[111]$ is stable dramatically and for $\sigma \approx 1.1\,\text{kbar}$ intensity can be observed above the critical field B_{c1} at ambient pressure.

At the moment, it is not possible to perform small-angle neutron scattering while rotating the sample and the magnetic field by an arbitrary angle. Typically the rotation range is constrained to $-5°$ to $5°$ around the incoming neutron beam. Thus it is not possible to determine carefully the value of B_{c1} from these measurements since one cannot establish that the not observable domains have coalesced to a single domain already. Instead, a new field value B_{dom} is defined at which the domains along $[111]$ has been completely depleted, cf. Fig. 4.5 (a). The dependencies of the critical transition fields $B_{c1}^{\perp}$ and $B_{c1}^{\parallel}$, for magnetic fields per-

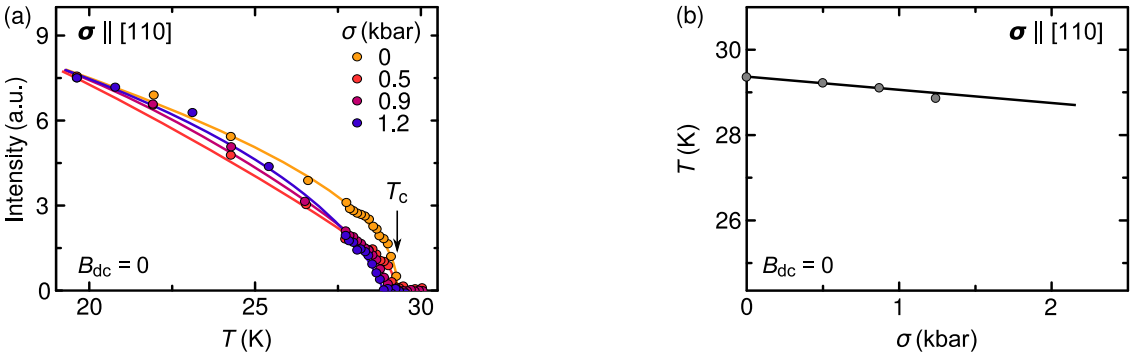

Figure 4.7: (a) Scattered neutron intensity from the helimagnetic order in MnSi at different uniaxial pressures σ. The critical temperature T_c is defined as the onset of intensity and marked by a black arrow. (b) With increasing uniaxial pressure the magnetic order is suppressed and the critical temperatures shifts to lower values as a consequence of isotropic pressure effects, the gray line is a fit with a slope of $dT/d\sigma \approx -0.24\,\mathrm{Kkbar}^{-1}$.

pendicular and parallel to the uniaxial pressure axis, respectively, are plotted in figure 4.6, together with B_{dom}, defined above. The critical field for $\boldsymbol{B} \perp \sigma$ increases with increasing uniaxial pressure. In contrast $B_{c1}^{\parallel}$ decreases linearly with increasing uniaxial pressure. While B_{dom} shows non-linear behavior for pressures below 1 kbar, and linear behavior above. This domain is perpendicular to the field, which means that usually there would be a discrete transition to one of the helical domains propagating closer to the magnetic field direction. Thus, the field dependence of B_{dom} can be interpreted as a transition to the conical phase through an intermediary helical domain below 1 kbar and a direct transition to the conical state for pressures above this value.

Regardless of the crystallographic direction the pressure is applied along, the anisotropic contribution arising from it exceeds the magneto-crystalline anisotropies above a few kbars and dominates the anisotropic phenomena related to the helical phase.

Suppression of the magnetic order from uniaxial pressure

The effects of uniaxial pressure on the helical phase discussed above are a consequence of symmetry breaking anisotropic strain. A different, isotropic effect of uniaxial stress on the magnetic order of MnSi is observed at the transition temperature from the paramagnetic to the helical state at zero magnetic field. The scattered intensity on the helical propagation peaks as a function of temperature is depicted in figure 4.7 (a). The onset of scattered neutrons intensity from the helical domains, indicated by the black arrow for ambient pressure, defines the critical transition temperature T_c. With increasing uniaxial stress σ the magnetic order is suppressed and the critical temperature T_c shifts to smaller values at a rate of $dT_c/d\sigma \approx -(0.24 \pm 0.03)\,\mathrm{Kkbar}^{-1})$, cf. Fig. 4.7 (b). A similar suppression of the magnetic order is observed under hydrostatic pressure at a rate of $-0.8\,\mathrm{Kkbar}^{-1} \approx 3dT_c/d\sigma$ [131]. The latter is a consequence of a reduction of the unit cell volume, leading to the conclusion that the uniaxial pressure-driven suppression of the magnetic order originates in isotropic effects which result in a smaller volume of the unit cell.

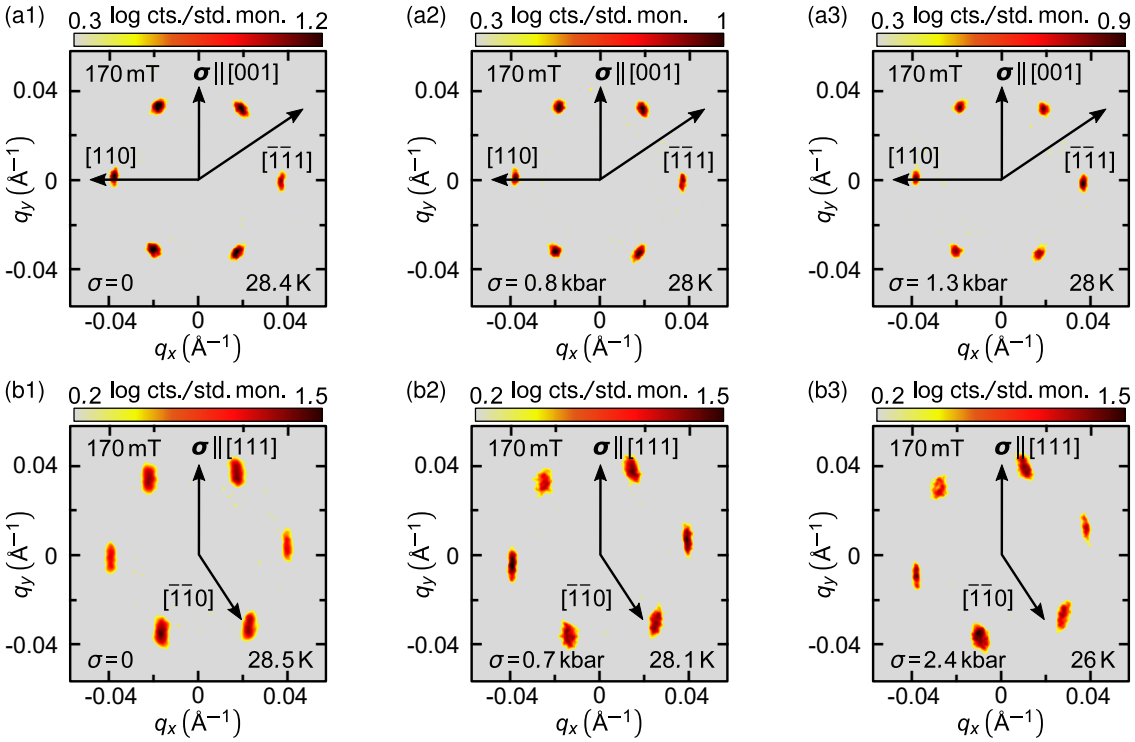

Figure 4.8: Scattering pattern of the skyrmion lattice for $\boldsymbol{B}_{\mathrm{dc}} \parallel [\bar{1}10]$ at different values of σ. (a1), (a2) and (a3), scattering patterns for $\sigma \parallel [001]$. The application of pressure does not break the intrinsic symmetries of the system. Thus the scattering pattern remains unchanged for all values of σ. (b1), (b2) and (b3), skyrmion lattice for $\sigma \parallel [111]$. In this case, the symmetry of the skyrmion lattice is broken by the uniaxial stress, leading to a smooth rotation of the scattering pattern towards the pressure axis with increasing pressure.

4.3 UNIAXIAL PRESSURE EFFECTS ON THE SKYRMION LATTICE

The seminal theoretical work of Bogdanov established the existence of skyrmion lattices P2_13 systems only under the existence of additional uniaxial anisotropy. As was discussed in the introduction, the skyrmion lattices are stabilized in these compounds by their effective coupling to thermal excitations closed to the transition temperature. Recent theoretical analysis on the effects of extrinsic uniaxial anisotropies on the phase diagram of MnSi established that a uniaxial tensile strain would result in the stabilization of the skyrmion lattice down to lowest temperatures. In agreement with this most recent work, the results presented here show that the application of uniaxial stress perpendicular to the magnetic field stabilizes the skyrmion lattice. However, the latter is suppressed if the uniaxial stress is parallel to the external magnetic field direction. These observations will be discussed in more detail towards the end of this subsection. First, the next paragraphs examine the effects on the microscopic characteristics of the magnetic order.

Small-angle neutron scattering and magnetic susceptibility measurements are combined to obtained a thorough characterization of the skyrmion lattice under pressure, using both experimental configurations with $\boldsymbol{B}_{\mathrm{dc}} \parallel \sigma$ and $\boldsymbol{B}_{\mathrm{dc}} \perp \sigma$. These are discussed separately in the following.

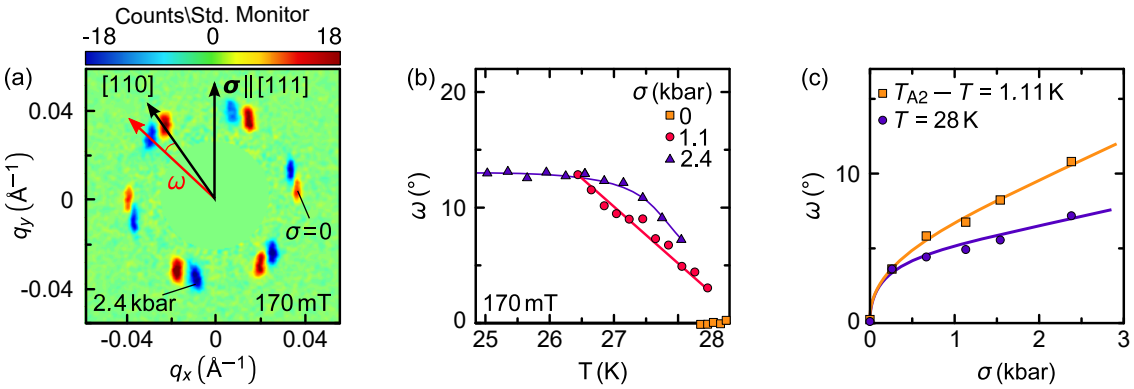

Figure 4.9: (a) Scattering pattern of the skyrmion lattice at ambient pressure subtracted by the scattering pattern obtained at $\sigma = 2.4\,\mathrm{kbar}$. The skyrmion lattice has rotated by an angle ω induced by pressure. (b) Temperature dependence of the rotation angle ω for different values of σ. The decrease close the transition temperature indicates thermally driven relaxation processes. (c) Uniaxial pressure dependence of the rotation angle ω for absolute temperatures $T = 28\,\mathrm{K}$ and for relative temperatures $T_{A2} - T = 1.1\,\mathrm{K}$. The rotation angle shows a smooth increase with increasing pressure, due to the breaking of the two-fold rotation symmetry around $[001]$ induced by the uniaxial stress.

Uniaxial pressure perpendicular to the external magnetic field

The SANS experiments carried out with $\boldsymbol{B}_{\mathrm{dc}} \parallel \boldsymbol{\sigma}$ included an external magnetic field applied along a $[\bar{1}10]$ axis to readily compare anisotropic effects arising from different pressure axis, i. e., $[001]$,$[110]$ and $[111]$. Figure 4.8 depicts typical scattering patterns for $\boldsymbol{\sigma} \parallel [001]$. The skyrmions order in a hexagonal lattice resulting in a scattering pattern consisting of three pairs of Bragg peaks. For $\boldsymbol{B}_{\mathrm{dc}} \parallel \langle 110\rangle$ one of these pairs points along a $\langle 110\rangle$. The orientation of the skyrmion lattice as a function of uniaxial pressure can be described with an effective potential given by

$$\mathcal{V}(\omega) = -\mathcal{V}(\sigma)\cos\{6[\omega - \omega_0(\sigma)]\}, \tag{4.2}$$

where $\mathcal{V}(\sigma)$ and $\omega_0(\sigma)$ are pressure dependent coefficients and ω quantifies the deviation of one of the Bragg peak pair from a $\langle 110\rangle$. At ambient pressure and magnetic fields parallel to $\langle 110\rangle$ the two-fold symmetry around the cubic $\langle 100\rangle$ axes of the system from the tetrahedral point group results in $\omega_0(0) = 0$. Hence $\mathcal{V}(0) > 0$ so that the contribution from $\mathcal{V}(\sigma)$ is minimized for $\omega = 0$. Applying uniaxial pressure along a $\langle 100\rangle$ axis does not break the rotation symmetry around the $[001]$ since σ is a director. Typical scattering patterns for $\boldsymbol{\sigma} \parallel [001]$ are shown in the first row of figure 4.8. Increasing uniaxial stress does not result in any changes on the magnetic structure of the skyrmion lattice. Thus, $\omega_0(\sigma) = 0$ and the coefficient $\mathcal{V}(\sigma)$ remains positive.

The rotation symmetry around the cubic $\langle 100\rangle$ axis is broken when uniaxial pressure is applied along a $\langle 111\rangle$ axis. This can be easily observed in the scattering patterns shown in the second row of figure 4.8. At ambient pressures the typical six-fold pattern is observed. Adding uniaxial stress leads to a rotation of the skyrmion lattice towards $\boldsymbol{\sigma}$, cf. Fig 4.8 (b2) and (b3).

Figure 4.9 contains a detailed characterization of the rotation angle ω . First, the rate of rotation is evident from a subtraction of the scattering pattern obtained at $\sigma = 2.4\,\mathrm{kbar}$ from the one measured at ambient pressures. The blue points represent the position of the Bragg

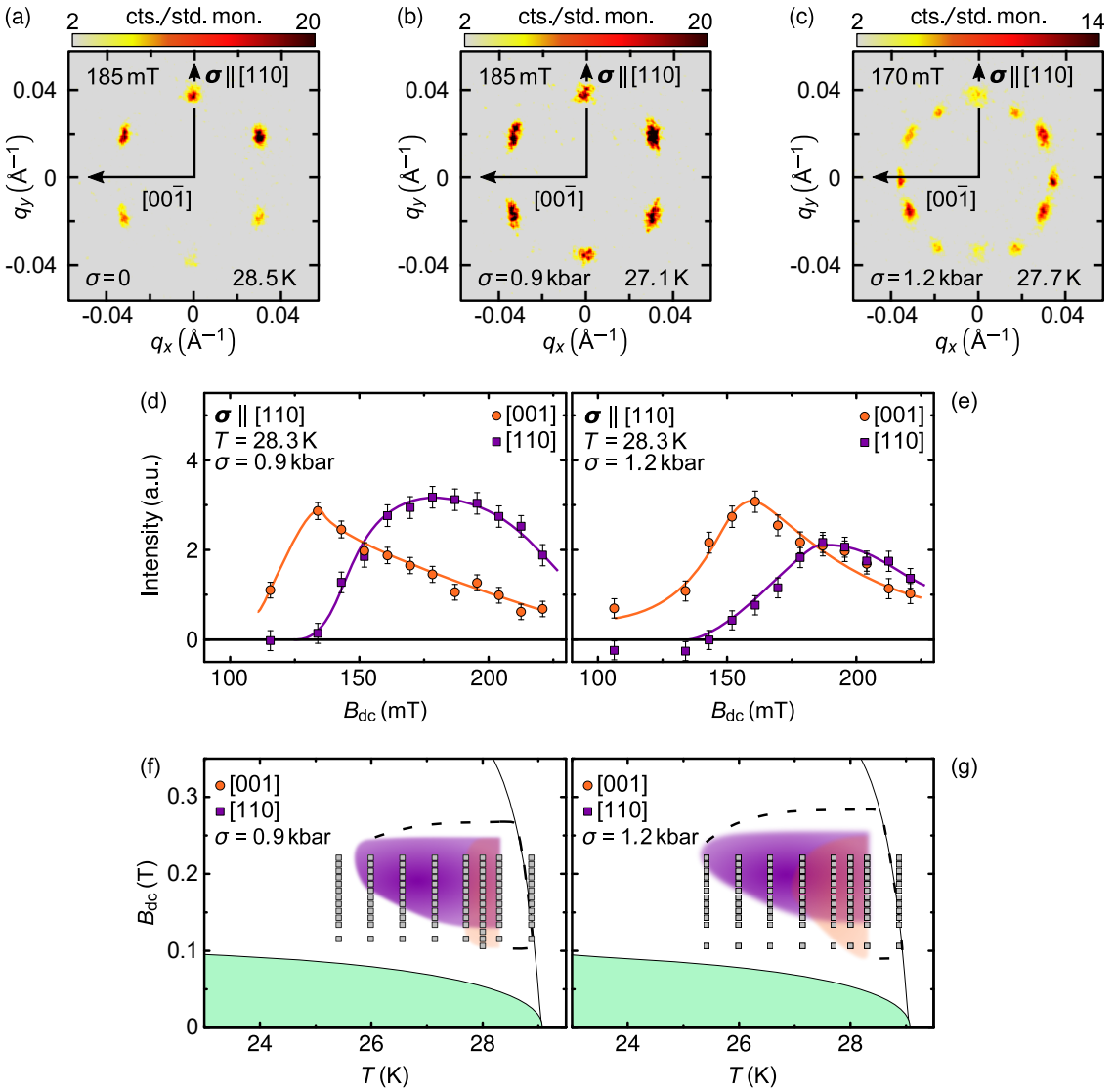

Figure 4.10: (a) Scattering pattern of the skyrmion lattice at ambient pressures. Intensity differences between Bragg peaks originate from incomplete rocking scans. (b) Skyrmion lattice at $\sigma = 0.9\,\mathrm{kbar}$ after the sample was cooled in an applied field $B_{\mathrm{dc}} = 185\,\mathrm{mT}$. There are no changes in the orientation of the skyrmion lattice. (c) Scattering pattern of the skyrmion lattice after zero-field cooling. The 12-fold pattern corresponds to two different domains, with a Bragg peak pair along $[110]$ and $[001]$, respectively. (d), (e) Scattered intensity from the $[001]$ and $[110]$ domains after zero-field cooling as a function of magnetic field at $\sigma = 0.9\,\mathrm{kbar}$ and $\sigma = 1.2\,\mathrm{kbar}$, respectively. The domains oriented along $[001]$ are observed at lower fields, while those oriented relative to the $[110]$ dominate in the typical field region of the skyrmion lattice phase. Increasing the uniaxial stress results in enhanced stability of the $[001]$ domain for larger fields. (f), (g) Schematic phase diagrams from neutron scattering measurements after zero-field cooling. Regimes of the $[001]$ and $[110]$ domains are shaded orange and purple, respectively. The squares represent points at which scattered neutrons were measured. The $[001]$ domain dominates the high temperature, low field regime, while the $[110]$ is observed to lowest temperatures. The regime of the $[001]$ domain increases with increasing pressure.

peaks under pressure rotated by the angle ω concerning the measurement at $\sigma = 0$. Interestingly the rotation angle has a temperature dependency, depicted for ambient, intermediate, and the maximum pressure measured in figure 4.9 (b). At ambient pressures, there is no rotation over the entire temperature window of the skyrmion lattice. At intermediate pressures, i. e., $\sim$ 1.1 kbar, ω shows a linear dependence on temperature, decreasing with increasing temperature. Finally, at $\sigma = 2.4$ kbar, the highest pressure measured, the rotation angle remains finite and constant with a value of $\sim 12.5°$ over must of the temperature regime of the skyrmion lattice and starts to decrease close to the transition to the intermediate regime. Thus, thermal fluctuations reduce the effects of uniaxial pressure, allowing a partial relaxation of the crystal lattice. These coupling to thermal fluctuations together with the suppression of the magnetic order, discussed in the last section, need to be considered when defining the dependence of ω on uniaxial stress σ. In figure 4.9 (c) two different approaches are plotted, i. e., constant temperature and constant distance from the transition to the intermediate regime, i. e., $T_{A2} - T$. Regardless of which approach is chosen the rotation angle ω shows a continuous dependence on the uniaxial pressure, which seems to be linear above 1 kbar. Hence breaking the two-fold symmetry leads to a finite $\omega_0(\sigma)$ and in turn a smooth increase in ω with increasing stress as the Bragg peaks rotate away from the $[110]$ axis.

Similarly to the case of uniaxial pressures along $[001]$, applying stress along a $[110]$ axis does not break the $180°$ rotation symmetry around the $[001]$ axis. From an experimental point of view, two different scenarios can be distinguished, field-cooling, and zero-field-cooling. In the former, the desired magnetic field value is applied, and the sample is then cooled below the critical temperature T_c. In the case of zero-field-cooling, there is no finite magnetic field during cooling. For field-cooling measurements, there are no changes in the six-fold pattern of the skyrmion lattice. For comparison, the measured scattering pattern at ambient pressure and at $\sigma = 0.9$ kbar are shown in figure 4.10 (a) and (b), respectively. Note that intensity differences between the Bragg peaks at ambient pressure are the consequence of incomplete rocking scans.

After cooling the sample in zero magnetic field, and subsequently increasing the latter, the scattering pattern shown in figure 4.10 (c) is observed. It consists of a total of 12 Bragg peaks, originating from two separate domains of skyrmion lattices, one with a pair of Bragg peaks pointing along the $[110]$ axis and a second with a pair of Bragg peaks along the $[001]$ axis. Each of these domains possesses its independent regime of stability in the phase diagram. The $[001]$ domain dominates at lower fields, even slightly lower than those at which the skyrmion lattice is stable at ambient pressures. Increments in the magnetic field lead to a population transfer from the $[100]$ domain to the $[110]$ one, cf. Fig. 4.10 (d) and (e). In contrast, the $[110]$ domain is stable at lower temperatures than the $[001]$ domain, this is illustrated in schematic phase diagrams shown in figure 4.10 (f) and (g). The regime of the $[001]$ domain is colored orange, while the regime of the $[110]$ is colored purple, the squares denote the points at which scattering patterns were measured. The scattered neutron intensity indicates that the $[001]$ domain becomes dominant over increasing field regions as the pressure increases.

As mentioned above, since the rotation symmetry remains unchanged $\omega_0(\sigma) = 0$ and the uniaxial pressure changes only the value of $\mathcal{V}(\sigma)$. With increasing pressure $\mathcal{V}(\sigma)$ decreases and it changes sign for $\sigma \approx 1$ kbar, hence the potential $\mathcal{V}(\omega)$ is minimized for $\omega = 30°$. The expansion of the temperature regime of the $[110]$ skyrmion domain demonstrates the limits of the effective potential described above. The $[110]$ domain can be stabilized by the temperature dependence of the coefficients of $\mathcal{V}(\omega)$ or the $[001]$ domain could be metastable and only an intermediate step between helical and $[110]$ skyrmion lattice.

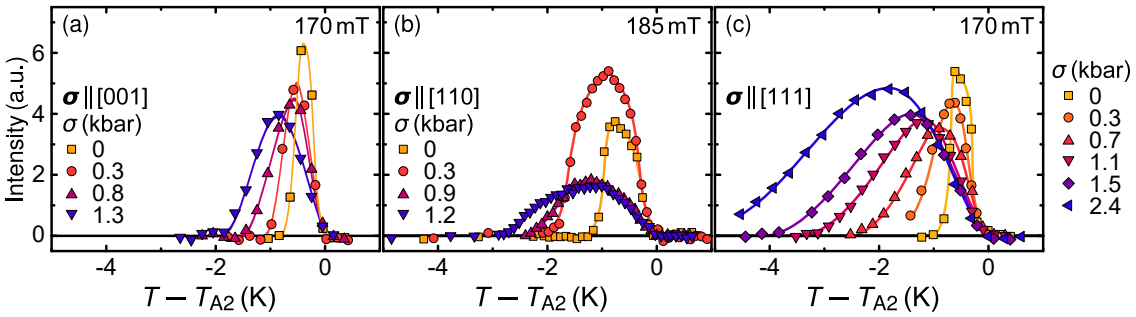

Figure 4.11: Temperature dependence of the scattered neutrons intensity from the skyrmion lattice for $\boldsymbol{B}_{\mathrm{dc}} \parallel [\bar{1}10]$ for different direction of σ. The temperature scale is relative to T_{A2} the transition to the intermediate regime for better comparison. (a) $\sigma \parallel [001]$, temperature window of the skyrmion lattice increases with increasing pressure and doubles around $\sigma \approx 1\,\mathrm{kbar}$. (b) $\sigma \parallel [110]$ the stabilization is stronger than for $\sigma \parallel [001]$, reaching three times the width of the ambient pressure phase at $\sigma \approx 1\,\mathrm{kbar}$. Strong intensity changes originate from incomplete rocking scans. (c) $\sigma \parallel [111]$, the expansion of the skyrmion phase is similar as for $\sigma \parallel [110]$.

In summary, there is no indication of microscopic changes to the magnetic order in the skyrmion lattice phase as a function of uniaxial pressure, for the range of stresses studied here. Regardless of the uniaxial stress direction, no intensity related to higher-order contributions was observed, indicating that the pressure does not affect the magnetic structure, only affecting their preferred spatial orientation. Additionally, σ should couple to the normal vector of the skyrmion lattice, causing a small tilt from a plane perfectly perpendicular to the applied magnetic field. Such a tilt was recently observed, in careful measurements of the skyrmion lattice orientation as a function of magnetic field direction on a spherical sample [132].

The main result for the experimental configuration with $\boldsymbol{B}_{\mathrm{dc}} \perp \sigma$ is the expansion of the thermodynamic stability of the skyrmion lattice, regardless of the crystallographic axis, the pressure is applied along. The increment in the stability is evident from the temperature dependence of the scattered intensity from the skyrmion lattice. The measured intensity is shown in figure 4.11 as a function of relative temperature $T - T_{\mathrm{A2}}$ for $\boldsymbol{B}_{\mathrm{dc}} \parallel [1\bar{1}0]$ and uniaxial stress applied along an axis of high symmetry perpendicular to $\boldsymbol{B}_{\mathrm{dc}}$. At ambient pressure, the temperature boundaries of the skyrmion lattice are about 1 K apart. A few kbars of uniaxial stress are enough to expand this temperature window dramatically, i. e., three times larger for $\sigma \approx 1\,\mathrm{kbar}$.

The thermodynamic stabilization also affects the magnetic field regime of the skyrmion lattice, as demonstrated by the scattered intensity as a function of the external magnetic field B_{dc} shown in figure 4.12. At ambient pressure, the skyrmion lattice is observed between, approximately, 150 and 225 mT. As the pressure increases, scattered intensity can be measured at both smaller and larger fields in comparison to the ambient pressure case. Interestingly, while the intensity at 130 mT increases continuously with σ, no intensity is measured at 110 mT demarcating a sharp low boundary for the skyrmion phase. In contrast, the intensity increments for larger fields are substantially greater than those for lower fields. Additionally, from the slope of the curve, it is reasonable to conclude that the transition to the conical phase shifts considerably with increasing pressure. As mentioned above, the available magnetic fields only reach a maximum of 250 mT. Thus it was not possible to measure the latter transition.

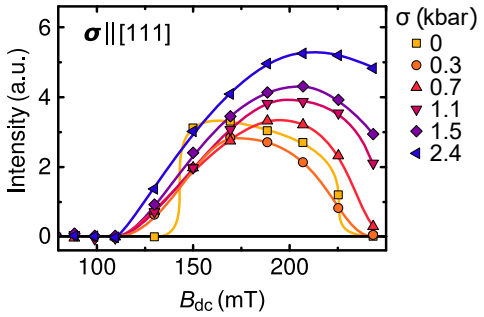

Figure 4.12: Scattered neutron intensity from the skyrmion lattice at different values of uniaxial stress σ applied along a $[111]$ crystallographic axis. At ambient pressure, the skyrmion lattice phase is observed between 150 and 225 mT. The curve progression indicates that the skyrmion lattice transition to the conical phase at large fields increases substantially with increasing pressure. At lower fields, there is a small expansion, but there is no intensity below 130 mT.

Uniaxial pressure parallel to the external magnetic field

The main result for a field applied parallel to the uniaxial pressure axis is the suppression of the skyrmion lattice. This is not surprising. The uniaxial pressure defines an easy-axis for the helical propagation, an effect that is enhanced by applying a finite magnetic field parallel to σ, thus leading to substantially smaller critical transition fields B_{c1} for the helical phase. In other words, uniaxial stress applied parallel to the external magnetic field favors a conical magnetic order.

The suppression of the skyrmion phase is summarized in figure 4.13, showing typical scattering patterns and the scattered intensity as a function of temperature. The uniaxial pressure axis is always perpendicular to the incoming neutron beam, cf. Fig. 4.1 (e). Thus only two from the six reflexes associated with the skyrmion lattice are observable simultaneously in such a configuration.

In the case of $\boldsymbol{B}_{dc} \parallel \langle 100 \rangle$ the skyrmion lattice changes its orientation such that one of its propagation vectors points along a $\langle 100 \rangle$ axis [132], cf. Fig 4.13 (a). Hence, after verifying the orientation of the sample with the helical scattering pattern at ambient pressures, the cryostat was turned by 45°, so that the neutron beam was parallel to a $[100]$ axis.

Figure 4.13 (b) depicts the scattered neutron intensity from the skyrmion lattice as a function of temperature for $\sigma \parallel [001]$. At ambient pressure the temperature window of the skyrmion phase is larger than for $\boldsymbol{B}_{dc} \parallel [110]$, this is a consequence of the additional contribution to the stabilization of the skyrmion lattice from the magnetocrystalline anisotropies since a field along a $\langle 100 \rangle$ axis is furthest from the easy-axis of propagation,i. e., $\langle 111 \rangle$. Increasing uniaxial pressure reduces both the temperature window in which the skyrmion lattice is observed as well as the scattered intensity from it. As the uniaxial anisotropy dominates over the magnetocrystalline contribution, the preferred axis of propagation rotates towards σ, with this rotation the stability of the skyrmion lattice is reduced. Note that for pressures $\gtrsim 1$ kbar the temperature window remains unchanged within the accuracy of this study, and the effect of uniaxial pressure is mainly captured by a decrease in the volume of the skyrmion phase, indirectly measured through the scattered neutron intensity, cf. Fig 4.13 (b). That last observation could be a consequence of pressure inhomogeneities in the sample.

Uniaxial stress along a $\langle 110 \rangle$ axis results in very similar behavior. Depicted in figure 4.13 (c) is a typical scattering pattern of the skyrmion lattice in this experimental configuration mea-

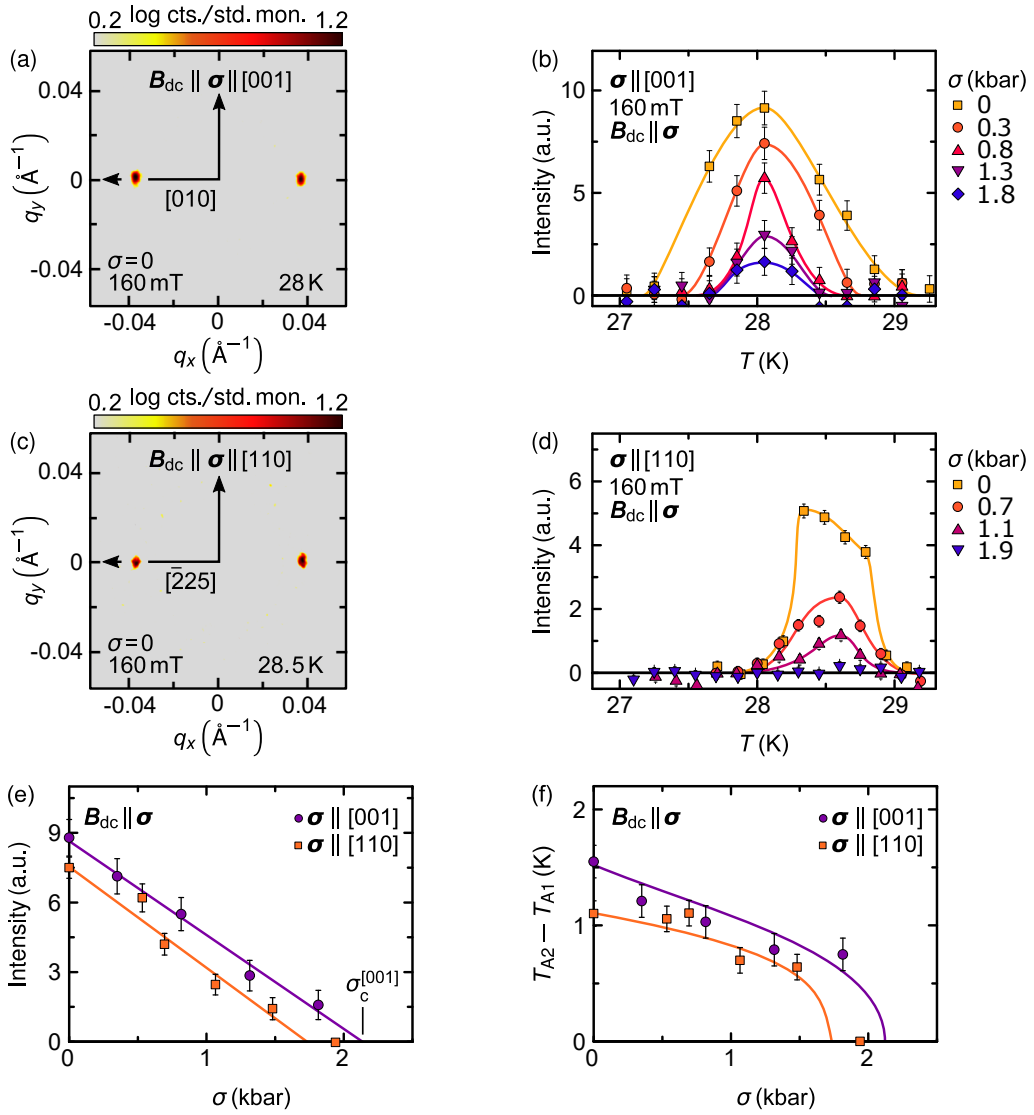

Figure 4.13: Neutron scattering data from the skyrmion lattice for $\boldsymbol{B}_{dc} \parallel \sigma$ (a), (b) Scattering pattern and scattered intensity from a skyrmion lattice with $\boldsymbol{B}_{dc} \parallel \sigma \parallel [001]$. Only two Bragg peaks are simultaneously measurable since the neutron beam is perpendicular to the magnetic field. A pair of Bragg peaks lie along $[010]$. With increasing uniaxial stress the scattered intensity decreases strongly and the temperature window of the skyrmion lattice is reduced. (c), (d) Scattering pattern and scattered intensity for $\boldsymbol{B}_{dc} \parallel \sigma \parallel [110]$. The Bragg peaks measured point along a $[\bar{2}25]$ axis, 60° away from a $[\bar{1}10]$ axis. The suppresion of the skyrmion lattice with increasing uniaxial pressure is very effective and no intensity is measured at $\sigma = 1.9$ kbar. (e), (f) Pressure dependence of the intensity and the temperature width of the skyrmion phase. As the pressure increases, the intensity decreases linearly. The intersection of a linear fit with the pressure axis (black arrow) defines the critical pressure that suppresses the skyrmion phase completely. The temperature width of the skyrmion phase decreases slightly with increasing uniaxial pressure and vanishes spontaneously at the critical pressure.

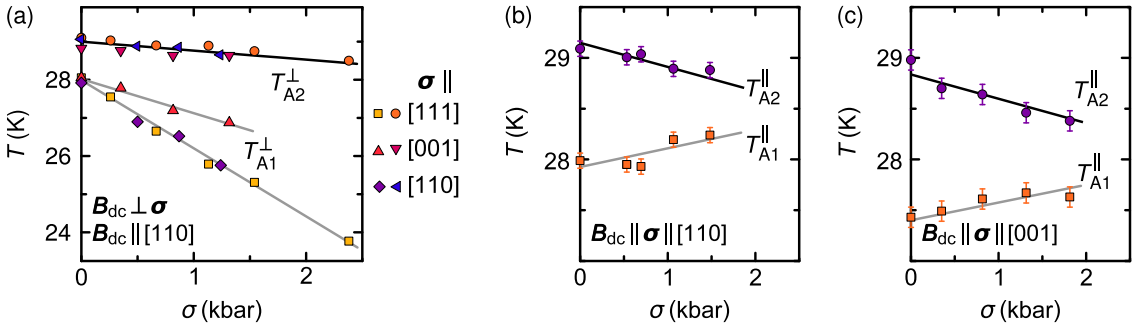

Figure 4.14: (a) Transition temperatures T_{A1} and T_{A2} as a function of uniaxial stress σ for pressures applied along $[111]$, $[001]$, and $[110]$, perpendicular to the magnetic field $\boldsymbol{B}_{dc}$. The suppression of the magnetic order observed in the decrease of T_{A2} shows the same slope dT_{A2}/d_σ as T_c, cf. Fig 4.7. The transition to the conical phase also shifts to lower temperatures indicating the extended region where the skyrmions are stable. (b), (c) Transition temperatures for $\boldsymbol{B}_{dc} \parallel \sigma \parallel [110]$ and $\boldsymbol{B}_{dc} \parallel \sigma \parallel [001]$, respectively. In contrast to $\boldsymbol{B}_{dc} \perp \sigma$ the effects of uniaxial pressure on the phase boundaries are very weak, and the transition temperature T_{A1} shows only a rate of increment $dT_{A2}/d_\sigma \approx (0.20 \pm 0.02)\,\mathrm{Kkbar}^{-1}$.

sured along a $[\bar{2}25]$ axis, $\sim 60°$ away from a $[\bar{1}10]$. As was the case for $\sigma \parallel [001]$, the scattering pattern of the helical phase for a neutron beam parallel to $[110]$ at ambient pressure verifies the sample orientation. The closest pair of skyrmion Bragg peaks are brought to a scattering condition by rotating the sample by 30°. The suppression of the skyrmion lattice phase for $\sigma \parallel [110]$ is very efficient and no intensity is measured at $B_{dc} = 160\,\mathrm{mT}$ for $\sigma = 1.9\,\mathrm{kbar}$.

The results discussed above are summarized in figure 4.13, where the intensity reduction and the temperature window of the skyrmion lattice, given by the difference of the transition temperatures $T_{A2} - T_{A1}$, are illustrated as a function of uniaxial stress in panel (e) and (f), respectively. T_{A1} denotes the transition from the conical to the skyrmion phase, while the transition to the intermediate regime defines T_{A2}. The progression of the intensity as a function of pressure shows a monotone reduction with increasing σ. The intersection of a linear fit of intensity with the pressure axis defines the critical pressure σ_c at which the skyrmion lattice would be completely suppressed, cf. Fig. 4.13 (e). Using this definition one obtains a critical stress $\sigma_c^{[110]} \approx 1.7\,\mathrm{kbar}$ for pressures along $[110]$ and $\sigma_c^{[001]} \approx 2.1\,\mathrm{kbar}$ for $\sigma \parallel [001]$. Extrapolation of the data obtained for $\sigma \parallel [001]$ results in a suppression of the skyrmion lattice for $\sigma_A \approx 2.2\,\mathrm{kbar}$. The changes in the temperature width of the skyrmion phase as a function of stress are smaller and reach a spontaneous collapse at the critical pressure.

The effects of uniaxial stress perpendicular and parallel to the external magnetic field are compared in figure 4.14, where the pressure dependency of the transition temperatures T_{A1} and T_{A2} has been plotted for all experimental configuration and samples measured using SANS. Note that regardless of crystallographic pressure axis or geometrical configuration, the temperature at which the skyrmion lattice transitions to the intermediate regime decreases with increasing pressure. The rate of the suppression $dT_{A2}/d\sigma$ is the same as the one observed for the critical temperature T_c, i. e., $dT_{A2}/d\sigma \approx -(0.24 \pm 0.03)\,\mathrm{Kkbar}^{-1}$. Thus the suppression of the magnetic order is dominated by the trace of the induced strain tensor. In a cubic crystal, the latter is independent of the orientation of the applied pressure.

The differences between $\boldsymbol{B}_{dc} \perp \sigma$ and $\boldsymbol{B}_{dc} \parallel \sigma$ are reflected in the behavior of T_{A1}. It decreases rapidly for pressures perpendicular to the external magnetic field, exhibiting a

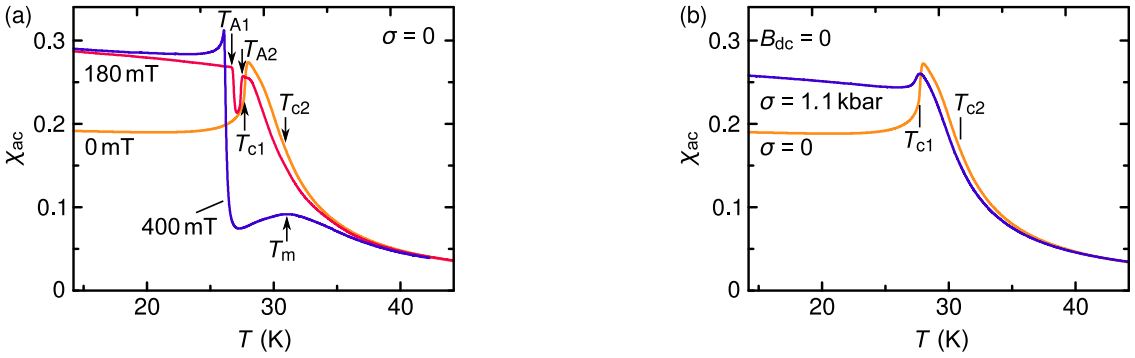

Figure 4.15: (a) χ_{ac} as a function of temperature for different magnetic fields at ambient pressure. Black arrows mark the different transition temperatures: T_{c1} helical phase to intermediate regime, T_{c2} intermediate regime to paramagnetic regime, T_{A1} conical to skyrmion phase, T_{A2} skyrmion phase to intermediate regime and T_m crossover between ferromagnetic and paramagnetic regime. (b) χ_{ac} as a function of temperature at zero-field for different values of stress. At $\sigma = 1.1$ kbar the susceptibility value increases as the propagation vector rotates to uniaxial stress direction, additionally the transitions move to lower temperatures, as the magnetic order is suppressed.

rate $dT_{A1}/d\sigma \approx -(2.00 \pm 0.05)$ Kkbar^{-1} and $dT_{A1}/d\sigma \approx -(1.00 \pm 0.05)$ Kkbar^{-1} for $\sigma \parallel [110]$ and $\sigma \parallel [111]$, and $\sigma \parallel [001]$, respectively. In contrast, uniaxial stress parallel to the external magnetic field results in an increase of the transition temperature T_{A1}, but the rate of increment $dT_{A1}/d\sigma \approx (0.20 \pm 0.02)$ Kkbar^{-1} is very small in comparison.

4.4 PHASE DIAGRAMS UNDER STRESS FROM MAGNETIC SUSCEPTIBILITY

The neutron scattering experiments discussed above are very useful to measure the microscopic details of the magnetic structures, at the same time they are very time consuming. Hence ac-magnetic susceptibility measurements are more suitable for the thorough determination of the phase boundaries. The results obtained from these measurements are presented below.

As mentioned above the excitation field for the ac magnetic susceptibility measurements B_{ac} is always parallel to the uniaxial stress axis σ. In the case of an external magnetic field B_{dc} parallel σ, the susceptometer is sensitive to the longitudinal component of the susceptibility of the conical phase, $\chi_{\parallel}$, cf. Ch. 3. Typical data obtained in this configuration at ambient pressure as function of temperature are shown in figure 4.15 (a). The different signatures associated with the different transitions in the sample are marked by arrows. At zero-field (yellow curve) and low temperatures, χ_{ac} has the average value resulting from the equal population of the domains along the different $\langle 111 \rangle$ axes. When the sample is warmed up the susceptibility increases reaching a peak related with the intermediate regime, where fluctuations of length Q_{hel} propagate along all directions. The point of inflection of the curve before reaching the maximum is designated T_{c1} and demarks the transition from the helical phase to the intermediate regime. At the transition from the intermediate regime to the paramagnetic phase the curve shows another inflection point, defined as T_{c2}. For fields within the region of the skyrmion phase (red curve), the susceptibility at low temperatures is determined by the conical phase. At higher temperatures the susceptibility drops spontaneously as the sample enters the skyrmion lattice phase. The point of the drop defines the transition temperature from the conical to the skyrmion phase T_{A1}. As the temperature is increased further, the

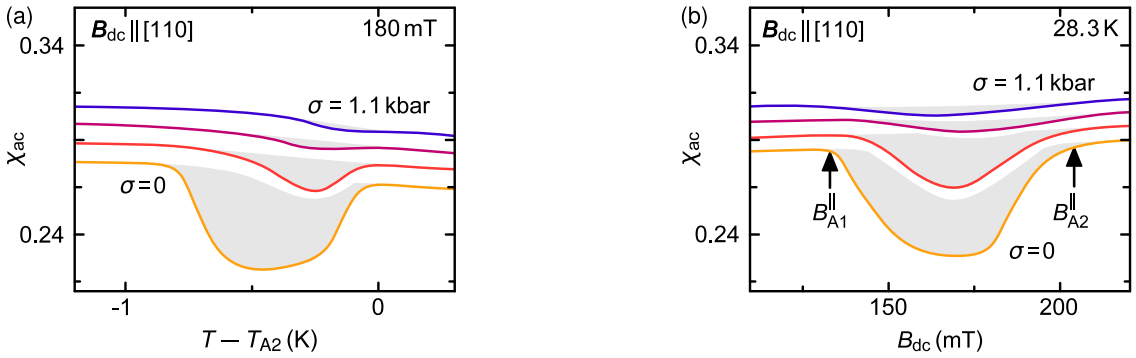

Figure 4.16: AC magnetic susceptibility χ_{ac} as a function of temperature, (a), and external magnetic field B_{dc}, (b), for different values of uniaxial stress σ. Data have been shifted to improve visibility. The areas filled in gray mark the region of the skyrmion phase. At ambient pressure the skyrmion signature is a dip in the value of χ_{ac} as the system transitions from and to the conical phase. With increasing uniaxial pressure the transitions become smoother and the absolute value of χ_{ac} increases.

susceptibility increases again, this point defines T_{A2}, and demarks the transition from the skyrmion phase to the intermediate regime. For the sake of completeness the plot includes a curve for high fields (blue). At low temperatures the susceptibility is defined by the conical phase, increasing the temperature leads to a sharp transition to a field polarized regime, further increment of the temperature leads to a crossover between the field polarized and the paramagnetic phases, separated by a broad maximum of the susceptibility defined as T_m. The latter will not be discussed further, note that no effects of uniaxial pressure were observed at T_m.

It was discussed thoroughly in section 4.2 that the uniaxial pressure creates a preferred axis of propagation for the helimagnetic domains of the system. Hence at high uniaxial stress the susceptibility at zero-field should the same as the one measured at high fields and ambient pressures. Accordingly we see an increase in the zero-field susceptibility at low temperatures with increasing uniaxial stress σ, as illustrated by the data at $\sigma = 1.1$ kbar in figure 4.15 (b). Additionally the suppression of the magnetic order with increasing uniaxial pressure is observed in a shift to lower temperatures of the transition signatures discussed above.

Typical ac-susceptibility values for the skyrmion lattice as a function of temperature and external magnetic field are shown in figure 4.16 (a) and (b), respectively, where the region of the skyrmion phase is filled gray. Note that the temperature scale has been changed to relative values with respect to the transition to the intermediate regime T_{A2} to readily compare the obtained data at different values of uniaxial stress. Taking into consideration that the curves have been shifted to improve visibility, as a reference point it is noted that the values of χ_{ac} for $T - T_{A2}$ below 1 K are the same for all pressures, i. e., the susceptibility of the conical phase remains unchanged. At ambient pressure a sharp dip into the reduced value of the susceptibility of the skyrmion lattice is observed. With increasing uniaxial pressure the sharp transitions becomes smoother and the value of the susceptibility of the skyrmion lattice increases, at the maximum pressure measured $\sigma = 1.1$ kbar the signature of the skyrmion phase in the susceptibility its reduces to a small smooth decline just below the transition to the intermediate regime.

As a function of the external magnetic field, the susceptibility curves around the skyrmion phase look very similar to the temperature dependence. At ambient pressure, the susceptibility decreases from the conical value to the skyrmion phase, B_{A1}, and increases again as the

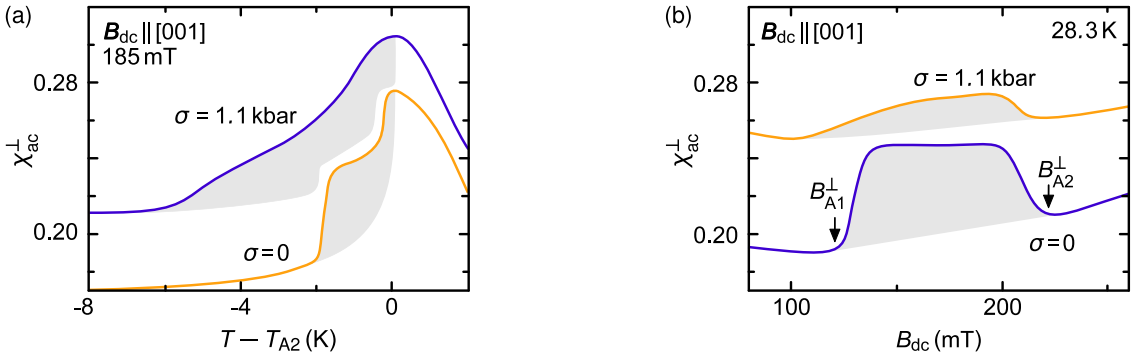

Figure 4.17: (a), (b)$\chi^{\perp}_{ac}$ around the skyrmion lattice phase for $\boldsymbol{B}_{dc} \perp \sigma$ as function of temperature and magnetic field, respectively. The signature of the skyrmion lattice at ambient pressure consists of an enhanced magnetic susceptibility. Uniaxial stress smooths the transitions, probably due to homogeneities in the pressure distribution. As a function of temperature, a dramatic expansion of the skyrmion lattice phase is observed. The stability enhancement as a function of the magnetic field is less pronounced.

systems transitions to the conical phase at higher magnetic fields, B_{A2}. Increasing uniaxial stress results in a smoother transition between conical and skyrmion phase and an increment of the susceptibility within the latter. The value of the transition does not change much as a function of uniaxial stress. The main effect is a change of the absolute value of χ_{ac}, and at the maximum pressure measured $\sigma = 1.1\,\mathrm{kbar}$ a very shallow valley in the ac-susceptibility as a function of B_{dc} signalizes the skyrmion phase. Note that the skyrmion phase has its largest region in magnetic field just below T_{A2} and the data shown in figure 4.16 (b) were all recorded at $T = 28.3\,\mathrm{K}$. The reduction in the transition temperature with increasing uniaxial pressure means that the measurement at $\sigma = 1.1\,\mathrm{kbar}$ is closer to the transition to the intermediate regime as the one measured at ambient pressure.

In the case of external magnetic fields applied perpendicular to the uniaxial stress axis, the excitation field $\boldsymbol{B}_{ac}$ is also perpendicular to $\boldsymbol{B}_{dc}$, thus the recorded response will be denoted $\chi^{\perp}_{ac}$ to avoid confusion. At ambient pressures and deep within the conical phase, $\chi^{\perp}_{ac}$ is sensitive to the perpendicular component of the magnetic susceptibility $\chi_{\perp}$, cf. chapter 3. As a function of field an temperature $\chi^{\perp}_{ac}$ maps a different component of the magnetic susceptibility in comparison with χ_{ac}.

Figure 4.17 (a) and (b) depict typical data of χ_{ac} in the vicinity of the skyrmion phase as a function of temperature and external magnetic field, respectively. At ambient pressures and starting from low temperatures warming up the sample at $B_{dc} = 185\,\mathrm{mT}$ leads to a smooth increase in $\chi^{\perp}_{ac}$ until the transition to the skyrmion lattice is reached, associated with a sharp rise of the susceptibility. Within the skyrmion phase, the susceptibility increases smoothly again with increasing temperature until the next transition to the intermediate regime is reached, also associated with a sharp increment of $\chi^{\perp}_{ac}$. At finite uniaxial stress, the sharp signatures in $\chi^{\perp}_{ac}$ are smoothed out, and the region of the skyrmion lattice expands greatly, in accordance with the observations made in small-angle neutron scattering.

For $\chi^{\perp}_{ac}$ as a function of the magnetic field, the skyrmion phase is denoted by a plateau of higher value in comparison to the conical phase. The gray filled region relates to the skyrmion lattice, and the boundaries are denoted B_{A1} and B_{A2}. Applying uniaxial pressure leads to a smoother signature of the skyrmion lattice in $\chi^{\perp}_{ac}$. At the same time, the value of the susceptibility of the conical phase increases, reducing the absolute difference between the skyrmion lattice and the conical phase. Regardless of the specific magnetic phase, $\chi^{\perp}_{ac}$

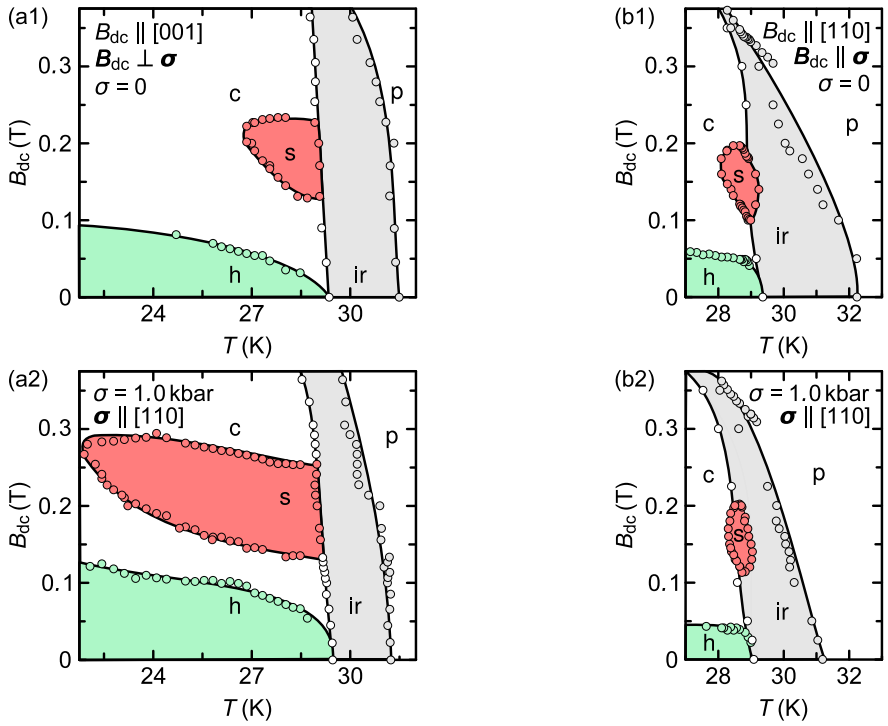

Figure 4.18: Magnetic phase diagram of MnSi. (a1) Magnetic phase diagram at ambient pressure for $\boldsymbol{B}_{dc} \parallel [001]$. The skyrmion lattice is stable at temperatures above ~ 27 K. (a2) A uniaxial pressure of $\sigma = 1.0$ kbar applied perpendicular to the magnetic field results in a substantial expansion of the skyrmion stability region. It survives down to temperatures around 22 K and shifts to larger magnetic fields with decreasing temperature. (b1), (b2) Comparison of the magnetic phase diagrams for $\sigma \parallel \boldsymbol{B}_{dc}$. At ambient pressure the skyrmion lattice is observable between 28 K and just above 29 K. The high temperature end of the skyrmion lattice phase is surrounded by the intermediate regime. Upon application of a uniaxial pressure $\sigma = 1.0$ kbar, the phase region shrinks, and it is almost completely embedded in the intermediate regime.

increases sharply just below the transition to the intermediate regime. The susceptibility enhancement in the conical phase originates in the suppression of the magnetic order as a function of temperature under pressure.

The magnetic susceptibility was measured for a large range of temperatures and magnetic fields. The critical values that defined the phase transitions are compiled in phase diagrams shown in figure 4.18. The main aspect that defines the effects of uniaxial pressure on the magnetic order of MnSi is its relation to the field direction, i. e., parallel or perpendicular to the latter. The left column shows the magnetic phase diagram for an experimental configuration with $\sigma \perp \boldsymbol{B}_{dc}$. At ambient pressure the skyrmion lattice is stable for temperatures above 27 K and below $\sim$ 29 K. As it concerns the magnetic field, skyrmions are observed between $\sim$ 140 mT and $\sim$ 225 mT. The transition from the helical to the conical phase takes place around 100 mT at low temperatures. Uniaxial stress perpendicular to the magnetic field expands the region of the skyrmion lattice phase substantially. For $\sigma = 1.0$ kbar skyrmions are stable down to $\sim$ 22 K and up to magnetic fields around $\sim$ 300 mT.

In contrast, uniaxial pressure parallel to the external magnetic field results in a suppression of the skyrmion lattice phase in favor of the conical magnetic order. At ambient pressures and for magnetic fields applied along the $[110]$ axis of the system, the skyrmion lattice phase encompasses the region between $\sim$ 28 K and $\sim$ 29.5 K, and from $\sim$ 100 mT to $\sim$ 200 mT. The

high-temperature limit of this phase is embedded in the intermediate regime. As discussed above, the application of uniaxial pressure suppresses the signatures of the skyrmion lattice phase in the magnetic susceptibility. The whole phase shrinks strongly in temperature, and shifts so that it is embedded completely in the intermediate regime. Note that these phase diagrams are taken from bulk measurements, it is possible that the skyrmion lattice has been almost completely suppressed at this point.

The high sensitivity of the skyrmion lattice to external elastic contributions opens an avenue of control and design of devices that exploit anisotropies to obtain the desired magnetic order. Furthermore, MnSi is a very well understood system. Hence it is ideal for the study of new phenomena. The enhanced stability of the helical modulation for pressures applied parallel to a $\langle 111 \rangle$ axis, should result in the stabilization of a soliton lattice in the presence of a magnetic field applied perpendicular to the axis of propagation. In the latter case, it is also of interest to study the competition between the skyrmion lattice and the helical propagation, which should arise at high pressures and intermediate magnetic fields. The information gained from such studies should help substantially to understand the magnetic order observed in epitaxially grown films, where a helical propagation constrained to the out-of-plane direction has been observed, and discrete changes in the helix pitch develop under a magnetic field applied in-plane.

5

INDEPENDENT SKYRMION PHASES IN A CHIRAL MAGNET

Skyrmion lattices couple very efficiently to external drivers such as strain and electric fields, which allow the manipulation of the phase boundaries in B/T phase diagrams or the metastable preparation of skyrmion lattices outside of their thermodynamic phase region through supercooling [123, 133, 134]. In the case of stress, a uniaxial anisotropy analogous to the one induced naturally in lacunar spinels, such as GaV_4S_8 and GaV_4Se_8, is introduced. In the latter, a Jahn-Teller distortion stretches the cubic unit cells along the space-diagonal into rhombohedral structures reducing the symmetry and resulting in a variate phase diagram, including a Néel type skyrmion phase [122, 135]. As a reminder, in B20 compounds MnSi, $Fe_{1-x}Co_xSi$, $Mn_{1-x}Co_xSi$, and FeGe, thermal fluctuations stabilize the skyrmions closed to the helimagnetic to the paramagnetic transition temperature. Skyrmions also profit from surface energies in systems with reduced dimensionalities, such as thin films and heterostructures.

The wide variety of paths leading to skyrmion lattices allow for the expectation that different stabilization mechanisms might lead to the observation of independent skyrmion lattices within the same system. This chapter discusses the recently published discovery of a second independent skyrmion lattice phase stabilized by standard cubic magnetic anisotropic contributions in the chiral cubic magnet Cu_2OSeO_3 using small-angle neutron scattering (SANS) [136]. The new phase develops at low temperatures and relatively high magnetic fields. Previous studies had reported hysteretic effects in this regime of the phase diagram whose origin remained unexplained [137, 138]. Before the publication of this study, Qian *et al.* reported the observation of the so-called tilted conical phase together with a mean-field analysis claiming it to be the ground state of the system [139]. The minimization of the free energy of the appropriate Ginzburg-Landau model taking skyrmions into account identifies the tilted conical phase as a metastable phase only.

The chapter is organized as follows: the first section 5.1 gives a brief introduction to the new phases, consisting of their scattering pattern and real space depiction. The following section, 5.2, discusses the characterization of both new phases and their corresponding correlations lengths. Section 5.3 presents the mapping of the magnetic phase diagram, separated, due to hysteretic effects, in temperature 5.3 and magnetic field 5.3 scans. Section 5.4 gives a theoretical description in the frame of a Ginzburg-Landau model, and the chapter concludes with a small summary of the most important aspects 5.5.

5.1 MAGNETIC PHASES IN CU_2OSEO_3

As discussed in the previous chapter, one of the main advantages of using small-angle neutron scattering (SANS) in the study of chiral magnets is its high sensitivity to each specific phase. Other techniques such as magnetization or susceptibility measure an averaged response of the whole sample. Thus, the coexistence of multiple phases is masked. In contrast, in SANS, the signals of different magnetic orders do not tend to overlap and allow their identification even when constrained to small sample volumes easily.

Typically, chiral magnets present four distinct magnetic phases below the magnetic ordering temperature, the helical, the conical, the skyrmion lattice and the field polarized phase, cf. Fig. 3.1. The previous chapters focused on the helical magnetic order and skyrmion lattices

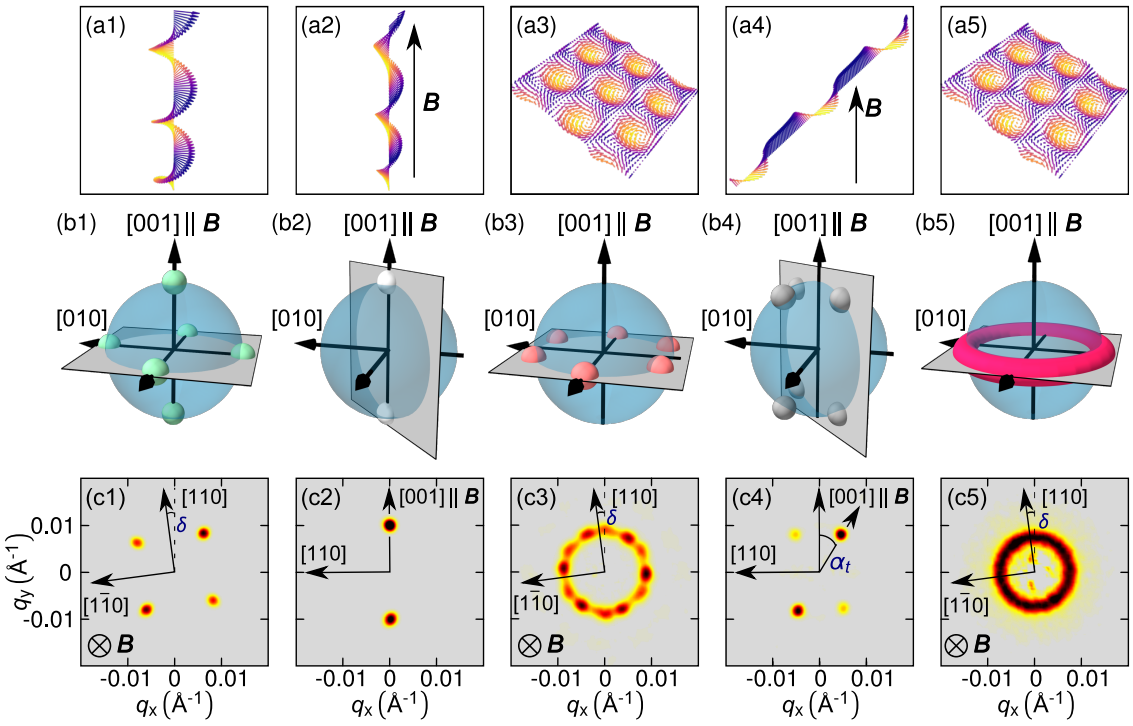

Figure 5.1: Summary of key characteristics of the different magnetic phases in Cu_2OSeO_3 for $\boldsymbol{B} \parallel [001]$ in the following order: helical, conical, high-temperature skyrmion, tilted conical, and low-temperature skyrmion phase. The first row shows a schematic representation of the real space magnetic configuration. The second row shows the resulting Bragg peaks while taking into consideration possible multiple domains. In each depiction, the solid spheres represent the position of the different Bragg peaks, while the grey plane represents the section of the Ewald sphere. The intersection of the latter with the Bragg peaks result in the scattering patterns show in the third row measurable with SANS.

in MnSi, before introducing the new phases identified in Cu_2OSeO_3 the following paragraphs revisit the basic details of helical, skyrmion lattice, and conical phase. In the helical phase, the spins rotate around the propagation vector $\boldsymbol{Q}$ with an aperture angle of or close to 90°. The direction of $\boldsymbol{Q}$ is defined by the magnetocrystalline and exchange anisotropy [83], cf. Fig. 5.1 (a1). In the case of Cu_2OSeO_3, the magnetic helices propagate along the crystallographic $\langle 100 \rangle$ axes resulting in three distinct domains. These translate into six Bragg peaks in reciprocal space illustrated as green spheres in figure 5.1 (b1). These Bragg peaks are observable if the Ewald sphere defined by the wavevector of the incoming neutrons $\boldsymbol{k}$ intersects them. In SANS $|\boldsymbol{k}| \gg |\boldsymbol{Q}|$, thus the section of the Ewald sphere which intersects the Bragg peaks is approximately flat, shown in gray in figure 5.1 (b1). The geometry illustrated belongs to a neutron beam parallel to $[001]$ which yields the scattering pattern shown in figure 5.1 (c1), the angle δ indicates a misalignment of the crystallographic $[110]$ axis from the sample's vertical rotation axis.

Figure 5.1 (a2) shows the real space spin configuration of the conical phase. The magnetic phase consists of a single domain with propagation vector $\boldsymbol{Q}$ parallel to the magnetic field, and the aperture angle of the spins with respect to the propagation vector decreases continuously with increasing magnetic field. In this study, the magnetic field $\boldsymbol{B}$ was applied along $[001]$. The transition between to helical and conical phase is discontinuous. The domains propagating perpendicular to the magnetic field are depopulated in favor of the one parallel to $\boldsymbol{B}$. As it is single domain with only one $\boldsymbol{Q}$ propagation vector, it translates into two

Bragg peaks as depicted schematically by white spheres in figure 5.1 (b2). An example of the scattering pattern of the conical phase is shown in figure 5.1 (c2).

The skyrmion lattice in Cu_2OSeO_3 can be described as an ensemble of particles, i. e., skyrmions, which ordered densely resulting in a hexagonal arrangement perpendicular to the magnetic field $\boldsymbol{B}$, cf. Fig. 5.1 (a3). This periodic arrangement translates in reciprocal space to six Bragg peaks at the same distance from the direct beam separated by $60°$ steps, rotated by $30°$ concerning the real space configuration. One of the Bragg peaks pairs lies along a $\langle 100 \rangle$ crystallographic axis, schematically shown in figure 5.1 (b3) as orange spheres. As mentioned above, $\boldsymbol{B}$ points along $[001]$. Thus the plane in which the Bragg peaks of the skyrmion lattice lies contains both the $[100]$ and the $[010]$ axes. Since both of these are energetically equal, two domains of skyrmion lattices can be observed, resulting in a scattering pattern with twelve maxima, as shown in figure 5.1 (c3).

In Cu_2OSeO_3 cubic magnetocrystalline contributions result in two new phases in the low temperature and high magnetic field region of the magnetic phase diagram when the field points along an easy axis. The first phase is labeled the tilted conical phase, due to its scattering pattern. While the name seems to refer to a usual conical phase propagating away from the magnetic field direction, the real space configuration of the magnetic spins is more complex. Over a wide range of the modulation, the spins point primarily parallel to the magnetic field, thus increasing the homogeneous magnetization in field direction, and then rotate over a small region within a plane almost completely perpendicular to $\boldsymbol{B}$, cf. Fig. 5.1 (a4). Due to the symmetry of the system, the magnetic order can tilt in four equivalent directions allowing for different domains to coexist. Thus the schematic representation of the reciprocal space in figure 5.1 (b4) includes a total of eight Bragg peaks (grey spheres) from which four can be measured simultaneously resulting in the scattering pattern shown in figure 5.1 (c4) with the angle α_t denoting the deviation of the propagation vector from the magnetic field.

The second phase only observed for this magnetic field direction is referred to as the low-temperature skyrmion phase (LT-Sky). The spin configuration of a single skyrmion in real space is the same as for the high-temperature skyrmion lattice (HT-Sky). In addition to the hexagonal configuration associated with the latter, the LT-Sky can order in a square lattice. According to the theoretical analysis presented below, both configurations have almost the same free energy resulting in a competition which leads to a ring of intensity as its scattering pattern, cf. Fig. 5.1 (c5). It is possible to prepare the LT-Sky phase in a well-ordered state showing a six-fold pattern. Further, the $\langle 100 \rangle$ axis the field was applied along defines the plane spanned by the propagation vectors of the low-temperature skyrmion lattice phase. Upon rotations of the magnetic field direction, the skyrmion lattice phase remains fixed, maintaining its propagation vectors perpendicular to the original $\langle 100 \rangle$ axis. In contrast, the high-temperature skyrmion lattice follows the magnetic field direction very well [132, 140]. The phase boundaries are highly hysteretic, and it is possible to expand the phase region of the LT-Sky to cover almost the entire phase diagram. The following section addresses these aspects further.

5.2 CHARACTERIZATION OF THE MAGNETIC PHASES

The sample chosen for this study was carefully polished to a spherical shape with a diameter of $2\,\mathrm{mm}$, as shown in figure 5.2 (a). Diffraction measurements performed at the instrument HEIDI at the MLZ confirmed its excellent single crystallinity and Laue x-ray diffraction was used to orient the sample which was then mounted on an Al sample holder using GE varnish.

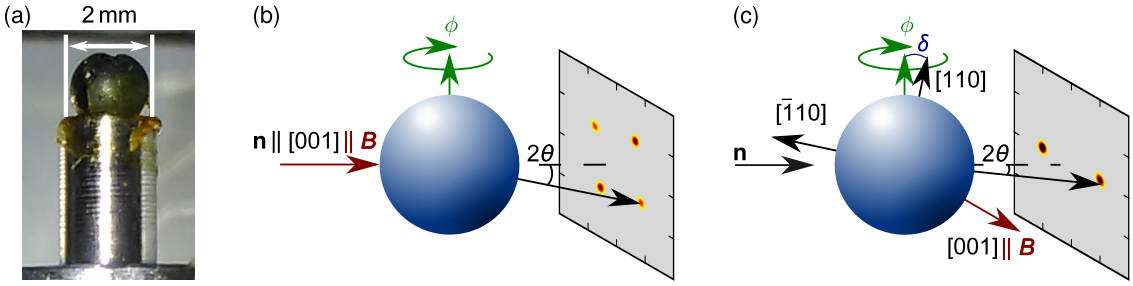

Figure 5.2: (a) Cu_2OSeO_3 spherical sample used in the experiments. (b) Experimental configuration with the magnetic field $\boldsymbol{B}$ parallel to the neutron beam $\boldsymbol{n}$. The angle ϕ determines the crystallographic axis that $\boldsymbol{B}$ is applied along. For $\boldsymbol{n} \parallel [001]$ this setup allows measuring the signal, of the helical, high temperature and low-temperature skyrmion phases. (c) Experimental setup with $\boldsymbol{B} \perp \boldsymbol{n}$. The signal of the conical and tilted conical phases, as well as part of the signature of the skyrmion lattices, can be measured in this setup.

A closed-cycle cryostat (CCR) was used to control the sample temperature, and the magnetic field originated from a 5 T superconducting magnet. The temperature of the sample was determined using a Cernox sensor placed in its close vicinity. The experiments were carried out at the beamline SANS-1 at the MLZ [88].

The magnetic helices in Cu_2OSeO_3 have a wavelength of $\sim$ 600 Å thus a neutron wavelength of $\lambda = 7$ Å was selected, with a FWHM wavelength spread of 10 % originating from the neutron selector. The neutron beam was collimated over a distance of 20 m with a beam diameter of 50 mm at the entry of the collimation and a pinhole sample aperture with a diameter of 4 mm located 350 mm in front of the sample. Scattered neutrons were then recorded using an area-sensitive detector of $1 \times 1\,\mathrm{m}^2$ consisting of 128 ^{3}He tubes resulting a spatial resolution of $8 \times 8\,\mathrm{mm}^2$. The distance between the sample and the detector was 20 m. The setup included two vertical rotation axis. The first defined the orientation of the magnetic field relative to the sample, by rotating the latter by angle ϕ, cf. Fig. 5.2 (b). The second one is used for rocking scans measurements, in which both sample and magnetic field are rotated together by angle ω relative to the incoming neutron beam, cf. Fig. 5.6 (a). This setup maintains a high neutron flux while the scattering condition yields Bragg peaks far enough of the direct beam to be resolved accurately. Specifically the radial resolution was $\Delta|\boldsymbol{q}| = 0.0011\,\text{Å}^{-1}$ while the resolution of the azimuthal and rocking angle were $\Delta\alpha = 6°$ and $\Delta\omega = 0.14°$ respectively. All phases could be measured using two different basic setups with the magnetic field either parallel or perpendicular to the incoming neutron beam, shown in figure 5.2 (b) and (c), respectively.

Propagation of tilted conical phase

Both new phases were initially characterized through rocking scans measured at different values of magnetic field and temperature. As shown in figure 5.3 the magnetic order of the tilted conical phase is not defined by a specific easy axis of propagation, as is the case in the helical phase. Instead, its orientation, as defined by the angle α_t, which changes continuously with the magnetic field strength and the temperature (note that the error bars represent the full width at half maximum of the intensity peak as a function of azimuthal angle). The observed propagation direction does not evidence a strong hysteresis between increasing and decreasing fields, as demonstrated by the comparison of the dependence on the magnetic field of α_t, for a sample cooled in zero-field (ZFC) and high-fields (HFC) well within the

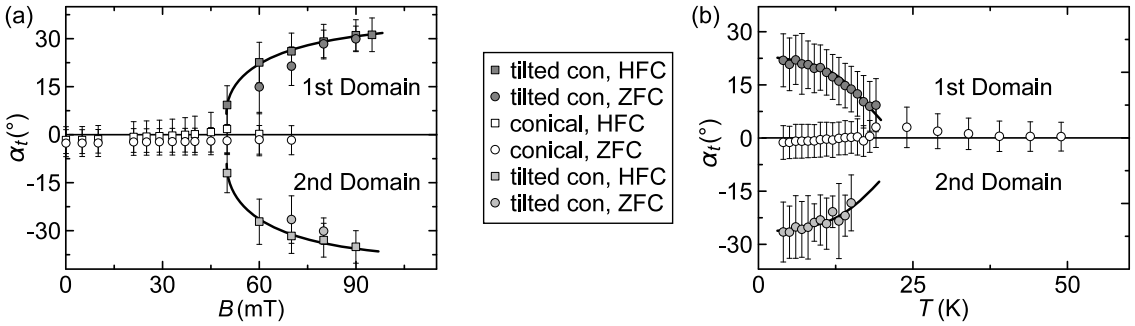

Figure 5.3: Azimuthal angle α_t enclosed by the propagation vector $\boldsymbol{Q}$ of the tilted conical and conical phases with the magnetic field $\boldsymbol{B}$. (a) As a function of the magnetic field, the tilted conical phase can be resolved between $\sim$ 50 mT and 90 mT. Its' deviation from $\boldsymbol{B}$ increases smoothly with increasing fields, and there is no hysteresis between increasing (ZFC) and decreasing (HFC) amplitudes, $|\boldsymbol{B}|$. (b) Temperature dependence of α_t obtained while heating the sample. Similar to the magnetic field dependence, the propagation of the tilted conical phase rotates smoothly towards the field with increasing temperature. All error bars shown represent the full width at half maximum of the intensity distribution over the azimuthal angle.

field polarized region, in figure 5.3 (a). Notice that the value of α_t related to the conical phase tends to increase close to the transition from the tilted conical phase, i. e., in high-field cooled measurements in 5.3 (a) (in (b) the transition shown is also from tilted conical to conical). This increment might be an artifact of the analysis arising from a superposition of the Bragg peaks of both phases, which could not be decomposed with the resolution of the detector used. Hence, vestigial domains of tilted conical phase appear to survived down to $\sim$ 45 mT and up to $\sim$ 40 K for the temperature versus field histories presented in figure 5.3. It is also possible for the conical phase to propagate with a small deviation to the external magnetic field due to demagnetization and other internal effects. Because of this uncertainty, the observation of a distinct additional Bragg peak defined the boundary between conical and tilted conical phase.

Correlations of tilted conical phase and low temperature skyrmion lattice

The intensity distribution as a function of azimuthal angle α, rocking angle ω and momentum transfer $|\boldsymbol{q}|$ provide insight into microscopic details of each phase. The interpretation of the first two depends on the experimental configuration used, and the latter provides information on typical length scales. Figure 5.4 contains the intensity distributions as a function of these three parameters for the tilted conical phase (top row) and the low-temperature skyrmion lattice (bottom row). Especially interesting is the width of the peaks shown, which indicates the distribution of domains with respect to the given parameter. For reference, the instrument resolution is shown as a colored area. The resolution of the rocking angle is so small that it reduces to a line. Consequently, it was omitted.

Figure 5.4 (a1) shows the intensity distribution as a function of azimuthal angle for the tilted conical phase. The magnetic field is applied perpendicular to the neutron beam which is parallel to a $\langle 110 \rangle$ axis. The plot represents the distribution of directions the magnetic domains point to within the (110) plane. The full width at half maximum (FWHM) is the same as observed for the conical and helical phases. Consequently, the magnetic mosaicity remains constant. The intensity as a function of rocking angle ω is in contrast very wide, cf.

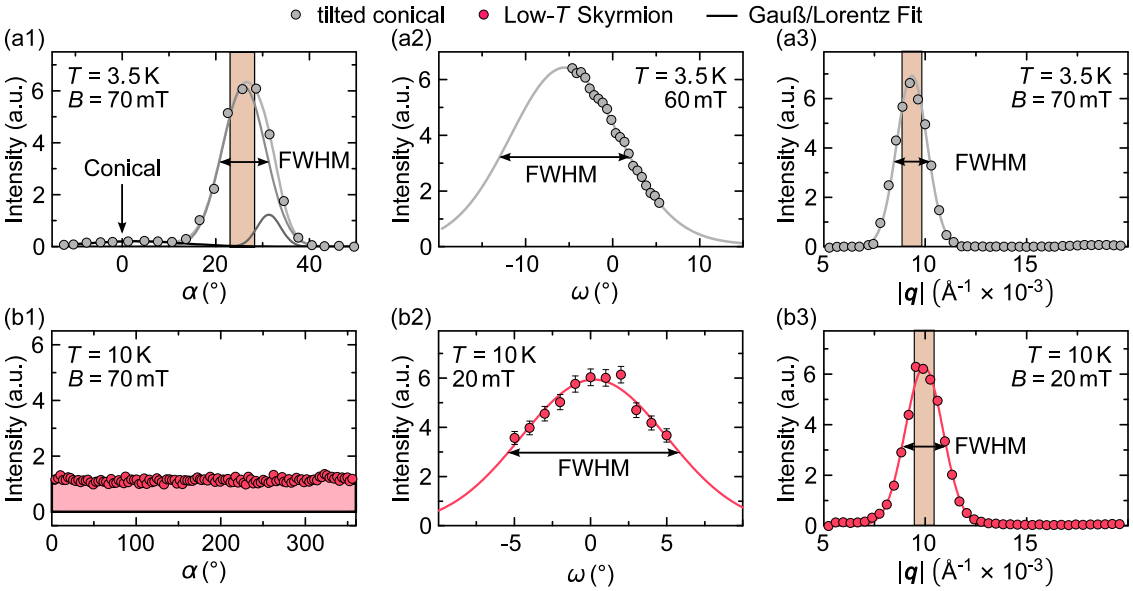

Figure 5.4: Intensity distribution of the tilted conical phase (first row) and the low-temperature skyrmion lattice (second row) as a function of azimuthal angle α (first column), of rocking angle ω (second column) and of reciprocal length $|\boldsymbol{q}|$. Each of this curves represents a cut through the Bragg peak (Ring) along the given dimension, except in the case of the azimuthal intensity distribution of the LT-Sky phase, where the homogenous intensity ring results in a flat distribution.

Fig. 5.4 (a2). The domains prefer to propagate in the plane spanned by the $[001]$ and $[110]$ crystallographic axes, as indicated by the peak maximum, consistent with a rotation towards a $[111]$ axis. The large FWHM indicates that the exact propagation direction is not associated with a significant energy gain. The domains gain energy by interacting with defects and take a small penalty for propagating in a slightly different direction. The intensity distribution as a function of momentum transfer $|\boldsymbol{q}|$ is consistent with those measured for the conical, helical, and high-temperature skyrmion lattice, cf. Fig. 5.4 (a3). All show a full width at half maximum of $\sim 0.0015\,\text{Å}^{-1}$, indicating that the correlation vanishes at lengths of a few µm independent of the phase.

As mentioned above the typical observation of the low-temperature skyrmion lattice lacks the six-fold pattern related to the HT-Sky phase. Instead, the intensity plot as a function of azimuthal angle α illustrated in figure 5.4 (b1), describing the order of the skyrmion lattice in the plane perpendicular to the magnetic field, is flat. The lack of maxima means that the magnetic domains are distributed equally over a range of 60°. Note that the data shown were obtained at $B = 70\,\text{mT}$ to avoid mixture with the intensity signatures from other phases. The distribution as a function of rocking angle is very wide, implying that several skyrmion lattice domains are described by propagation vectors which are not perpendicular to the magnetic field direction, cf. Fig. 5.4 (b2). The function remains centered around 0° hence the lowest energy for a skyrmion domain is still achieved propagating perpendicular to the magnetic field. It was mentioned above and will be discussed further below that the low-temperature skyrmion lattice plane is not defined by the magnetic field direction but rather by the $[001]$ crystallographic axis, the former was applied along. The full width at half maximum of the intensity peak as a function of momentum transferred $|\boldsymbol{q}|$ is slightly larger then than one observed for the other magnetic phases when specifically comparing the sharpest distribution

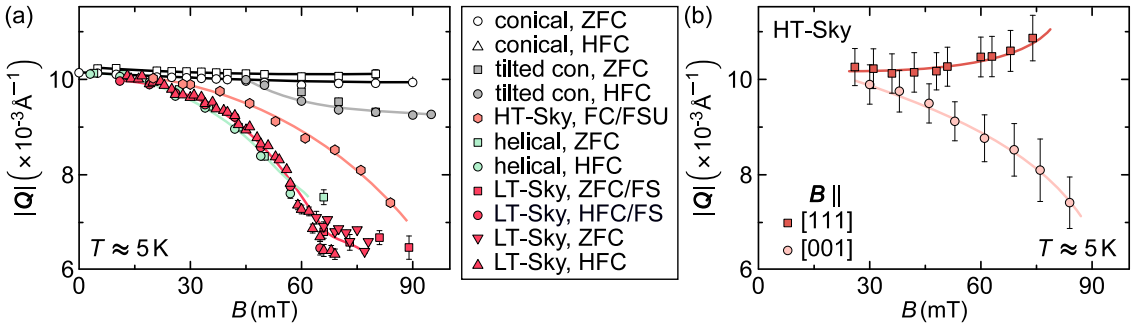

Figure 5.5: (a) Propagation length $|\boldsymbol{Q}|$ as a function of magnetic field for the different magnetic phases in Cu_2OSeO_3. Magnetic order described by propagation vectors perpendicular to the magnetic field $\boldsymbol{B}$ show a strong dependence on the latter and the propagation length decreases strongly as the magnetic field increases. In contrast, the conical and tilted conical phases show almost no dependence on $|\boldsymbol{B}|$. Note that there is no hysteresis between different measurement protocols, refer to text for details. (b) Comparison of the propagation length of the skyrmion lattice for fields parallel to a $\langle 111 \rangle$ (squares) and $\langle 100 \rangle$ crystallographic axes as a function of the magnetic field. The markedly different behavior indicates the anisotropic origin of the field dependence.

measured for each phase. For the LT-Sky phase, this is the case at the low magnetic field phase boundary. Therefore the data was obtained at $B = 20\,\mathrm{mT}$, cf. Fig. 5.4 (b3).

Propagation length as a function of magnetic field amplitude

The broader distribution in $I(|\boldsymbol{q}|)$ for the low-temperature skyrmion lattice may be explained as a consequence of demagnetization and anisotropic effects on the correlation length $\boldsymbol{Q}$. As is shown in figure 5.5 (a) the propagation length of the different magnetic phases is $|\boldsymbol{Q}| = 0.01\,\text{Å}^{-1}$ at low fields, but it responds differently to changes in magnetic field amplitude $|\boldsymbol{B}|$. In essence, two groups can be distinguished, characterized by the direction of the propagation vectors concerning the applied magnetic field. On the one hand, the phases with a large component of $\boldsymbol{Q}$ parallel to $\boldsymbol{B}$ show only a small change in $|\boldsymbol{Q}|(B)$, i. e., less than 10% for the tilted conical phase. On the other hand, magnetic phases propagating perpendicular to $\boldsymbol{B}$ show a reduction larger than 30% in the length of their propagation vector $\boldsymbol{Q}$ with increasing magnetic field amplitude. The helical and low-temperature skyrmion phases show the same dependence on $|\boldsymbol{B}|$, while the rate of change in $|\boldsymbol{Q}(B)|$ of the high-temperature skyrmion lattices is lower. Note that different temperature vs. magnetic field protocols were followed to obtain the broadest magnetic field range for each phase, and that there are no substantial differences between the different measurement protocols. Consequently, the slightly broader intensity distribution for the LT-Sky phase can be explained by demagnetization effects on the sample leading to a mixture of domains with different $|\boldsymbol{Q}|$.

A comparison with data measured on the high temperature skyrmion phase for $\boldsymbol{B} \parallel \langle 111 \rangle$ following the same measurement protocol demonstrates that the dependence of $|\boldsymbol{Q}|$ on the applied magnetic field is indeed anisotropic in nature, as in contrast to the case of $\boldsymbol{B} \parallel \langle 100 \rangle$ the scattering length increases slightly with increasing fields. The stronger effects observed for an easy axis magnetic field also lead to an increment in the peak width illustrated as the error bars in figure 5.5 (b).

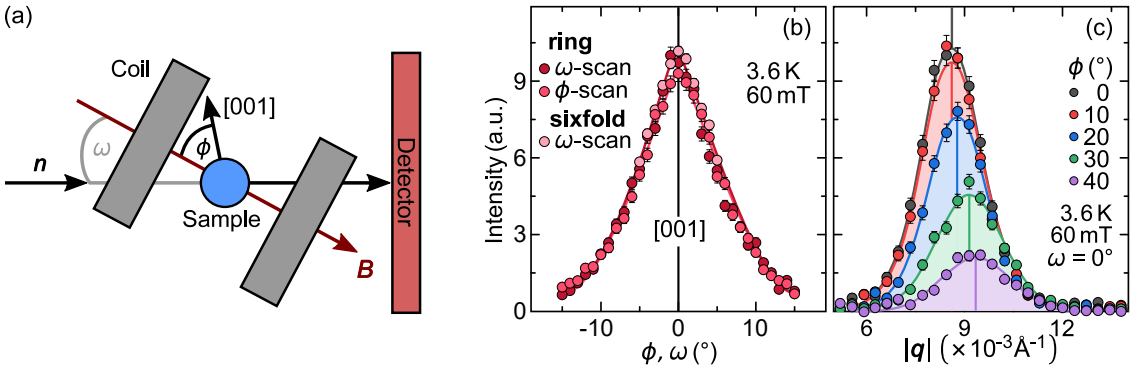

Figure 5.6: (a) View of the experimental setup from above detailing the two rotation axes available. The angle ϕ defines the direction of the magnetic field concerning a $[001]$ crystallographic axis, while ω denotes the angle of the magnetic field $\boldsymbol{B}$ and the sample with respect to the incoming neutron beam $\boldsymbol{n}$. (b) Intensity as a function of ϕ and ω (during a scan over one parameter the other remains constant). As both distributions match exactly, the skyrmion lattice plane is perpendicular to the $[001]$ axis instead of the magnetic field. (c) Intensity distribution over the reciprocal length $|\boldsymbol{q}|$ for different angles of ϕ. The shift of the peak center to larger values of $|\boldsymbol{q}|$ indicates that the skyrmion lattice in mostly sensitive to the component of $\boldsymbol{B}$ parallel to $[001]$.

Orientation of the low temperature skyrmion lattice with respect to the magnetic field

One of the aspects the has attracted much interest in skyrmion lattices is their very efficient manipulation using electrical currents. Magnetic skyrmions can be driven with very low current densities [15], a consequence, in part, of the weak coupling to the underlying crystal lattice. Except for the lacunar spinels, bulk skyrmion hosting samples show an isotropic skyrmion phase, in the sense that the direction of the magnetic field has only minor effects on its stability, i. e., the size of the phase pocket in the B/T phase diagram [11, 90, 122, 141]. Regarding the effects on the orientation and propagation of the skyrmion phase, a recent study reviewing in detail the skyrmion lattice in MnSi for fields applied along different crystallographic directions established that the plane spanned by its propagation vectors lies always perpendicular to the applied magnetic field except for corrections in the order of a few degrees $\sim 3°$ due to cubic magnetocrystalline anisotropies. Adams *et al.* reset the magnetic order by heating the sample over the transition temperature before each change of field direction to avoid hysteretical effects due to magnetic pinning centers. Mühlbauer *et al.* studied the effects of pinning centers on the motion of the skyrmion lattice driven by the magnetic field direction using time-dependent small-angle neutron scattering (TISANE) [140]. Similar to the current-driven motion of the skyrmion lattice, Mühlbauer observes a smooth motion following the magnetic field above a certain threshold angle of deviation. TISANE experiments on Cu_2OSeO_3 show the same behavior for the high-temperature skyrmion lattice in this material. Hence, generally, the skyrmion lattice can be described as independent of the crystal lattice.

Not surprisingly, the low-temperature skyrmion phase in Cu_2OSeO_3 does not exhibit the aforementioned isotropic characteristic. Instead, it is only observable for fields close to a $\langle 100 \rangle$ crystallographic axis. As described above the experimental setup included a rotation axis connected only to the sample. Hence, it determines which crystallographic axis is parallel to $\boldsymbol{B}$ defined by the angle ϕ with respect to the crystallographic axis $[001]$. A second rotation axis is coupled to both sample and magnetic field to measure rocking scans under an applied field and is defined by an angle ω concerning the incoming neutron beam, cf. Fig. 5.6 (a). A

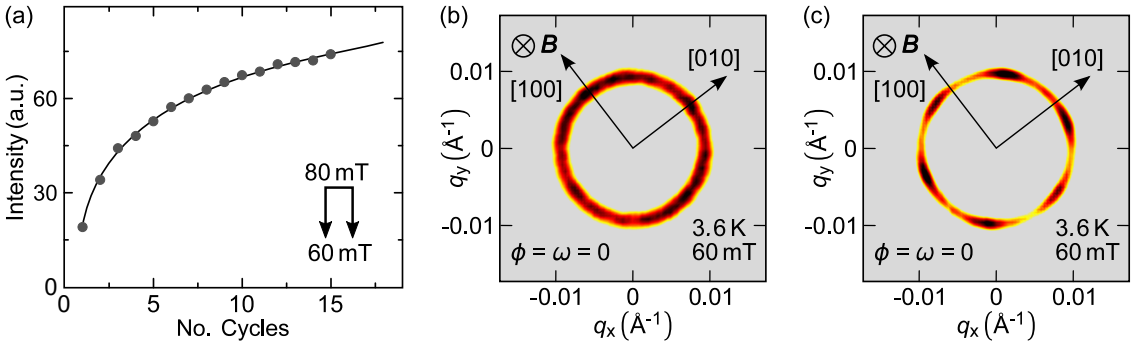

Figure 5.7: (a) Intensity as a function of number of cycles from 60 mT to 80 mT and back. With each cycle the intensity of scattered neutrons from low temperature skyrmion lattice increases. (b) Typical scattering pattern at $B = 60$ mT after rotating the sample by $\phi \sim 15°$ against the magnetic field and back a six-fold pattern develops (c) indicating the improvement of order in the skyrmion plane.

scan over the angle ϕ probes the effects of changing the field direction relative to the crystal. As plotted in figure 5.6 (b), the intensity distribution as a function of ϕ for fixed ω matches perfectly to the one obtained as a function of ω for fixed ϕ. The magnetic field direction does not affect the plane of the propagation vectors of the LT-Sky phase. These are instead constrained to the (001) plane. The low -temperature skyrmion phase is predominately sensitive to the component of the magnetic field along the $[001]$, as demonstrated by the intensity distribution as function of $|q|$, which shifts to larger values for increasing values of ϕ related to a smaller component along the main crystallographic axis, cf. Fig. 5.6 (c), reproducing the changes in $|Q|$ illustrated in figure 5.5 (a).

Before conducting the scan described above the sample was cooled in an applied field of 250 mT down to 3.6 K, cycling the magnetic field from 60 mT to 80 mT leads to an enhancement in the measured intensity from the low-temperature skyrmion lattice, cf. Fig. 5.7 (a), providing, thus, further evidence that the former is the ground state in this region of the magnetic phase diagram. Rotating the sample against the magnetic field also led to a reordering of the intensity distribution from a homogenous ring, shown in figure 5.7 (b), to a six-fold pattern consisting of broad Bragg peaks, illustrated in figure 5.7 (c). The well-ordered phase develops after a rotation of $\phi \sim 15°$, consistent with a lifting of the in-plane degeneracy trough a more significant component of the magnetic field lying in the (001) plane. An ω rocking scan taken after the six-fold pattern forms shows the same width as both the ϕ and ω scan discussed in the previous paragraph. Therefore, the reordering of the skyrmion lattices takes place only in the plane perpendicular to $\boldsymbol{B}$.

5.3 MAPPING OF THE MAGNETIC PHASE DIAGRAMS

It is possible to obtain all relevant information to characterize the different five magnetic phases using two different experimental setups. The first one, with the magnetic field $\boldsymbol{B}$ parallel to the incoming neutron beam $\boldsymbol{n}$, provides information on the helical phase and both high-temperature and low-temperature skyrmion phases. In the second experimental setup, the magnetic field points perpendicular to the incoming neutron beam. Consequently, both conical and tilted conical phase are observable. Note that due to the multiple domains in both skyrmion lattices part of their signal can be measured in the second experimental configuration as well. Both experimental setups are shown schematically in figure 5.2 (b) and (c)

respectively. The angle ϕ refers to the rotation axis discussed above. Note the deviation δ of the $[110]$ axis from the rotation axis, in an ideal experimental setup both of these axes would lay parallel to each other. Since the divergence of the magnetic field direction from the $[001]$ axis resulting from δ was approximately $1°$, it does not affect the results presented here.

The characterization of the magnetic structures was based on their behavior as a function of temperature and magnetic field. That can be done twofold by either keeping the magnetic field constant, while different temperature values are scanned known as a temperature scan, or keeping the temperature of the sample constant while recording the scattering patterns at different values of B also known as a magnetic field scan. Both temperature and magnetic field scans were performed as the results were strongly hysteretical.

Sample preparation before temperature dependent measurements

Data during temperature scans were recorded using three different protocols of temperature versus magnetic field depicted in figure 5.8, to investigate how the behavior of the sample depends on the starting state. All measurements started at a temperature of ~ 70 K well above the helimagnetic transition at $T_c \approx 57$ K, deep in the paramagnetic phase. The superconducting magnet was degaussed to minimize the amount of trapped flux following the same procedure before each new temperature scan. That is necessary because the critical fields are in the order of a few mT. Thus even small trapped flux may affect the measurements significantly.

Typically SANS experiments are carried out at a constant temperature and magnetic field. Scans over an external parameter are obtained by collections of discrete measurements at different values of the given parameter. In the case of temperature, for example, this means a chosen value is set, the cryostat regulates until it is sufficiently stable at the chosen temperature and scattered neutrons are recorded, then the procedure is followed again for the next measurement point. The relation between the heat capacity of the measuring system and the cooling power of the cryostat is complex and temperature-dependent. Smooth temperature control in different regions, ensuring a fast cooling and, more importantly, a fast stabilization at the set temperature requires careful tuning of the parameters controlling the cooling cycle. Best-case scenarios are typically associated with waiting times of several minutes between set points, sharply reducing the efficiency of the allocated time at the beamline. In the present case, the chosen material system,i. e., Cu_2OSeO_3, yields a strong signal to noise ratio in just a couple of seconds, making the process described above even more inefficient. Thus, data were recorded continuously. Once the scan began scattered neutrons were counted for a period of 5 s and the scattering pattern was then stored. The storing of the scattering patterns is associated with a dead time of 1 s. Thus data points were recorded every 6 s for the duration of the scan.

Since data is being recorded continuously, gradients in temperature present during the scan cannot be neglected. These were determined in a set of systematic control measurements cooling and heating the sample under different sweep rates. For the fastest sweep rate measured i. e., $8\,\mathrm{K\,min^{-1}}$ the gradients vanished at low temperatures and were as a high as a few % near ~ 60 K. Note that data recorded under a sweep rate of $2\,\mathrm{K\,min^{-1}}$ did not show any gradient. The temperature of the data shown below has been corrected to account for the temperature gradient where needed. The following temperature vs. field protocols were followed for temperature scans, see also figure 5.8:

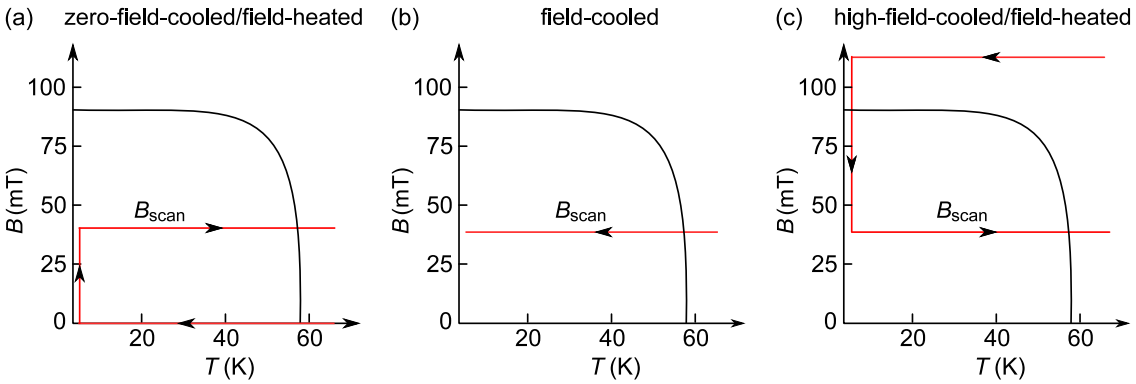

Figure 5.8: Schematic representation of the three different temperature versus magnetic field protocols followed to obtain data for temperature scans. (a) zero-field-cooled/field-heated (ZFC/FH): the sample is cooled down to the lowest temperature at zero magnetic field. At the lowest temperature the magnetic field magnitude is increased to B_{scan}. Data is recorded at B_{scan} while the sample is heated continuously. (b) field-cooled (FC): the magnetic field value is set to B_{scan} at a temperature well above the helimagnetic transition. Scattering patterns are recorded while cooling the sample continuously. (c) high-field-cooled/field-heated (HFC/FH): well above the helimagnetic transition the magnetic field value is increased well above the critical field B_{c2} of the conical to field polarized transition. The sample is cooled to the lowest temperature accessible. At the lowest temperature the magnetic field magnitude is set to B_{scan} and data is recorded while heating the sample continuously.

(a) **ZFC/FH**: Zero-field-cooled/field-heated, cf. Fig. 5.8 (a). Starting well above the helimagnetic transition, the sample is cooled in zero magnetic field at a rate of $8\,\mathrm{K\,min^{-1}}$ to the lowest temperature accessible $\sim$ 3.5 K. At the lowest temperature, the magnetic field magnitude is increased to the field value of interest B_{scan}. Scattered intensity is then recorded at B_{scan} while the sample is heated at a rate of $2\,\mathrm{K\,min^{-1}}$ up to 65 K. Each data point requires a total of 6 s. Thus it yields the average scattering intensity in a temperature region $\sim$ 200 mK. After the scan was finished the procedure to degaussed the magnet was started.

(b) **FC**: Field-cooled, cf. Fig. 5.8 (b). Starting well above the helimagnetic transition, the magnitude of the magnetic field is increased to the field value of interest B_{scan}. At B_{scan} scattered neutrons are recorded while the sample is cooled at a rate of $4\,\mathrm{K\,min^{-1}}$ ($\boldsymbol{B} \parallel \boldsymbol{n}$) or $6\,\mathrm{K\,min^{-1}}$ ($\boldsymbol{B} \perp \boldsymbol{n}$) down to 3.5 K. Each data point represents then the average of scattered intensity over a change of temperature of $\sim$ 400 mK or $\sim$ 600 mK . At the lowest temperature the superconducting magnet was degaussed and the sample heated up to $\sim$ 70 K.

(c) **HFC/FH**: High-field-cooled/field-heated, cf. Fig. 5.8 (c). Well above the helimagnetic transition temperature T_c, the magnetic field value is set at $B = 250$ mT well above the critical field for the transition from the conical to the field polarized phase. The sample is then cooled under a sweep rate of $8\,\mathrm{K\,min^{-1}}$ down to $\sim$ 3.5 K. At the lowest temperature, the field magnitude is decreased to the field value of interest B_{scan}. Scattering patterns are then recorded while the sample is continuously heated at a rate of $2\,\mathrm{K\,min^{-1}}$. Thus each data point represents the average scattered intensity over a temperature region $\sim$ 200 mK wide. Note that the superconducting magnet is not degaussed after each scan

for this protocol as 250 mT is well above any trapped magnetic flux and thus nullifies the effects of degaussing.

Typical data obtained from zero-field-cooled/field-heated scans

Typical scattering patterns obtained at $T = 3.5$ K after cooling the sample in zero-field are shown in figure 5.9 (a1) and (b1), for a magnetic field parallel $\boldsymbol{B}$ to the neutron beam $\boldsymbol{n}$ and for $\boldsymbol{B} \perp \boldsymbol{n}$, respectively. The scattering patterns include sectors which define the area over which the intensity is integrated for the different phases. Sectors 1 (solid green) on figure 5.9 (a1) are centered around the $[100]$ and $[010]$ crystallographic axes of the system. When the sample is prepared in zero-field, there is no coexistence of the helical domains with neither the high-temperature nor the low-temperature skyrmion phase. Therefore the intensity integrated over sectors 1 can be readily identified as the helical phase. If scattered neutrons are recorded

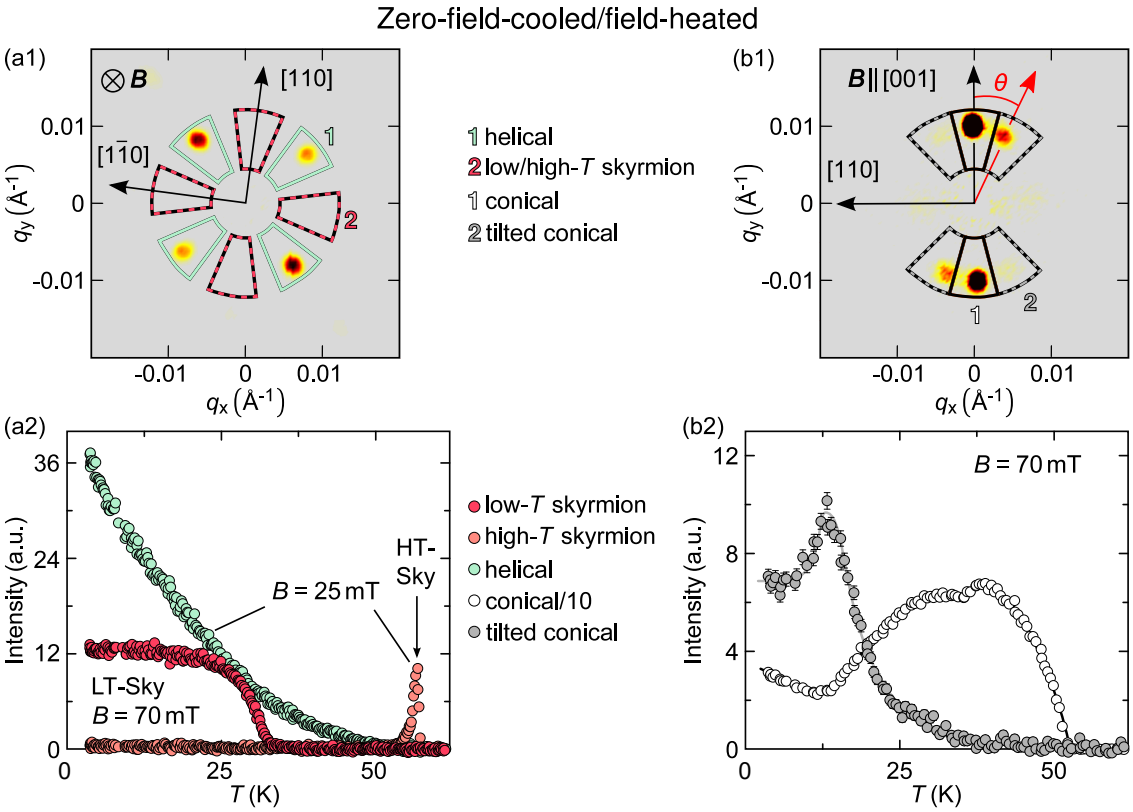

Figure 5.9: Typical scattering patterns and extracted intensity from small angle neutron scattering for ZFC/FH. (a1) Helical phase for $\boldsymbol{B} \parallel \boldsymbol{n}$. There is no coexistence of helical and skyrmion phases, thus no overlapping signal. Sector 1 (solid green) contains intensity scattered by the helical phase, while sector 2 (dashed red) is the region where intensity related to the LT- and HT-sky would be found. (a2) Temperature dependence of the intensity as obtained from the sectors shown in (a1) for the helical (green circles) and HT-sky (orange circles) phases at $B = 25$ mT and the LT-sky (red circles) at $B = 70$ mT. (b1) Conical and the tilted conical phase at higher magnetic fields for $\boldsymbol{B} \perp \boldsymbol{n}$. Sectors 1 (solid black) and 2 (dashed grey) correspond to the conical and tilted conical phase, respectively. Both phases coexist over a substantial portion of the phase diagram. (b2) Temperature dependence of the scattered intensity from the conical (white circles) and tilted conical (grey circles) phase at 70 mT. Note the increment in the tilted conical intensity up to ~ 12 K corresponding to a decrease in the conical intensity.

within the sectors 2 (dashed red) in this experimental configuration, it is always related to one of the skyrmion phases, regardless of the protocol followed.

Figure 5.9 (a2) shows examples of the temperature dependence of the scattered neutron intensity for all phases. The helical phase (green circles) at $B = 25\,\mathrm{mT}$ shows a substantial decline with increasing temperature indicating a decrease in the volume of the sample populating these domains. As mentioned above, $\boldsymbol{B} \parallel [001]$, thus the helical domain propagating parallel to the $\boldsymbol{B}$ gains energy from the Zeemann interaction, in contrast to the domains propagating along either $[100]$ or $[010]$. The non-vanishing population in these domains is related to pinning centers and magnetic defects, among others, creating an energy barrier, as discussed in chapter 3. With increasing temperature, the domains can overcome the small energy barriers and turn to propagate along $\boldsymbol{B}$. The helical intensity vanishes completely around 50 K. Around 55 K the intensity associated with the high-temperature skyrmion (HT-Sky) lattice rises (orange circles), creating a small peak in the typical region of stability of this phase just below the critical temperature T_c. At higher magnetic field values the situation is different, e. g. at $B = 70\,\mathrm{mT}$, the low-temperature skyrmion phase scatters neutrons in this plane. This intensity remains constant with increasing temperature up to $\sim$ 28 K and decreases steeply vanishing around $\sim$ 34 K.

The conical and the tilted conical phase can be seen in the scattering pattern shown in figure 5.9 (b1) for $\boldsymbol{B} \perp \boldsymbol{n}$. Both phases coexist at low temperatures for almost all magnetic fields measured. The domain of the tilted conical phase on the right hand side of the scattering pattern is preferred, this may be a consequence of the small misalignment of the magnetic field from the $[001]$ axis, which is $\sim 1°$. Note that the experimental setups chosen were not sensitive to the additional two domains of the tilted conical phase, as depicted in figure 5.1 (b4). Sectors 1 (solid black) on the scattering diagram is the area related to the conical phase, while the sectors 2 (dashed grey) mark the region of the detector where neutrons scattered from the tilted conical phase would be recorded. The temperature dependence of the intensity at $B = 70\,\mathrm{mT}$ is shown in figure 5.9 (b2), note that the conical intensity has been divided by 10. The conical phase is very well ordered, and there are no energetically degenerate competing domains yielding very sharp peaks. Consequently, there is a significant difference in intensity measured in a single image scan as the one performed here. A quantitative analysis of the scattered intensity is out of the scope of this works. Instead, the qualitative features will be in the foreground when comparing different phases. The intensity from the tilted conical phase increases with increasing temperature until $T \approx 12\,\mathrm{K}$. The intensity of the conical phase decreases in the same temperature region, suggesting that, below this temperature, the tilted conical phase is indeed energetically preferable to the conical magnetic order. Thus an increase of thermal excitation allows possible pinned domains to overcome their pinning potential and reorder in the new phase. Above $\sim$ 12 K the tilted conical phase starts to decrease and the conical phase starts to increase, as the population from the former is transferred to the later. The conical phase reaches a plateau of intensity around $\sim$ 30 K followed by a small peak at $\sim$ 40 K after which it steeply decreases when approaching the transition to the paramagnetic phase.

Typical data obtained from field-cooled scans

The most prominent behavior, when measuring scattered neutrons following the field-cooled protocol, is related to the high-temperature skyrmion phase if the magnetic field value applied is in the vicinity of the HT-Sky phase then a portion of it survives in a metastable state down

to the lowest temperature. A typical scattering pattern at low temperatures, i. e., at the end of the scan, is shown in figure 5.10 (a1). One can recognize twelve Bragg peaks corresponding to the two different domains of the HT-Sky phase. Additionally, the Bragg peaks along the $[100]$ crystallographic axes are stronger than the rest. That is due to the coexistence of the metastable HT-Sky phase with the helical phase. In contrast to the ZFC/FH measurements sector 1 (solid green) now contains the overlapping signal from the helical and skyrmion phase. However, the intensity in sector 2 (dashed red) belongs only to the skyrmion phase. Hence, subtracting the integrated intensity of sectors 2 from that of sectors 1 yields the helical

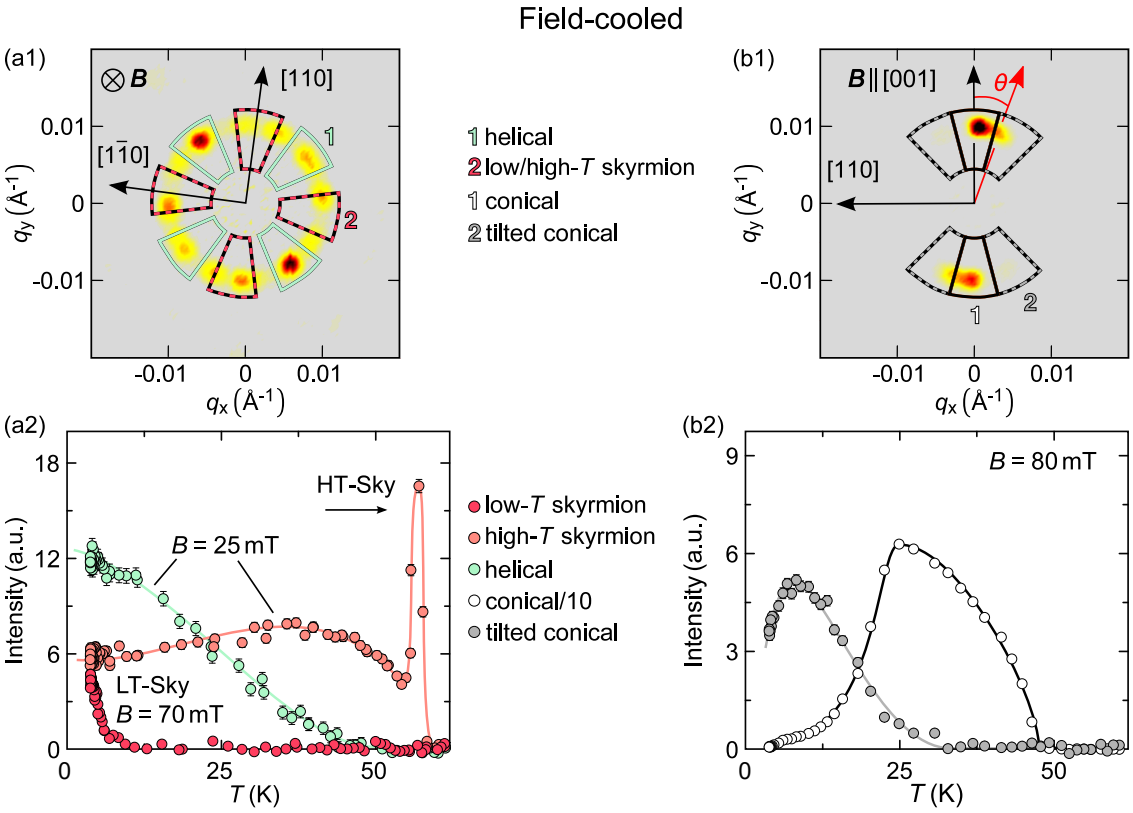

Figure 5.10: Typical scattering patterns and extracted intensity from small-angle neutron scattering for FC. (a1) Coexistence of a metastable high-temperature skyrmion and a helical phase at low temperatures recorded for $\boldsymbol{B} \parallel \boldsymbol{n}$. Sectors 1 (solid green) contain the overlapping intensity from neutrons scattered by the helical and HT-Sky phase, while the intensity in sectors 2 (dashed red) originates solely from the HT-Sky phase. (a2) Temperature dependence of the intensity as obtained from the sectors shown in (a1). Subtracting sectors 2 from sector 1 yields the helical intensity (green circles) at $B = 25\,\mathrm{mT}$. The remnant intensity of the HT-Sky phase (orange circles) below $\sim 54\,\mathrm{K}$ belongs to the metastable state. The LT-Sky phase (red circles) at $B = 70\,\mathrm{mT}$ is constrained to a smaller region at very low temperatures. (b1) Conical and tilted conical phase at higher magnetic fields for $\boldsymbol{B} \perp \boldsymbol{n}$. In a similar case as with the LT-Sky phase, the tilted conical order is weaker than for ZFC/FH measurements. Its Bragg peaks are barely visible, and the angle of propagation θ is smaller than in ZFC/FH scans. Sectors 1 (solid black) and 2 (dashed grey) correspond to the conical and tilted conical phase, respectively. (b2) Temperature dependence of the scattered intensity from the conical (white circles) and tilted conical (grey circles) phase at $B = 80\,\mathrm{mT}$. Note that the decline in the tilted conical intensity at very low temperature correlates with the temperature region where the LT-Sky phase is observed.

intensity. Sectors 2 were enlarged and then averaged to correspond to the same detector area encompassed by sectors 1 to control for the variation of intensity as a function of the azimuthal angle. Finally, note that under this measurement protocol, the signature of the low-temperature skyrmion phase does not coexist with the helical phase.

Figure 5.10 (a2) shows the extracted intensities as a function of temperature for the helical and the high-temperature skyrmion phase at $B = 25\,\mathrm{mT}$ and the low-temperature skyrmion phase in an applied field of $B = 70\,\mathrm{mT}$. Starting from high temperatures, the first feature observed is a peak in the HT-Sky intensity (orange circles). This sharp increment in intensity corresponds to the sample entering the reversible HT-Sky pocket. The intensity then reaches a maximum deep in the skyrmion phase. As the temperature decreases further, the sample approaches the low-temperature boundary, and the intensity declines sharply, yet it does not vanish completely; instead, the intensity stops at an intermediate value and starts increasing with decreasing temperature. This increment is associated with the rise of the magnetic moment with decreasing temperature. As the sample is cooled, the curve shows a change in curvature reaching a maximum around $\sim 38\,\mathrm{K}$ and declines slowly with decreasing temperature. Typically, cooling the sample in a moderate finite magnetic field pointing along an easy axis will not yield a helical phase. Nonetheless, the helical intensity (green circles) starts increasing with decreasing temperature around $\sim 50\,\mathrm{K}$, close to the point of inflection of the intensity resulting from scattering from the HT-Sky. The small misalignment between the magnetic field and the $[001]$ axis may allow the emergence of domains along the two axes perpendicular to the field direction. With decreasing temperature, the helical intensity increases and reaches a plateau just below $10\,\mathrm{K}$. The behavior of the low-temperature skyrmion phase is quite simple, around $\sim 10\,\mathrm{K}$ the associated intensity starts to increase sharply with decreasing temperature, as LT-Sky domains condensate and start to grow.

In comparison to the ZFC/FH measurements, the signal of the tilted conical phase is weaker, and θ is smaller as can be seen in a typical scattering pattern at low temperatures, shown in figure 5.10 (b1). The intensities of the conical and tilted conical phase at $B = 80\,\mathrm{mT}$ as extracted using sectors 1 and 2, respectively, are plotted in figure 5.10 (b2). The conical phase (white circles) shows increasing intensity with decreasing temperature until it reaches a maximum just over $T = 25\,\mathrm{K}$. Around this temperature, the intensity corresponding to the tilted conical phase (gray circles) starts increasing. As the temperature keeps decreasing the intensity of the conical phase falls solidly, while the tilted conical phase intensity increases, albeit at a slower rate. While only small remnants of the conical phase are left at the lowest temperatures measured, the tilted conical phase shows a maximum around $T = 8\,\mathrm{K}$ and decreases sharply as the sample is cooled further. Note that this sharp reduction of the tilted conical intensity correlates with the region in which the LT-Sky phase emerges.

Typical data obtained from high-field-cooled/field-heated scans

A high-field-cooled/field-heated measurement protocol typically favors the conical magnetic order in chiral magnets, when the field is parallel to one of the easy axis of the system. While the effects on the skyrmion lattice are minimal, due to its relatively high temperature, the helical phase is generally suppressed in large portions of the phase diagram only reappearing at temperatures close to the helical to the paramagnetic phase transition. That is not the case for Cu_2OSeO_3. Instead, both new phases, i. e., the tilted conical and the low-temperature skyrmion phase, show very well defined signatures and, in the case of the LT-Sky, expand their region in the phase diagram substantially.

Typical scattering patterns recorded at low temperatures are shown in figure 5.11 (a1) and (b1). The former was obtained in a experimental setup with $\boldsymbol{B} \parallel \boldsymbol{n}$, after reducing the magnetic field magnitude from $B = 250\,\mathrm{mT}$ down to $B = 25\,\mathrm{mT}$. The LT-Sky scattering pattern consists of a ring showing a complete homogeneous azimuthal intensity distribution. The four Bragg peaks observed correspond to helical propagations coexisting with the low-temperature skyrmion phase. As it was the case for field-cooled measurements, the remaining intensity, after subtracting sectors 2 (dashed red in figure 5.11 (a1)) from sectors 1 (solid green), originates from the helical phase. The results are shown in figure 5.11 (a2). The helical phase shows a typical behavior decreasing slowly with increasing temperature vanishing completely at $T = 48\,\mathrm{K}$. The intensity of the LT-Sky phase also decreases at first, albeit slower than the helical phase. At $T = 50\,\mathrm{K}$, a sharp peak develops, yet there are no changes

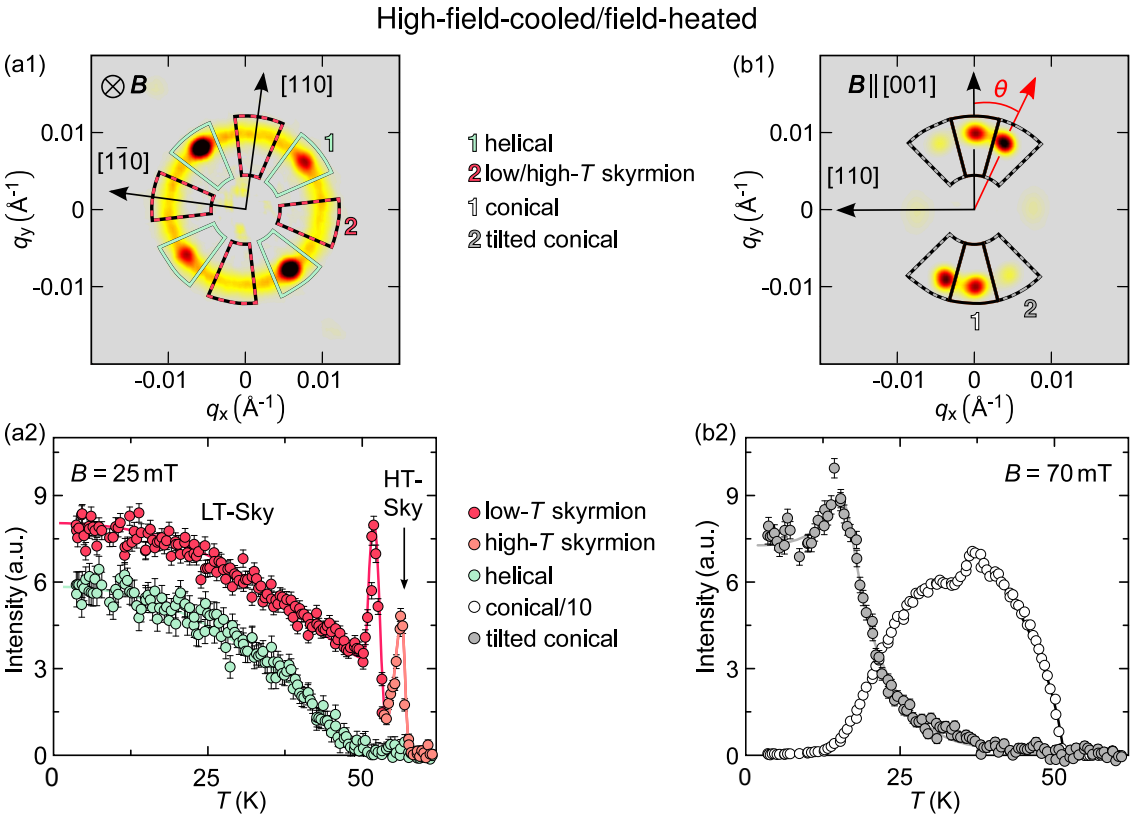

Figure 5.11: Typical scattering patterns and extracted intensity from small angle neutron scattering for HFC/FH. (a1) Coexistence of LT-Sky (ring) and helical (Bragg peaks) phases at low temperatures for $\boldsymbol{B} \parallel \boldsymbol{n}$. Sectors 1 (solid green) contain overlapping signal of the coexisting phases. Sectors 2 (dashed red) contain intensity from the LT-skyrmion phase only. (a2) Examples for the temperature dependence of the intensity at $B = 25\,\mathrm{mT}$. The helical intensity (green circles) decreases slowly with increasing temperature and vanishes completely at $T = 48\,\mathrm{K}$. For low temperatures the intensity of the LT-Sky phase decreases slowly (red circles). The peak at $T = 50\,\mathrm{K}$ marks a transition from the LT-Sky to the HT-Sky (orange circles) phase. (b1) Typical scattering pattern at lower temperatures for $\boldsymbol{B} \perp \boldsymbol{n}$ showing both the conical and the tilted conical phase. The smudges of intensity along the $[110]$ direction correspond to the low- temperature skyrmion phase. (b2) Temperature dependence of the scattered intensity from the conical (white circles) and tilted conical (grey circles) phase at $B = 70\,\mathrm{mT}$, extracted using sectors 1 (solid black) and 2 (dashed grey) from (b1). The tilted conical transitions to the conical phase starting at $T = 15\,\mathrm{K}$, vanishing completely at $T = 38\,\mathrm{K}$.

to the scattering pattern recorded. The intensity falls sharply and increases again at $T = 54\,\mathrm{K}$ as the LT-Sky phase transitions into the HT-Sky phase showing again the twelve peaks corresponding to the two domains observed for this experimental configuration.

A typical scattering pattern for $\boldsymbol{B} \perp \boldsymbol{n}$ is shown in figure 5.11 (b1). Note how clear the Bragg peaks for the tilted conical phase are. Their positions are separated from the coexisting conical phase. The second domain is not as strong, due in part to the misalignment between field and crystallographic axis, as well as the chosen field value to be able to demonstrate the coexistent of both phases for this measurement protocol. Additionally, there are two light intensity patterns along $[110]$. These correspond to the low-temperature skyrmion phase. As for the previous examples, the intensity is obtained by integrating over the different sectors depicted. Specifically, sectors 1 (solid black) and sectors 2 (dashed grey) for the conical and tilted conical phase, respectively. Figure 5.11 (b2) contains the resulting curves for $B = 70\,\mathrm{mT}$. At low temperatures only the tilted conical phase is populated and the related intensity remains fairly constant up to $T = 12\,\mathrm{K}$. After a small increase while the sample is heated further the intensity of the tilted conical phase starts to decrease as the conical phase emerges at $T = 15\,\mathrm{K}$. The former vanishes at $T = 38\,\mathrm{K}$ while the latter shows a small peak and then decreases sharply as the system reaches the transition to the paramagnetic regime.

Magnetic phase diagrams from temperature scans

Based on the dense mesh of data recorded as a function of temperature for the different aforementioned measurement protocols, a set of magnetic phase diagrams was determined. The boundaries were defined at the data point at which the intensity differed from the background by at least five standard deviations, 5σ. Note that this definition of phase boundary did not intend to reproduce the phase diagram as observed with other thermodynamic physical properties, such as magnetization and magnetic susceptibility measurements. The high sensitivity of SANS can lead to larger cirtical values for the phase boundaries than expected in case of hysteresis and metastability. Furthermore, the experimental results presented here are the first thorough mapping of the new phases, i. e., tilted conical and low-temperature skyrmion phase, so the definition was chosen to ensure consistency and transparency. Subsequent precise measurements of the magnetization and the ac susceptibility defined phase boundaries different from the ones shown here, their relation to the following phase diagrams is obtained by virtue of a direct comparison of the data sets [142].

The magnetic phase diagrams for the different temperature versus magnetic field protocols were obtained by combining both measurements with $\boldsymbol{B} \parallel \boldsymbol{n}$ and $\boldsymbol{B} \perp \boldsymbol{n}$ and are depicted in figure 5.13 (b1) through (b3). For comparison the phase diagram for $\boldsymbol{B} \parallel [111]$ as extracted from magnetization measurements following a zero-field-cooled/field-heated protocol is shown in figure 5.13 (a). The ZFC/FH phase diagrams for $\boldsymbol{B} \parallel [111]$ and $\boldsymbol{B} \parallel [001]$ are very similar for temperatures just below the transition to the helimagnetic order T_c down to the $T = 44\,\mathrm{K}$. The helical phase is observed in low magnetic fields, followed by the skyrmion lattice at intermediate field values and the conical phase just below the transition to the field polarized phase at high fields. The small apparent difference in the temperature width of the high-temperature skyrmion phase (orange circles) is due to the boundary definition, as is the strong difference in sizes of the helical phase (green circles).

Both tilted conical and low-temperature skyrmion phases are not observed for $\boldsymbol{B} \parallel [111]$. Moreover, the conical to field polarized phase transition shows a strong temperature dependence decreasing steadily with increasing temperature. This is not only in stark contrast to

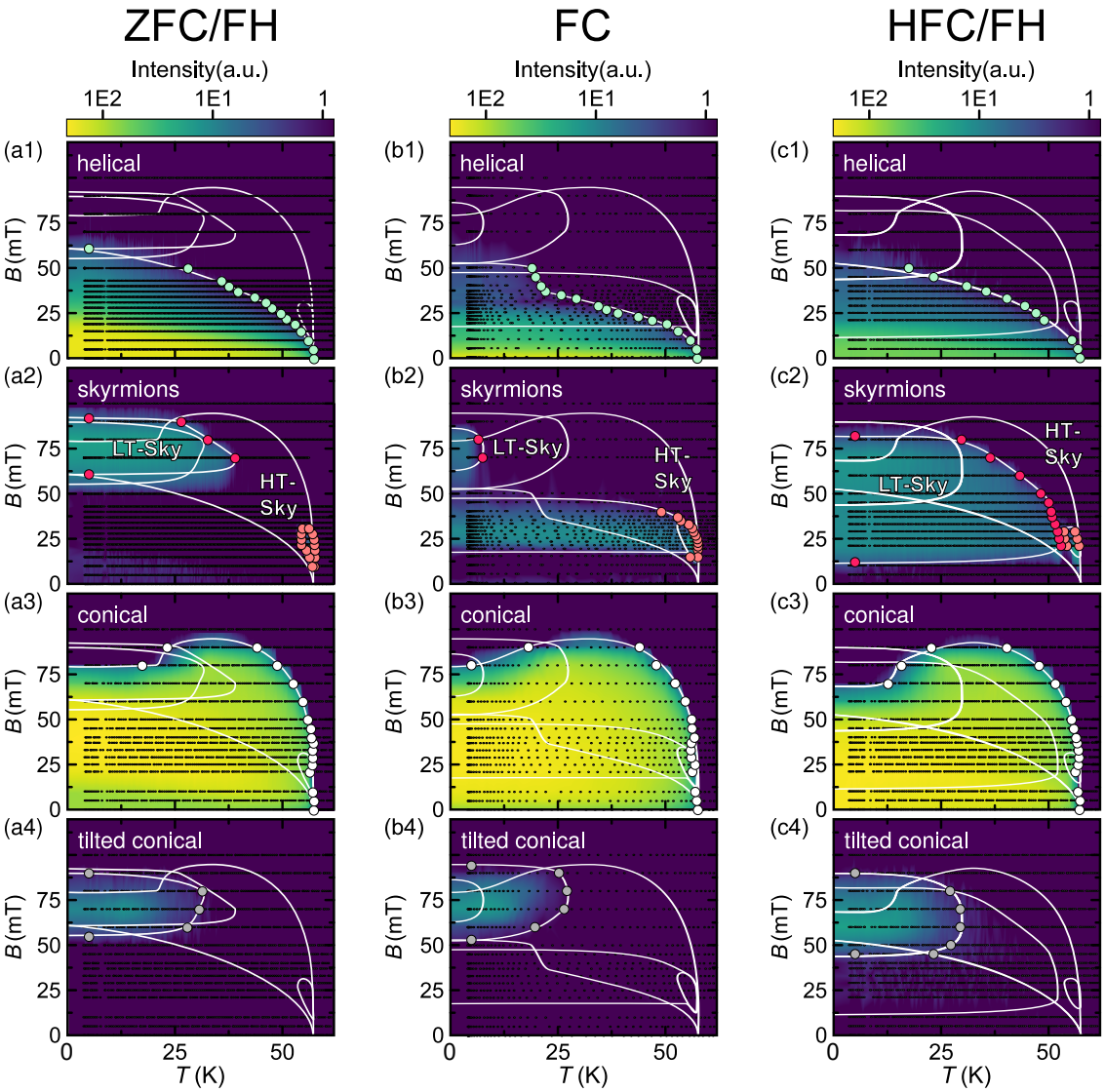

Figure 5.12: Intensity maps for the different protocols of temperature versus magnetic fields and magnetic phases. Scattered neutron intensities were obtained from the four sectors as defined in the typical scattering patterns, e.g., figure 5.10. The data is organized by magnetic phases (rows) and measurement protocols(columns). The white lines are the phase boundaries of the phase diagrams presented in figure 5.13, while the circles mark the phase boundaries. The black dots represent points were scattered neutron data were recorded.

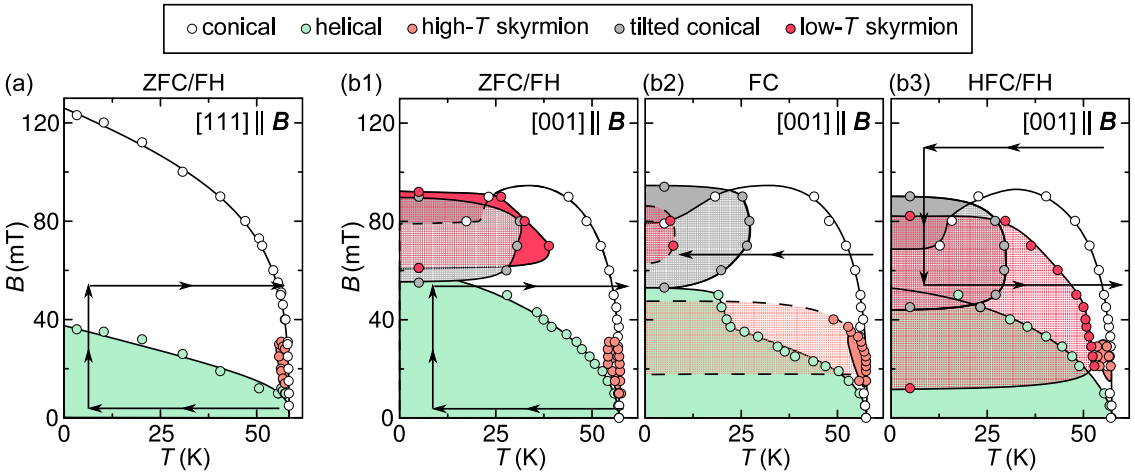

Figure 5.13: Magnetic phase diagrams for different experimental protocols of Cu_2OSeO_3: (a) $\boldsymbol{B} \parallel [111]$. Typical magnetic phase diagram from literature, see text for details of phase boundary definitions. (b1) ZFC/FH measurements. Note that at low temperatures the low-temperature skyrmion phase transitions directly into the field polarized regime. (b2) FC scans. For fields in the range of the high-temperature skyrmion phase a metastable phase survives down to lowest temperature. The LT-Sky region shrinks substantially. (b3) HFC/FH measurements. The low-temperature skyrmion phase expands to cover almost the entire phase diagram.

the transition to the polarized phase observed for $\boldsymbol{B} \parallel [001]$ which is almost constant below $T = 44\,\mathrm{K}$, but it also differs from the behavior observed for other chiral magnets such as MnSi and $Fe_{1-x}Co_xSi$, where the transition shows a vanishing temperature dependence at very low temperatures. The characteristic dependence on the direction of the field is a strong indication that magnetocrystalline anisotropies play an important role determining the magnetic order in Cu_2OSeO_3.

As it was discussed in chapter 3, the critical fields defining the transition from the helical to the conical phase are determined by the angle $\beta_{\boldsymbol{B},\boldsymbol{Q}_i}$ between the field direction $\boldsymbol{B}$ and the different propagation vectors $\boldsymbol{Q}_i$ of the helical domains. In the case of Cu_2OSeO_3 the helices propagate along $\langle 100 \rangle$ axes, thus the case of $\boldsymbol{B} \parallel [111]$ and $\boldsymbol{B} \parallel [001]$ are not so different as both are characterized by relatively large angles, i. e., $\beta^{[111]}_{\boldsymbol{B},\boldsymbol{k}_i} = 55°$ and $\beta^{[001]}_{\boldsymbol{B},\boldsymbol{Q}_i} = 90°$. Hence, the critical field B_{c1} at which all domains coalesce into a single domain propagating along $\boldsymbol{B}$ is similar for both field directions.

A very different scenario develops when a single domain state breaks up into several domains, i. e., the transition from the conical phase to the helical phase. For $\boldsymbol{B} \parallel [111]$ all domains are equivalent concerning the magnetic field direction. Thus, such a transition results in all of them being equally populated. In contrast for magnetic fields applied along $\langle 100 \rangle$, the conical domain propagates along an easy axis, and there is no energetic advantage in splitting up this domain in the absence of a magnetic field. It follows that the helical phase would show a strong hysteresis depending on the temperature versus magnetic field protocol followed. If the experimental protocol 'passes through' the conical phase, a multidomain helical phase should not be observed.

As mentioned above, in this study, scattering from helical domains perpendicular to the magnetic field can be observed up to large fields, $\sim 0.5\,B_{c2}$, for both field-cooled and high-field-cooled/field-heated measurement protocols, cf. figure 5.13 (b2) and (b3). The critical fields are slightly lower in comparison to ZFC/FH, but these differences are small in compar-

ison to the region in which the helical signal survives. Note also that for field-cooled measurements the temperature at which the helical signal emerges for fields around $40\,\mathrm{mT}$ is almost constant, indicating the temperature at which the anisotropic contributions favoring helical domains perpendicular to the field become strong enough. A simple explanation for this behavior is the combination of the small deviation of the magnetic field from the intended $[001]$ axis and the field-dependent contribution from the magnetocrystalline anisotropies. Recent careful measurements of magnetization M and ac-susceptibility χ substantiated this explanation [142]. As part of that study, a conical to helical transition was observed for small deviations of the magnetic field direction from a $\langle 100 \rangle$ crystallographic axis. Careful alignment of the sample suppresses the signature completely, as shown in [142].

The boundaries of the tilted conical phase show a small hysteresis between the different measurement protocols, cf. figure 5.13 (b1) - (b3). The differences in the phase boundaries as related to temperature are small and the highest critical temperature, at which the phase vanishes, is constantly $\sim 30\,\mathrm{K}$. Relatively more significant hysteretical effects are observed as a function of field, especially around the lower field boundary. The work of Halder *et al.* shows that these effects disappear when demagnetization corrections are taken into account (lack of magnetization data on the specific sample used in the study presented here prevented such a correction).

Depending on the temperature vs. magnetic field history, the region in the magnetic phase diagram where the low-temperature skyrmion phase can be observed changes dramatically. The smallest phase is observed when cooling the sample in an applied field (FC), cf. figure 5.13 (b2), and it relates to the phase extent after ZFC as well as HFC. Note that on the one hand, the low field boundary of the ZFC/FH measurements is close to that obtained for the FC measurement. On the other hand, the high field boundary of the FC measurments matches the one observed in HFC/FH experiments.

One observes the largest phase area for the LT-Sky phase in HFC/FH measurements for which the phase extends down to $\sim 15\,\mathrm{mT}$ and up to temperatures just below the HT-Sky. The phase region of low-temperature skyrmion lattice after ZFC/FH is reduced to fields between $60\,\mathrm{mT}$ and $90\,\mathrm{mT}$ and it transitions directly into the field polarized regime at lowest temperatures. Note that the transition temperature for both ZFC/FH at $70\,\mathrm{mT}$ and $80\,\mathrm{mT}$ are very close to those obtained from HFC/FH measurements, the differences might be explained by demagnetization effects, which shift the magnetic field scale slightly.

Sample preparation before magnetic field dependent measurements

Magnetic field scans followed typically the same protocol as hysteresis loop in which the measurement starts from zero-field, and the magnetic field is increased until the saturation is reached (in this case the field polarized region), at that point the magnetic field magnitude decreases until it reaches $0\,\mathrm{mT}$ where the polarization switches and the magnitude increases again until saturation is reached in the opposite direction. In the following, we denote the first leg of the measurement zero-field-cooled/field-scan (ZFC-FS) and the second leg high-field/field-scan (HF/FS), as the sample needs to be prepared in the zero-field state by cooling from above the critical temperature T_c before every scan. Due to the behavior of the high-temperature skyrmion lattice observed after field-cooled scans two additional temperature versus magnetic field protocols were followed to investigate the boundaries of the metastable HT-Sky phase. The details of the different measurements are as follows:

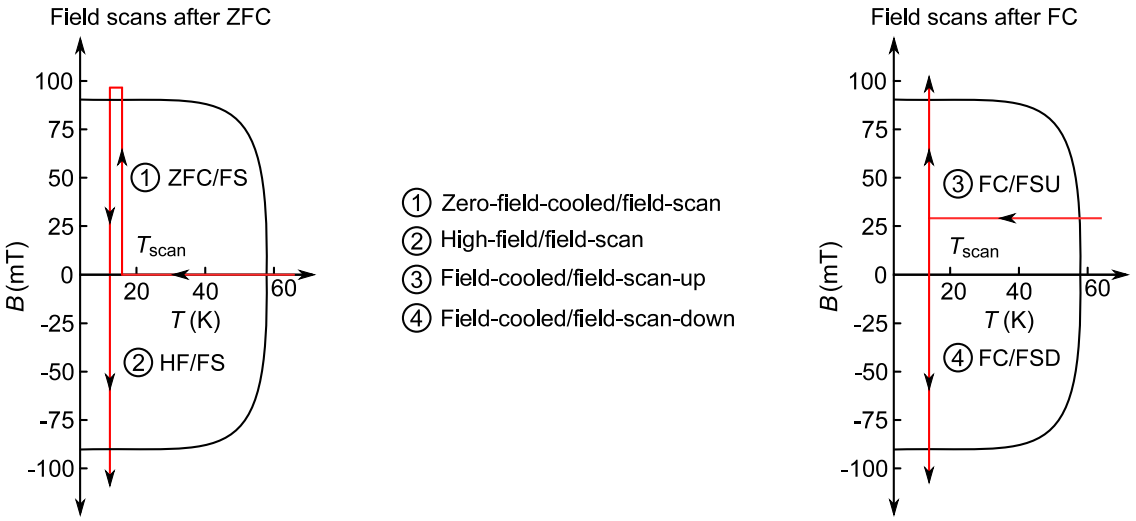

Figure 5.14: Schematic representation of the different temperature versus magnetic field protocols followed to obtain data for magnetic field scans. (1) Zero-field-cooled/field-scan (ZFC/FS): the sample is cooled down to the lowest temperature at zero magnetic field. At the desired temperature, T_{scan}, scattered intensity is recorded while the magnetic field magnitude is increase continuously to above B_{c2}. (2) High-field/field-scan (HF/FS): Following (1) data is again recorded continuously while the field is decreased continuously below $-B_{\text{c2}}$. (3), (4) Field scans after field cooled: the magnetic field value is set to B_{FC} at a temperature well above the helimagnetic transition. The sample is cooled to the temperature of interest, T_{scan}, at which data is recorded while the magnetic field is either increased (FC/FSU) or decreased (FC/FSD) until the field polarized phase is reached.

(a) **ZFC/FS**: Zero-field-cooled/field-scan, cf. Fig. 5.14 (1). Starting well above the helimagnetic transition with a previously degaussed magnet the sample is cooled in zero magnetic field at a rate of $8\,\text{K}\,\text{min}^{-1}$ to the desired temperature for the scan, T_{scan}. Scattered neutron intensity is recorded over a 5 s interval, while the magnetic field is increased continuously at a rate of $0.2\,\text{mTs}^{-1}$ to a field higher than B_{c2}. Due to the dead time of 1 s for the storage of the file, each data point represents an average over a change of field of $\sim 1.2\,\text{mT}$.

(b) **HF/FS**: High-field/field-scan, cf. Fig. 5.14 (2). Starting deep in the field polarized phase and at the temperature of interest T_{scan}, data is recorded while the magnetic field strength changes continuously at a rate of $-0.2\,\text{mTs}^{-1}$ until a field well below $-B_{\text{c2}}$ is reached. As for ZFC/FS each data point is an average over 1.25 mT.

(c) **FC/FSU**: field-cooled/field-scan-up, cf. Fig. 5.14 (3). Starting with a degaussed magnet well above the helimagnetic transition temperature T_c the field value is set to $B_{\text{FC}} = 29\,\text{mT}$. The sample is then cooled at a rate of $8\,\text{K}\,\text{min}^{-1}$ down to the temperature of interest T_{scan}. Scattered neutrons are recorded while the magnetic field is increased at a rate of $0.2\,\text{mTs}^{-1}$ up to a field value greater than B_{c2}. As above data points are an average over 1.2 mT.

(d) **FC/FSD**: field-cooled/field-scan-down, cf. Fig. 5.14 (4). Starting with a degaussed magnet well above the helimagnetic transition temperature T_c the field value is set to $B_{\text{FC}} = 29\,\text{mT}$. The sample is then cooled at a rate of $8\,\text{K}\,\text{min}^{-1}$ down to the temperature of interest T_{scan}. Scattered neutrons are recorded while the magnetic field is change at a rate of

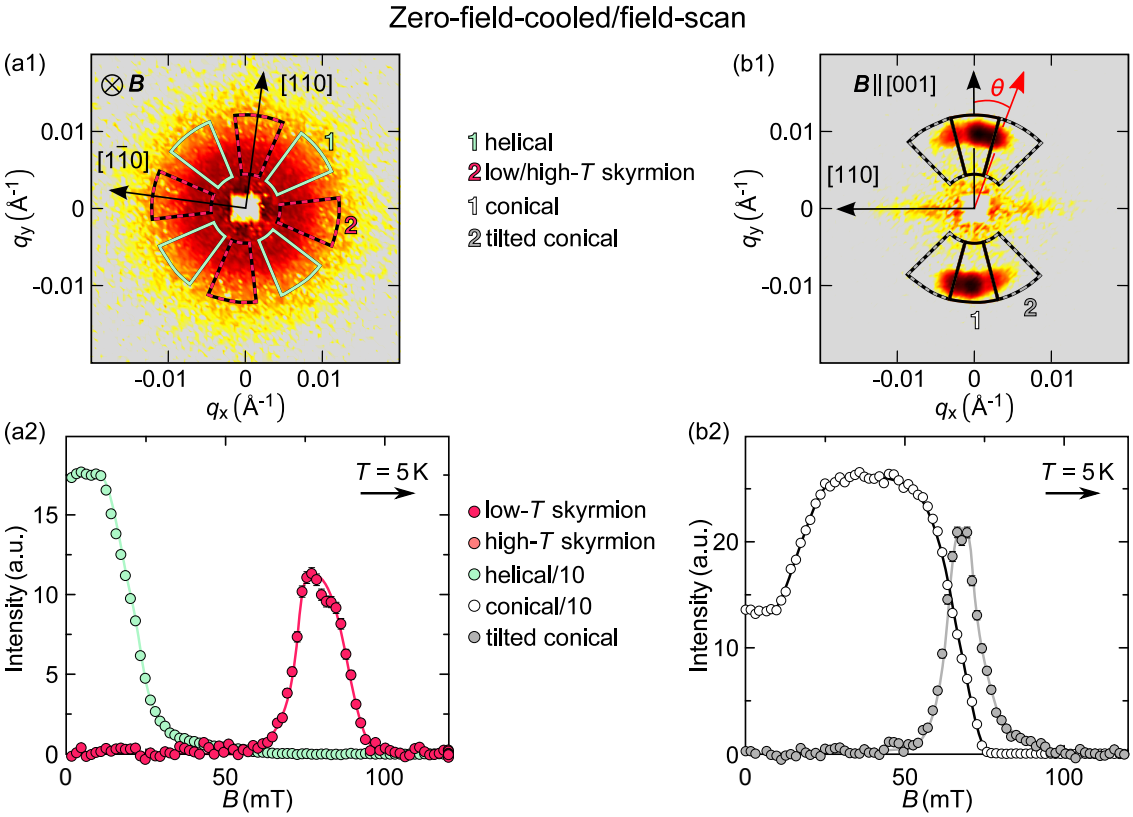

Figure 5.15: Typical data obtained from neutron scattering during field scans after zero-field-scan for $\boldsymbol{B} \parallel \boldsymbol{n}$ (left column) and $\boldsymbol{B} \perp \boldsymbol{n}$ (right column). (a1) Scattering pattern obtained in the phase pocket of the low-temperature skyrmion lattice, note that the signal concentrates around the direct beam indicating a small value of $|\boldsymbol{Q}|$. (a2) Intensity as a function of magnetic field obtained at $T = 5\,\mathrm{K}$. (b1) Scattering pattern including the conical and tilted conical phase, at this intermediate field both phases coexist, and their Bragg peaks overlap. The streaks along the $[110]$ axis belong to the low-temperature skyrmion lattice. (b2) Conical and tilted conical intensity as a function of the magnetic field. The increase in the conical intensity at low fields is related to the depopulation of helical domains. Note that the decline of the conical intensity at higher fields is accompanied by the rise of the tilted conical phase indicating the transition from the former to the latter.

$-0.2\,\mathrm{mTs}^{-1}$ up to a field value below $-B_{c2}$. As above data points are an average over $1.2\,\mathrm{mT}$.

Typical data obtained from zero-field-cooled/field-scan

Figure 5.15 shows representative results obtained during field scans after cooling the sample in zero-field. The image has the same layout as the typical data illustrations for the temperature scans. The scattering patterns are in a logarithmic scale in order to emphasize certain features in them. The scattering pattern on the top left was obtained with a magnetic field parallel to the incoming neutron beam in the middle of the low-temperature skyrmion phase. The main feature consists of a ring with a small radius, i. e., very close to the direct beam. There is also a stronger contribution from higher order components or double scattering than observed for the other magnetic phases. The captured scattered neutrons intensity as a function of the magnetic field B for the LT-Sky and helical phase is plotted in figure 5.15 (a2). The helical

phase (green circles) shows a strong signal at very low fields, which starts to decrease just above 10 mT but maintains a substantial intensity value up to 50 mT. Note that the intensity for the helical phase has been divided by 10. The low-temperature skyrmion phase (red circles) is given by a broad intensity peak centered around 75 mT and $\sim$ 40 mT wide. The scattering pattern obtained for $\boldsymbol{B} \perp \boldsymbol{n}$, cf. Fig. 5.15 (b1), also shows a clear signal related to the low-temperature skyrmion phase, i. e., the intensity strides on both sides. The Bragg peaks from the conical and tilted conical phase do not show any notable differences to those observed from temperature scans following a similar protocol, i. e., zero-field-cooled/field-heated.

This type of scans showcases the transition from the helical to the conical phase. As illustrated in figure 5.15 (b2), the intensity of the helical domain propagating along the magnetic field direction (white circles) shows a strong increase between 10 mT and 25 mT. Typically, the point of inflection of this increasing flank in the vicinity of 20 mT would define the phase boundary and should coincide with the point of inflection of the helical state in 5.15 (a2). Following that definition would yield similar boundaries as those obtained from magnetization. However, the intensity as a function of temperature lacks an inflection point. Thus alternating definitions of phase boundaries would be necessary depending on the measurement protocol. To maintain the analysis transparent and straight forward, the same boundary definition as used in the temperature scans was applied here. As it was the case with the low-temperature-skyrmion phase, a peak in the intensity as a function of magnetic field defines the phase region of the tilted conical phase. The center of the peak lies at $\sim$ 70 mT and it is $\sim$ 25 mT wide. Notice that the onset of the tilted conical phase correlates with a decline in the intensity of the conical magnetic order. The peak is asymmetrical, and the decreasing flank (towards larger magnetic fields) possesses a longer tail. Both the conical phase and tilted-conical phase are in decline as the intensity of the LT skyrmion phase rises, this is a strong indicator that the skyrmion lattice represents the ground state at this point in the phase diagram.

Typical data obtained from high-field/field-scan

After reaching the field polarized phase, the magnetic field ramp is reversed, and scattered neutrons are recorded starting from high positive fields and finishing at high negative fields. The results from the temperature scan already demonstrate a large hysteresis between measurements starting from zero-field and those that start above B_{c2}. In the latter case, the first unusual observation is that the radius of intensity ring close to the direct beam, cf. Fig. 5.15 (a1), increases with decreasing magnetic field as illustrated in figure 5.16 (a1). Hence, the ring is very well defined and easily recognizable as a new form of magnetic order, instead of a signal arising from domain walls related to the field polarized transition, which would not survive far from the latter. The intensity as a function of the magnetic field (red circles plotted in figure 5.16 (a2)) increases sharply around 80 mT, reaches a maximum just below 70 mT and falls slightly to reach a plateau. The latter extends down below 20 mT, at which point the intensity sharply decreases. On the negative magnetic field side of the curve, the same shape is observed as in the field scans starting from zero-field-cooled discussed above, i. e., a peak just below the transition to the field polarized phase. The helical phase (green circles) shows a broad peak around 0 mT, with long tails reaching pass 50 mT. The center of the curve is not at zero magnetic field, which is likely a consequence of trapped flux in the superconducting magnet.

The strong signal of the low temperature skyrmion lattice at small positive fields, can also be observed in the experimental setup with $\boldsymbol{B} \perp \boldsymbol{n}$. Figure 5.16 (b1) contains a scattering

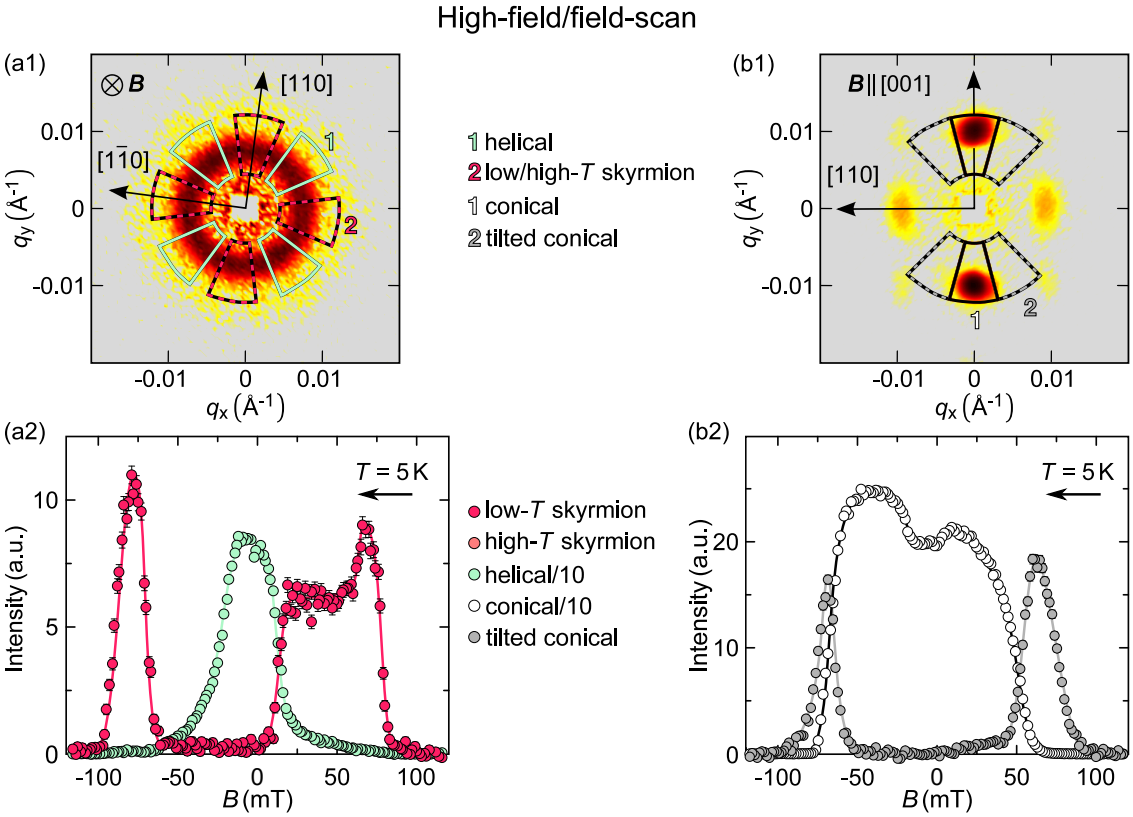

Figure 5.16: Typical data obtained from field scans starting from high-fields well above the transition to the field polarized phase for $\boldsymbol{B} \parallel \boldsymbol{n}$ (left column) and $\boldsymbol{B} \perp \boldsymbol{n}$ (right column). (a1) Scattering pattern within the low-temperature skyrmion lattice phase, the disorder skyrmion domains yield a ring of intensity. By expanding the phase metastably to lower field values, the ring expands and is easier resolved from the direct beam. (a2) Scattered neutrons intensity for the helical and low-T skyrmion phase as a function of the magnetic field at $T = 5\,\mathrm{K}$. On decreasing field magnitudes the skyrmion phase expands to very low magnetic fields, upon reaching $B = 0$ and increasing the magnitude again, the boundaries look almost the same as in ZFC/FC measurements, cf. Fig. 5.15 (a2). (b1) Scattering pattern deep in the conical phase, the tilted conical phase is not observable. Instead, a strong signal from the low-temperature skyrmion phase is observed along the $[110]$ axis. The four weaker spots observed arise from double scattering processes, including the LT-sky and the conical phase. (b2) Intensity of scattered neutrons from the conical and tilted conical phases. Small hysteretic effects are observed at the boundaries of both phases as a consequence of demagnetization.

pattern obtained in this configuration at low fields. The broad Bragg peaks left and right, arise from scattering from LT-Sky phase. Note that there is also double scattering originating from neutrons the scattered from the conical phase and the from skyrmion lattice or the other way around. This signal is captured partially by the integration windows used for the tilted conical phase, resulting in a longer tail to small magnetic fields, that could not be extracted from the data efficiently. The tilted conical intensity as a function of magnetic field plotted in 5.16 (b2) (gray circles) shows clearly this artifact. The curve progression does not change, the tilted conical phase is still described by an intensity peak as a function of magnetic field. The phase region on the positive magnetic field side sets on at $\sim 85\,\mathrm{mT}$ and reaches its maximum at $63\,\mathrm{mT}$. The tilted conical phase vanishes just below $50\,\mathrm{mT}$. The linear behavior observed below that is associated with the double scattering from the LT-Sky phase. On the

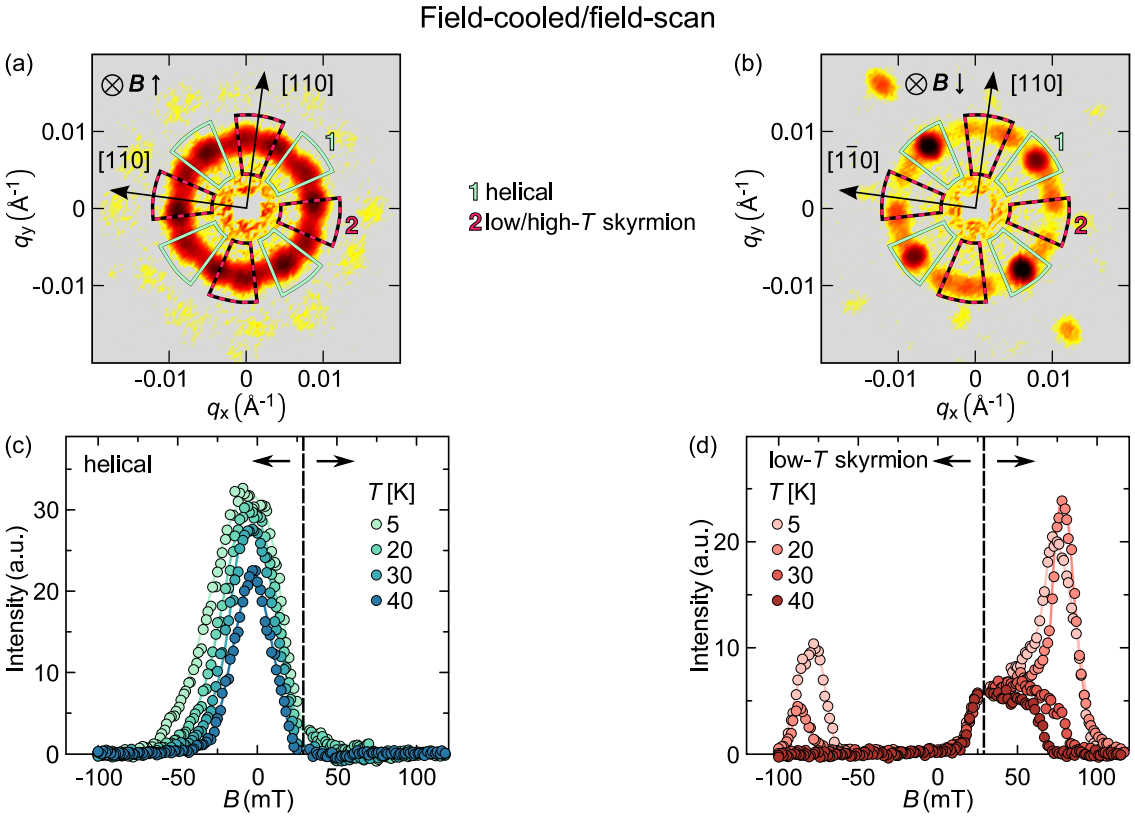

Figure 5.17: Typical data obtained from field scans after cooling the sample in a field $B_{\mathrm{FC}} = 29\,\mathrm{mT}$ for $\boldsymbol{B} \parallel \boldsymbol{n}$. (a) Scattering pattern of the metastable skyrmion lattice in a finite field larger than B_{FC}. There is no contribution from the helical order. (b) Scattering pattern obtained for a field just below B_{FC}. The Bragg peaks related to the skyrmion domains become very weak rapidly while scattering from the helical phase increases. (c) Intensity of scattered neutron from the helical phase as a function of the magnetic field for different temperatures. The curves are not centered around $B = 0$ due to frozen flux in the superconducting magnet. (d) Intensity of scattered neutrons from the skyrmion lattice as a function of B for different temperatures. Note that increasing the field after field cooling leads to a large peak just below the transition to the field polarized phase up to $T \approx 25\,\mathrm{K}$. In contrast, negative fields show the behavior related to the low-temperature skyrmion phase, and increasing temperature leads to a strong reduction in intensity, and no intensity is observed above $T \approx 25\,\mathrm{K}$.

negative field side the curve shape is exactly the same as observed after zero-field cooled. For decreasing magnetic field strength the tilted conical phase reaches its peak without coexistence with the conical phase (white circles), thus allowing a clear signature to be observed. In contrast, for increasing magnetic field strength the conical phase is still observable well after the tilted conical intensity has reached its peak and starts declining again.

Typical data obtained from field-cooled/field-scan

The boundaries of the metastable skyrmion lattice related to the HT-Sky phase were obtained through field scans measured after the sample was cooled in an applied field $B_{\mathrm{FC}} = 29\,\mathrm{mT}$, denoted field-cooled/field-scans. This protocol was carried out with the magnetic field parallel to the neutron beam only. Scattering patterns for increasing and decreasing fields are depicted in figure 5.17 (a) and (b), respectively. The former consists only of a skyrmion lattice

signal, while the latter shows coexistence of helical and skyrmion domains. The helical intensity as a function of magnetic field for different temperatures is obtained by combining both measurement protocols, cf. Fig. 5.17 (c). There are some important difference between the positive and negative field sides of the curve. The helical state is not favored when cooling the sample in a finite magnetic field. Hence, the magnitude of the critical field B_{c1} is larger for negative fields than for positive ones, note that there is a small shift due to frozen magnetic flux in the superconducting magnet but it does not account for the differences observed.

The magnetic field dependence of the intensity resulting from scattering from the skyrmion lattice is complex, cf. Fig. 5.17 (d). When increasing the magnetic field after reaching temperatures below $\sim$ 25 K the intensity remains constant and then increases strongly above 50 mT it reaches a peak and decreases rapidly as the transition to the field polarized phase is reached. There is no significant change in the scattering pattern that would point to a transition from the out-of-equilibrium HT-Sky to the LT-Sky phase. Under a negative field ramp, the recorded signal from the skyrmion lattice rapidly declines and completely vanishes until the typical peak related to the LT-Sky phase develops at the same absolute field values observed for zero-field-cooled/field-scan measurements. The LT-Sky phase exhibits a strong reduction in intensity as the temperature increases.

In contrast, the HT-Sky phase remains constant and seems to gain intensity as the temperature comes closer to 25 K. Above this temperature there is no contribution from the low-temperature skyrmion lattice and the peak of the metastable high-temperature phase just below the field polarized region vanishes, resulting in a broad plateau which falls slowly with increasing magnetic field to decline very fast at ever smaller magnetic fields. The data thus evade explanation by a simple superposition of the contributions from both skyrmion phases.

Neutron scattering measurements following an incomplete minor hysteresis loop in which the magnetic field was increased up to $B = 85$ mT just below the transition to the field polarized phase and then reduced to the starting value again, either B_{FC} or $B = 0$, cf. Fig. 5.18 (a1) and (b1), help to clarify the origin of the increment in the intensity from the metastable skyrmion phase. The measurements were carried out at $T = 23$ K at which the maximum value of the metastable peak was observed. When starting with a zero-field-cooled sample, the intensity of the different magnetic phases is consistent with expectations from the measurements discussed above. Specifically, the tilted conical intensity is strongest when the magnitude of the magnetic field decreases from larger values, and the signal of the low-temperature skyrmion lattice survives down to very low magnetic fields, the conical intensity vanishes at higher magnetic fields and below $\sim$ 50 mT its larger for decreasing than for increasing magnetic fields, indicating a helical domain favored by the field direction.

The incomplete minor loop for a sample field-cooled in B_{FC} yields the same magnetic field dependence for the tilted conical phase as the ZFC measurement. Upon decreasing the magnetic field after reaching $B = 85$ mT, the intensity from the metastable HT-Sky domains grows slightly with the decreasing amplitude of B. At the same time, in contrast to the behavior after ZFC, the conical intensity for a negative field ramp is smaller than the one observed for the positive ramp, leading to the conclusion that the skyrmions domain grow and maintain the gained volume after reversing the field ramp. The scattering patterns for the skyrmion lattice in the latter case show some small differences. When starting the measurement, there is evidence of domains oriented along both $[100]$ and $[010]$ crystallographic axes, with the latter showing stronger Bragg peaks than the former. Upon decreasing the magnetic field, we cannot distinguish between both, due to a reduction of the reciprocal scattering vector length Q, as the starting field value is reached again, the scattering pattern shows only Bragg peaks for a skyrmion lattice oriented along the $[100]$ axes and a ring of scattering indicating disordered

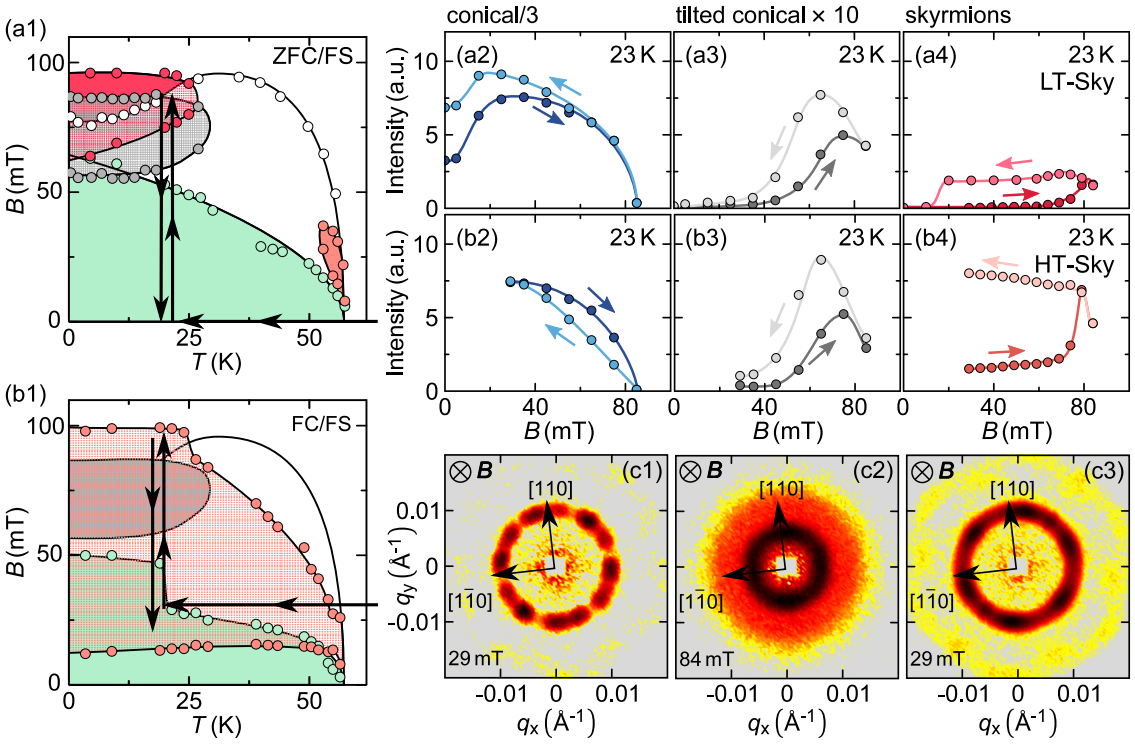

Figure 5.18: Depiction of minor loop measurement and the corresponding starting phase diagram for ZFC and after cooling the sample in B_{FC}, (a1) and (b1), respectively. (a2) - (a4) Measured intensity as a function of the magnetic field for the conical, tilted conical and skyrmion phases after zero-field-cooled. (b2) - (b4) Intensity as a function of the magnetic field obtained after cooling the sample in B_{FC}. The HT-Sky phase shows a substantial enhancement after the minor loop, note that the intensity of the conical phase is significantly reduced on the leg of the decreasing field. (c1) Scattering patterns at the start of the minor loop after cooling in B_{FC}. (c2) Scattering pattern at the maximum field of the loop. (c3) Scattering pattern back at B_{FC} after the minor loop.

skyrmion lattices. Thus, the domains are not only growing, but there is an extensive rearrangement of the magnetic order, which favors one type of domains, likely as a consequence of a small deviation from the magnetic field resulting in a small component along $[010]$.

Magnetic phase diagram from field dependent scans

Magnetic phase diagrams were constructed as discussed for temperature scans. Figure 5.19 contains the results. It is helpful to disregard the helical phase in the following discussion since its phase volume is very small except for magnetic fields close to zero. The tilted conical phase shows a constant upper transition field value for both zero-field- and high-field-cooled measurements. The small hysteresis in the lower critical field originates in demagnetizing effects. The conclusion derived from the conical boundaries is consistent with the observations made in temperature scans, i. e., the transition from the conical to field polarized phase shifts to lower values below $\sim$ 30 K. Below $\sim$ 10 K there is an additional reduction in the critical field of the conical phase, these correlate with the temperatures for which the low-temperature skyrmion lattice is strongest in field scans starting at high-fields. Note that this is also the same temperature region in which the LT-Sky phase is observed in field-cooled measurements (cf. Fig. 5.13 (b2)). Above 10 K the intensity from the LT-Sky in HFC-FS measurements

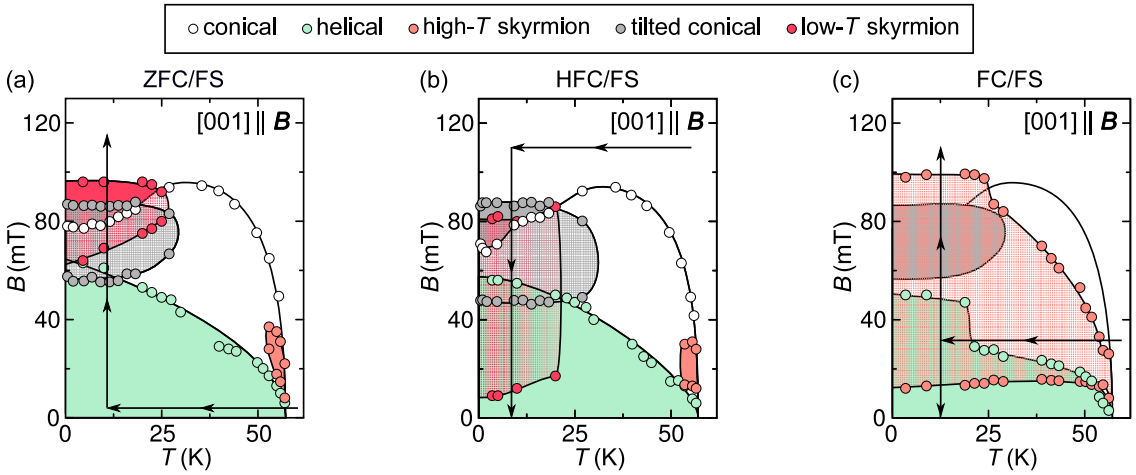

Figure 5.19: Magnetic phase diagrams from field scan measurements. (a) ZFC/FS At low temperatures the transition to the polarized phase occurs last for the low-temperature skyrmion lattice. (b) HFC/FS: At low temperatures the extent of the LT-Sky phase expands considerably. Note that above $\sim$ 10 K the intensity of the latter sharply decreases. (c) FC/FS: The metastable state of the HT-Sky phase covers almost the entire phase diagram, and below $\sim$ 25 K its the last phase to transition to the field polarized state.

declines substantially as a consequence of irreversible processes, as demonstrated by the fact that no such reduction is observed in temperature scans nor field scans following a zero-field cooling. Otherwise, the boundaries are consistent with the characteristics observed in temperature scans, i. e., the boundaries are highly hysteretic depending on the sign of the field ramp.

The phase boundaries resulting from measurements after cooling the sample through the skyrmion phase show two important properties: 1. there is an enhancement of the critical field related with temperatures at which the low-temperature skyrmion lattice is observed and 2. the low field boundary shows almost no temperature dependence, a fact hinted at by the temperature scans and corroborated by the field-cooled/field-scans. The high-temperature skyrmion phase profits from the increasing anisotropy with decreasing temperature and increasing field, resulting in larger domains.

5.4 MEAN FIELD ANALYSIS INCLUDING CUBIC ANISOTROPIES

The most important developments in the field of magnetic skyrmions in chiral magnets have been accompanied by theoretical analysis based on a Ginzburg-Landau ϕ^4-Model already discussed in the first paper identifying the skyrmion lattice in MnSi by Mühlbauer *et al.*[11]. It was further used in the analysis of the skyrmion decay [75], as well as the study of the universal magnetic excitations in chiral magnets with $P2_13$ space group [143]. Here the same approach is followed to explain the appearance of the low-temperature skyrmion lattice and the tilted conical phase. The increment of the ring intensity, after cycling of the magnetic field amplitude, establishes the connection of the former to the ground state of the system. The origin of both new phases is constrained by the anisotropic character of the phase diagram, i. e., both phases are only observable for $\boldsymbol{B} \parallel \langle 100 \rangle$, and the fact that these are observed for 'high' fields, in contradiction with the well-understood phase diagram of MnSi, where an alignment of the helices parallel to the magnetic field is energetically favorable. Hence, the anisotropy increases nonlinearly with the magnetization squared.

$$F_a = -K \int \mathrm{d}^3\boldsymbol{r} \left(M_x^4 + M_y^4 + Mz^4 \right) \tag{5.1}$$

represents the only anisotropic term to lowest order in spin-orbit coupling in the $P2_13$ space group of Cu_2OSeO_3 which fulfills the constrains described above, where K is a constant. Most research neglects its effects, instead opting for the introduction of uniaxial anisotropies and their effects on the stabilization of skyrmions, especially in thin samples [53, 99, 144, 145].

This cubic anisotropy term is found in typical textbooks discussing the effects of crystalline structure in ferromagnets such as Fe and Ni. Recently, Grigoriev and collaborators reviewed its effects on the stability of the helical order, as well as its contributions to the critical field of the field polarized transition [146] and found that the latter decreases in the presence of cubic anisotropies of comparable size to the Dzyaloshinskii-Moriya interaction. Specifically, the helical order becomes unstable at a finite spin angle concerning the propagation direction, and the system undergoes a first-order phase transition into the field polarized phase. Their conclusions are derived for a model of helix under consideration of all major contributions to its energy without considering further magnetic structures that might be stabilized by the anisotropic contributions. Still, their main observations are in agreement with the results presented here. The tilted conical phase can be understood as an attempt to avoid the first-order transition to the homogeneous state. Magnetization and susceptibility measurements on Cu_2OSeO_3 published recently support this conclusion as the tilted conical phase is related to a steep increment in the magnetization [142].

The experimental results are already a strong indication that the new phase related to the ring of intensity consists of some skyrmion lattice order. A plausibility check can be obtained by verifying whether 5.1 is able to stabilize a skyrmion lattice versus a conical, tilted conical, and ferromagnetic phase, where stable is the phase of lowest free energy in a model considering all relevant contributions. In the present case, such an energy functional can be separated into three components $F = F_0 + F_d + F_a$. In momentum space, the first one reads:

$$\begin{aligned} F_0[\boldsymbol{M}] = \sum_{Q} \Bigg(& \frac{J}{2}(\boldsymbol{Q}\cdot\boldsymbol{Q})(\boldsymbol{M}_{\boldsymbol{Q}}\cdot\boldsymbol{M}_{-\boldsymbol{Q}}) + iD\boldsymbol{M}_{-\boldsymbol{Q}}\cdot(\boldsymbol{Q}\times\boldsymbol{M}_{\boldsymbol{Q}}) + r_0\boldsymbol{M}_{\boldsymbol{Q}}\cdot\boldsymbol{M}_{-\boldsymbol{Q}} + \\ & + U \sum_{\boldsymbol{Q}_2,\boldsymbol{Q}_3,\boldsymbol{Q}_4} (\boldsymbol{M}_{\boldsymbol{Q}}\cdot\boldsymbol{M}_{\boldsymbol{Q}_2})(\boldsymbol{M}_{\boldsymbol{Q}_3}\cdot\boldsymbol{M}_{\boldsymbol{Q}_4})\delta_{\boldsymbol{Q}+\boldsymbol{Q}_2+\boldsymbol{Q}_3+\boldsymbol{Q}_4,0} \Bigg) - \boldsymbol{B}\cdot\boldsymbol{M}_0 \end{aligned} \tag{5.2}$$

and is able to reproduce key qualitative characteristics of chiral magnets, such as the helical and conical phase [83, 94], as well as the high temperature skyrmion phase [11, 75, 101, 143]. This is the same functional used in the derivation of the magnetic susceptibility in chapter 3.

The parameter r_0 quantifies the distance from the phase transition while U stabilizes the functional. J accounts for the exchange strength, while D is given by the strength of the Dzyaloshinskii-Moriya interactions and $\boldsymbol{B}$ the magnetic field.

$$F_d[\boldsymbol{M}] = \tau \left(\boldsymbol{M}_0 N \boldsymbol{M}_0 + \sum_{\boldsymbol{Q}} \frac{(\boldsymbol{Q}\cdot\boldsymbol{M}_{\boldsymbol{Q}})(\boldsymbol{Q}\cdot\boldsymbol{M}_{-\boldsymbol{Q}})}{\boldsymbol{Q}\cdot\boldsymbol{Q}} \right), \tag{5.3}$$

is the second contribution and accounts for dipolar interactions with a relative strength of τ. N is the demagnetization tensor, with $\mathrm{tr}(N) = 1$. The third and final contribution F_a arises from the cubic anisotropies and is given by:

$$F_a[\boldsymbol{M}] = -K \sum_{\boldsymbol{Q},\boldsymbol{Q}_2,\boldsymbol{Q}_3,\boldsymbol{Q}_4} \left(M^x_{\boldsymbol{Q}} M^x_{\boldsymbol{Q}2} M^x_{\boldsymbol{Q}3} M^x_{\boldsymbol{Q}4} + \ldots \right) \delta_{\boldsymbol{Q}+\boldsymbol{Q}_2+\boldsymbol{Q}_3+\boldsymbol{Q}_4,0} \tag{5.4}$$

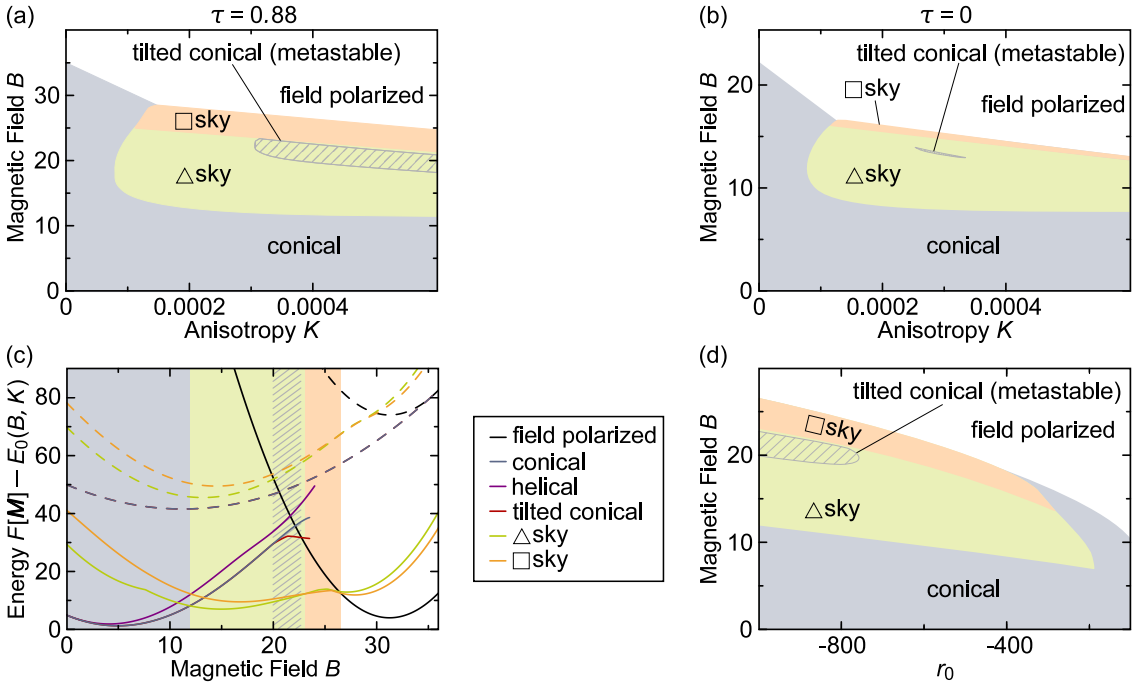

Figure 5.20: Phase diagrams resulting from Ginzburg-Landau model as a function of anisotropy K and magnetic field B for dipolar interactions $\tau = 0.88$ as reported for Cu_2OSeO_3, (a), and for comparison in the absence of the former, i. e., $\tau = 0$, (b). Above a critical anisotropy value K_c, skyrmion lattices are stabilized at finite magnetic fields. There are two forms of morphology, i. e., a square lattice, and a triagonal (hexagonal) lattice. Increasing the anisotropy further leads to a region in phase diagram where the tilted conical phase has energy lower than the conical phase (hatched region), but the skyrmion lattices remained the ground state of the system.

with K the anisotropic constant. Other anisotropy terms of similar strength, such as $(Q_x^4 + ...)\boldsymbol{M}_{\boldsymbol{Q}} \cdot \boldsymbol{M}_{-\boldsymbol{Q}}$ and $Q_x^2 M_{\boldsymbol{Q}}^x M_{-\boldsymbol{Q}}^x$, do not fulfill the conditions set out before and are not necessary to understand the experimental results obtained. Additionally, terms of higher order in spin orbit coupling are neglected since they are formally weaker. A rescaling transformation permits J, D and U to be eliminated, thus in the consecutive discussion these are set $J = D = U = 1$. Dipolar interactions suppress the transition to the field polarized state and for Cu_2OSeO_3 there are reports of $\tau \approx \chi_{\text{con}}^{\text{int}}/2 \approx 0.88$ [143]. Hence the free paramaters of the model are B, r_0, K and N, unless stated otherwise the results discussed here were obtained for $r_0 = -1000$ (equivalent to very low temperatures), $K = 0.004$ and $N = \frac{1}{3}\mathbb{1}$ (corresponding to a sphere).

As stated by its name, the low-temperature skyrmion lattice becomes more stable towards the low-temperature limit. Hence fluctuations can be neglected, and a mean-field approximation is followed using the magnetization $\boldsymbol{M}_{\boldsymbol{Q}}$, which has been parametrized to respect the relevant symmetries on a lattice in momentum-space corresponding to a specific phase. Note that such a parametrization does not prevent states involving phases beyond the one of interest, e. g., the field polarized state is in most cases a special solution with infinite wave vector. The mean-field approach entails the identification of the minima of $F[\boldsymbol{M}]$, these are often close to each other, and thus the identification of the global minimum is cumbersome. Thus a combination of different methods, including random starting values, manually scripted starting values, results of previous minimizations with similar starting parameters and interpolation of several previous results, was used to generate starting values for a quasi-Newton

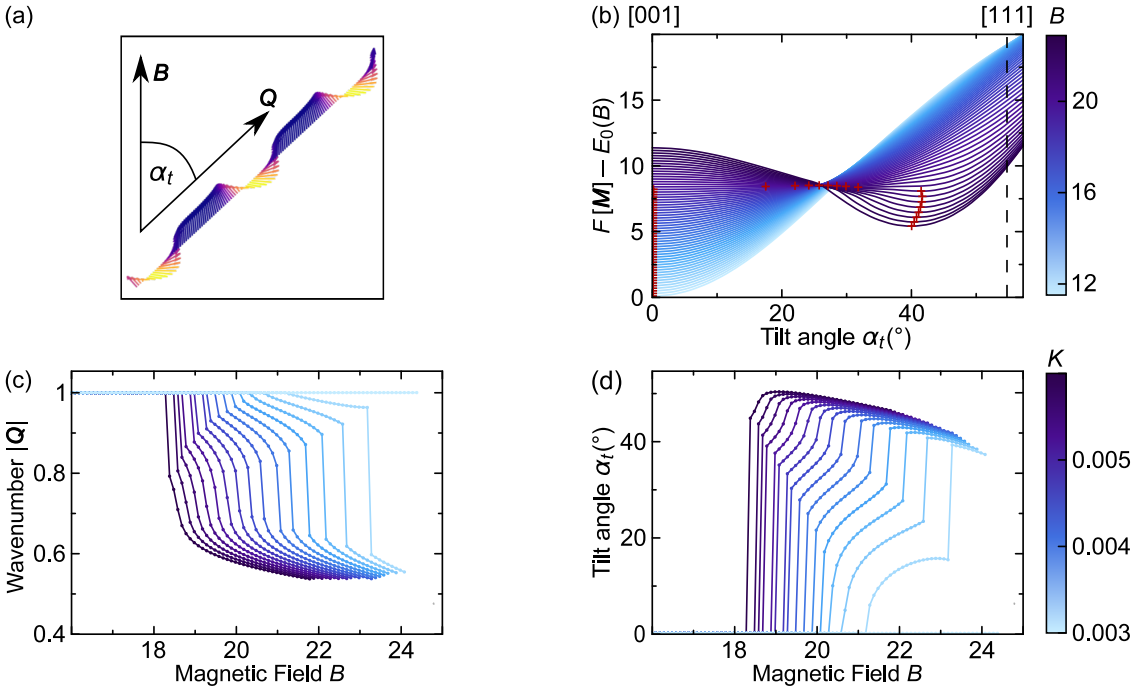

Figure 5.21: (a) Real space depiction of the tilted conical phase. The angle enclosed by the propagation vector $\boldsymbol{k}$ and the magnetic field $\boldsymbol{B}$ is denoted α_t and measured in a big circle connecting $[001]$ and $[111]$. (b) Energy of the tilted conical phase as a function of tilt angle α_t for different values of magnetic field B, calculated for $r_0 = -1000, K = 0.004, \tau = 0.88$ and $N = \frac{1}{3}\mathbb{1}$. For $B > 19.9$, the energy minimum moves towards finite values of α_t. Note that $\alpha_t = 0$ represents the conventional conical phase. (c) Wavenumber $|\boldsymbol{Q}|$ of the tilted conical phase as a function of the magnetic field for different values of anisotropy K. (d) Evolution of the tilt angle α_t of the tilted conical phase as a function of B for different values of K. Both values show discontinuities as a function of the magnetic field. The lowest values of K seem to reproduce the experimental results best.

minimization, resulting in a solution for each parametrization at each point in phase space. The results are summarized in a phase diagram as a function of K and B in figure 5.20 (a), for comparison the phase diagram obtained for $\tau = 0$ is depicted in figure 5.20 (b).

The viability of a tilted conical phase is determined by calculating its energy as a function of an angle α_t between the propagation vector $\boldsymbol{Q}$ and $\boldsymbol{B} \parallel [001]$ at different field values, cf. 5.21 (a), where α_t is measured along a great circle connecting $[001]$ and $[111]$. The calculated energy for different field values is plotted in figure 5.21 (b). Starting at a critical value $B_{ct} \approx 19.9$ the minimum in energy shifts from $\alpha_t = 0$ to finite values indicating the instability of the conical phase, hence the tilted conical phase becomes energetically favorable. The field polarized phase also gains energy from the contributions arising from F_a for $K > 0$, and in the presence of weak dipolar interactions ($\tau \ll 1$) it becomes the ground state in the same field region as the tilted conical would be favored with respect to the conical phase. The dipolar interactions in Cu_2OSeO_3 are strong and penalized the polarized state enough for a larger phase space to developed in which the tilted conical would be preferred, marked by the hatched regions in the phase diagrams in figure 5.20. The model described above does not yield a set of parameters for which the tilted conical phase becomes the ground state. It is metastable and masked by the skyrmion lattice. One could consider further anisotropic terms and their extensions for which the tilted conical state is the ground state for specific parameters, but these models also yielded a helical phase propagating along $\langle 111 \rangle$ directions

of the system at $B = 0$. That is in clear contradiction to experimental observations; thus, these extensions cannot explain the phase diagram obtained for Cu_2OSeO_3.

The length of the propagation vector $|\boldsymbol{Q}|$ and the angle α_t can be obtained from the model. Both are plotted as a function of magnetic field B for different values of anisotropy K in figure 5.21 (c) and (d), respectively. The results from the model agree qualitatively with the experimental observations, i. e., α_t increases with the increasing magnetic field, while $|\boldsymbol{Q}|$ decreases. There are discontinuities in both of these values which are not present in the experimental results. These indicate spontaneous changes to the magnetic structure, which involved a rearrangement of the spins over large sample areas. Additional anisotropy terms have a strong effect on the details of these jumps, hence the presence of defects might smear them out.

A similar analysis considering skyrmions as the magnetic order yielded *at least two* different skyrmion lattices which are stabilized for anisotropy values higher than $K_c \approx 0.001$, i. e., a triangular and a square lattice, as already indicated in the phase diagrams shown in figure 5.20. Using $K_\mathrm{c} = K_{\sigma,\mathrm{c}}/M_\mathrm{s}^4$ the critical anisotropy can also be expressed in terms of material-specific parameters as the ratio $K_{\sigma,\mathrm{c}}/(B_{\mathrm{c2}}^{\mathrm{int}} M_\mathrm{s}) = 0.07$, with the cubic anisotropy in units of energy density $K_{\sigma,\mathrm{c}}$, the critical field for the transition to the field-polarized phase $B_{\mathrm{c2}}^{\mathrm{int}}$ and the saturate magnetization M_s, a roughly estimate sets the cubic anisotropy for Cu_2OSeO_3 at $K_{\sigma,\mathrm{c}} \approx 400\,\mathrm{J m^{-3}}$. On the one hand the ratio $K_{\sigma,\mathrm{c}}/(B_{\mathrm{c2}}^{\mathrm{int}} M_\mathrm{s})$ scales with λ_{SOC}^2, hence the skyrmion lattice is stable only if λ_{SOC} is strong enough, on the other hand it is less susceptible to the effects of dipolar interactions and does not depend on their presence to avoid masking by the field polarized state, cf. Fig. 5.22 (d).

The wavenumber $|\boldsymbol{Q}|$ obtained from these calculations shows a good qualitative agreement with the experimental results, specifically a reduction with increasing magnetic field for different values of anisotropy K, as illustrated in figure 5.22. Independent of the value of the latter both types of skyrmion lattices show discontinuities in $|\boldsymbol{Q}|$ as a function of magnetic field, related to deformations of the lattice or the skyrmions themselves in the case of the triangular lattice, or changes in the orientation in the case of the square lattice between $\boldsymbol{Q} \parallel \langle 100 \rangle$ or $\boldsymbol{Q} \parallel \langle 110 \rangle$. Real space representations of the skyrmion phases associated with solutions of the mean-field approach are shown in figure 5.22 (c). The sharp transition out of the skyrmion phase at low fields for decreasing magnitude could be related with the deformation demanded by the model, in the sense that it could facilitate the transition to the conical state. An overview of the field dependence of the propagation length $|\boldsymbol{Q}|$ for all different magnetic phases is plotted in figure 5.22 (d) for an extended field region independent of the phase stability. The stable phase is illustrated by the background color and denoted on top of the graph. The agreement between theory and experiment is excellent, regardless of the phase. Importantly, none of the abrupt changes in wavenumber are observed in neutron scattering, either due to instabilities arising from large reconfigurations of the spin magnetic order or to masking originating from higher order anisotropic contributions.

Unbeknownst to the author before the publication of the study above, Andrey Leonov had analysed the stabilization of the skyrmion lattice by cubic anisotropies in a paper published in 2014 [147].

5.5 SUMMARY

A thorough small-angle neutron scattering study of the magnetic phase diagram of Cu_2OSeO_3 identified a new independent skyrmion lattice phase ground state at temperatures below

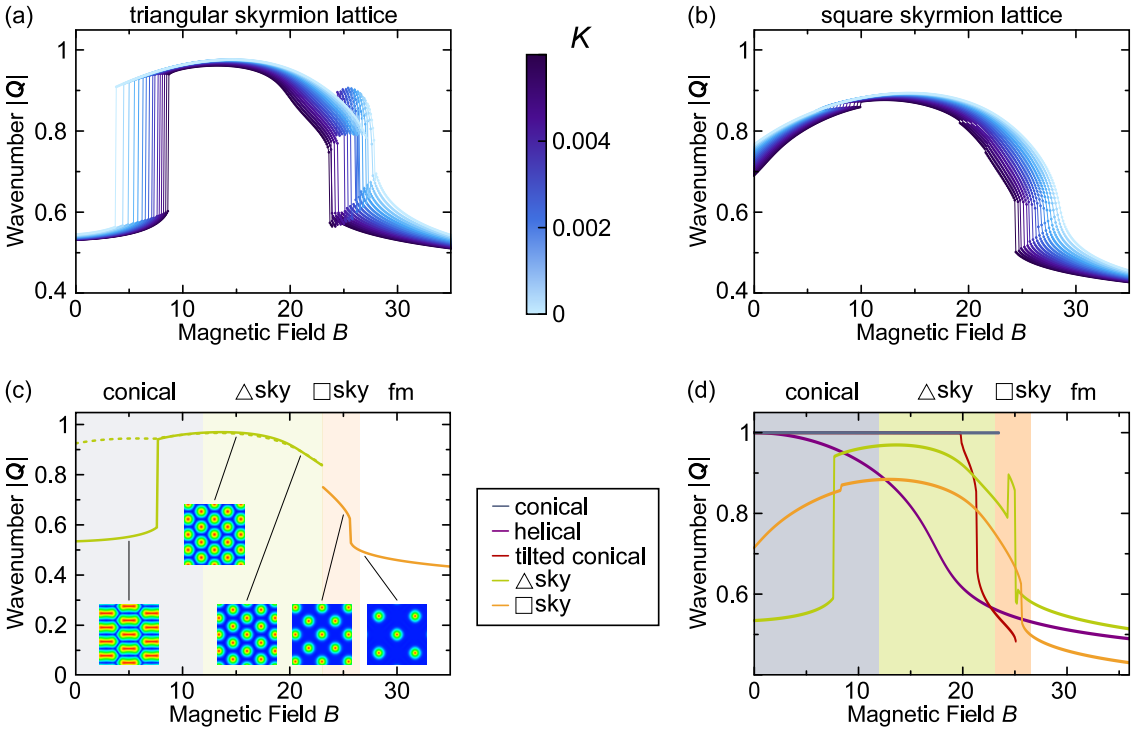

Figure 5.22: Wavenumber $|\boldsymbol{Q}|$ as a function of the magnetic field for the triangular (a) and square skyrmion lattice (b) for different values of anisotropy K. Both show discontinuities associated with changes in the morphology of the lattices. These are depicted in (c), note that only the triangular lattice is observed directly experimentally. (d) Wavenumbers for the different phases as a function of the magnetic field. Qualitatively these results match experimental observations very well, note that the phases are not stable over the entire magnetic field region depicted.

$\sim$ 10 K, between $\sim 0.7 B_{c2}$ and B_{c2}, for $\boldsymbol{B} \parallel \langle 100 \rangle$. Additionally, a so-called tilted conical phase was also observed for this magnetic field configurations. Minimization of the free energy from an appropriate Ginzburg-Landau model including an anisotropic term of the form

$$F_a = -K \int \mathrm{d}^3\boldsymbol{r} \left(M_x^4 + M_y^4 + M z^4 \right) \tag{5.5}$$

confirms that for values of $K > K_c = K_{\sigma,\mathrm{c}} / M_\mathrm{s}^4$, a skyrmion configuration has a lower energy than the conical phase observed in this region of magnetic phase diagram in similar materials such as MnSi, where $K_{\sigma,\mathrm{c}} \approx 400\ \mathrm{J m^{-3}}$ using material-specific parameters. Larger values of K result in a tilted conical phase with lower energy than the conical and field polarized phases.

The transition to and from the skyrmion lattice phase is strong first-order, resulting is strong hysteresis on the phase boundaries leading to large areas of the phase diagram in which the new low-temperature skyrmion phase survives metastably. Overall experiment and theory are in good qualitative agreement, and the latter is able to reproduce the magnetic field dependence of characteristic parameters such as the wavenumber $|\boldsymbol{Q}|$ describing the different phases and the tilt angle of tilted conical phase. Furthermore, it is possible to obtain a B/T magnetic phase diagram from the theory which confirms the confinement of the new skyrmion lattice ground state to low temperature and relatively high fields.

This study constitutes the first observation of two independent, disconnected skyrmion phase pockets stabilized by different mechanisms, i. e., thermal fluctuations and magnetocrystalline anisotropy for the high temperature and low-temperature skyrmion phases, re-

spectively. Most of the cubic system thoroughly studied to time of writing have very small anisotropic contributions, thus resulting is subtle but distinguishable effects as the ones discussed in chapter 3. Some of the data published on the β-Mn compounds resemble that from Cu_2OSeO_3, hence the metastable skyrmion phase and the associated structural transition observed in the former might be driven by magnetocrystalline contributions as the ones discussed here.

6

SUMMARY AND OUTLOOK

The scientific interest in complex magnetic structures increased substantially with the discovery of magnetic skyrmions in MnSi, especially in the context of modern technologies [10, 11]. The spin arrangement of a magnetic skyrmion forms a sphere when mapped into order space, which puts them in a different topological category as other types of magnetic order such as ferromagnetism. The former are topologically non-trivial and, thus, cannot be continuously transformed into the trivial ferromagnetic order. The topology of skyrmions is at the heart of exciting new properties, such as spin-transfer torques, and the topological hall effect [14–17]. These properties have inspired new types of magnetic storage media [19]. Their particle-like nature is at the heart new type of transistors and logic gates [20, 21]. One of the challenges on the path of these technological applications is the region of stability of skyrmions, as most materials able to host these magnetic textures, do so at low temperatures and in finite magnetic fields. This thesis presented results regarding the role magnetic anisotropies play in the phase diagrams of cubic helimagnets, and especially in the stabilization of magnetic skyrmions.

A brief introduction into magnetic interactions, topology and the study of magnetic skyrmions was given in chapter 1. Chapter 2 presented the theory behind neutron scattering and emphasizing magnetic neutron scattering. The chapter also reviewed important aspects in the study of cubic helimagnets using small-angle neutron scattering and finished with the presentation of the resolution and specific capabilities of the instruments used for the experiments discussed in this study.

The effects of magnetocrystalline anisotropies on the transition from the helical to the conical phase were discussed in chapter 3. The helical phase consists of magnetic helices propagating along a preferred direction with its spin pointing perpendicular to it, the features observed in bulk measurements such as magnetization and ac magnetic susceptibility arise from the coexistence of helices propagating parallel to equivalent crystallographic directions. The study was carried out on MnSi, the preferred axis of propagation are the space diagonals i. e., $\langle 111 \rangle$ crystallographic axes, resulting in four degenerate configurations. The conical phase, in contrast, is characterized by a single propagation direction pointing parallel to the magnetic field. The spins are no longer perpendicular to it but instead, rotate towards it with increasing magnetic field.

The role of magnetocrystalline anisotropies was investigated by looking at the transition between conical and helical phases for magnetic fields applied in different crystallographic directions. A theoretical study carried out by collaborators revealed that there are three distinct scenarios: (1) a magnetic field along the axis with the highest symmetry i. e.,$\langle 100 \rangle$, results in two elastic Ising transitions, (2) if the field points along $\langle hk0 \rangle$ a single elastic transitions is observed and (3) for all other directions there is no elastic transition, instead the reorientation represents a crossover phenomenon, which means that a phase transition is not discernible. A thorough magnetization and ac-susceptibility study was complemented by small-angle neutron scattering measurements. The experimental results are in remarkable agreement with the theoretical calculations, and the expected transitions were all observed. However the experimental results showed a hysteresis in nominal continuous elastic Ising transitions, and the features measured were sharper and more robust when the transition was approached

from the single domain conical state. A possible explanation is the formation of non-trivial topological defects that inhibit the coalescence of magnetic domains.

Regarding the role of uniaxial anisotropies, the first theoretical studies about the magnetic skyrmions suggested that such an additional contribution was needed to stabilize these textures in MnSi [39]. This assertion and subsequent theoretical studies motivated the study of the magnetic phase diagram in MnSi under uniaxial pressure. The results of this study were presented in chapter 4. Using a bespoke He-loaded uniaxial pressure cell different crystals of MnSi were placed under uniaxial pressures up to $\sim 2\,\mathrm{kbar}$. The different crystals allowed the pressure to be applied in different crystallographic directions, enabling the observation of the interplay between uniaxial and magnetocrystalline anisotropies. The main experimental probe was small-angle neutron scattering, complemented by ac-susceptibility measurements.

In general, uniaxial pressure in MnSi creates a new preferred axis of propagation. In zero-field, the helices start rotate towards the stress axis with increasing pressure. This can be exploited for experimental probes that demand a single domain helical state, which is obtained if pressure is applied parallel to a $\langle 111 \rangle$ axis. The area of stability of the skyrmion lattice may be tuned via the application of uniaxial pressure. However, the geometric relation between the magnetic field and the pressure axis is critical. If they point parallel to each other the skyrmion lattice is suppressed, as both magnetic field and anisotropy favor a conical propagation. When the magnetic field and pressure are perpendicular, the skyrmion lattice is stabilized to substantially lower temperatures.

Chapter 5 discussed the recent discovery of a second independent skyrmion lattice phase in the cubic chiral magnet Cu_2OSeO_3. The second phase is only observed when the magnetic field is applied parallel to a $\langle 100 \rangle$ crystallographic axis, which happens to be the easy-axis of the system. Skyrmion phases in chiral magnets are stabilized by thermal fluctuations and are observed for small temperatures regimes just below the transition to the paramagnetic phase. In contrast, the new skyrmion is stable below $\sim 10\,\mathrm{K}$ and for magnetic fields just below the transition to the field polarized phase. It shows a strong dependence on the magnetic field, as the skyrmions become larger as the former increases. Its boundaries are strongly hysteretic and demark completely different regions of stability depending on the magnetic field and temperature history.

In addition to this low-temperature skyrmion phase, a so-called tilted conical phase was also observed below $\sim 20\,\mathrm{K}$ for fields close to the field polarized transition. This magnetic order consists of a complex twist of the spins the result in a larger homogeneous magnetization when compared with a typical conical propagation. The boundaries of this phase showed almost no hysteresis and it seems to function as a sort of catalyst for the formation of the low-temperature skyrmion phase, as it was always observed before the skyrmion phase nucleates.

Collaborators from the University of Cologne carried out a mean field analysis as a plausibility check that the observe Bragg peaks, were indeed related to a skyrmion lattice. Their results confirmed that cubic anisotropies can reduce the energy of the skyrmion lattice enough for it to become the ground state at low temperatures and high magnetic fields. The calculations do not foresee the emergence of the tilted conical phase.

Cubic anisotropies may be at the heart of interesting phenomena observed in other skyrmion hosting compounds, such as the transition to a square lattice at low temperatures in β-Mn compounds [46]. The study of the effects of uniaxial pressure in this new phase in Cu_2OSeO_3 might open a door into new phenomena regarding magnetic skyrmions. The avenue of tuning the anisotropies in the search of skyrmion hosting materials suitable for technological devices

might be very fruitful and resolve some of the issues encountered so far, such as skyrmion size and even their existence in some thin films. The observation of skyrmions at very low temperatures and very small magnetic fields, could facilitate the study their interaction with vortices in superconductors.

A

APPENDIX: CORRECTION TO NEUTRON SCATTERING ANALYSIS

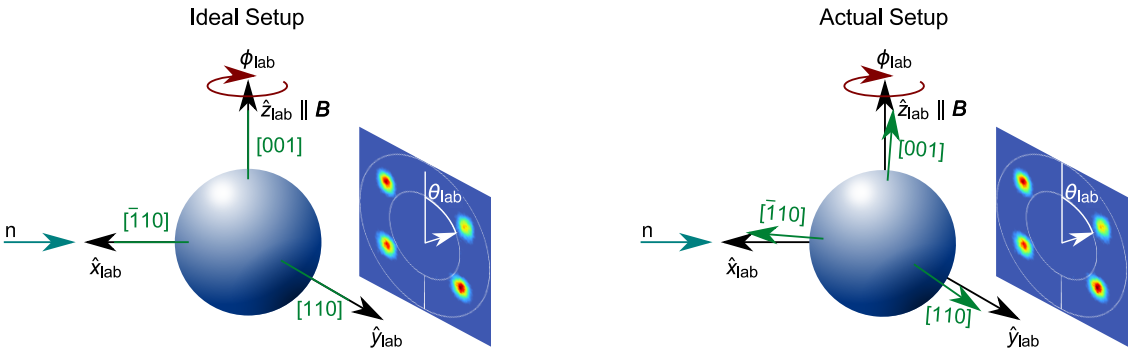

Figure A.1: Ideal and actual setup for the measurements presented in chapter 3. The orientation of the sample is defined by a rotation axis perpendicular to the $\hat{z}_{lab}$ axis. A second rotation axis parallel to $\hat{z}_{lab}$ allows to measure a sphere in reciprocal space by rotating the sample by ϕ_{lab}. The measured position of the Bragg peak is defined as a θ_{lab}. In the actual setup a deviation from both rotation axes results in a shifted coordinate system.

The measurements performed in chapter 3 were unusual, due to the fact that it combined measurements over a full sphere in reciprocal space while comparing results for magnetic fields applied along different crystallographic directions. The ideal setup to achieve both these goals requires a axis of rotation along the laboratory vertical axis $\hat{z}_{lab}$ parallel to the magnetic field direction and a second axis of rotation perpendicular to $\hat{z}_{lab}$ parallel to a $\langle 110 \rangle$ axis to select any crystal orientation with respect to the magnetic field. Such an ideal experimental setup is depicted in figure A.1. There were two origins of discrepancy from the aforementioned setup, the rotation axis perpendicular to $\hat{z}_{lab}$ has a small deviation with respect to a $\langle 110 \rangle$ axis and the sample stick is not perfectly straight, resulting in a precession of the sample when rotated by the angle ϕ_{lab}. This is illustrated in figure A.2 (a) by the scattering patterns obtained for crystallographic directions 90° apart, note how the center of the scattering pattern shifts for the different orientations.

The effects of this shift are schematically portrayed in figure A.2 (b), where the observable values are denoted with a prime and the intrinsic values without one. The change in position of the center is parametrized by an angle γ and a distance ΔR. The analysis carried out here averages the intensity over a radius range, hence one can disregard Q'_- and Q'_+, concentrating instead on the values of the azimuthal angles θ'_{-Q} and θ'_{+Q}, cf. figure A.1. The arithmetic mean of these two angles is designated $\bar{\theta}'$ for a given helical propagation direction. This average is the value we used for our fits, as it is closed to the intrinsic value of theta for precessions with a small amplitude.

Consider first the measured values for each Bragg peak:

$$\theta'_{+Q} = \theta + \alpha$$
$$\theta'_{-Q} = \theta - \beta$$
$$\hat{\theta}' = \theta + \frac{\alpha - \beta}{2}$$

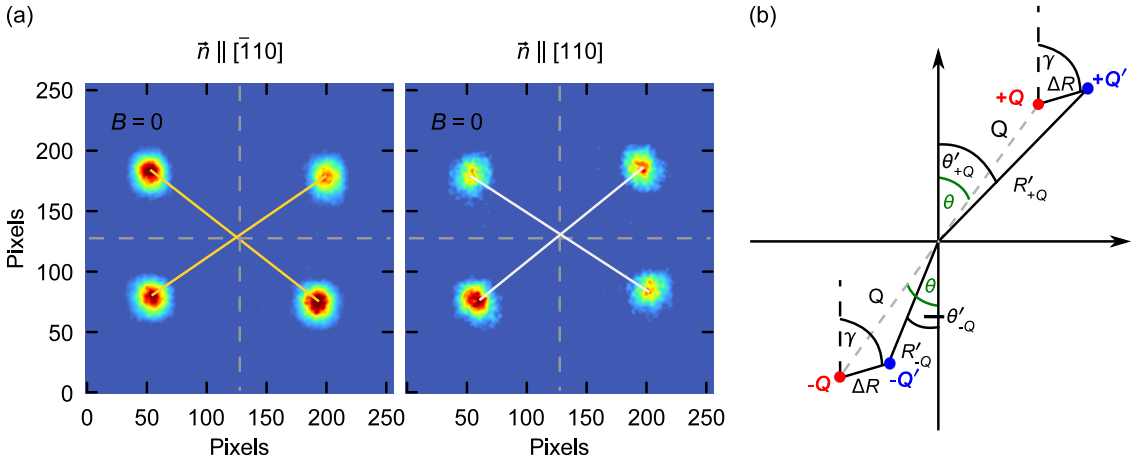

Figure A.2: Precession of the sample due to small deviation of the sample stick from a straight line. (a) Scattering patterns obtained for a neutron beam $\vec{n}$ parallel to a $[\bar{1}10]$ and $[110]$ axes. Note how the center of the scattering plane, where both lines cross, moves from one image to the next. (b) Schematic representation of the shift of the Bragg peaks as a consequence of the precession, the movement of the center of the scattering plane is parametrized by γ and ΔR.

Both angles α and β are defined by the intrinsic positions Q, θ and the shift of the center $\Delta R, \gamma$:

$$\alpha = \arccos\left(\frac{Q + \Delta R\cos(\gamma-\theta)}{R'_{+Q}}\right) = \arccos\left(\frac{Q + \Delta R\cos(\gamma-\theta)}{\sqrt{Q^2+\Delta R^2+2Q\Delta R\cos(\gamma-\theta)}}\right)$$
$$\beta = \arccos\left(\frac{Q - \Delta R\cos(\gamma-\theta)}{R'_{-Q}}\right) = \arccos\left(\frac{Q - \Delta R\cos(\gamma-\theta)}{\sqrt{Q^2+\Delta R^2-2Q\Delta R\cos(\gamma-\theta)}}\right)$$

The discrepancy between the average of the measured theta angle and the intrinsic value is then given by

$$\Delta\bar{\theta}' = \bar{\theta}' - \theta = \frac{\alpha-\beta}{2}.$$

Considering the summation rule for arccosines

$$\arccos x_1 - \arccos x_2 = \arccos x_1x_2 + \sqrt{(1-x_1^2)(1-x_2^2)}$$

it yields

$$\Delta\bar{\theta}' = \frac{1}{2}\arccos\left(\frac{Q^2-\Delta R^2\cos(2\gamma-2\theta)}{\sqrt{Q^4-2Q^2\Delta R^2\cos(2\gamma-2\theta)+\Delta R^4}}\right).$$

A careful look at this expression reveals that the largest value of $\Delta\bar{\theta}'$ is obtained when the cosine becomes zero, which means that the relative angle between γ and θ is 45°. Hence the largest deviation as a function of $\Delta R/Q$ reads

$$\Delta\hat{\theta}'_{\text{max}} = \frac{1}{2}\arccos\left(\frac{1}{\sqrt{1+\frac{\Delta R}{Q}^4}}\right)$$

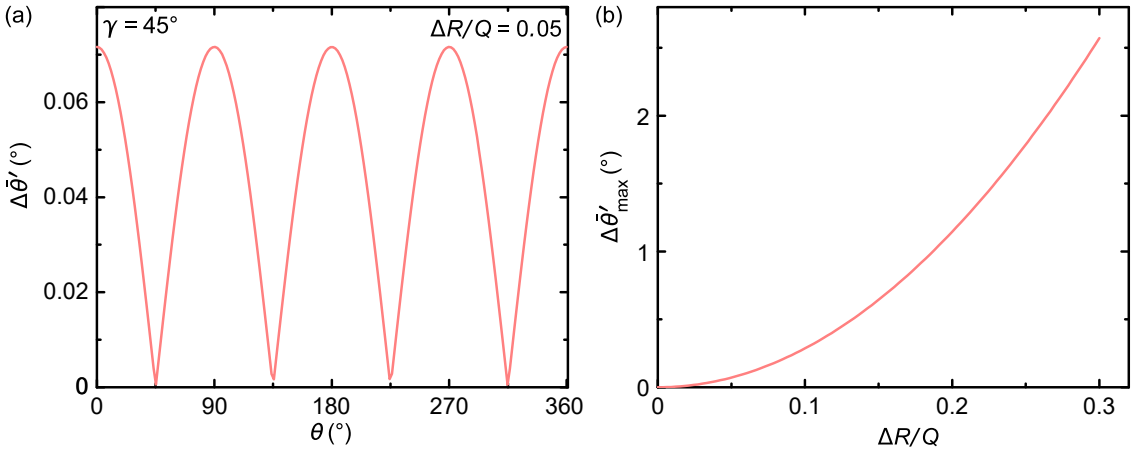

Figure A.3: Analysis of discrepancy between averaged angle $\bar{\theta}'$ and intrinsic azimuthal angle θ, defining the position of the Bragg peaks. (a) $\Delta\bar{\theta}'$ as a function of intrinsic azimuthal angle θ for a shift of $\Delta R/Q = 0.05$ along an angle of $\gamma = 45°$. (b) Maximal discrepancy $\Delta\bar{\theta}'$ as a function of relative shift $\Delta R/Q$, note the small values of the maximum discrepancy.

The magnitude of the discrepancy $\Delta\hat{\theta}'$ between the measured averaged and intrinsic azimuthal angle as a function of intrinsic angle θ is plotted in figure A.3 (a) for a shift of $\Delta R/Q = 0.05$ along an angle $\gamma = 45°$. The relative shift represents a typical value observed in this experiment. Note that a change in γ results in a motion of the curve along the θ axis. In this case the maximum discrepancy is $\sim 0.07°$, which is much smaller than our experimental resolution in the azimuthal direction. Exploring the maximum value of $\Delta\bar{\theta}'$ reveals that for shifts below $\Delta R/Q \approx 0.3$ the discrepancy in the measured angle remain below $3°$. Hence the effects of the precession are neglected in the analysis of the Bragg peak position presented in chapter 3 and the $\bar{\theta}'$ has been used instead.

It is important to regard the measured values of $\hat{\theta}'$ and ϕ_{lab} in an intrinsic coordinate system, which was defined in chapter 3, cf. figure 3.6, in order to compare them with the theoretical calculations. For that purpose one needs to carefully determined the orientation of the sample. This can be defined by the direction of the $[\bar{1}10]$ and $[110]$ axes. These can be described by two angles δ_1 and δ_2, which described the angle between the crystallographic directions and a imaginary horizontal line, representing the ideal orientation. These angles are defined by:

$$\delta_1 = \frac{\bar{\theta}'^{[111]} - \bar{\theta}'^{[\bar{1}\bar{1}1]}}{2} \qquad \delta_2 = \frac{\bar{\theta}'^{[\bar{1}11]} - \bar{\theta}'^{[1\bar{1}1]}}{2}$$

where $\bar{\theta}$ are the averaged angles for each domain measured after zero-field cooling, the measured tilts for a setup with $[100]$ parallel to $\hat{z}_{\text{lab}}$ are shown in figure A.4. In this case the scattering patterns yield $\delta_1 = 2.3°$ and $\delta_2 = -2.8°$. After extracting the domain positions $\boldsymbol{Q}$ parametrized by ϕ_{lab} and $\bar{\theta}'$, two rotation matrixes are applied to obtain θ and ϕ in the intrinsic coordinate system.

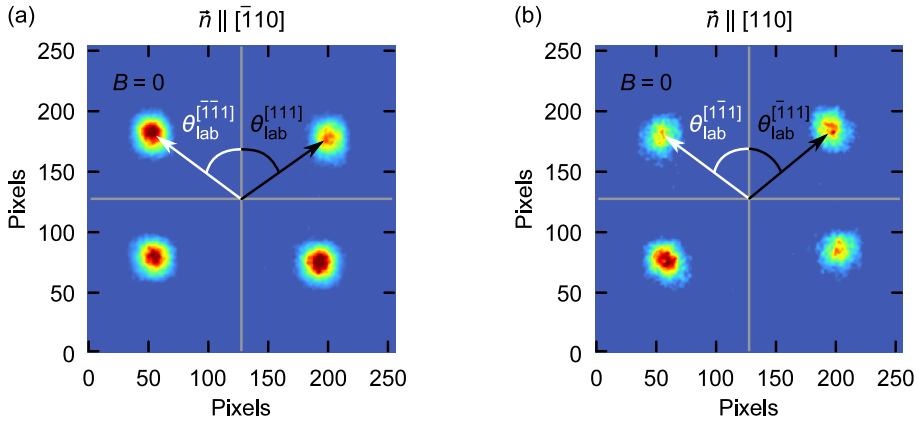

Figure A.4: Scattering patterns for $\vec{n} \parallel [\bar{1}10]$ and $\vec{n} \parallel [110]$ used to determine the deviations of both these axis from the horizontal line, thus defining the necessary rotational transformations to map the extracted values to the intrinsic coordinate system.

1. **Search for pressure-induced tricriticality in Cr**
   A. Schade, T. Adams, A. Chacon, R. Georgii, and P. Böni
   Physical Review B **100**, 035122 (2019)

2. **Evolution of magnetocrystalline anisotropies in $Mn_{1-x}Fe_xSi$ and $Mn_{1-x}Co_xSi$ as observed in small angle neutron scattering**
   J. Kindervater, T. Adams, A. Bauer, F. Haslbeck, A. Chacon, S. Mühlbauer, F. Jonietz, A . Neubauer, U. Gasser, G. Nagy, N. Martin, W. Häußler, R. Georgii, M. Garst, and C. Pfleiderer
   submitted (2019)

3. **Thermodynamic evidence of a second skyrmion lattice phase and tilted conical phase in Cu_2OSeO_3**
   M. Halder, A. Chacon, A. Bauer, W. Simeth, S. Mühlbauer, H. Berger, L. Heinen, M. Garst, A. Rosch, and C. Pfleiderer
   Physical Review B **98**, 144429 (2018)

4. **Observation of two independent skyrmion phases in a chiral magnetic material**
   A. Chacon, L. Heinen, M. Halder, A. Bauer, W. Simeth, S. Mühlbauer, H. Berger, M. Garst, A. Rosch, and C. Pfleiderer
   Nature Physics **14**, 936-941 (2018)

5. **Skyrmion lattices far from equilibrium**
   A. Bauer, A. Chacon, M. Halder, and C. Pfleiderer
   In: J. Zang, V. Cros, A. Hoffman (eds), Topology in Magnetism. Springer series in solid-state sciences, **192**, (2018)

6. **Reciprocal space mapping of magnetic order in thick epitaxial MnSi films**
   B. Wiedemann, A. Chacon, S.L. Zhang, Y. Khaydukov, T. Hesjedal, O. Soltwedel, T. Keller, S. Mühlbauer, T. Adams, M. Halder, C. Pfleiderer and P. Böni
   ArXiv, 1710.00544 (2017)

7. **Entropy-limited topological protection of skyrmions**
   J. Wild, T. N. G. Meier, S. Pöllath, M. Kronseder, A. Bauer, A. Chacon, M. Halder, M. Schowalter, A. Rosenauer, J. Zweck, J. Müller, A. Rosch, C. Pfleiderer, and C. H. Back
   Science Advances **3**, 9 (2017)

8. **Symmetry breaking, slow relaxation dynamics, and topological defects at the field-induced helix reorientation in MnSi**
   A. Bauer, A. Chacon, M. Wagner, M. Halder, R. Georgii, A. Rosch, C. Pfleiderer, and M. Garst
   Physical Review B **95**, 024429 (2017)

9. **Uniaxial pressure dependence of magnetic order in Mnsi**
   A. Chacon, A. Bauer, T. Adams, F. Rucker, G. Brandl, R. Georgii, M. Garst, and C. Pfleiderer
   Physical Review Letters **115**, 267202 (2015)

10. **Versatile module for experiments with focussing neutron guides**
    T. Adams, G. Brandl, A. Chacon, J. N. Wagner, M. Rahn, S. Mühlbauer, R. Georgii, C. Pfleiderer, and P. Böni
    Applied Physics Letters **105**, 123505 (2014)

11. **Unwinding of a skyrmion lattice by magnetic monopoles**
    P. Milde, D. Köhler, J. Seidel, L. M. Eng, A. Bauer, A. Chacon, J. Kindervater, S. Mühlbauer, C. Pfleiderer, S. Buhrandt, C. Schütte, and A. Rosch
    Science **340**, 1076 (2013)

12. **Long-wavelength helimagnetic order and skyrmion lattice phase in Cu_2OSeO_3**
    T. Adams, A. Chacon, M. Wagner, A. Bauer, G. Brandl, B. Pedersen, H. Berger, P. Lemmens, and C. Pfleiderer
    Physical Review Letters **108**, 237204 (2012)

ACKNOWLEDGEMENTS

This thesis is the result of a long colorful process full of several projects, which allow me to visit different very interesting conferences and come into touch with leading scientists in the field of condensed matter physics. This experience was enriching and constantly intellectually motivating. I am very thankful to Prof. Christian Pfleiderer and Prof. Peter Böni for giving me the opportunity to take on this challenge and allowing me to follow my scientific interests. The results presented here would not have been possible without the help of:

- Dr. Sebastian Mühlbauer and his support in several beam times at the SANS-1 instrument at the MLZ.
- Dr. Robert Georgii and his assistance performing experiments at MIRA at the MLZ.
- Dr. Marco Halder for being my sparring partner in several discussions and his help with some python programming problems.
- Dr. Andreas Bauer for providing and preparing all the samples I've ever measured.
- Dr. Felix Rucker for several discussions, which provided insights into nuances of the ac-susceptibility in chiral magnets.
- Prof. Markus Garst, who showed a lot of patience explaining several theoretical concepts regarding our research.
- Wolfgang Simeth und Franz Haslbeck for their help performing some experiments at the LLB and HZB.
- All the people at the central workshop, without their work non of the necessary bespoke equipment would have been possible.
- Andreas Mantwill who provided pieces of equipment with very short notice, essential for some of our experiments.
- Helmuth Berger for providing the Cu_2OSeO_3 samples.
- Many thanks to the rest of the crew at E21/E51. I have very fond entertaining memories of conferences, triple D-Days, PHD defenses, sunny days BBQs in front of the physics department, and glorious participations in Quattro-Ball tournaments. It is time to watch the Big Lebowski again.
- Special thanks to my flat mates Jan Spallek, Pau Jorba, Andreas Zeidler and Matthaeus Schwarz-Schilling. I am grateful for the 'deep' philosophical conversations, the embarassing photos, and the great meals.
- Big thanks to the usual suspects, Susi, Chisco, Mehdi, Maya, Miri, Caro, Chrissy, and of course Simon. You and your families always made me feel at home away from home.
- Finally, my family has played an important role in this process. I would not be here if my mom María Gabriela Roldán Villalobos had not put me on this path over 23 years ago. All of this is the fruit of your efforts.

BIBLIOGRAPHY

[1] K. v. Klitzing, G. Dorda, and M. Pepper. “New Method for High-Accuracy Determination of the Fine-Structure Constant Based on Quantized Hall Resistance.” en. In: *Phys. Rev. Lett.* 45.6 (Aug. 1980), pp. 494–497. DOI: 10.1103/PhysRevLett.45.494.

[2] D. J. Thouless, M. Kohmoto, M. P. Nightingale, and M. den Nijs. “Quantized Hall Conductance in a Two-Dimensional Periodic Potential.” en. In: *Phys. Rev. Lett.* 49.6 (Aug. 1982), pp. 405–408. DOI: 10.1103/PhysRevLett.49.405.

[3] K. S. Novoselov, A. K. Geim, S. V. Morozov, D Jiang, Y. Zhang, S. V. Dubonos, I. V. Grigorieva, and A. A. Firsov. “Electric Field Effect in Atomically Thin Carbon Films.” en. In: *Science* 306.5696 (Oct. 2004), pp. 666–669. DOI: 10.1126/science.1102896.

[4] C. L. Kane and E. J. Mele. “Quantum Spin Hall Effect in Graphene.” en. In: *Phys. Rev. Lett.* 95.22 (Nov. 2005). DOI: 10.1103/PhysRevLett.95.226801.

[5] F. D. M. Haldane. “Model for a Quantum Hall Effect without Landau Levels: Condensed-Matter Realization of the "Parity Anomaly".” en. In: *Phys. Rev. Lett.* 61.18 (Oct. 1988), pp. 2015–2018. DOI: 10.1103/PhysRevLett.61.2015.

[6] B. A. Bernevig, T. L. Hughes, and S.-C. Zhang. “Quantum Spin Hall Effect and Topological Phase Transition in HgTe Quantum Wells.” en. In: *Science* 314.5806 (Dec. 2006), pp. 1757–1761. DOI: 10.1126/science.1133734.

[7] M. Konig, S. Wiedmann, C. Brune, A. Roth, H. Buhmann, L. W. Molenkamp, X.-L. Qi, and S.-C. Zhang. “Quantum Spin Hall Insulator State in HgTe Quantum Wells.” en. In: *Science* 318.5851 (Nov. 2007), pp. 766–770. DOI: 10.1126/science.1148047.

[8] Albert Fert, Nicolas Reyren, and Vincent Cros. “Magnetic Skyrmions: Advances in Physics and Potential Applications.” en. In: *Nat. Rev. Mater.* 2.7 (July 2017), p. 17031. DOI: 10.1038/natrevmats.2017.31.

[9] Naoto Nagaosa and Yoshinori Tokura. “Topological Properties and Dynamics of Magnetic Skyrmions.” en. In: *Nat Nano* 8.12 (Dec. 2013), pp. 899–911. DOI: 10.1038/nnano.2013.243.

[10] K. Everschor-Sitte, J. Masell, R. M. Reeve, and M. Kläui. “Perspective: Magnetic Skyrmions—Overview of Recent Progress in an Active Research Field.” In: *Journal of Applied Physics* 124.24 (Dec. 2018), p. 240901. DOI: 10.1063/1.5048972.

[11] S. Mühlbauer, B. Binz, F. Jonietz, C. Pfleiderer, A. Rosch, A. Neubauer, R. Georgii, and P. Böni. “Skyrmion Lattice in a Chiral Magnet.” en. In: *Science* 323.5916 (Feb. 2009), pp. 915–919. DOI: 10.1126/science.1166767.

[12] Stefan Heinze, Kirsten von Bergmann, Matthias Menzel, Jens Brede, André Kubetzka, Roland Wiesendanger, Gustav Bihlmayer, and Stefan Blügel. “Spontaneous Atomic-Scale Magnetic Skyrmion Lattice in Two Dimensions.” en. In: *Nat Phys* 7.9 (Sept. 2011), pp. 713–718. DOI: 10.1038/nphys2045.

[13] C. Moreau-Luchaire et al. “Additive Interfacial Chiral Interaction in Multilayers for Stabilization of Small Individual Skyrmions at Room Temperature.” en. In: *Nat. Nanotechnol.* 11.5 (May 2016), pp. 444–448. DOI: 10.1038/nnano.2015.313.

[14] A. Neubauer, C. Pfleiderer, B. Binz, A. Rosch, R. Ritz, P. G. Niklowitz, and P. Böni. “Topological Hall Effect in the {A} Phase of MnSi.” In: *Phys. Rev. Lett.* 102.18 (May 2009), p. 186602. DOI: 10.1103/PhysRevLett.102.186602.

[15] F. Jonietz, S. Mühlbauer, C. Pfleiderer, A. Neubauer, W. Münzer, A. Bauer, T. Adams, R. Georgii, P. Böni, R. A. Duine, K. Everschor, M. Garst, and A. Rosch. “Spin Transfer Torques in MnSi at Ultralow Current Densities.” en. In: *Science* 330.6011 (Dec. 2010), pp. 1648–1651. DOI: 10.1126/science.1195709.

[16] Wanjun Jiang, Xichao Zhang, Guoqiang Yu, Wei Zhang, Xiao Wang, M. Benjamin Jungfleisch, John E. Pearson, Xuemei Cheng, Olle Heinonen, Kang L. Wang, Yan Zhou, Axel Hoffmann, and Suzanne G. E. te Velthuis. “Direct Observation of the Skyrmion Hall Effect.” en. In: *Nat. Phys.* 13.2 (Feb. 2017), pp. 162–169. DOI: 10.1038/nphys3883.

[17] T. Schulz, R. Ritz, A. Bauer, M. Halder, M. Wagner, C. Franz, C. Pfleiderer, K. Everschor, M. Garst, and A. Rosch. “Emergent Electrodynamics of Skyrmions in a Chiral Magnet.” en. In: *Nat Phys* 8.4 (Apr. 2012), pp. 301–304. DOI: 10.1038/nphys2231.

[18] Albert Fert, Vincent Cros, and João Sampaio. “Skyrmions on the Track.” en. In: *Nat Nano* 8.3 (Mar. 2013), pp. 152–156. DOI: 10.1038/nnano.2013.29.

[19] Jan Müller. “Magnetic Skyrmions on a Two-Lane Racetrack.” en. In: *New J. Phys.* 19.2 (Feb. 2017), p. 025002. DOI: 10.1088/1367-2630/aa5b55.

[20] Xichao Zhang, Motohiko Ezawa, and Yan Zhou. “Magnetic Skyrmion Logic Gates: Conversion, Duplication and Merging of Skyrmions.” en. In: *Sci. Rep.* 5 (Mar. 2015), p. 9400. DOI: 10.1038/srep09400.

[21] Shijiang Luo, Min Song, Xin Li, Yue Zhang, Jeongmin Hong, Xiaofei Yang, Xuecheng Zou, Nuo Xu, and Long You. “Reconfigurable Skyrmion Logic Gates.” In: *Nano Lett.* 18.2 (Feb. 2018), pp. 1180–1184. DOI: 10.1021/acs.nanolett.7b04722.

[22] Julie Grollier, Damien Querlioz, and Mark D. Stiles. “Spintronic Nanodevices for Bioinspired Computing.” en. In: *Proc. IEEE* 104.10 (Oct. 2016), pp. 2024–2039. DOI: 10.1109/JPROC.2016.2597152.

[23] Robert M. White. *Quantum Theory of Magnetism: Magnetic Properties of Materials*. en. 3., compl. rev. ed. Springer Series in Solid-State Sciences 32. OCLC: 255207108. Berlin: Springer, 2007.

[24] Mathias Getzlaff. *Fundamentals of Magnetism*. en. OCLC: ocn190859538. Berlin ; New York: Springer, 2008.

[25] I. Dzyaloshinskii. “A Thermodynamic Theory of “Weak” Ferromagnetism of Antiferromagnetics.” In: *J. Phys. Chem. Solids* 4.4 (Jan. 1958), pp. 241–255. DOI: 10.1016/0022-3697(58)90076-3.

[26] Tôru Moriya. “New Mechanism of Anisotropic Superexchange Interaction.” In: *Phys. Rev. Lett.* 4.5 (Mar. 1960), pp. 228–230. DOI: 10.1103/PhysRevLett.4.228.

[27] G. M. De Luca, G. Ghiringhelli, M. Moretti Sala, S. Di Matteo, M. W. Haverkort, H. Berger, V. Bisogni, J. C. Cezar, N. B. Brookes, and M. Salluzzo. “Weak Magnetism in Insulating and Superconducting Cuprates.” In: *Phys. Rev. B* 82.21 (Dec. 2010), p. 214504. DOI: 10.1103/PhysRevB.82.214504.

[28] L. H. Thomas. “The Motion of the Spinning Electron.” En. In: *Nature* 117.2945 (Apr. 1926), p. 514. DOI: 10.1038/117514a0.

[29] Skyrme T. H. R. and Schonland Basil Ferdinand Jamieson. “A Non-Linear Field Theory.” In: *Proceedings of the Royal Society of London. Series A. Mathematical and Physical Sciences* 260.1300 (Feb. 1961), pp. 127–138. DOI: 10.1098/rspa.1961.0018.

[30] Skyrme T. H. R. and Penney William George. “Particle States of a Quantized Meson Field.” In: *Proceedings of the Royal Society of London. Series A. Mathematical and Physical Sciences* 262.1309 (July 1961), pp. 237–245. DOI: 10.1098/rspa.1961.0115.

[31] T. H. R. Skyrme. “A Unified Field Theory of Mesons and Baryons.” In: *Nuclear Physics* 31 (Mar. 1962), pp. 556–569. DOI: 10.1016/0029-5582(62)90775-7.

[32] Prashanth Jaikumar and Rachid Ouyed. “Skyrmion Stars: Astrophysical Motivations and Implications.” en. In: *ApJ* 639.1 (Mar. 2006), pp. 354–362. DOI: 10.1086/499267.

[33] Mannque Rho and Ismail Zahed, eds. *The Multifaceted Skyrmion*. en. Second edition. New Jersey: World Scientific, 2017.

[34] A. Schmeller, J. P. Eisenstein, L. N. Pfeiffer, and K. W. West. “Evidence for Skyrmions and Single Spin Flips in the Integer Quantized Hall Effect.” In: *Phys. Rev. Lett.* 75.23 (Dec. 1995), pp. 4290–4293. DOI: 10.1103/PhysRevLett.75.4290.

[35] Usama Al Khawaja and Henk Stoof. “Skyrmions in a Ferromagnetic Bose–Einstein Condensate.” En. In: *Nature* 411.6840 (June 2001), p. 918. DOI: 10.1038/35082010.

[36] Gregory S. Adkins, Chiara R. Nappi, and Edward Witten. “Static Properties of Nucleons in the Skyrme Model.” In: *Nuclear Physics B* 228.3 (Dec. 1983), pp. 552–566. DOI: 10.1016/0550-3213(83)90559-X.

[37] I. Zahed and G. E. Brown. “The Skyrme Model.” In: *Physics Reports* 142.1 (Sept. 1986), pp. 1–102. DOI: 10.1016/0370-1573(86)90142-0.

[38] A N Bogdanov and D A Yablonskii. “Thermodynamically Stable "Vortices" in Magnetically Ordered Crystals.The Mixed State of Magnets.” en. In: *J. Exp. Theor. Phys.* 68.1 (1989), p. 101.

[39] A. Bogdanov and A. Hubert. “Thermodynamically Stable Magnetic Vortex States in Magnetic Crystals.” In: *Journal of Magnetism and Magnetic Materials* 138.3 (Dec. 1994), pp. 255–269. DOI: 10.1016/0304-8853(94)90046-9.

[40] A. N. Bogdanov and U. K. Rößler. “Chiral Symmetry Breaking in Magnetic Thin Films and Multilayers.” In: *Phys. Rev. Lett.* 87.3 (June 2001), p. 037203. DOI: 10.1103/PhysRevLett.87.037203.

[41] U. K. Rößler, A. N. Bogdanov, and C. Pfleiderer. “Spontaneous Skyrmion Ground States in Magnetic Metals.” en. In: *Nature* 442.7104 (Aug. 2006), pp. 797–801. DOI: 10.1038/nature05056.

[42] Yoshikazu Ishikawa and Masatoshi Arai. “Magnetic Phase Diagram of MnSi near Critical Temperature Studied by Neutron Small Angle Scattering.” In: *J. Phys. Soc. Jpn.* 53.8 (Aug. 1984), pp. 2726–2733. DOI: 10.1143/JPSJ.53.2726.

[43] S. V. Grigoriev, S. V. Maleyev, A. I. Okorokov, Yu. O. Chetverikov, and H. Eckerlebe. “Field-Induced Reorientation of the Spin Helix in MnSi near {${T}_{c}$}.” In: *Phys. Rev. B* 73.22 (June 2006), p. 224440. DOI: 10.1103/PhysRevB.73.224440.

[44] X. Z. Yu, Y. Onose, N. Kanazawa, J. H. Park, J. H. Han, Y. Matsui, N. Nagaosa, and Y. Tokura. “Real-Space Observation of a Two-Dimensional Skyrmion Crystal.” en. In: *Nature* 465.7300 (June 2010), pp. 901–904. DOI: 10.1038/nature09124.

[45] Stuart S. P. Parkin, Masamitsu Hayashi, and Luc Thomas. “Magnetic Domain-Wall Racetrack Memory.” en. In: *Science* 320.5873 (Apr. 2008), pp. 190–194. DOI: 10.1126/science.1145799.

[46] K. Karube, J. S. White, N. Reynolds, J. L. Gavilano, H. Oike, A. Kikkawa, F. Kagawa, Y. Tokunaga, H. M. Rønnow, Y. Tokura, and Y. Taguchi. “Robust Metastable Skyrmions and Their Triangular–Square Lattice Structural Transition in a High-Temperature Chiral Magnet.” en. In: *Nat. Mater.* 15.12 (Dec. 2016), pp. 1237–1242. DOI: 10.1038/nmat4752.

[47] M. N. Wilson, E. A. Karhu, A. S. Quigley, U. K. Rößler, A. B. Butenko, A. N. Bogdanov, M. D. Robertson, and T. L. Monchesky. “Extended Elliptic Skyrmion Gratings in Epitaxial MnSi Thin Films.” In: *Phys. Rev. B* 86.14 (Oct. 2012), p. 144420. DOI: 10.1103/PhysRevB.86.144420.

[48] M. N. Wilson, E. A. Karhu, D. P. Lake, A. S. Quigley, S. Meynell, A. N. Bogdanov, H. Fritzsche, U. K. Rößler, and T. L. Monchesky. “Discrete Helicoidal States in Chiral Magnetic Thin Films.” In: *Phys. Rev. B* 88.21 (Dec. 2013), p. 214420. DOI: 10.1103/PhysRevB.88.214420.

[49] Y. Tokunaga, X. Z. Yu, J. S. White, H. M. Rønnow, D. Morikawa, Y. Taguchi, and Y. Tokura. “A New Class of Chiral Materials Hosting Magnetic Skyrmions beyond Room Temperature.” In: *Nat. Commun.* 6 (July 2015), p. 7638. DOI: 10.1038/ncomms8638.

[50] K. Karube, J. S. White, D. Morikawa, M. Bartkowiak, A. Kikkawa, Y. Tokunaga, T. Arima, H. M. Rønnow, Y. Tokura, and Y. Taguchi. “Skyrmion Formation in a Bulk Chiral Magnet at Zero Magnetic Field and above Room Temperature.” In: *Phys. Rev. Materials* 1.7 (Dec. 2017), p. 074405. DOI: 10.1103/PhysRevMaterials.1.074405.

[51] Yufan Li, N. Kanazawa, X. Z. Yu, A. Tsukazaki, M. Kawasaki, M. Ichikawa, X. F. Jin, F. Kagawa, and Y. Tokura. “Robust Formation of Skyrmions and Topological Hall Effect Anomaly in Epitaxial Thin Films of MnSi.” In: *Phys. Rev. Lett.* 110.11 (Mar. 2013), p. 117202. DOI: 10.1103/PhysRevLett.110.117202.

[52] T. L. Monchesky, J. C. Loudon, M. D. Robertson, and A. N. Bogdanov. “Comment on “Robust Formation of Skyrmions and Topological Hall Effect Anomaly in Epitaxial Thin Films of MnSi”.” In: *Phys. Rev. Lett.* 112.5 (Feb. 2014), p. 059701. DOI: 10.1103/PhysRevLett.112.059701.

[53] M. N. Wilson, A. B. Butenko, A. N. Bogdanov, and T. L. Monchesky. “Chiral Skyrmions in Cubic Helimagnet Films: The Role of Uniaxial Anisotropy.” In: *Phys. Rev. B* 89.9 (Mar. 2014), p. 094411. DOI: 10.1103/PhysRevB.89.094411.

[54] S. A. Meynell, M. N. Wilson, K. L. Krycka, B. J. Kirby, H. Fritzsche, and T. L. Monchesky. “Neutron Study of In-Plane Skyrmions in MnSi Thin Films.” en. In: *Phys. Rev. B* 96.5 (Aug. 2017). DOI: 10.1103/PhysRevB.96.054402.

[55] Tomoyuki Yokouchi, Naoya Kanazawa, Atsushi Tsukazaki, Yusuke Kozuka, Akiko Kikkawa, Yasujiro Taguchi, Masashi Kawasaki, Masakazu Ichikawa, Fumitaka Kagawa, and Yoshinori Tokura. “Formation of In-Plane Skyrmions in Epitaxial MnSi Thin Films as Revealed by Planar Hall Effect.” In: *J. Phys. Soc. Jpn.* 84.10 (Sept. 2015), p. 104708. DOI: 10.7566/JPSJ.84.104708.

[56] B. Wiedemann, A. Chacon, S. L. Zhang, Y. Khaydukov, T. Hesjedal, O. Soltwedel, T. Keller, S. Mühlbauer, T. Adams, M. Halder, C. Pfleiderer, and P. Böni. "Reciprocal Space Mapping of Magnetic Order in Thick Epitaxial MnSi Films." In: *ArXiv171000544 Cond-Mat* (Oct. 2017). arXiv: 1710.00544 [cond-mat].

[57] S. X. Huang and C. L. Chien. "Extended Skyrmion Phase in Epitaxial FeGe(111) Thin Films." In: *Phys. Rev. Lett.* 108.26 (June 2012), p. 267201. DOI: 10.1103/PhysRevLett.108.267201.

[58] J. C. Gallagher, K. Y. Meng, J. T. Brangham, H. L. Wang, B. D. Esser, D. W. McComb, and F. Y. Yang. "Robust Zero-Field Skyrmion Formation in FeGe Epitaxial Thin Films." In: *Phys. Rev. Lett.* 118.2 (Jan. 2017), p. 027201. DOI: 10.1103/PhysRevLett.118.027201.

[59] N. Kanazawa, J. S. White, H. M. Rønnow, C. D. Dewhurst, Y. Fujishiro, A. Tsukazaki, Y. Kozuka, M. Kawasaki, M. Ichikawa, F. Kagawa, and Y. Tokura. "Direct Observation of Anisotropic Magnetic Field Response of the Spin Helix in FeGe Thin Films." In: *Phys. Rev. B* 94.18 (Nov. 2016), p. 184432. DOI: 10.1103/PhysRevB.94.184432.

[60] Filipp N. Rybakov, Aleksandr B. Borisov, Stefan Blügel, and Nikolai S. Kiselev. "New Type of Stable Particlelike States in Chiral Magnets." In: *Phys. Rev. Lett.* 115.11 (Sept. 2015), p. 117201. DOI: 10.1103/PhysRevLett.115.117201.

[61] Adam S. Ahmed, James Rowland, Bryan D. Esser, Sarah R. Dunsiger, David W. McComb, Mohit Randeria, and Roland K. Kawakami. "Chiral Bobbers and Skyrmions in Epitaxial FeGe/Si(111) Films." In: *Phys. Rev. Materials* 2.4 (Apr. 2018), p. 041401. DOI: 10.1103/PhysRevMaterials.2.041401.

[62] M. A. Armstrong. *Basic Topology*. en. Undergraduate Texts in Mathematics. New York: Springer-Verlag, 1983.

[63] L. E. J. Brouwer. "Über Abbildung von Mannigfaltigkeiten." de. In: *Math. Ann.* 71.1 (Mar. 1911), pp. 97–115. DOI: 10.1007/BF01456931.

[64] Hans-Benjamin Braun. "Topological Effects in Nanomagnetism: From Superparamagnetism to Chiral Quantum Solitons." In: *Adv. Phys.* 61.1 (Feb. 2012), pp. 1–116. DOI: 10.1080/00018732.2012.663070.

[65] David Thouless. *Topological Quantum Numbers in Nonrelativistic Physics*. English. Singapore ; River Edge, N.J: World Scientific Pub Co Inc, Mar. 1998.

[66] Jiadong Zang, Vincent Cros, and Axel Hoffmann. *Topology in Magnetism*. en. New York, NY: Springer Berlin Heidelberg, 2018.

[67] Ajaya K. Nayak, Vivek Kumar, Tianping Ma, Peter Werner, Eckhard Pippel, Roshnee Sahoo, Franoise Damay, Ulrich K. Rößler, Claudia Felser, and Stuart S. P. Parkin. "Magnetic Antiskyrmions above Room Temperature in Tetragonal Heusler Materials." en. In: *Nature* 548.7669 (Aug. 2017), pp. 561–566. DOI: 10.1038/nature23466.

[68] Alexander G. Kolesnikov, Maksim E. Stebliy, Alexander S. Samardak, and Alexey V. Ognev. "Skyrmionium – High Velocity without the Skyrmion Hall Effect." En. In: *Sci. Rep.* 8.1 (Nov. 2018), p. 16966. DOI: 10.1038/s41598-018-34934-2.

[69] Jan Seidel. *Topological Structures in Ferroic Materials*. en. New York, NY: Springer Berlin Heidelberg, 2016.

[70] Minhyea Lee, W. Kang, Y. Onose, Y. Tokura, and N. P. Ong. “Unusual Hall Effect Anomaly in MnSi under Pressure.” In: *Phys. Rev. Lett.* 102.18 (May 2009), p. 186601. DOI: 10.1103/PhysRevLett.102.186601.

[71] R. Ritz, M. Halder, C. Franz, A. Bauer, M. Wagner, R. Bamler, A. Rosch, and C. Pfleiderer. “Giant Generic Topological Hall Resistivity of MnSi under Pressure.” In: *Phys. Rev. B* 87.13 (Apr. 2013), p. 134424. DOI: 10.1103/PhysRevB.87.134424.

[72] C. Pfleiderer, P. Böni, T. Keller, U. K. Rößler, and A. Rosch. “Non-Fermi Liquid Metal Without Quantum Criticality.” English. In: *Science* 316.5833 (June 2007), pp. 1871–1874. DOI: 10.1126/science.1142644. pmid: 17600211.

[73] Masaru Onoda, Gen Tatara, and Naoto Nagaosa. “Anomalous Hall Effect and Skyrmion Number in Real and Momentum Spaces.” In: *J. Phys. Soc. Jpn.* 73.10 (Oct. 2004), pp. 2624–2627. DOI: 10.1143/JPSJ.73.2624.

[74] G. Blatter, M. V. Feigel’man, V. B. Geshkenbein, A. I. Larkin, and V. M. Vinokur. “Vortices in High-Temperature Superconductors.” en. In: *Rev. Mod. Phys.* 66.4 (Oct. 1994), pp. 1125–1388. DOI: 10.1103/RevModPhys.66.1125.

[75] P. Milde, D. Köhler, J. Seidel, L. M. Eng, A. Bauer, A. Chacon, J. Kindervater, S. Mühlbauer, C. Pfleiderer, S. Buhrandt, C. Schütte, and A. Rosch. “Unwinding of a Skyrmion Lattice by Magnetic Monopoles.” en. In: *Science* 340.6136 (May 2013), pp. 1076–1080. DOI: 10.1126/science.1234657.

[76] Johannes Wild, Thomas N. G. Meier, Simon Pöllath, Matthias Kronseder, Andreas Bauer, Alfonso Chacon, Marco Halder, Marco Schowalter, Andreas Rosenauer, Josef Zweck, Jan Müller, Achim Rosch, Christian Pfleiderer, and Christian H. Back. “Entropy-Limited Topological Protection of Skyrmions.” en. In: *Sci. Adv.* 3.9 (Sept. 2017), e1701704. DOI: 10.1126/sciadv.1701704.

[77] M. T. Birch, R. Takagi, S. Seki, M. N. Wilson, F. Kagawa, A. Štefančič, G. Balakrishnan, R. Fan, P. Steadman, C. J. Ottley, M. Crisanti, R. Cubitt, T. Lancaster, Y. Tokura, and P. D. Hatton. “Increased Lifetime of Metastable Skyrmions by Controlled Doping.” In: *Phys. Rev. B* 100.1 (July 2019), p. 014425. DOI: 10.1103/PhysRevB.100.014425.

[78] W. Friedrich, P. Knipping, and M. Laue. “Interferenzerscheinungen bei Röntgenstrahlen.” de. In: *Ann. Phys.* 346.10 (1913), pp. 971–988. DOI: 10.1002/andp.19133461004.

[79] J. Chadwick. “The Existence of a Neutron.” en. In: *Proc. R. Soc. Math. Phys. Eng. Sci.* 136.830 (June 1932), pp. 692–708. DOI: 10.1098/rspa.1932.0112.

[80] Gordon Leslie Squires. *Introduction to the Theory of Thermal Neutron Scattering*. English. Courier Corporation, 1978.

[81] O. Halpern and M. H. Johnson. “On the Magnetic Scattering of Neutrons.” In: *Phys Rev* 55.10 (May 1939), pp. 898–923. DOI: 10.1103/PhysRev.55.898.

[82] Pierre-Gilles De Gennes. “Theory of Neutron Scattering by Magnetic Crystals.” English. In: *Magnetism*. Ed. G. T. Rado and H. Suhl. Vol. III. New York: Academic Press, 1963, p. 115.

[83] P. Bak and M. H. Jensen. “Theory of Helical Magnetic Structures and Phase Transitions in MnSi and FeGe.” en. In: *J. Phys. C: Solid State Phys.* 13.31 (1980), p. L881. DOI: 10.1088/0022-3719/13/31/002.

[84] J. S. Pedersen, D. Posselt, and K. Mortensen. “Analytical Treatment of the Resolution Function for Small-Angle Scattering.” en. In: *J Appl Cryst* 23.4 (Aug. 1990), pp. 321–333. DOI: 10.1107/S0021889890003946.

[85] Robert Georgii and Klaus Seemann. “MIRA: Dual Wavelength Band Instrument.” en. In: *J. Large-Scale Res. Facil. JLSRF* 1.0 (Aug. 2015), p. 3. DOI: 10.17815/jlsrf-1-21.

[86] T. Adams, G. Brandl, A. Chacon, J. N. Wagner, M. Rahn, S. Mühlbauer, R. Georgii, C. Pfleiderer, and P. Böni. “Versatile Module for Experiments with Focussing Neutron Guides.” In: *Appl Phys Lett* 105.12 (Sept. 2014), p. 123505. DOI: 10.1063/1.4896295.

[87] Martin Klein and Christian J. Schmidt. “CASCADE, Neutron Detectors for Highest Count Rates in Combination with ASIC/FPGA Based Readout Electronics.” In: *Nucl. Instrum. Methods Phys. Res. Sect. Accel. Spectrometers Detect. Assoc. Equip.* 628.1 (Feb. 2011), pp. 9–18. DOI: 10.1016/j.nima.2010.06.278.

[88] S. Mühlbauer, A. Heinemann, A. Wilhelm, L. Karge, A. Ostermann, I. Defendi, A. Schreyer, W. Petry, and R. Gilles. “The New Small-Angle Neutron Scattering Instrument SANS-1 at MLZ—Characterization and First Results.” In: *Nuclear Instruments and Methods in Physics Research Section A: Accelerators, Spectrometers, Detectors and Associated Equipment* 832 (Oct. 2016), pp. 297–305. DOI: 10.1016/j.nima.2016.06.105.

[89] S. Seki, X. Z. Yu, S. Ishiwata, and Y. Tokura. “Observation of Skyrmions in a Multiferroic Material.” en. In: *Science* 336.6078 (Apr. 2012), pp. 198–201. DOI: 10.1126/science.1214143.

[90] T. Adams, A. Chacon, M. Wagner, A. Bauer, G. Brandl, B. Pedersen, H. Berger, P. Lemmens, and C. Pfleiderer. “Long-Wavelength Helimagnetic Order and Skyrmion Lattice Phase in \cso.” In: *Phys. Rev. Lett.* 108.23 (June 2012), p. 237204. DOI: 10.1103/PhysRevLett.108.237204.

[91] Y. Ishikawa, K. Tajima, D. Bloch, and M. Roth. “Helical Spin Structure in Manganese Silicide MnSi.” In: *Solid State Communications* 19.6 (July 1976), pp. 525–528. DOI: 10.1016/0038-1098(76)90057-0.

[92] K. Motoya, H. Yasuoka, Y. Nakamura, and J. H. Wernick. “Helical Spin Structure in MnSi-NMR Studies.” In: *Solid State Communications* 19.6 (July 1976), pp. 529–531. DOI: 10.1016/0038-1098(76)90058-2.

[93] I. E. Dzyaloshinskii. “Thermodynamical Theory of ’Weak" Ferromagnetism in Antiferromagnetic Substances.” In: *Sov Phys JETP* 5.6 (Dec. 1957), p. 1259.

[94] O. Nakanishi, A. Yanase, A. Hasegawa, and M. Kataoka. “The Origin of the Helical Spin Density Wave in MnSi.” In: *Solid State Communications* 35.12 (Sept. 1980), pp. 995–998. DOI: 10.1016/0038-1098(80)91004-2.

[95] G. G. Lonzarich and L. Taillefer. “Effect of Spin Fluctuations on the Magnetic Equation of State of Ferromagnetic or Nearly Ferromagnetic Metals.” English. In: *J Phys C Solid State Phys* 18.22 (1985), p. 4339. DOI: 10.1088/0022-3719/18/22/017.

[96] Tôru Moriya. *Spin Fluctuations in Itinerant Electron Magnetism | Toru Moriya | Springer*. Springer Series in Solid-State Sciences. Berlin: Springer, 1985.

[97] C. Pfleiderer, S. R. Julian, and G. G. Lonzarich. “Non-Fermi-Liquid Nature of the Normal State of Itinerant-Electron Ferromagnets.” English. In: *Nature* 414.6862 (Nov. 2001), pp. 427–430. DOI: 10.1038/35106527.

[98] R. Ritz, M. Halder, M. Wagner, C. Franz, A. Bauer, and C. Pfleiderer. “Formation of a Topological Non-Fermi Liquid in MnSi.” en. In: *Nature* 497.7448 (May 2013), pp. 231–234. DOI: 10.1038/nature12023.

[99] A. B. Butenko, A. A. Leonov, U. K. Rößler, and A. N. Bogdanov. “Stabilization of Skyrmion Textures by Uniaxial Distortions in Noncentrosymmetric Cubic Helimagnets.” In: *Phys. Rev. B* 82.5 (Aug. 2010), p. 052403. DOI: 10.1103/PhysRevB.82.052403.

[100] J. Villain, R. Bidaux, J.-P. Carton, and R. Conte. “Order as an Effect of Disorder.” English. In: *J Phys Fr.* 41.11 (Nov. 1980), pp. 1263–1272. DOI: 10.1051/jphys:0198000410110126300.

[101] Stefan Buhrandt and Lars Fritz. “Skyrmion Lattice Phase in Three-Dimensional Chiral Magnets from Monte Carlo Simulations.” In: *Phys. Rev. B* 88.19 (Nov. 2013), p. 195137. DOI: 10.1103/PhysRevB.88.195137.

[102] Y. Ishikawa, Y. Noda, C. Fincher, and G. Shirane. “Low-Energy Paramagnetic Spin Fluctuations in the Weak Itinerant Ferromagnet MnSi.” In: *Phys Rev B* 25.1 (Jan. 1982), pp. 254–263. DOI: 10.1103/PhysRevB.25.254.

[103] B. Lebech, J. Bernhard, and T. Freltoft. “Magnetic Structures of Cubic FeGe Studied by Small-Angle Neutron Scattering.” English. In: *J Phys Condens Matter* 1.35 (1989), p. 6105. DOI: 10.1088/0953-8984/1/35/010.

[104] S. V. Grigoriev, V. A. Dyadkin, D. Menzel, J. Schoenes, Yu. O. Chetverikov, A. I. Okorokov, H. Eckerlebe, and S. V. Maleyev. “Magnetic Structure of {Fe$_{1-X}$Co$_x$Si} in a Magnetic Field Studied via Small-Angle Polarized Neutron Diffraction.” In: *Phys Rev B* 76.22 (Dec. 2007), p. 224424. DOI: 10.1103/PhysRevB.76.224424.

[105] D. Bloch, J. Voiron, V. Jaccarino, and J. H. Wernick. “The High Field-High Pressure Magnetic Properties of MnSi.” In: *Physics Letters A* 51.5 (Mar. 1975), pp. 259–261. DOI: 10.1016/0375-9601(75)90438-7.

[106] P. Aarosin Hansen. *Magnetic Anisotropy and Related Matters. Studied by Neutron Diffraction*. Report. 1977.

[107] A. Bauer, A. Neubauer, C. Franz, W. Münzer, M. Garst, and C. Pfleiderer. “Quantum Phase Transitions in Single-Crysta {Mn$_{1-X}$Fe$_x$Si} and {Mn$_{1-X}$Co$_x$Si}: Crystal Growth, Magnetization, Ac Susceptibility, and Specific Heat.” In: *Phys. Rev. B* 82.6 (Aug. 2010), p. 064404. DOI: 10.1103/PhysRevB.82.064404.

[108] M. L. Plumer and M. B. Walker. “Wavevector and Spin Reorientation in MnSi.” en. In: *J. Phys. C: Solid State Phys.* 14.31 (1981), p. 4689. DOI: 10.1088/0022-3719/14/31/016.

[109] Mitsuo Kataoka and Osamu Nakanishi. “Helical Spin Density Wave Due to Antisymmetric Exchange Interaction.” In: *J. Phys. Soc. Jpn.* 50.12 (Dec. 1981), pp. 3888–3896. DOI: 10.1143/JPSJ.50.3888.

[110] M. B. Walker. “Phason Instabilities and Successive Wave-Vector Reorientation Phase Transitions in MnSi.” In: *Phys. Rev. B* 40.13 (Nov. 1989), pp. 9315–9317. DOI: 10.1103/PhysRevB.40.9315.

[111] S. V. Grigoriev, S. V. Maleyev, A. I. Okorokov, Yu. O. Chetverikov, P. Böni, R. Georgii, D. Lamago, H. Eckerlebe, and K. Pranzas. “Magnetic Structure of MnSi under an Applied Field Probed by Polarized Small-Angle Neutron Scattering.” In: *Phys Rev B* 74.21 (Dec. 2006), p. 214414. DOI: 10.1103/PhysRevB.74.214414.

[112] Yusuke Kousaka, Naoki Ikeda, Takahiro Ogura, Toha Yoshii, Jun Akimitsu, Kazuki Ohishi, Jun-ichi Suzuki, Haruhiko Hiraka, Marina Miyagawa, Sadafumi Nishihara, Katsuya Inoue, and Jun-ichiro Kishine. “Chiral Magnetic Soliton Lattice in MnSi.” In: *Proceedings of the International Symposium on Science Explored by Ultra Slow Muon*. Vol. 2. 0 vols. JPS Conference Proceedings 2. Journal of the Physical Society of Japan, Mar. 2014. DOI: 10.7566/JPSCP.2.010205.

[113] M. Janoschek, M. Garst, A. Bauer, P. Krautscheid, R. Georgii, P. Böni, and C. Pfleiderer. “Fluctuation-Induced First-Order Phase Transition in Dzyaloshinskii-Moriya Helimagnets.” In: *Phys. Rev. B* 87.13 (Apr. 2013), p. 134407. DOI: 10.1103/PhysRevB.87.134407.

[114] A. Neubauer, J. Bœuf, A. Bauer, B. Russ, H. v. Löhneysen, and C. Pfleiderer. “Ultra-High Vacuum Compatible Image Furnace.” In: *Rev. Sci. Instrum.* 82.1 (Jan. 2011), p. 013902. DOI: 10.1063/1.3523056.

[115] A. Bauer, A. Neubauer, W. Münzer, A. Regnat, G. Benka, M. Meven, B. Pedersen, and C. Pfleiderer. “Ultra-High Vacuum Compatible Induction-Heated Rod Casting Furnace.” In: *Rev. Sci. Instrum.* 87.6 (June 2016), p. 063909. DOI: 10.1063/1.4954926.

[116] A. Bauer and C. Pfleiderer. “Magnetic Phase Diagram of MnSi Inferred from Magnetization and Ac Susceptibility.” In: *Phys. Rev. B* 85.21 (June 2012), p. 214418. DOI: 10.1103/PhysRevB.85.214418.

[117] I. Levatić, V. Šurija, H. Berger, and I. Živković. “Dissipation Processes in the Insulating Skyrmion Compound {\cso}.” In: *Phys. Rev. B* 90.22 (Dec. 2014), p. 224412. DOI: 10.1103/PhysRevB.90.224412.

[118] A. Bauer, M. Garst, and C. Pfleiderer. “History Dependence of the Magnetic Properties of Single-Crystal Fe$_{1-X}$Co$_x$Si.” In: *Phys. Rev. B* 93.23 (June 2016), p. 235144. DOI: 10.1103/PhysRevB.93.235144.

[119] Fuxiang Li, T. Nattermann, and V. L. Pokrovsky. “Vortex Domain Walls in Helical Magnets.” In: *Phys Rev Lett* 108.10 (Mar. 2012), p. 107203. DOI: 10.1103/PhysRevLett.108.107203.

[120] A. Dussaux, P. Schoenherr, K. Koumpouras, J. Chico, K. Chang, L. Lorenzelli, N. Kanazawa, Y. Tokura, M. Garst, A. Bergman, C. L. Degen, and D. Meier. “Local Dynamics of Topological Magnetic Defects in the Itinerant Helimagnet FeGe.” en. In: *Nat. Commun.* 7 (Aug. 2016), p. 12430. DOI: 10.1038/ncomms12430.

[121] A. Bogdanov and A. Hubert. “The Stability of Vortex-like Structures in Uniaxial Ferromagnets.” In: *Journal of Magnetism and Magnetic Materials* 195.1 (Apr. 1999), pp. 182–192. DOI: 10.1016/S0304-8853(98)01038-5.

[122] I. Kézsmárki, S. Bordács, P. Milde, E. Neuber, L. M. Eng, J. S. White, H. M. Rønnow, C. D. Dewhurst, M. Mochizuki, K. Yanai, H. Nakamura, D. Ehlers, V. Tsurkan, and A. Loidl. “Néel-Type Skyrmion Lattice with Confined Orientation in the Polar Magnetic Semiconductor GaV_4S_8.” en. In: *Nat. Mater.* 14.11 (Nov. 2015), pp. 1116–1122. DOI: 10.1038/nmat4402.

[123] S. Seki, Y. Okamura, K. Shibata, R. Takagi, N. D. Khanh, F. Kagawa, T. Arima, and Y. Tokura. “Stabilization of Magnetic Skyrmions by Uniaxial Tensile Strain.” In: *Phys. Rev. B* 96.22 (Dec. 2017), p. 220404. DOI: 10.1103/PhysRevB.96.220404.

[124] Y. Nii, T. Nakajima, A. Kikkawa, Y. Yamasaki, K. Ohishi, J. Suzuki, Y. Taguchi, T. Arima, Y. Tokura, and Y. Iwasa. “Uniaxial Stress Control of Skyrmion Phase.” en. In: *Nat. Commun.* 6 (Oct. 2015), p. 8539. DOI: 10.1038/ncomms9539.

[125] A. I. Figueroa, S. L. Zhang, A. A. Baker, R. Chalasani, A. Kohn, S. C. Speller, D. Gianolio, C. Pfleiderer, G. van der Laan, and T. Hesjedal. “Strain in Epitaxial MnSi Films on Si(111) in the Thick Film Limit Studied by Polarization-Dependent Extended x-Ray Absorption Fine Structure.” In: *Phys. Rev. B* 94.17 (Nov. 2016), p. 174107. DOI: 10.1103/PhysRevB.94.174107.

[126] A. Chacon, A. Bauer, T. Adams, F. Rucker, G. Brandl, R. Georgii, M. Garst, and C. Pfleiderer. “Uniaxial Pressure Dependence of Magnetic Order in MnSi.” In: *Phys. Rev. Lett.* 115.26 (Dec. 2015), p. 267202. DOI: 10.1103/PhysRevLett.115.267202.

[127] S. Waffenschmidt, C. Pfleiderer, and H. v. Löhneysen. “Critical Behavior of the Conductivity of Si:P at the Metal-Insulator Transition under Uniaxial Stress.” en. In: *Phys. Rev. Lett.* 83.15 (Oct. 1999), pp. 3005–3008. DOI: 10.1103/PhysRevLett.83.3005.

[128] C. Pfleiderer, E. Bedin, and B. Salce. “He Activated Loading Device for Low Temperature Uniaxial and Anvil Cell Pressure Experiments.” In: *Rev. Sci. Instrum.* 68.8 (Aug. 1997), pp. 3120–3124. DOI: doi:10.1063/1.1148254.

[129] A. Chacon. “Neutron Scattering and Susceptibility Studies of Skyrmion Lattices under Uniaxial Pressure.” English. Master Thesis. Munich, Germany: Technische Universität München, Dec. 2011.

[130] C. Pfleiderer. “Miniature Ac Susceptometers for Use inside Clamp Type Pressure Cells.” In: *Rev. Sci. Instrum.* 68.3 (Mar. 1997), pp. 1532–1535. DOI: 10.1063/1.1147642.

[131] C. Pfleiderer, G. J. McMullan, S. R. Julian, and G. G. Lonzarich. “Magnetic Quantum Phase Transition in MnSi under Hydrostatic Pressure.” In: *Phys Rev B* 55.13 (Apr. 1997), pp. 8330–8338. DOI: 10.1103/PhysRevB.55.8330.

[132] T. Adams, M. Garst, A. Bauer, R. Georgii, and C. Pfleiderer. “Response of the Skyrmion Lattice in MnSi to Cubic Magnetocrystalline Anisotropies.” In: *Phys. Rev. Lett.* 121.18 (Nov. 2018), p. 187205. DOI: 10.1103/PhysRevLett.121.187205.

[133] I. Levatić, P. Popčević, V. Šurija, A. Kruchkov, H. Berger, A. Magrez, J. S. White, H. M. Rønnow, and I. Živković. “Dramatic Pressure-Driven Enhancement of Bulk Skyrmion Stability.” In: *Sci Rep* 6 (Feb. 2016). DOI: 10.1038/srep21347.

[134] Y. Okamura, Y. Yamasaki, D. Morikawa, T. Honda, V. Ukleev, H. Nakao, Y. Murakami, K. Shibata, F. Kagawa, S. Seki, T. Arima, and Y. Tokura. “Directional Electric-Field Induced Transformation from Skyrmion Lattice to Distinct Helices in Multiferroic {\cso}.” In: *Phys. Rev. B* 95.18 (May 2017), p. 184411. DOI: 10.1103/PhysRevB.95.184411.

[135] S. Bordács, A. Butykai, B. G. Szigeti, J. S. White, R. Cubitt, A. O. Leonov, S. Widmann, D. Ehlers, H.-A. Krug Nidda, V. Tsurkan, A. Loidl, and I. Kézsmárki. “Equilibrium Skyrmion Lattice Ground State in a Polar Easy-Plane Magnet.” en. In: *Sci. Rep.* 7.1 (Aug. 2017), p. 7584. DOI: 10.1038/s41598-017-07996-x.

[136] A. Chacon, L. Heinen, M. Halder, A. Bauer, W. Simeth, S. Mühlbauer, H. Berger, M. Garst, A. Rosch, and C. Pfleiderer. “Observation of Two Independent Skyrmion Phases in a Chiral Magnetic Material.” en. In: *Nat. Phys.* (June 2018), p. 1. DOI: 10.1038/s41567-018-0184-y.

[137] M. Belesi, I. Rousochatzakis, M. Abid, U. K. Rößler, H. Berger, and J.-Ph. Ansermet. “Magnetoelectric Effects in Single Crystals of the Cubic Ferrimagnetic Helimagnet {\cso}.” In: *Phys. Rev. B* 85.22 (June 2012), p. 224413. DOI: 10.1103/PhysRevB.85.224413.

[138] F. Qian, H. Wilhelm, A. Aqeel, T. T. M. Palstra, A. J. E. Lefering, E. H. Brück, and C. Pappas. “Dissipation Phenomena and Magnetic Phase Diagram of {\cso} below 50 K.” In: *ArXiv161106014 Cond-Mat* (Nov. 2016). arXiv: 1611.06014 [cond-mat].

[139] Fengjiao Qian, Lars J. Bannenberg, Heribert Wilhelm, Grégory Chaboussant, Lisa M. Debeer-Schmitt, Marcus P. Schmidt, Aisha Aqeel, Thomas T. M. Palstra, Ekkes Brück, Anton J. E. Lefering, Catherine Pappas, Maxim Mostovoy, and Andrey O. Leonov. “New Magnetic Phase of the Chiral Skyrmion Material {\cso}.” en. In: *Sci. Adv.* 4.9 (Sept. 2018), eaat7323. DOI: 10.1126/sciadv.aat7323.

[140] S. Mühlbauer, J. Kindervater, T. Adams, A. Bauer, U. Keiderling, and C. Pfleiderer. “Kinetic Small Angle Neutron Scattering of the Skyrmion Lattice in MnSi.” en. In: *New J. Phys.* 18.7 (2016), p. 075017. DOI: 10.1088/1367-2630/18/7/075017.

[141] W. Münzer, A. Neubauer, T. Adams, S. Mühlbauer, C. Franz, F. Jonietz, R. Georgii, P. Böni, B. Pedersen, M. Schmidt, A. Rosch, and C. Pfleiderer. “Skyrmion Lattice in the Doped Semiconductor {Fe$_{1-x}$Co$_x$Si}.” en. In: *Phys. Rev. B* 81.4 (Jan. 2010). DOI: 10.1103/PhysRevB.81.041203.

[142] M. Halder, A. Chacon, A. Bauer, W. Simeth, S. Mühlbauer, H. Berger, L. Heinen, M. Garst, A. Rosch, and C. Pfleiderer. “Thermodynamic Evidence of a Second Skyrmion Lattice Phase and Tilted Conical Phase in {\cso}.” In: *Phys. Rev. B* 98.14 (Oct. 2018), p. 144429. DOI: 10.1103/PhysRevB.98.144429.

[143] T. Schwarze, J. Waizner, M. Garst, A. Bauer, I. Stasinopoulos, H. Berger, C. Pfleiderer, and D. Grundler. “Universal Helimagnon and Skyrmion Excitations in Metallic, Semiconducting and Insulating Chiral Magnets.” en. In: *Nat Mater* 14.5 (May 2015), pp. 478–483. DOI: 10.1038/nmat4223.

[144] E. A. Karhu, U. K. Rößler, A. N. Bogdanov, S. Kahwaji, B. J. Kirby, H. Fritzsche, M. D. Robertson, C. F. Majkrzak, and T. L. Monchesky. “Chiral Modulations and Reorientation Effects in MnSi Thin Films.” In: *Phys. Rev. B* 85.9 (Mar. 2012), p. 094429. DOI: 10.1103/PhysRevB.85.094429.

[145] S. A. Meynell, M. N. Wilson, H. Fritzsche, A. N. Bogdanov, and T. L. Monchesky. “Surface Twist Instabilities and Skyrmion States in Chiral Ferromagnets.” In: *Phys. Rev. B* 90.1 (July 2014), p. 014406. DOI: 10.1103/PhysRevB.90.014406.

[146] S. V. Grigoriev, A. S. Sukhanov, and S. V. Maleyev. “From Spiral to Ferromagnetic Structure in B20 Compounds: Role of Cubic Anisotropy.” In: *Phys. Rev. B* 91.22 (June 2015), p. 224429. DOI: 10.1103/PhysRevB.91.224429.

[147] A. O. Leonov. “Chiral Skyrmion States in Non-Centrosymmetric Magnets.” In: *ArXiv14062177 Cond-Mat* (June 2014). arXiv: 1406.2177 [cond-mat].